Universität Rostock
Traditio et Innovatio

Dipole-dipole interactions in confined planar geometries

Dissertation
zur
Erlangung des akademischen Grades
doctor rerum naturalium (Dr. rer. nat.)
der Mathematisch-Naturwissenschaftlichen Fakultät
der Universität Rostock

vorgelegt von

Helge Dobbertin, geb. am 31.03.1992 in Crivitz
aus Rostock

Rostock, den 10.11.2021

https://doi.org/10.18453/rosdok_id00003563

Referees:

Prof. Dr. Stefan Scheel

Institut für Physik, Universität Rostock
Albert-Einstein-Str. 23
18059 Rostock, Germany

Dr. Daniel Bloch, Directeur de recherche

Laboratoire de Physique des Lasers
Université Paris 13 - Institut Galilée - CNRS UMR7538
99, avenue Jean-Baptiste Clément
93430 Villetaneuse, France

Opening of the doctoral degree procedure: 24.11.2021
Date of scientific colloquium: 25.02.2022

Zusammenfassung

Um Quanteneffekte aus dem Labor in praktische Anwendungen zu überführen, werden skalierbare Plattformen benötigt. Ein Ansatz besteht darin, thermische Gase mit Nanostrukturen zu koppeln, die die atomaren Wechselwirkungen kontrollieren. Um die zugrundeliegenden Prozesse besser zu verstehen, untersucht diese Arbeit die Wechselwirkungen thermischer Gase an einer Oberfläche oder in einer Nanokavität, die nahe ihrer Resonanz angeregt werden. Ein Schwerpunkt ist der Casimir–Polder Effekt, eine durch thermische und Quantenfluktuationen verursachte Wechselwirkung zwischen Atomen und Oberflächen. Die zu seiner Messung verwendeten spektroskopischen Methoden quantifizieren ihn mit einem effektiven Wechselwirkungskoeffizienten. Es zeigt sich, dass sich dieser effektive Koeffizient nicht unmittelbar mit den üblichen Theoriewerten vergleichen lässt. Außerdem werden die Atom-Atom-Wechselwirkungen von dichten, thermischen Gasen in Nanokavitäten untersucht. Es zeigen sich dichteabhängige Linienverschiebungen und -verbreiterungen, die Modelle aus der kontinuierlichen Elektrodynamik nicht erklären können. Sie lassen sich durch die Eigenschaften der Kavität steuern.

Abstract

Scalable platforms are needed to transfer quantum effects from the laboratory to real-world applications. One approach is to interface thermal vapors with nanostructures that control the atomic interactions. To better understand these processes, this thesis investigates the interactions of thermal vapors that are confined by a planar surface or a nanocavity and subjected to near-resonant light. One focus is on the Casimir–Polder effect, an atom-wall interaction caused by thermal and quantum fluctuations. The spectroscopic methods used to measure the effect quantify it with an effective interaction coefficient. It turns out that this effective coefficient cannot be directly compared with the usual theoretical values. Furthermore, the atom-atom interactions of dense thermal vapors in nanocavities are investigated. Density-dependent line shifts and broadenings beyond continuous electrodynamics models are found. They can be controlled by the properties of the nanocavities.

Contents

1. Introduction **1**

2. Foundations of atom-field interactions **5**

- 2.1. Classical electrodynamics 5
  - 2.1.1. Meaning of the Green's tensor 6
  - 2.1.2. Properties of the Green's tensor 8
  - 2.1.3. Computation of the Green's tensor 9
- 2.2. Field quantization in media 12
- 2.3. Equation of motion 13
  - 2.3.1. The quantum optical master equation 15
  - 2.3.2. The Heisenberg equation of motion 17
  - 2.3.3. The coupled dipole model 19
  - 2.3.4. Limitations of the coupled dipole model 25
  - 2.3.5. Polarizability and atom-atom interactions at zero temperature 28
- 2.4. The scattered light field 29
  - 2.4.1. Light transmission and reflection of an atomic ensemble 31

3. The Casimir–Polder effect in spectroscopy **34**

- 3.1. Computation of Casimir–Polder shifts 35
  - 3.1.1. The nonretarded limit 36
  - 3.1.2. Rigorous computations for the rubidium D_2 line 38
  - 3.1.3. The polarizability of the rubidium D_2 line 41
  - 3.1.4. The answer to life, the universe, and everything 42
- 3.2. The continuous medium approximation 43
  - 3.2.1. Formal solution and nonlocal response 45
  - 3.2.2. Local limit in absence of atom-wall interactions 46
  - 3.2.3. Lorentz–Lorenz relation 49
  - 3.2.4. Atomic collisions 51
  - 3.2.5. The velocity distribution in front of a surface 53
- 3.3. Theoretical description of spectroscopic techniques 53
  - 3.3.1. Selective reflection spectroscopy 53
  - 3.3.2. Frequency-modulated selective reflection spectroscopy 55
  - 3.3.3. Thin cell spectroscopy 57
- 3.4. Calculation of spectra 57
  - 3.4.1. Low-density frequency-modulated selective reflection spectra 58
  - 3.4.2. Low-density thin cell transmission spectra 60
  - 3.4.3. Atom-atom interactions in thin cell spectra 63

4. Atom-atom interactions in nanocavities 66
4.1. The collective Lamb shift . . . 66
4.1.1. Derivation and discussion . . . 67
4.2. Atom-atom interactions in sapphire nanocavities . . . 70
4.2.1. Granular model . . . 70
4.2.2. Continuous fit model . . . 71
4.2.3. Simulation procedure . . . 71
4.2.4. Theory vs. experiment . . . 74
4.3. Atom-atom interactions in coated nanocavities . . . 76
4.4. Cold gases in free space . . . 79
4.4.1. Renormalization group approach . . . 81

5. Conclusion and outlook 83

A. Electromagnetic Green's tensors 86
A.1. The Green's tensor of bulk media . . . 86
A.2. The image dipole method . . . 87
A.3. Construction of surface and cavity Green's tensors . . . 88
A.3.1. Vector wave functions . . . 88
A.3.2. Boundary conditions and Fresnel reflection coefficients . . . 90
A.3.3. Surface and cavity Green's tensors . . . 91
A.4. The uniaxial birefringent surface . . . 94
A.5. Cylindrical symmetry and 1-D Green's function . . . 95
A.6. The discrete dipole approximation . . . 96
A.6.1. Block Toeplitz matrices . . . 98

B. Auxiliary calculations on atom-light interactions 100
B.1. Field quantization in homogeneous media . . . 100
B.2. Commutation rules of partial atom and field operators . . . 101
B.3. Expectation values of thermal fields . . . 101
B.4. Position memory of the Green's tensor . . . 102
B.5. Green's tensor contour integration . . . 104
B.6. Transformation between quantum mechanical pictures . . . 105
B.7. Conducting the rotating wave approximation . . . 106
B.8. The two-atom coupled dipole model at zero temperature . . . 108

C. Transition dipole moments 109

D. Permittivity models 111

E. Additions regarding spectra and their computation **114**
E.1. Oscillation correction 114
E.2. Input-output relation for multilayered media 114
E.3. Casimir–Polder effect with an atom-surface resonance 115
E.3.1. Frequency-modulated selective reflection spectrum 118
E.4. Additional dense vapor spectra 120

Bibliography **121**

Specific notations

Tensor product between states and density operators	$\lvert g_A\rangle \otimes \lvert g_B\rangle = \lvert g_A, g_B\rangle$, $\hat{\rho} = \hat{\rho}_A \otimes \hat{\rho}_B$
Dyadic product between vectors	$\mathbf{a} \otimes \mathbf{b} = \mathbf{a}\mathbf{b}^T$
Scalar products between vectors	$\mathbf{a} \cdot \mathbf{b} = \mathbf{a}^T\mathbf{b}$, $\mathbf{a} \cdot \boldsymbol{M}\mathbf{b} = \mathbf{a}^T\boldsymbol{M}\mathbf{b} = \mathbf{b}^T\boldsymbol{M}^T\mathbf{a}$
Commutator between vector-valued operators	$\left[\hat{\mathbf{E}}, \hat{\mathbf{B}}\right] = \hat{\mathbf{E}} \otimes \hat{\mathbf{B}} - (\hat{\mathbf{B}} \otimes \hat{\mathbf{E}})^T$

Acronyms

CP	Casimir–Polder
CLS	collective Lamb shift
DDA	discrete dipole approximation
EM field	electromagnetic field
(FM)SR	(frequency-modulated) selective reflection
FWHM	full width at half maximum
KK relation	Kramers–Kronig relation
LDOS	local density of states
LL shift	Lorentz–Lorenz shift
QED	quantum electrodynamics
RG	renormalization group
VWF	vector wave function

1. Introduction

The understanding of light-matter interactions and the technologies derived from it shape our daily lives. We have become accustomed to light sources like lasers and LEDs, the sensors of our digital cameras, the global positioning system (GPS) enabled by atomic clocks, medical imaging that utilizes x-ray or magnetic resonance imaging (MRI), and many more. The realization that both light and matter are quantized gave rise to the research field of quantum optics. Today it has matured to the degree that quantum effects are to be used to open new fields of applications, marking the beginning of a “second quantum revolution” [1]. Specifically, scientists aim to construct quantum-enhanced sensors, erect secure quantum communication networks, and solve simulation and computation problems that lie beyond the reach of classical computers [2, 3]. Many physical platforms are investigated as candidates to implement their share of these technologies. One idea is to use hot [4] or cold atoms coupled to nanophotonic structures [5].

Atoms offer a small radiative linewidth and optimal reproducibility because all atoms of the same kind are equal. Therefore, even photons emitted by two different atoms may be near identical. This sets atoms apart from artificial light emitters like quantum dots or nitrogen-vacancy (NV) centers that can be tuned and tailored to the user’s needs, but vary in their exact properties and feature additional coupling to their environment, e.g. with phonons. Often alkali atoms are used because of their simple electronic structure with one valence electron, their long-lived nuclear spins, the high vapor pressure at moderate temperatures [6, 7], and the transition frequencies accessible by common laser systems. Furthermore, atoms can be excited to a Rydberg state [8] characterized by a high principal quantum number. Rydberg atoms are highly sensitive to external fields and exhibit strong dipolar interactions with other particles. The interaction between two Rydberg atoms can be so strong that the induced line shift exceeds the linewidth of the laser. This prohibits the excitation of a second Rydberg atom in the vicinity of a first one, an effect known as Rydberg blockade [9, 10]. Recently, it has been utilized to build a single-photon source in a thermal vapor [11]. Additionally, experiments demonstrated coherent light storage [12] in a room-temperature vapor over one second [13]. Such a quantum memory is a key resource for quantum repeaters [14] that are required for long-distance quantum networks. The advances described above fuel the vision of atomic vapor-based quantum networks operating under room temperature conditions.

Thermal atomic vapors are usually handled in chemically resilient vapor cells, see Fig. 1.1. They are attached to a reservoir with an alkali metal deposit which can be heated to release more atoms into the gaseous phase. Atomic vapor cells are used in a wide variety of applications. Examples are Faraday filters [19, 20], optical isolators [21], gas detectors [22], motional sensors [23], DC field sensors [24], microwave electrometers [25, 26] with high spatial resolution [27, 28], atomic clocks the size of a grain of rice [29, 30], gyroscopes [31, 32] and optical magnetometers [33–37]. Room-temperature, vapor-cell-based magnetometers are utilized in life science to

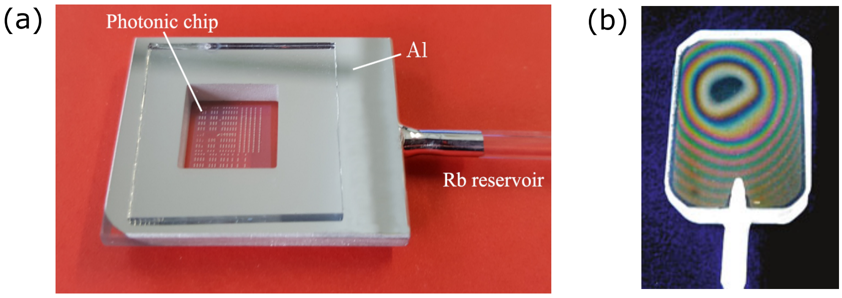

Figure 1.1: (a) Vapor cell attached to a rubidium reservoir and bonded with a photonic chip taken from Refs. [15, 16]. (b) Wedged vapor cell taken from Refs. [17, 18] with visible Newton's rings interference patterns. At the center of the rings, the windows are 30 nm apart, which increases to 2 µm near the stem at the bottom of the photo.

record nerve impulses in animals [38] or the activity of human hearts [39, 40] and brains [41–43]. Many of the above devices are enabled or improved by the trend of miniaturization, which reduces power consumption and cost, and increases spatial resolution and portability. Atoms can become confined only nanometers, i.e. only a fraction of a transition wavelength, away from macroscopic surfaces, e.g., in wedged vapor cell [18, 44] and atomic cladding waveguide [16, 45] experiments.

In these cases, the electromagnetic properties of the macroscopic environment shape the interactions between the atomic dipoles. The effects can be studied in the framework of macroscopic quantum electrodynamics (QED) [46–48] whose modern version was developed in the 1990s [49, 50]. It provides a representation of field operators in arbitrary absorbing and dispersing linear media in terms of the classical electromagnetic Green's tensor. This can be seen as a generalized mode expansion where photons occupy the same modes as their classical wave counterparts.

The theory accounts for the quantum fluctuations in matter and fields that can spontaneously polarize neutral particles such as atoms and introduce an effective interaction with the surrounding macroscopic bodies. This atom-wall interaction leads to a radiative line shift [47, 51, 52] named after Casimir and Polder who computed it in 1948 [53]. It is one of several[1] so-called dispersion forces [51] which are caused by fluctuations of the quantum vacuum and depend on the variations of atom and body properties with frequency[2].

The atoms close to the walls of a vapor cell experience a strong shift of their resonance lines. For most applications, this Casimir–Polder shift constitutes an obstacle. But here it creates the opportunity to measure the effect accurately. A suitable method for this is selective reflection (SR) spectroscopy [57] which has already been used over a century ago [58]. In SR, one observes the change in reflectivity at an interface of a dielectric and an atomic vapor when tuning the

---

[1] Analogously, interactions arise between two microscopic particles, called van der Waals interactions, or between two macroscopic bodies, which are known as Casimir forces [47, 51, 52].

[2] Fluctuations are linked to dissipation (fluctuation-dissipation theorem) which is linked to a dispersive real part of the refractive index (Kramers–Kronig relations). Therefore, the fluctuations in a medium (in thermal equilibrium) depend on its frequency-dependent response function.

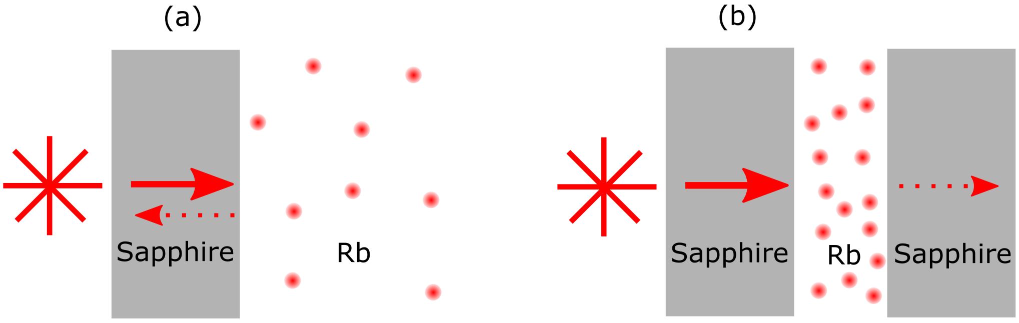

Figure 1.2: Concept sketches of two spectroscopic techniques studied in this thesis. Near-resonant laser light impinges on (a) a thin rubidium vapor behind a dielectric surface and (b) a dense rubidium vapor in a planar nanocavity whose width is less or equal to the transition wavelength of rubidium. In (a) the presence of the vapor causes changes to the reflectivity of the interface that are recorded as a function of the laser detuning. This so-called selective reflection spectroscopy allows measuring the Casimir–Polder interaction between the atoms and the dielectric wall. In (b) the transmission through the cavity is recorded to probe the properties of a slab of thermal atoms with nanometer thickness. Wedged vapor cells [54, 55] offer thicknesses that vary linearly along the wedge over macroscopic distances. The increase is so small that locally the walls can be assumed to be parallel as in (b). Sapphire is an established cell material that can withstand chemically aggressive rubidium vapor [56].

laser frequency across the atomic resonance, see Fig. 1.2 a. Since atoms with different distances to the wall contribute to the SR signal, a theoretical model is required to extract information on the Casimir–Polder shift[3]. Usually, one assumes the shift to decay as C_3/z^3, where z is the atom-surface distance and C_3 is a constant interaction coefficient that is to be determined [60]. However, an exact computation via macroscopic QED shows that the C_3 coefficient is not constant but changes just 10 nm away from the surface. Therefore we rederive the theory of SR spectroscopy in the framework of macroscopic QED and explore the consequences of the more complex behavior on the determination of the Casimir–Polder effect. In addition, we do the same for the transmission spectra of thin cells, see Fig. 1.2 b. This setup has the advantage that the cell walls, which can be only tens or hundreds of nanometers apart, limit the atom-surface distances that contribute to the signal.

Experiments to detect atom-wall interactions are usually conducted with a low vapor density. However, thermal vapor cells are also ideal for studying the interactions in dense vapors because the number of atoms in the gas phase varies nearly exponentially with temperature [6, 7]. When such a vapor is resonantly excited, transient atomic dipoles are produced, which mutually interact. This thesis analyzes how the presence of material boundaries modifies these resonant dipole-dipole interactions.

In an ensemble of atoms, where many dipoles interact simultaneously, new properties can emerge. Famous examples are suppressed or enhanced spontaneous emission rates, known as sub- or superradiance [61, 62], which were first predicted by Dicke in 1954 [63]. Resonant atom-atom interactions can be undesired, e.g., in an array of atomic clocks where the additional interaction degrades the precision [64–66]. In contrast, they can also be an asset, e.g., to enhance light-matter interfaces and to create a perfect mirror out of a single layer of atoms [67, 68].

---

[3] One could imagine measuring the shift for each atom-surface distance individually, given that a single atom can be trapped at a definite position in front of a nanostructure using optical tweezers [59]. However, at short distances (< 100 nm in Ref. [59]), the Casimir–Polder force exceeds the retention force of the optical trap. In addition, the trapping potential is challenging to design as the exact Casimir–Polder interaction and the reflections of the trapping beam from the surface must be taken into account.

One of the most fundamental collective effects is the local field correction that has already been established in the 19th century [69, 70]. When an atom in a continuous medium is excited, it polarizes its surrounding. The excited atomic dipole that interacts with the induced dipoles behaves as if the original field was modified, hence the name local field correction. In a homogeneously broadened system, the effect can be expressed as a density-dependent line shift, the so-called Lorentz–Lorenz shift. Since 2014 a series of surprising theoretical [71, 72] and experimental [73–75] works showed the absence of the Lorentz–Lorenz shift in a dense cold vapor subjected to near-resonant light. This deviation from textbook electrodynamics stems from the granular nature of the gas that is not a continuous medium. Theories [71, 72] suggested that a part of the Lorentz–Lorenz shift is recovered at higher temperatures. This motivated an experiment with dense thermal vapors in a wedged cell published in 2018 [44]. Wedged cells, like the one shown in Fig. 1.1 b, feature a gas-filled gap whose thickness varies linearly between 0 nm and the micrometer scale [54, 55]. They can reach an averaged surface roughness of 1 Å [55] and are a couple of centimeters long. When a laser illuminates a small area, the local cell walls are almost parallel as in Fig. 1.2 b. One can investigate different vapor layer thicknesses by illuminating different parts of the wedge. Therefore both density and geometry dependence can be explored. The experimental transmission spectra could only be fitted if an additional broadening and shift are included that grow linearly with density [44]. These collective shifts and broadenings did not comply with the textbook Lorentz–Lorenz theory and instead featured an unprecedented oscillatory dependence on the thickness of the vapor layer. Our theory can reproduce the observed effects for the first time. Furthermore, we predict that the collective effects can be tuned using cavity coatings so that our model can be tested in future experiments.

In this thesis, we focus on simple planar geometries because they allow the closest and clearest comparison between theory and state-of-the-art thermal vapor experiments. However, by utilizing macroscopic QED our results can be transferred to any other system for which the electromagnetic Green's tensor is available. Thereby, they might contribute to the future description and design of devices that couple atoms and photonic nanostructures in the spirit of the "second quantum revolution".

In chapter 2, we derive our basic formalism using the framework of macroscopic QED. In chapter 3, we investigate the Casimir–Polder effect and the methods with which it is commonly determined in vapor cells. In chapter 4, we study atom-atom interactions in nanocavities and compare our findings to recent experiments. Finally, we summarize our findings and give an outlook on future research.

2. Foundations of atom-field interactions

In this chapter, we present the theoretical foundations that will enable us to study the interactions of atoms driven by a coherent laser field, thermal fluctuations, and quantum fluctuations in the planar layered macroscopic environments illustrated in Fig. 1.2. We begin by reviewing the Green's functions of classical electrodynamics. They are used to express the quantized electromagnetic (EM) field in linear macroscopic environments [46, 47]. This field representation and the standard theory of open quantum systems [76] allow us to derive atomic equations of motion that explicitly account for atom-wall and resonant atom-atom interactions. Their stationary solutions provide the atomic dipole moments that lead to the reflection and transmission spectra that are investigated in the following chapters.

2.1. Classical electrodynamics

The Maxwell equations form the basis for studying electromagnetic interactions. With free charge density $\rho(\mathbf{r},t)$ and currents $\mathbf{j}(\mathbf{r},t)$ they read

$$\boldsymbol{\nabla}\cdot\mathbf{D}(\mathbf{r},t)=\rho(\mathbf{r},t), \tag{2.1}$$

$$\boldsymbol{\nabla}\cdot\mathbf{B}(\mathbf{r},t)=0, \tag{2.2}$$

$$\boldsymbol{\nabla}\times\mathbf{E}(\mathbf{r},t)=-\dot{\mathbf{B}}(\mathbf{r},t), \tag{2.3}$$

$$\boldsymbol{\nabla}\times\mathbf{H}(\mathbf{r},t)=\mathbf{j}(\mathbf{r},t)+\dot{\mathbf{D}}(\mathbf{r},t), \tag{2.4}$$

and are completed by a set of constitutive relations

$$\mathbf{D}(\mathbf{r},t)=\epsilon_0\mathbf{E}(\mathbf{r},t)+\mathbf{P}(\mathbf{r},t),\quad \mathbf{H}(\mathbf{r},t)=\mathbf{B}(\mathbf{r},t)/\mu_0-\mathbf{M}(\mathbf{r},t), \tag{2.5}$$

specific to the respective environment. Throughout this thesis, we assume linear, spatially local, isotropic, and non-magnetic media. The latter assumption is common to optics as the magnetic response of natural materials vanishes above the Gigahertz regime. With electric susceptibility $\chi(\mathbf{r},t)$, the polarization density can be written as

$$\mathbf{P}(\mathbf{r},t)=\epsilon_0\int_{-\infty}^{\infty}dt'\,\chi(\mathbf{r},t')\mathbf{E}(\mathbf{r},t-t'). \tag{2.6}$$

We transform into the Fourier domain, where the constitutive relations become[1]

$$\mathbf{D}(\mathbf{r},\omega)=\epsilon_0\epsilon(\mathbf{r},\omega)\mathbf{E}(\mathbf{r},\omega),\quad \mathbf{H}(\mathbf{r},\omega)=\mathbf{B}(\mathbf{r},\omega)/\mu_0, \tag{2.7}$$

and the dielectric permittivity is given by

$$\epsilon(\mathbf{r},\omega)=1+\int_{-\infty}^{\infty}dt\,\chi(\mathbf{r},t)e^{i\omega t}. \tag{2.8}$$

---

[1] We incorporate free charges within metals into the permittivity $\epsilon(\mathbf{r},\omega)=\epsilon_{bound}(\mathbf{r},\omega)+i\sigma(\mathbf{r},\omega)/\omega$ [51].

Because $\chi(\mathbf{r},t)$ is real, $\epsilon(\mathbf{r},\omega)$ obeys the Schwarz reflection principle [51]

$$\epsilon^*(\mathbf{r},\omega)=\epsilon(\mathbf{r},-\omega^*), \tag{2.9}$$

and because $\chi(\mathbf{r},t)$ is causal[2], $\epsilon(\mathbf{r},\omega)$ obeys the Kramers–Kronig relations [51, 77]

$$\mathrm{Re}\,\epsilon(\mathbf{r},\omega)=1+\frac{1}{\pi}P\int_{-\infty}^{\infty}d\omega'\,\frac{\mathrm{Im}\,\epsilon(\mathbf{r},\omega')}{\omega'-\omega}, \tag{2.10}$$

$$\mathrm{Im}\,\epsilon(\mathbf{r},\omega)=\frac{\sigma(\mathbf{r},0)}{\omega}-\frac{1}{\pi}P\int_{-\infty}^{\infty}d\omega'\,\frac{\mathrm{Re}\,\epsilon(\mathbf{r},\omega')-1}{\omega'-\omega}, \tag{2.11}$$

with conductivity $\sigma(\mathbf{r},\omega)$. The Fourier transformed Maxwell equations become

$$\epsilon_0\,\boldsymbol{\nabla}\cdot[\epsilon(\mathbf{r},\omega)\mathbf{E}(\mathbf{r},\omega)]=\rho(\mathbf{r},\omega), \tag{2.12}$$

$$\boldsymbol{\nabla}\cdot\mathbf{B}(\mathbf{r},\omega)=0, \tag{2.13}$$

$$\boldsymbol{\nabla}\times\mathbf{E}(\mathbf{r},\omega)=i\omega\mathbf{B}(\mathbf{r},\omega), \tag{2.14}$$

$$\boldsymbol{\nabla}\times\mathbf{B}(\mathbf{r},\omega)=\mu_0\mathbf{j}(\mathbf{r},\omega)-\frac{i\omega}{c^2}\epsilon(\mathbf{r},\omega)\mathbf{E}(\mathbf{r},\omega). \tag{2.15}$$

Combing the last two relations, we obtain the vectorial Helmholtz equation

$$\boldsymbol{\nabla}\times\boldsymbol{\nabla}\times\mathbf{E}(\mathbf{r},\omega)-\frac{\omega^2}{c^2}\epsilon(\mathbf{r},\omega)\mathbf{E}(\mathbf{r},\omega)=i\mu_0\omega\,\mathbf{j}(\mathbf{r},\omega), \tag{2.16}$$

for the electric field whose solution can be written with a classical Green's tensor as

$$\mathbf{E}(\mathbf{r},\omega)=i\mu_0\omega\int d^3\mathbf{r}'\,\boldsymbol{G}(\mathbf{r},\mathbf{r}',\omega)\mathbf{j}(\mathbf{r}',\omega). \tag{2.17}$$

The Green's tensor is uniquely determined by its own vectorial Helmholtz equation

$$\boldsymbol{\nabla}\times\boldsymbol{\nabla}\times\boldsymbol{G}(\mathbf{r},\mathbf{r}',\omega)-\frac{\omega^2}{c^2}\epsilon(\mathbf{r},\omega)\,\boldsymbol{G}(\mathbf{r},\mathbf{r}',\omega)=\delta(\mathbf{r}-\mathbf{r}')\boldsymbol{I}, \tag{2.18}$$

and the radiation boundary condition $\boldsymbol{G}(\mathbf{r},\mathbf{r}',\omega)\to 0$ at $|\mathbf{r}-\mathbf{r}'|\to\infty$.

2.1.1. Meaning of the Green's tensor

Let us consider an oscillating dipole moment $\mathbf{p}(\omega)$ at $\mathbf{r}_0$ and its current density

$$\mathbf{j}(\mathbf{r},\omega)=-i\omega\mathbf{p}(\omega)\delta(\mathbf{r}-\mathbf{r}_0). \tag{2.19}$$

---

[2] An action at $\mathbf{r}'$ can cause a reaction at $\mathbf{r}$ only if a time $t\geq|\mathbf{r}-\mathbf{r}'|/c$ has passed. In our local system with $\mathbf{r}=\mathbf{r}'$, this means $\chi(\mathbf{r},t)=\Theta(t)\chi(\mathbf{r},t)$. After Fourier transformation, this equality leads to the usual Kramers–Kronig relations. The term $\sigma(\mathbf{r},0)/\omega$ is caused by the non-vanishing long-time asymptote in metals [51, 77].

According to Eq. (2.17), the field produced by that dipole current is given by

$$\mathbf{E}(\mathbf{r},\omega)=\mu_0\omega^2\boldsymbol{G}(\mathbf{r},\mathbf{r}_0,\omega)\mathbf{p}(\omega). \tag{2.20}$$

Thus, the Green's tensor describes the field that a dipole located at $\mathbf{r}_0$ produces at a probe point $\mathbf{r}$. Let us further compute the power radiated by our dipole. Using Eqs. (2.19) and (2.20), we find [78]

$$P(\omega)=-\frac{1}{2}\int d^3\mathbf{r}\,\mathrm{Re}\,\{\mathbf{j}^*(\mathbf{r},\omega)\cdot\mathbf{E}(\mathbf{r},\omega)\}=\frac{\mu_0}{2}\omega^3\mathbf{p}^*(\omega)\cdot\mathrm{Im}\,\boldsymbol{G}(\mathbf{r}_0,\mathbf{r}_0,\omega)\mathbf{p}(\omega). \tag{2.21}$$

The emitted power is proportional to the imaginary part of the Green's tensor with probe and source point at the dipole's location. The same Green's tensor also appears in the spontaneous decay rate of an atom, as we derive later in Eq. (2.98). In a two-level system with transition dipole moment $\mathbf{d}_{eg}$ between ground and excited states g and e, the spontaneous decay rate at zero temperature is

$$\Gamma_{eg}=\frac{2\mu_0}{\hbar}\omega_{eg}^2\mathbf{d}_{eg}\cdot\mathrm{Im}\,\boldsymbol{G}(\mathbf{r}_0,\mathbf{r}_0,\omega_{eg})\mathbf{d}_{ge}. \tag{2.22}$$

One can even determine the fraction of light emitted into a specific mode [16, 79] by expanding the Green's tensor into a corresponding basis [80]. The Green's tensor appears in the radiated power and the spontaneous decay rate because it determines the number of available modes for the photons that are about to be emitted. The local density of states (LDOS), i.e. the number of modes per unit volume and angular frequency for a dipole axis along the $\mathbf{e}_p$ direction, is [78, 81]

$$\rho_p(\mathbf{r},\omega)=\frac{6\omega}{\pi c^2}\mathbf{e}_p\cdot\mathrm{Im}\,\boldsymbol{G}(\mathbf{r},\mathbf{r},\omega)\mathbf{e}_p. \tag{2.23}$$

It is instructive to insert the Green's tensor of a bulk medium, Eq. (A.8) in App. A.1, in the above relations to retrieve known results from fundamental physics. Denoting the distance as $\boldsymbol{\rho}=\mathbf{r}-\mathbf{r}_0$, we obtain the near- and far-field limits of a dipole in a homogeneous medium as

$$\mathbf{E}^{\mathrm{far}}(\mathbf{r},\omega)=\frac{k^2e^{ik\rho}}{4\pi\epsilon_0\epsilon(\omega)\rho}\left[\boldsymbol{I}-\mathbf{e}_\rho\otimes\mathbf{e}_\rho\right]\mathbf{p}(\omega)\quad\text{for }|k\rho|\gg 1, \tag{2.24}$$

$$\mathbf{E}^{\mathrm{near}}(\mathbf{r},\omega)=-\frac{\delta(\boldsymbol{\rho})\mathbf{p}(\omega)}{3\epsilon_0\epsilon(\omega)}-\frac{\boldsymbol{I}-3\mathbf{e}_\rho\otimes\mathbf{e}_\rho}{4\pi\epsilon_0\epsilon(\omega)\rho^3}e^{ik\rho}\mathbf{p}(\omega)\quad\text{for }|k\rho|\ll 1. \tag{2.25}$$

In the near field, the dipole field decays as $1/\rho^3$, while in the far field, we obtain a transverse electric field that decays as $e^{ik\rho}/\rho$. Furthermore, we obtain the spontaneous decay rate in free space predicted by Wigner and Weisskopf [82] and the density of states[3]

$$\Gamma_{eg} = \frac{\omega_{eg}^3 |\mathbf{d}_{eg}|^2}{3\pi\epsilon_0 c^3 \hbar}, \quad \rho = \frac{\omega^2}{\pi^2 c^3}. \tag{2.26}$$

The decay rate is the well-known Einstein A coefficient, while the density of states is often used to derive Planck's law. The strength of the Green's formalism is that we are not limited to free space or homogeneous media. We can immediately determine all of the above characteristics in any environment once we have obtained the Green's tensor by solving the corresponding Helmholtz equation (2.18).

2.1.2. Properties of the Green's tensor

The Green's tensor possesses a series of useful, general properties. Like the permittivity, it obeys the Schwarz reflection principle [51]

$$\boldsymbol{G}(\mathbf{r}, \mathbf{r}', -\omega^*) = \boldsymbol{G}^*(\mathbf{r}, \mathbf{r}', \omega). \tag{2.27}$$

which implies that the Cauchy-Riemann equations are fulfilled in the upper half of the complex ω plane. We can quickly derive the high-frequency limit [51]

$$\lim_{|\omega| \to \infty} \frac{\omega^2}{c^2} \boldsymbol{G}(\mathbf{r}, \mathbf{r}', \omega) = -\delta(\mathbf{r} - \mathbf{r}') \boldsymbol{I}, \tag{2.28}$$

noting that $\epsilon(\infty) = 1$ and the ω^2 term dominates the Helmholtz equation (2.18) when $\omega \to \infty$. Combining these two facts, $\omega^2 \boldsymbol{G}(\mathbf{r}, \mathbf{r}', \omega)$ is analytic in the upper half of the complex ω plane and on the real axis[4]. Therefore, we can treat frequency integrals through contour integration techniques. Furthermore, the Green's tensor follows reciprocity. If positions and orientations of source and probe points are exchanged, we have $\mathbf{e}_2 \cdot \boldsymbol{G}(\mathbf{r}_2, \mathbf{r}_1, \omega) \mathbf{e}_1 = \mathbf{e}_1 \cdot \boldsymbol{G}(\mathbf{r}_1, \mathbf{r}_2, \omega) \mathbf{e}_2$ [51] and

$$\boldsymbol{G}^T(\mathbf{r}', \mathbf{r}, \omega) = \boldsymbol{G}(\mathbf{r}, \mathbf{r}', \omega). \tag{2.29}$$

Additionally, a useful integral relation can be derived. Starting from the Green's tensor as the left- and the right-inverse of the Helmholtz equation (2.18), we multiply with $\boldsymbol{G}^*$ and $\boldsymbol{G}$, respectively. Integrating over space and subtracting the two equations leads to [51]

$$\int d^3\mathbf{s} \, \frac{\omega^2}{c^2} \mathrm{Im}\, \epsilon(\mathbf{s}, \omega) \, \boldsymbol{G}(\mathbf{r}, \mathbf{s}, \omega) \boldsymbol{G}^*(\mathbf{s}, \mathbf{r}', \omega) = \mathrm{Im}\, \boldsymbol{G}(\mathbf{r}, \mathbf{r}', \omega). \tag{2.30}$$

Finally, we can utilize the superposition principle of linear optics. Assuming that both source and probe point reside in the same layer, we can decompose the Green's tensor into a bulk and

---

[3] $\mathrm{Im}\, G_{\mathrm{bulk}}(\mathbf{r}, \mathbf{r}, \omega) = \mathrm{Re}\, k(\omega)/(6\pi) \boldsymbol{I}$ obtained from Eq. (A.8) through a Taylor expansion of $\exp(ik\rho)$ [48].

[4] As an exception, $\omega^2 \boldsymbol{G}(\mathbf{r}, \mathbf{r}', \omega)$ can have a simple pole at $\omega = 0$ if the probe point $\mathbf{r}$ is located in a metallic material. This is caused by the fact that in metals $\mathrm{Im}\, \epsilon \propto 1/\omega$ when $\omega \to 0$ whereas in dielectrics $\mathrm{Im}\, \epsilon \propto \omega$. The pole becomes apparent in an appropriate decomposition of the Green's tensor, see Refs. [46, 51].

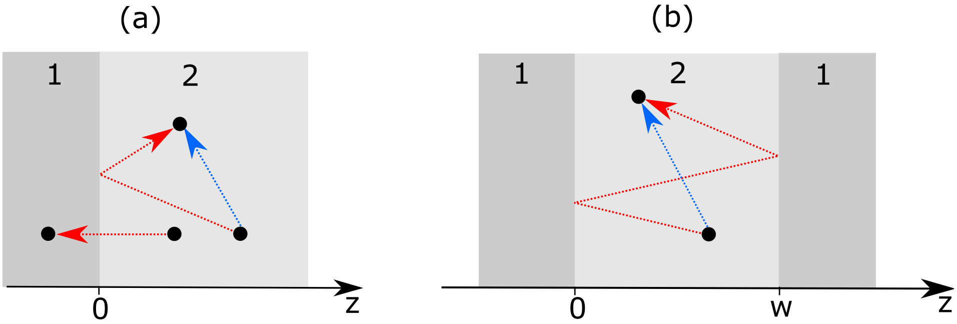

Figure 2.1: Sketch of photon pathways propagated by the bulk (blue dashed lines) and scattering (red dashed lines) contribution of the Green's tensor for (a) a surface and (b) a cavity geometry.

a scattering contribution [51], see Fig. (2.1),

$$\boldsymbol{G}(\mathbf{r},\mathbf{r}',\omega) = \begin{cases} \boldsymbol{G}_{\text{bulk}}(\mathbf{r},\mathbf{r}',\omega) + \boldsymbol{G}_{\text{sc}}(\mathbf{r},\mathbf{r}',\omega), & \mathbf{r},\mathbf{r}' \text{ in same layer} \\ \boldsymbol{G}_{\text{sc}}(\mathbf{r},\mathbf{r}',\omega), & \mathbf{r},\mathbf{r}' \text{ in different layers} \end{cases}. \tag{2.31}$$

The bulk contribution describes the field that would be created if all space was filled with the material of layer j and includes the singularity when probe and source point are equal. The scattering contribution ensures matching boundary conditions with other materials and describes the modifications due to the reflections at the material boundaries, as well as the transmission through different materials, see Fig. (2.1). Hence, the Helmholtz equation (2.18) is split up as

$$\left[\boldsymbol{\nabla} \times \boldsymbol{\nabla} \times -k_j^2(\mathbf{r},\omega)\right] \boldsymbol{G}_{\text{bulk}}(\mathbf{r},\mathbf{r}',\omega) = \delta(\mathbf{r}-\mathbf{r}')\boldsymbol{I}, \tag{2.32}$$

$$\left[\boldsymbol{\nabla} \times \boldsymbol{\nabla} \times -k_j^2(\mathbf{r},\omega)\right] \boldsymbol{G}_{\text{sc}}(\mathbf{r},\mathbf{r}',\omega) = \mathbf{0}. \tag{2.33}$$

2.1.3. Computation of the Green's tensor

Whereas the Green's tensor of bulk media is known analytically (see derivation in App. A.1) the scattering contribution of Green's tensor is often challenging to compute. When source and probe points both lie close to the macroscopic body, the Green's tensor can be approximated with the image dipole approach presented in App. A.2. In the nonretarded limit, the source dipole produces a quasi-static image of itself inside the macroscopic body that can be propagated to the probe point through the bulk Green's tensor. This is the simplest method to obtain an approximate Green's tensor of a planar surface but may be cumbersome to conduct in other geometries. An exact, closed-form expression for Green's tensor is only known for specific geometries, e.g., planar layered [83], cylindrical layered [84], or spherical layered [85] media. The Green's tensors for layered planar surfaces and cavities used in this thesis are derived in App. A.3 using vector wave functions [86]. Vector wave functions are constructed to fulfill the homogeneous vector Helmholtz equation and form a complete orthogonal basis in which the Green's tensor is expanded. The set of functions is chosen such that the expansion coefficients, which ensure that the boundary coefficients are met, can be obtained with reasonable effort for the given geometry.

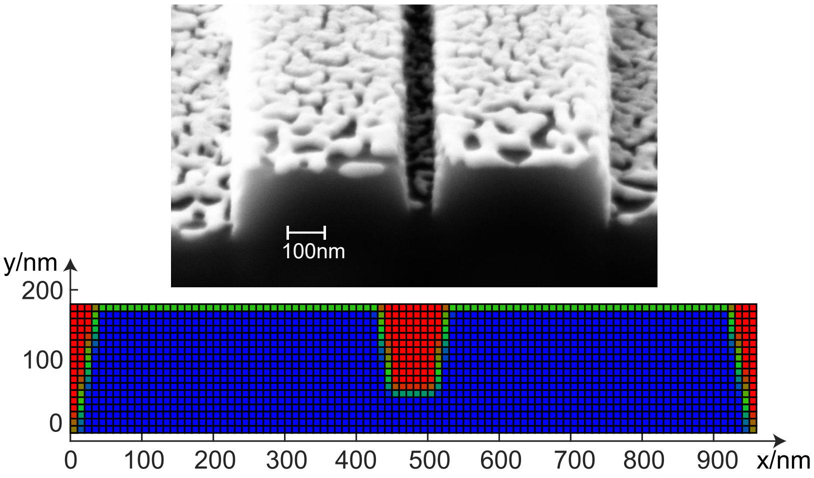

Figure 2.2: Upper part: Scanning electron microscopy (SEM) image of a slot waveguide structure [16]. The structure was sputtered with gold and cut with a focused ion beam (FIB) to record the cross section. Lower part: Model of the slot waveguide discretized with cubical unit cells colored according to the material: vacuum red, sapphire green, and silicon nitrite blue. Cells with multiple materials have been assigned an average permittivity, weighted according to the respective volume contribution, as a simple anti-aliasing filter.

In general scenarios, the Green's tensor can only be obtained by numerical techniques. Here we describe one of them: the discrete dipole approximation (DDA) [87]. First, we split the permittivity of our system into a background, for which we know the Green's tensor $\bar{\boldsymbol{G}}(\mathbf{r},\mathbf{r}',\omega)$, and the remaining material, $\epsilon(\mathbf{r},\omega)=\bar{\epsilon}(\mathbf{r},\omega)+\chi(\mathbf{r},\omega)$. As an example, let us consider the slot waveguide geometry in Fig. 2.2. The background consists of the substrate and the free space above it. $\chi(\mathbf{r},\omega)$ describes the contrast between the waveguide material and the free space background. We split the Helmholtz equation of the total system into two,

$$\left[\boldsymbol{\nabla}\times\boldsymbol{\nabla}\times-\frac{\omega^2}{c^2}\bar{\epsilon}(\mathbf{r},\omega)\right]\bar{\boldsymbol{G}}(\mathbf{r},\mathbf{r}',\omega)=\delta(\mathbf{r}-\mathbf{r}')\boldsymbol{I}, \tag{2.34}$$

$$\left[\boldsymbol{\nabla}\times\boldsymbol{\nabla}\times-\frac{\omega^2}{c^2}\bar{\epsilon}(\mathbf{r},\omega)\right]\left[\boldsymbol{G}(\mathbf{r},\mathbf{r}',\omega)-\bar{\boldsymbol{G}}(\mathbf{r},\mathbf{r}',\omega)\right]=\frac{\omega^2}{c^2}\chi(\mathbf{r},\omega)\boldsymbol{G}(\mathbf{r},\mathbf{r}',\omega), \tag{2.35}$$

such that the additional material behaves as a source term. Thus, we find

$$\boldsymbol{G}(\mathbf{r},\mathbf{r}',\omega)=\bar{\boldsymbol{G}}(\mathbf{r},\mathbf{r}',\omega)+\int d^3\mathbf{s}\,\bar{\boldsymbol{G}}(\mathbf{r},\mathbf{s},\omega)\frac{\omega^2}{c^2}\chi(\mathbf{s},\omega)\boldsymbol{G}(\mathbf{s},\mathbf{r}',\omega), \tag{2.36}$$

a volume integral integration that needs to be solved self-consistently. A simple approach is to approximate the integral by a sum over small elements (see Fig. 2.2), which then act as point-like, artificial dipoles, hence the name discrete dipole approximation. The discretization introduces local field corrections depending on the shape and size of the unit cells, see App. A.6.

For each source point $\mathbf{r}'$, one needs to compute the tensors $\boldsymbol{G}(\mathbf{r}_j, \mathbf{r}')$ once. Then, one obtains the Green's tensor at any probe point $\mathbf{r}$ via

$$\boldsymbol{G}(\mathbf{r}, \mathbf{r}', \omega) = \bar{\boldsymbol{G}}(\mathbf{r}, \mathbf{r}', \omega) + \frac{\omega^2}{c^2} \sum_j^N \bar{\boldsymbol{G}}(\mathbf{r}, \mathbf{r}_j, \omega) V_j \, \chi(\mathbf{r}_j, \omega) \boldsymbol{G}(\mathbf{r}_j, \mathbf{r}', \omega). \tag{2.37}$$

The discretized version of Eq. (2.36) is given in App. A.6 and can be solved in several ways. One is to reinsert the equation in itself, leading to the Born series expansion [52]. However, the Born series is often oscillatory rather than convergent. In some cases, convergence can be reached by admixing the zeroth-order term in each step with an appropriate weight [88, 89]. But in general, one needs to solve the linear equation system exactly [87]. A straightforward attempt has storage requirements of $\mathcal{O}(n^2)$ and a computation cost of $\mathcal{O}(n^3)$ for n discrete dipoles. This is usually too high. Therefore, one utilizes a regular grid of equally sized unit cells. The resulting matrices involve many repetitions giving rise to a Block Toeplitz structure [90, 91]. These special matrices feature storage requirements of $\mathcal{O}(n_x)$ and vector-matrix products which can be conducted with $\mathcal{O}(n_x \log n_x)$ effort instead of $\mathcal{O}(n_x^2)$, see App. A.6.

The discrete dipole approximation has several advantages: It is relatively easy to implement and can be directly used to compute Green's tensors at imaginary frequencies, which we require to compute dispersion interactions. Furthermore, we only need to discretize those parts of the system that are not covered by our analytical solutions. On the other hand, there are structures like the waveguide in Fig. 2.2 with a translational symmetry that the DDA cannot exploit. Instead, we truncate to a finite computational domain introducing an abrupt cutoff. Furthermore, no adaptive grid can be used without losing the advantages of the Block Toeplitz structure. This can render the DDA inaccurate or inoperable when the entire structure needs to be discretized at a fine resolution.

As an alternative to the DDA, one could consider finite difference methods in frequency [92] or time [93] domain. However, they also discretize known backgrounds such as surfaces and become cumbersome to implement on non-uniform grids. Green's tensors have also been computed with the boundary element method (BEM) [94], which uses flexible meshes, making it accurate and efficient at the same time [95]. However, the BEM method is tedious to implement and the existing scuff-em code [96] does not provide Green's tensors where probe and source points are non-identical. Recently, there have been promising approaches [97, 98] based on the expansion of the Green's tensors into modes that can be computed by the finite element method (FEM) [94]. They naturally provide Green's tensors between two arbitrary points and offer decent evaluation times with precomputed modes. In the following, we only apply Green's tensors of planar structures that can be derived analytically and are very fast to evaluate on a computer.

2.2. Field quantization in media

We now quantize the EM field in presence of macroscopic bodies utilizing Langevin noise [46, 48, 51]. In this thesis, the bodies will be surfaces or cavities but the approach applies to any geometry. The following quantization procedure does not concern the atomic vapor. Its interaction with the quantized field will be considered in the next section. The effect of quantum fluctuations can be incorporated into the classical Maxwell equations by introducing a noise charge $\rho_N(\mathbf{r},\omega)$ and a noise current density $\mathbf{j}_N(\mathbf{r},\omega)$. They derive from the Langevin noise polarization field $\mathbf{P}_N(\mathbf{r},\omega)$ as

$$\rho_N(\mathbf{r},\omega) = -\boldsymbol{\nabla}\cdot\mathbf{P}_N(\mathbf{r},\omega), \quad \mathbf{j}_N(\mathbf{r},\omega) = -i\omega\mathbf{P}_N(\mathbf{r},\omega), \tag{2.38}$$

and fulfill the continuity equation

$$\boldsymbol{\nabla}\cdot\mathbf{j}_N(\mathbf{r},\omega) = i\omega\rho_N(\mathbf{r},\omega). \tag{2.39}$$

According to Eq. (2.17), the electric field in presence of this noise is

$$\mathbf{E}(\mathbf{r},\omega) = i\mu_0\omega\int d^3\mathbf{r}'\,\boldsymbol{G}(\mathbf{r},\mathbf{r}',\omega)\,\mathbf{j}_N(\mathbf{r}',\omega). \tag{2.40}$$

We introduce ladder operators that create or annihilate polariton-like excitation quanta in the coupled medium-field system

$$\hat{\mathbf{f}}^\dagger(\mathbf{r},\omega)\left|\mathbf{n}(\mathbf{r},\omega)\right\rangle = \sqrt{n+1}\left|\mathbf{n}+\mathbf{1}(\mathbf{r},\omega)\right\rangle, \tag{2.41}$$

$$\hat{\mathbf{f}}(\mathbf{r},\omega)\left|\mathbf{n}(\mathbf{r},\omega)\right\rangle = \sqrt{n}\left|\mathbf{n}-\mathbf{1}(\mathbf{r},\omega)\right\rangle, \tag{2.42}$$

where $|\mathbf{n}(\mathbf{r},\omega)\rangle$ is a state with n excitation quanta and $|0\rangle$ is the ground state with $\hat{\mathbf{f}}(\mathbf{r},\omega)\,|0\rangle = \mathbf{0}$. The ladder operators follow the bosonic commutation relations

$$\left[\hat{\mathbf{f}}(\mathbf{r},\omega),\hat{\mathbf{f}}^\dagger(\mathbf{r}',\omega')\right] = \delta(\mathbf{r}-\mathbf{r}')\delta(\omega-\omega')\hat{\boldsymbol{I}}, \tag{2.43}$$

$$\left[\hat{\mathbf{f}}(\mathbf{r},\omega),\hat{\mathbf{f}}(\mathbf{r}',\omega')\right] = \left[\hat{\mathbf{f}}^\dagger(\mathbf{r},\omega),\hat{\mathbf{f}}^\dagger(\mathbf{r}',\omega')\right] = \hat{\mathbf{0}}. \tag{2.44}$$

All that is missing to achieve quantization is the relationship between the ladder operators and the Langevin noise field [46, 48, 51],

$$\hat{\mathbf{P}}_N(\mathbf{r},\omega) = i\sqrt{\frac{\hbar\epsilon_0}{\pi}\mathrm{Im}\,\epsilon(\mathbf{r},\omega)}\,\hat{\mathbf{f}}(\mathbf{r},\omega). \tag{2.45}$$

Combining Eqs. (2.38), (2.40), and (2.45), the spectral electric field operator takes the form

$$\hat{\mathbf{E}}(\mathbf{r},\omega) = i\sqrt{\frac{\hbar}{\pi\epsilon_0}}\frac{\omega^2}{c^2}\int d^3\mathbf{r}'\,\sqrt{\mathrm{Im}\,\epsilon(\mathbf{r}',\omega)}\boldsymbol{G}(\mathbf{r},\mathbf{r}',\omega)\hat{\mathbf{f}}(\mathbf{r}',\omega), \tag{2.46}$$

from which we can infer the spectral magnetic field operator by

$$\hat{\mathbf{B}}(\mathbf{r},\omega) = (i\omega)^{-1}\boldsymbol{\nabla}\times\hat{\mathbf{E}}(\mathbf{r},\omega). \tag{2.47}$$

The complete field operators read

$$\hat{\mathbf{E}}(\mathbf{r}) = \int_0^\infty d\omega\,\left(\hat{\mathbf{E}}(\mathbf{r},\omega)+\hat{\mathbf{E}}^\dagger(\mathbf{r},\omega)\right), \tag{2.48}$$

$$\hat{\mathbf{B}}(\mathbf{r}) = \int_0^\infty d\omega\,\left(\hat{\mathbf{B}}(\mathbf{r},\omega)+\hat{\mathbf{B}}^\dagger(\mathbf{r},\omega)\right). \tag{2.49}$$

Eq. (2.46) can be seen as a generalized mode expansion in terms of the classical Green's tensor. The quantum mechanics is solely handled by simple bosonic ladder operators $\hat{\mathbf{f}}(\mathbf{r},\omega)$ and $\hat{\mathbf{f}}^\dagger(\mathbf{r},\omega)$. The consistency of the quantization scheme is reflected in the preservation of the equal-time field commutation relations [46, 48, 51] [5]

$$\left[\hat{\mathbf{E}}(\mathbf{r}),\hat{\mathbf{B}}(\mathbf{r}')\right] = \frac{i\hbar}{\epsilon_0}\boldsymbol{\nabla}_{\mathbf{r}}\times\boldsymbol{I}\,\delta(\mathbf{r}-\mathbf{r}'), \tag{2.50}$$

$$\left[\hat{\mathbf{E}}(\mathbf{r}),\hat{\mathbf{E}}(\mathbf{r}')\right] = \left[\hat{\mathbf{B}}(\mathbf{r}),\hat{\mathbf{B}}(\mathbf{r}')\right] = \hat{\mathbf{0}}. \tag{2.51}$$

The transition from Eq. (2.46) to the free-space case might not be obvious. In App. B.1, we insert the bulk Green's tensor to obtain an explicit form of the quantized field in a homogeneous medium. In the limit $\epsilon(\omega)\to 1$, we retrieve the free-space plane-wave expansion as [46, 49]

$$\hat{\mathbf{E}}_{\text{free}}(z,\omega) = i\sqrt{\frac{\hbar\omega}{4\pi\epsilon_0 c\mathcal{A}}}\left(\hat{\mathbf{a}}_+(\omega)e^{\frac{\omega}{c}z}+\hat{\mathbf{a}}_-(\omega)e^{-\frac{\omega}{c}z}\right), \tag{2.52}$$

$$\hat{\mathbf{a}}_\pm(\omega) = \lim_{n(\omega)\to 1} i\sqrt{2n_I(\omega)\frac{\omega}{c}}\,e^{\mp n_I(\omega)\frac{\omega}{c}z}\int_{-\infty}^{\pm z} dz'\,\boldsymbol{I}^\perp\hat{\mathbf{f}}(\pm z',\omega)e^{-i\frac{\omega}{c}n(\omega)z'}, \tag{2.53}$$

with $\left[\hat{\mathbf{a}}_\pm(\omega),\hat{\mathbf{a}}_\pm^\dagger(\omega')\right] = \hat{\boldsymbol{I}}^\perp\delta(\omega-\omega')$.

2.3. Equation of motion

Based on the field quantization, we can formulate a Hamiltonian for the atom-light interactions. It consists of an atom $\hat{H}_A$, a field $\hat{H}_F$, and an atom-field coupling term $\hat{H}_{AF}$ [51, 52],

$$\hat{H} = \hat{H}_A + \hat{H}_F + \hat{H}_{AF} \tag{2.54}$$

$$\hat{H} = \sum_A \frac{\hat{\mathbf{p}}_A^2}{2m_A} + \sum_A\sum_n E_{A,n}\hat{\sigma}_{A,nn} + \int d^3\hat{\mathbf{r}}\int_0^\infty d\omega\,\hat{\mathbf{f}}^\dagger(\hat{\mathbf{r}},\omega)\cdot\hat{\mathbf{f}}(\hat{\mathbf{r}},\omega)\hbar\omega + \hat{H}_{AF}, \tag{2.55}$$

with atomic population or flip operators $\hat{\sigma}_{A,mn} = |m_A\rangle\langle n_A|$ and energies $E_{A,n}$ of atomic state $|n_A\rangle$. Atom-atom interactions do not directly appear in the Hamiltonian but result from the interactions of different atoms with the same field. In our study, we only include the energy levels of the valence electrons of the alkali atoms. That means that the core electrons of the atoms are considered to be inert to interactions with the EM field, which is certainly justified at the optical frequencies of an external laser field. However, the quantum fluctuations of the EM field involve frequencies that can induce (virtual) transitions of the inner electrons. We will discuss the consequences of this fact and the impact of the valence electron approximation in Section 2.3.4.

---

[5] In index notation $[\hat{E}_m(\mathbf{r}),\hat{B}_n(\mathbf{r}')] = \frac{i\hbar}{\epsilon_0}(\boldsymbol{\nabla}_{\mathbf{r}}\times\hat{\boldsymbol{I}})_{mn}\delta(\mathbf{r}-\mathbf{r}') = \frac{i\hbar}{\epsilon_0}\epsilon_{klm}\,\partial_k^{\mathbf{r}}\,\delta_{ln}\,\delta(\mathbf{r}-\mathbf{r}')\hat{1} = -\frac{i\hbar}{\epsilon_0}\epsilon_{mnk}\,\partial_k^{\mathbf{r}}\,\delta(\mathbf{r}-\mathbf{r}')\hat{1}$.

We describe the atom-field interactions in a multipolar coupling scheme [48, 99, 100]. Because the relevant wavelengths of the EM field are usually larger than the extend of the atom (on the order of 1Å), we can focus on the leading-order electric dipole term. The next order corrections, namely magnetic dipole, electric quadrupole, and diamagnetic interactions, are suppressed by 10^{-3} in the far field[6]. In electric dipole approximation, the atom-field interaction Hamiltonian takes the form [51, 52]

$$\hat{H}_{AF} = -\sum_A \hat{\mathbf{d}}_A \cdot \hat{\mathbf{E}}(\hat{\mathbf{r}}_A) + \sum_A \dot{\hat{\mathbf{r}}}_A \cdot \left[\hat{\mathbf{d}}_A \times \hat{\mathbf{B}}(\hat{\mathbf{r}}_A)\right], \quad \hat{\mathbf{d}}_A = \sum_{mn} \hat{\sigma}_{A,mn} \mathbf{d}_{A,mn}. \tag{2.56}$$

The calculation of the transition dipole matrix elements, $\mathbf{d}_{A,mn} = \langle m_A | \hat{\mathbf{d}}_A | n_A \rangle$, is shown in App. C. The second summand in Eq. (2.56), called Röntgen term[7], describes that a moving electric dipole appears to carry a magnetic dipole moment that interacts with the magnetic field. Compared to the electric dipole term, it scales as v/c [102] and can be neglected for thermal atoms with velocities $v \sim 100\,\mathrm{m/s}$.

Furthermore, we make use of the Born–Oppenheimer approximation [106] and separate the fast electron and atom-field dynamics from the slow center-of-mass motions of the atoms. As a result, the center-of-mass operators become parameters, which we replace by their classical counterparts, $\hat{\mathbf{r}}_A \mapsto \mathbf{r}_A$, $\dot{\hat{\mathbf{r}}}_A \mapsto \dot{\mathbf{r}}_A$. This also allows us to rescale our Hamiltonian by the kinetic energy term that now is a classical number. Summarizing, the Hamiltonian used in this thesis is

$$\hat{H} = \underbrace{\sum_{A,n} E_{A,n} \hat{\sigma}_{A,nn}}_{\equiv \hat{H}_A} + \underbrace{\int d^3\mathbf{r} \int_0^\infty d\omega\, \hat{\mathbf{f}}^\dagger(\mathbf{r},\omega) \cdot \hat{\mathbf{f}}(\mathbf{r},\omega) \hbar\omega}_{\equiv \hat{H}_F} \underbrace{- \sum_A \hat{\mathbf{d}}_A \cdot \int_0^\infty d\omega \left[\hat{\mathbf{E}}(\mathbf{r}_A,\omega) + \hat{\mathbf{E}}^\dagger(\mathbf{r}_A,\omega)\right]}_{\equiv \hat{H}_{AF}}. \tag{2.57}$$

Field and atomic operators with the same time argument always commute as atoms and field are initially decoupled[8]. Therefore, the terms of the atom-field Hamiltonian can be arbitrarily rearranged. Often, they are brought into normal order[9], but all ordering schemes eventually lead to the same results [107, 108]. Bear in mind that parts of atom and field operators do not necessarily commute, see App. B.2.

---

[6] According to Refs. [101] and [102], magnetic dipole, electric quadrupole, and diamagnetic interactions are suppressed by a factor of $(Z_{\mathrm{eff}}\,\alpha_0)^2$ compared to the electric dipole term. Inserting the fine structure constant, $\alpha_0 \approx 1/137$, and the effective nuclear charge felt by the valence electron, e.g. $Z_{\mathrm{eff}} \approx 5$ for rubidium [103, 104], we obtain $(5/137)^2 \sim 10^{-3}$.

[7] Röntgen was the first to observe a force exerted by a magnetic field that originated from a dielectric moving through an electric field [105].

[8] The decoupled operators initially obey $[\hat{A}(0), \hat{B}(0)] = \hat{0}$. Thus $[\hat{A}(t), \hat{B}(t)] = \hat{U}^\dagger(t)[\hat{A}(0), \hat{B}(0)]\hat{U}(t) = \hat{0}$. Unequal time commutators are usually unknown because they depend on the system's interactions.

2.3.1. The quantum optical master equation

Following Refs. [76, 109], we introduce a theoretical framework that allows us to make the atom-atom interactions explicit by tracing over the field degrees of freedom. This will result in a quantum master equation. We start with a brief recap of the interaction picture by defining the uncoupled system Hamiltonian, $\hat{H}_0 = \hat{H}_A + \hat{H}_F$, and the unitary time evolution operators

$$\hat{U}_0(t) = \exp\left(-\frac{i}{\hbar}\hat{H}_0 t\right), \quad \hat{U}(t) = \exp\left(-\frac{i}{\hbar}\hat{H} t\right), \quad \hat{U}_I(t) = \hat{U}_0^\dagger(t)\hat{U}(t). \tag{2.58}$$

By computing the expectation value of Schrödinger picture operators $\hat{O}^S(t)$, we can infer the interaction picture representation of operators $\hat{O}^I(t)$ and the density matrix $\hat{\rho}^I(t)$,

$$\langle\hat{O}(t)\rangle = \mathrm{Tr}\left(\hat{O}^S(t)\hat{U}(t)\hat{\rho}(0)\hat{U}^\dagger(t)\right) = \mathrm{Tr}\left(\underbrace{\hat{U}_0^\dagger(t)\hat{O}^S(t)\hat{U}_0(t)}_{=\hat{O}^I(t)}\underbrace{\hat{U}_I(t)\hat{\rho}(0)\hat{U}_I^\dagger(t)}_{=\hat{\rho}^I(t)}\right). \tag{2.59}$$

The system Hamiltonian commutes with itself and remains unchanged in the interaction picture, $\hat{H}_0^I = \hat{H}_0$, while the atom-field interaction Hamiltonian transforms according to

$$\hat{H}_{AF}^I(t) = \hat{U}_0^\dagger(t)\hat{H}_{AF}^S\hat{U}_0(t). \tag{2.60}$$

With the above definition and some algebra, we quickly arrive at the equations of motion of the interaction picture operators

$$\frac{d}{dt}\hat{U}_I(t) = -\frac{i}{\hbar}\hat{H}_{AF}^I(t)\hat{U}_I(t), \quad \frac{d}{dt}\hat{\rho}^I(t) = -\frac{i}{\hbar}\left[\hat{H}_{AF}^I(t), \hat{\rho}^I(t)\right]. \tag{2.61}$$

The atomic part of the density matrix can be extracted by conducting the partial trace over the field degrees of freedom, $\hat{\rho}_A(t) = \mathrm{Tr}_F\,\hat{\rho}$. In our vapor cells, we are dealing with two sources of light: an external laser field (a coherent state) that excites the atoms and the thermal field (or the vacuum if $T = 0\,\mathrm{K}$) of the environment. We assume these two fields to be completely uncorrelated as they are generally independent of one another [110–112]. As in classical physics, the response of the system becomes a sum of the coherent and thermal contribution, identified by an index C or T

$$\frac{d}{dt}\hat{\rho}_A^I(t) = \frac{d}{dt}\mathrm{Tr}_F\,\hat{\rho}^I(t) = -\frac{i}{\hbar}\mathrm{Tr}_C\left[\hat{H}_{AF}^I(t), \hat{\rho}^I(t)\right] - \frac{i}{\hbar}\mathrm{Tr}_T\left[\hat{H}_{AF}^I(t), \hat{\rho}^I(t)\right]. \tag{2.62}$$

---

[9] Normal order puts $\hat{\mathbf{f}}(\mathbf{r},\omega)$ to the right and $\hat{\mathbf{f}}^\dagger(\mathbf{r},\omega)$ to the left, i.e. $-\sum_A\int_0^\infty d\omega\,[\hat{\mathbf{d}}_A\cdot\hat{\mathbf{E}}(\mathbf{r}_A,\omega)+\hat{\mathbf{E}}^\dagger(\mathbf{r}_A,\omega)\cdot\hat{\mathbf{d}}_A]$.

In order to understand the role of the thermal field, we compute its electric field expectation values in App. B.3 (see also Refs. [52, 113]) and find

$$
\begin{aligned}
\langle\hat{\mathbf{E}}^\dagger(\mathbf{r},\omega)\rangle_T &= \langle\hat{\mathbf{E}}(\mathbf{r},\omega)\rangle_T = \mathbf{0}, && (2.63)\\
\langle\hat{\mathbf{E}}^\dagger(\mathbf{r},\omega)\otimes\hat{\mathbf{E}}^\dagger(\mathbf{r}',\omega')\rangle_T &= \langle\hat{\mathbf{E}}(\mathbf{r},\omega)\otimes\hat{\mathbf{E}}(\mathbf{r}',\omega')\rangle_T = \mathbf{0}, && (2.64)\\
\langle\hat{\mathbf{E}}^\dagger(\mathbf{r},\omega)\otimes\hat{\mathbf{E}}(\mathbf{r}',\omega')\rangle_T &= \frac{\hbar\mu_0}{\pi}n(\omega)\omega^2\mathrm{Im}\,\boldsymbol{G}(\mathbf{r},\mathbf{r}',\omega)\delta(\omega-\omega'), && (2.65)\\
\langle\hat{\mathbf{E}}(\mathbf{r},\omega)\otimes\hat{\mathbf{E}}^\dagger(\mathbf{r}',\omega')\rangle_T &= \frac{\hbar\mu_0}{\pi}\left[1+n(\omega)\right]\omega^2\mathrm{Im}\,\boldsymbol{G}(\mathbf{r},\mathbf{r}',\omega)\delta(\omega-\omega'), && (2.66)\\
n(\omega) &= \frac{1}{e^{\hbar\omega/(k_BT)}-1}, && (2.67)
\end{aligned}
$$

where $n(\omega)$ is the Bose–Einstein distribution. The electric field vanishes on average, but the square of the electric field, i.e. the intensity, does not. In Sec. 2.3.3, it will become clear that these contributions lead to stimulated emission and absorption triggered by thermal photons (the terms $\propto n(\omega)$) and the vacuum (the term with prefactor 1), respectively. The latter case is better known as spontaneous emission. To utilize Eqs. (2.65) and (2.66), we need expressions that contain the field operator at least to second order. Thus, we insert the formal solution of Eq. (2.61), $\hat{\rho}^I(t)=\hat{\rho}(0)-\frac{i}{\hbar}\int_0^t dt'\left[\hat{H}^I_{AF}(t'),\hat{\rho}^I(t')\right]$, into Eq. (2.62) to obtain[10]

$$
\frac{d}{dt}\hat{\rho}^I_A(t) = -\frac{i}{\hbar}\,\mathrm{Tr}_C\left[\hat{H}^I_{AF}(t),\hat{\rho}^I(t)\right]-\frac{1}{\hbar^2}\,\mathrm{Tr}_T\int_0^t dt'\left[\hat{H}^I_{AF}(t),\left[\hat{H}^I_{AF}(t'),\hat{\rho}^I(t')\right]\right]. \qquad (2.68)
$$

Initially, atoms and field are uncoupled such that the density matrix is the direct product of the atom and field contribution $\hat{\rho}(0)=\hat{\rho}_A(0)\otimes\hat{\rho}_F$. When the coupling between field and atoms is weak, the field is approximately unchanged and the density matrix remains a direct product $\hat{\rho}^I(t)\approx\hat{\rho}^I_A(t)\otimes\hat{\rho}_F$ where $\hat{\rho}_F$ is the stationary state of the field. This factorization is known as the Born approximation [76]. Furthermore, when the typical timescale, over which the atomic subsystem $\hat{\rho}^I_A(t)$ varies, is much larger than the typical decay time of the field correlations, we can replace $\hat{\rho}^I_A(t')$ by $\hat{\rho}^I_A(t)$. Additionally, we can transform the integral $\int_0^t dt' f(t')=\int_0^t ds f(t-s)$. Carrying on our assumption that the period from 0 to t can be considered infinite with regard to the field correlations, we set $\int_0^t ds f(t-s)\approx\int_0^\infty ds f(t-s)$. As a result, the evolution of the density matrix only depends on its current state at time t and bears no memory of its previous values. This is the Markov approximation [76]. The combination of Born and Markov approximation yields

$$
\frac{d}{dt}\hat{\rho}^I_A(t) = \underbrace{-\frac{i}{\hbar}\,\mathrm{Tr}_C\left[\hat{H}^I_{AF}(t),\hat{\rho}^I_A(t)\otimes\hat{\rho}_F\right]}_{=T_C}\underbrace{-\frac{1}{\hbar^2}\,\mathrm{Tr}_T\int_0^\infty ds\left[\hat{H}^I_{AF}(t),\left[\hat{H}^I_{AF}(t-s),\hat{\rho}^I_A(t)\otimes\hat{\rho}_F\right]\right]}_{=T_T}. \qquad (2.69)
$$

---

[10] Since the average value of electric field is zero, Eq. (2.63), $\mathrm{Tr}_T\left[\hat{H}^I_{AF}(t),\hat{\rho}_A(0)\otimes\hat{\rho}_F\right]=0$ vanishes.

In a weakly coupled system, the atomic evolution is usually governed by decay rates and level flopping frequencies in the Megahertz to Gigahertz range or even lower. The corresponding timescales (nanoseconds and longer) are six orders of magnitude larger than those of optical fields (femtoseconds) and their correlations. Thus, the Born–Markov approximation is excellently suited to study atom-light interactions under our assumptions. Sometimes Eq. (2.69) is referred to as quantum optical master equation [76].

2.3.2. The Heisenberg equation of motion

Next, we determine the time evolution of the atomic observables that results from the master equation (2.69). First, we must transform the atom-field Hamiltonian into the interaction picture. Since atom and field operators commute, we have

$$\hat{H}^I_{AF}(t) = -\sum_B e^{i\hat{H}_A t/\hbar}\hat{\mathbf{d}}_B e^{-i\hat{H}_A t/\hbar} \cdot e^{i\hat{H}_F t/\hbar}\int_0^\infty d\omega \left[\hat{\mathbf{E}}(\mathbf{r}_B,\omega) + \hat{\mathbf{E}}^\dagger(\mathbf{r}_B,\omega)\right] e^{-i\hat{H}_F t/\hbar}. \tag{2.70}$$

The ladder operators are eigenoperators to their respective Hamiltonian [76], i.e.

$$[\hat{H}_A, \hat{\sigma}_{B,mn}] = \hbar\omega_{B,mn}\hat{\sigma}_{B,mn}, \quad \omega_{B,nm} = [E_{B,n} - E_{B,m}]/\hbar, \tag{2.71}$$

$$[\hat{H}_F, \hat{\mathbf{f}}(\mathbf{r},\omega)] = -\hbar\omega\hat{\mathbf{f}}(\mathbf{r},\omega), \quad [\hat{H}_F, \hat{\mathbf{f}}^\dagger(\mathbf{r},\omega)] = \hbar\omega\hat{\mathbf{f}}^\dagger(\mathbf{r},\omega). \tag{2.72}$$

With some helpful lemmas from operator algebra [114]

$$e^{\hat{X}}\hat{Y}e^{-\hat{X}} = \sum_{m=0}^\infty \frac{1}{m!}[\hat{X},\hat{Y}]_m, \text{ with } [\hat{X},\hat{Y}]_m = [\hat{X},[\hat{X},\hat{Y}]_{m-1}] \text{ and } [\hat{X},\hat{Y}]_0 = \hat{Y}, \tag{2.73}$$

$$e^{\hat{X}}\hat{Y}e^{-\hat{X}} = e^s\hat{Y}, \text{ if } [\hat{X},\hat{Y}] = s\hat{Y}, \tag{2.74}$$

we conclude that

$$\hat{H}^I_{AF}(t) = -\sum_B \underbrace{\sum_{mn}\mathbf{d}_{B,mn}\hat{\sigma}_{B,mn}e^{it\omega_{B,mn}}}_{=\hat{\mathbf{d}}^I_B(t)} \cdot \underbrace{\int_0^\infty d\omega \left(\hat{\mathbf{E}}(\mathbf{r}_B,\omega)e^{-i\omega t} + \hat{\mathbf{E}}^\dagger(\mathbf{r}_B,\omega)e^{i\omega t}\right)}_{=\hat{\mathbf{E}}^I(\mathbf{r}_B,t)}. \tag{2.75}$$

We can now compute the contribution of the coherent laser field T_C. With the right-hand eigenstate property of coherent states [48, 52], $\hat{\mathbf{E}}(\mathbf{r},\omega)\left|\mathbf{E}_{\text{inc}}(\mathbf{r},\omega)\right\rangle = \mathbf{E}_{\text{inc}}(\mathbf{r},\omega)\left|\mathbf{E}_{\text{inc}}(\mathbf{r},\omega)\right\rangle$,

$$T_C = \frac{i}{\hbar}\left[\sum_B \hat{\mathbf{d}}^I_B(t) \cdot \int_0^\infty d\omega\, \mathrm{Tr}_C\left\{\hat{\mathbf{E}}(\mathbf{r}_B,\omega)e^{-i\omega t}\hat{\rho}_F + \hat{\mathbf{E}}^\dagger(\mathbf{r}_B,\omega)e^{i\omega t}\hat{\rho}_F\right\}, \hat{\rho}^I_A(t)\right] \tag{2.76}$$

$$= \frac{i}{\hbar}\left[\sum_B \hat{\mathbf{d}}^I_B(t) \cdot \int_0^\infty d\omega\, \mathbf{E}_{\text{inc}}(\mathbf{r}_B,\omega)e^{-i\omega t} + \mathbf{E}^*_{\text{inc}}(\mathbf{r}_B,\omega)e^{i\omega t}, \hat{\rho}^I_A(t)\right] \tag{2.77}$$

$$= \frac{i}{\hbar}\left[\sum_B \hat{\mathbf{d}}^I_B(t) \cdot \mathbf{E}_{\text{inc}}(\mathbf{r}_B,t), \hat{\rho}^I_A(t)\right]. \tag{2.78}$$

In the last line, we have conducted the inverse Fourier transformation [52]. The thermal contribution T_T becomes

$$\begin{aligned}T_T = \int_0^\infty ds \sum_{C,D} \Big(&- \hat{\mathbf{d}}_C^I(t) \cdot \boldsymbol{\Xi}_{CD}(t,s) \hat{\mathbf{d}}_D^I(t-s) \rho_A^I(t) + \hat{\mathbf{d}}_C^I(t) \rho_A^I(t) \cdot \boldsymbol{\Psi}_{DC}^T(t,s) \hat{\mathbf{d}}_D^I(t-s) \\ &+ \hat{\mathbf{d}}_D^I(t-s) \cdot \boldsymbol{\Xi}_{CD}^T(t,s) \rho_A^I(t) \hat{\mathbf{d}}_C^I(t) - \rho_A^I(t) \hat{\mathbf{d}}_D^I(t-s) \cdot \boldsymbol{\Psi}_{DC}(t,s) \hat{\mathbf{d}}_C^I(t) \Big), \end{aligned} \tag{2.79}$$

with coefficients $\boldsymbol{\Xi}_{CD}(t,s)$ and $\boldsymbol{\Psi}_{CD}(t,s)$ evaluated using Eqs. (2.75), (2.64), (2.65), (2.66),

$$\begin{aligned}\boldsymbol{\Xi}_{CD}(t,s) &= \frac{1}{\hbar^2} \operatorname{Tr}_F \left\{ \hat{\mathbf{E}}^I(\mathbf{r}_C,t) \otimes \mathbf{E}^I(\mathbf{r}_D,t-s) \rho_F^I \right\} &(2.80)\\ &= \frac{\mu_0}{\pi\hbar} \int_0^\infty d\omega \left\{ [1+n(\omega)]\, e^{-is\omega} + n(\omega) e^{is\omega} \right\} \omega^2 \operatorname{Im} \boldsymbol{G}(\mathbf{r}_C(t), \mathbf{r}_D(t-s), \omega) &(2.81)\\ &\approx \frac{\mu_0}{\pi\hbar} \int_0^\infty d\omega \left\{ [1+n(\omega)]\, e^{-is\omega} + n(\omega) e^{is\omega} \right\} \omega^2 \operatorname{Im} \boldsymbol{G}(\mathbf{r}_C(t), \mathbf{r}_D(t), \omega), &(2.82)\\ \boldsymbol{\Psi}_{CD}(t,s) &= \frac{1}{\hbar^2} \operatorname{Tr}_F \left\{ \hat{\mathbf{E}}^I(\mathbf{r}_C,t-s) \otimes \mathbf{E}^I(\mathbf{r}_D,t) \rho_F^I \right\} = \boldsymbol{\Xi}_{CD}^*(t,s). &(2.83)\end{aligned}$$

The approximation of the time argument within the Green's tensor is justified for slow, thermal atoms in the weak coupling regime and detailed in App. B.4. Next, we can conduct the time integral over s using the identity[11]

$$\int_0^\infty ds\, e^{-i\omega s} \simeq \lim_{\epsilon\to 0^+} \int_0^\infty ds\, e^{-i\omega s - \epsilon s} = \pi\delta(\omega) - i\mathcal{P}\frac{1}{\omega}, \tag{2.84}$$

and the complete equation of motion becomes

$$\begin{aligned}\frac{d}{dt}\rho_A^I(t) = \frac{i}{\hbar} \sum_C \sum_{m,n} e^{it\omega_{C,mn}} \mathbf{d}_{C,mn} \cdot \mathbf{E}_{\text{inc}}(\mathbf{r}_C,t) \left[\hat{\sigma}_{C,mn}, \hat{\rho}_A^I(t) \right] + \sum_{C,D} \sum_{m,n} \sum_{i,j} e^{it(\omega_{C,mn}+\omega_{D,ij})} \\ \times \Bigg\{ \mathbf{d}_{C,mn} \cdot \boldsymbol{\mathcal{H}}_{D,ji}(\mathbf{r}_C,\mathbf{r}_D) \mathbf{d}_{D,ij} \left(\hat{\sigma}_{C,mn} \hat{\sigma}_{D,ij} \rho_A^I(t) - \hat{\sigma}_{D,ij} \rho_A^I(t) \hat{\sigma}_{C,mn} \right) \\ + \mathbf{d}_{C,mn} \cdot \boldsymbol{\mathcal{H}}_{D,ij}^*(\mathbf{r}_C,\mathbf{r}_D) \mathbf{d}_{D,ij} \left(-\hat{\sigma}_{C,mn} \rho_A^I(t) \hat{\sigma}_{D,ij} + \rho_A^I(t) \hat{\sigma}_{D,ij} \hat{\sigma}_{C,mn} \right) \Bigg\},\end{aligned} \tag{2.85}$$

where we introduced the abbreviations

$$\begin{aligned}\boldsymbol{\mathcal{H}}_{A,nm}(\mathbf{r},\mathbf{r}') &= -\frac{1}{2}\boldsymbol{\mathcal{E}}_{A,nm}(\mathbf{r},\mathbf{r}') - i\,\boldsymbol{\mathcal{F}}_{A,nm}(\mathbf{r},\mathbf{r}'), &(2.86)\\ \boldsymbol{\mathcal{E}}_{A,nm}(\mathbf{r},\mathbf{r}') &= \boldsymbol{\mathcal{A}}_{A,nm}(\mathbf{r},\mathbf{r}') + \boldsymbol{\mathcal{C}}_{A,nm}(\mathbf{r},\mathbf{r}') + \boldsymbol{\mathcal{C}}_{A,mn}(\mathbf{r},\mathbf{r}'), &(2.87)\\ \boldsymbol{\mathcal{F}}_{A,nm}(\mathbf{r},\mathbf{r}') &= \boldsymbol{\mathcal{D}}_{A,nm}(\mathbf{r},\mathbf{r}') + \boldsymbol{\mathcal{B}}_{A,nm}(\mathbf{r},\mathbf{r}') - \boldsymbol{\mathcal{D}}_{A,mn}(\mathbf{r},\mathbf{r}'), &(2.88)\end{aligned}$$

---

[11] We utilize the Sokhotski–Plemelj theorem, $\lim_{\epsilon\to 0^+}(x \pm i\epsilon)^{-1} = \frac{P}{x} \mp i\pi\delta(x)$, see, e.g., Chapter 3.1 of Ref. [115]. Another approach to the identity is presented in Chapter 4.9 of Ref. [107].

$$\boldsymbol{\mathcal{A}}_{A,nm}(\mathbf{r},\mathbf{r}') = \frac{2\mu_0}{\hbar}\Theta(\omega_{A,nm})\omega_{A,nm}^2 \mathrm{Im}\,\boldsymbol{G}(\mathbf{r},\mathbf{r}',\omega_{A,nm}), \tag{2.89}$$

$$\boldsymbol{\mathcal{B}}_{A,nm}(\mathbf{r},\mathbf{r}') = -\frac{\mu_0}{\hbar\pi}\mathcal{P}\int_0^\infty d\omega\, \frac{\omega^2 \mathrm{Im}\,\boldsymbol{G}(\mathbf{r},\mathbf{r}',\omega)}{\omega-\omega_{A,nm}}, \tag{2.90}$$

$$\boldsymbol{\mathcal{C}}_{A,nm}(\mathbf{r},\mathbf{r}') = \frac{2\mu_0}{\hbar}\Theta(\omega_{A,nm})n(\omega_{A,nm})\omega_{A,nm}^2 \mathrm{Im}\,\boldsymbol{G}(\mathbf{r},\mathbf{r}',\omega_{A,nm}), \tag{2.91}$$

$$\boldsymbol{\mathcal{D}}_{A,nm}(\mathbf{r},\mathbf{r}') = -\frac{\mu_0}{\hbar\pi}\mathcal{P}\int_0^\infty d\omega\, \frac{n(\omega)\omega^2 \mathrm{Im}\,\boldsymbol{G}(\mathbf{r},\mathbf{r}',\omega)}{\omega-\omega_{A,nm}}. \tag{2.92}$$

The coefficients $\boldsymbol{\mathcal{B}}_{A,nm}(\mathbf{r},\mathbf{r}')$ and $\boldsymbol{\mathcal{F}}_{A,nm}(\mathbf{r},\mathbf{r}')$ can be transformed using contour integration techniques, demonstrated in App. B.5.

As a next step, we transform the master equation (2.85) into the Schrödinger picture. Recalling that $\rho_A^I(t) = e^{i\hat{H}_A t/\hbar}\rho_A^S(t)e^{-i\hat{H}_A t/\hbar}$ and after some of algebra (see App. B.6), we find

$$\begin{aligned}\frac{d}{dt}\rho_A^S(t) = &-\frac{i}{\hbar}\left[\hat{H}_A - \sum_C\sum_{m,n}\mathbf{d}_{C,mn}\cdot\mathbf{E}_{\mathrm{inc}}(\mathbf{r}_C,t)\hat{\sigma}_{C,mn},\hat{\rho}_A^S(t)\right] + \sum_{C,D}\sum_{m,n}\sum_{i,j} \\ &\times\Bigg\{\mathbf{d}_{C,mn}\cdot\boldsymbol{\mathcal{H}}_{D,ji}(\mathbf{r}_C,\mathbf{r}_D)\mathbf{d}_{D,ij}\left(\hat{\sigma}_{C,mn}\hat{\sigma}_{D,ij}\rho_A^S(t) - \hat{\sigma}_{D,ij}\rho_A^S(t)\hat{\sigma}_{C,mn}\right) \\ &+\mathbf{d}_{C,mn}\cdot\boldsymbol{\mathcal{H}}_{D,ij}^*(\mathbf{r}_C,\mathbf{r}_D)\mathbf{d}_{D,ij}\left(-\hat{\sigma}_{C,mn}\rho_A^S(t)\hat{\sigma}_{D,ij} + \rho_A^S(t)\hat{\sigma}_{D,ij}\hat{\sigma}_{C,mn}\right)\Bigg\}.\end{aligned} \tag{2.93}$$

Finally, we can infer the corresponding evolution of an operator $\hat{O}(t)$ in the Heisenberg picture. The expectation values are independent of the quantum mechanical picture, i.e. $\mathrm{Tr}\left\{\hat{O}(0)\hat{\rho}(t)\right\} = \mathrm{Tr}\left\{\hat{O}(t)\hat{\rho}(0)\right\}$ and $\mathrm{Tr}\left\{\hat{O}(0)\partial_t\hat{\rho}(t)\right\} = \mathrm{Tr}\left\{\partial_t\hat{O}(t)\hat{\rho}(0)\right\}$. Thus, we obtain (see App. B.6)

$$\begin{aligned}\frac{d}{dt}\hat{O}(t) = &\frac{i}{\hbar}\left[\hat{H}_A(t) - \sum_C\sum_{m,n}\mathbf{d}_{C,mn}\cdot\mathbf{E}_{\mathrm{inc}}(\mathbf{r}_C,t)\hat{\sigma}_{C,mn}(t),\hat{O}(t)\right] \\ &+\sum_{C,D}\sum_{m,n}\sum_{i,j}\mathbf{d}_{C,mn}\cdot\Bigg\{\boldsymbol{\mathcal{H}}_{D,ji}(\mathbf{r}_C,\mathbf{r}_D)\left(\hat{O}(t)\hat{\sigma}_{C,mn}(t)\hat{\sigma}_{D,ij}(t) - \hat{\sigma}_{C,mn}(t)\hat{O}(t)\hat{\sigma}_{D,ij}(t)\right) \\ &+\boldsymbol{\mathcal{H}}_{D,ij}^*(\mathbf{r}_C,\mathbf{r}_D)\left(-\hat{\sigma}_{D,ij}(t)\hat{O}(t)\hat{\sigma}_{C,mn}(t) + \hat{\sigma}_{D,ij}(t)\hat{\sigma}_{C,mn}(t)\hat{O}(t)\right)\Bigg\}\mathbf{d}_{D,ij}.\end{aligned} \tag{2.94}$$

2.3.3. The coupled dipole model

With the Heisenberg equation of motion, we can now study the atomic dipole moments produced by the atom-light interactions. They are the key to infer the spectroscopic profiles that are the subject of the next chapters. We take our laser field to be monochromatic, i.e. $\mathbf{E}_{\mathrm{inc}}(\mathbf{r},t) = \mathbf{E}_{\mathrm{inc}}(\mathbf{r})e^{-i\omega_L t}$. Furthermore, it shall be near-resonant to an atomic transition from the ground state ($S_{1/2}$) to one of the first excited states ($P_{1/2}$ or $P_{3/2}$), i.e. the D_1 or D_2 line of our interacting alkali atoms. The atomic energy levels possess magnetic substates that are degenerate in free space, see Fig. 2.3. We label the ground state energy level g, the

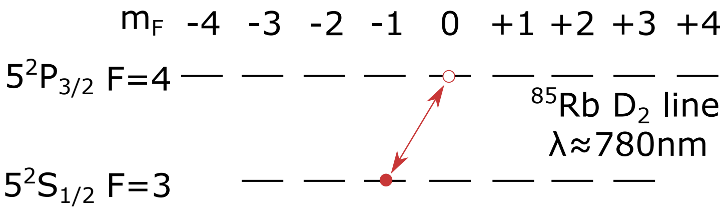

Figure 2.3: A ground state and an excited state of ^{85}Rb with magnetic m_F sublevels. The red arrow shows one example coherence that can be excited by a dipole-allowed transition.

targeted excited state energy level e, and the selected substates μ and ν, respectively. To compute the dipole moment of the overall transition, we need to sum over the substate pairs, $\langle \hat{\mathbf{d}}_{A,ge} \rangle = \sum_{\mu,\nu} \langle \hat{\sigma}_{A^{ge}_{\mu\nu}} \rangle \, \mathbf{d}_{A^{ge}_{\mu\nu}}$. Hence, Eq. (2.94) has to be solved for the expectation value of the ground and excited state coherence $\langle \hat{\sigma}_{A^{ge}_{\mu\nu}}(t) \rangle$. The corresponding equation of motion can be greatly simplified through four approximations that get us closer to classical physics.

First, following Ref. [116], we assume the operators of two different atoms A and B to be uncorrelated such that we can factorize the expectation values $\langle \hat{\sigma}_{A^{kl}_{\kappa\mu}} \hat{\sigma}_{B^{ij}_{\delta\epsilon}} \rangle \approx \langle \hat{\sigma}_{A^{kl}_{\kappa\mu}} \rangle \langle \hat{\sigma}_{B^{ij}_{\delta\epsilon}} \rangle$.

Second, we perform the rotating wave approximation, which is often undertaken in conjunction with the previous Born–Markov approximation [76]. The atomic operators feature a free time evolution $\langle \hat{\sigma}_{A,mn} \rangle \propto e^{it\omega_{A,mn}}$. Multiplying our equation with $e^{it\omega_L}$, we keep the slowly evolving terms $\propto e^{it(\omega_L - \omega_{A,eg})}$ and discard all other fast-rotating terms $\propto e^{it(\omega_L - \omega_{A,mn})}$. The latter presumes that the laser field is far detuned from all transitions other than $g \to e$ such that $(\omega_L - \omega_{A,mn}) \gg (\omega_L - \omega_{A,eg})$. Finally, we transform into the rotating frame of the laser field, and to introduce the slowly varying amplitudes $\langle \hat{\hat{\sigma}}_{A^{ge}_{\mu\nu}} \rangle = e^{i\omega_L t} \langle \hat{\sigma}_{A^{ge}_{\mu\nu}} \rangle$ accordingly. Conducting the algebra of the decorrelation assumption and the rotating wave approximation, we find (see App. B.7)

$$\begin{aligned}
\frac{d}{dt} \langle \hat{\hat{\sigma}}_{A^{ge}_{\mu\nu}}(t) \rangle &= i(\omega_{A,ge} + \omega_L) \langle \hat{\hat{\sigma}}_{A^{ge}_{\mu\nu}}(t) \rangle + \frac{i}{\hbar} \sum_{\kappa} \left(\langle \hat{\hat{\sigma}}_{A^{gg}_{\mu\kappa}}(t) \rangle \, \mathbf{d}_{A^{eg}_{\nu\kappa}} - \langle \hat{\hat{\sigma}}_{A^{ee}_{\kappa\nu}}(t) \rangle \, \mathbf{d}_{A^{eg}_{\kappa\mu}} \right) \cdot \mathbf{E}_{\mathrm{inc}}(\mathbf{r}_A) \\
&+ \sum_{B \neq A} \sum_{\delta\epsilon\kappa} \Bigg\{ \mathbf{d}_{A^{eg}_{\nu\kappa}} \cdot \frac{i}{\hbar} \boldsymbol{\mathcal{G}}(\mathbf{r}_A, \mathbf{r}_B, \omega_{B,eg}) \mathbf{d}_{B^{ge}_{\delta\epsilon}} \langle \hat{\hat{\sigma}}_{A^{gg}_{\mu\kappa}}(t) \rangle \langle \hat{\hat{\sigma}}_{B^{ge}_{\delta\epsilon}}(t) \rangle \\
&- \mathbf{d}_{A^{eg}_{\kappa\mu}} \cdot \frac{i}{\hbar} \boldsymbol{\mathcal{G}}(\mathbf{r}_A, \mathbf{r}_B, \omega_{B,eg}) \mathbf{d}_{B^{ge}_{\delta\epsilon}} \langle \hat{\hat{\sigma}}_{A^{ee}_{\kappa\nu}}(t) \rangle \langle \hat{\hat{\sigma}}_{B^{ge}_{\delta\epsilon}}(t) \rangle \Bigg\} \\
&+ i \sum_{\epsilon} \left(-\omega^{\mathrm{CP}}_{A^{e}_{\nu\epsilon}} + \frac{i}{2} \Gamma_{A^{e}_{\nu\epsilon}} \right) \langle \hat{\hat{\sigma}}_{A^{ge}_{\mu\epsilon}}(t) \rangle + i \sum_{\epsilon} \left(\omega^{\mathrm{CP}}_{A^{g}_{\mu\epsilon}} + \frac{i}{2} \Gamma_{A^{g}_{\mu\epsilon}} \right) \langle \hat{\hat{\sigma}}_{B^{ge}_{\epsilon\nu}}(t) \rangle \, .
\end{aligned} \tag{2.95}$$

For brevity, we have introduced

$$\boldsymbol{\mathcal{G}}(\mathbf{r}, \mathbf{r}', \omega) = \mu_0 \omega^2 \boldsymbol{G}(\mathbf{r}, \mathbf{r}', \omega). \tag{2.96}$$

After conducting the second approximation, we can see the meaning of the first approximation which has decorrelated the population of atom A from the coherence of atom B. For a near-resonant laser field our atoms have become quasi two-level systems, where levels other than g and e only enter via the coefficients (see App. B.7 and App. B.5)

$$\begin{aligned}\omega^{\mathrm{CP}}_{A^{n}_{\nu\delta}} = &-\frac{1}{\hbar}\sum_{\substack{k\\ \kappa}} \mathbf{d}_{A^{nk}_{\nu\kappa}} \cdot \Bigg\{ \{\Theta(\omega_{A,nk})[n(\omega_{A,nk})+1] - \Theta(\omega_{A,kn})n(\omega_{A,kn})\} \operatorname{Re}\boldsymbol{\mathcal{G}}_{\mathrm{cav}}(\mathbf{r}_A,\mathbf{r}_A,\omega_{A,nk}) \\ &- \frac{2k_BT}{\hbar}\sum_{j=0}^{\infty}{}' \frac{\omega_{A,nk}\boldsymbol{\mathcal{G}}_{\mathrm{cav}}(\mathbf{r}_A,\mathbf{r}_A,i\xi_j)}{\xi_j^2+(\omega_{A,nk})^2}\Bigg\} \mathbf{d}_{A^{kn}_{\kappa\delta}},\end{aligned} \tag{2.97}$$

$$\begin{aligned}\Gamma_{A^{n}_{\nu\delta}} = &\frac{2}{\hbar}\sum_{\substack{k\\ \kappa}} \mathbf{d}_{A^{nk}_{\nu\kappa}} \cdot \Bigg\{ \Theta(\omega_{A,nk})[1+n(\omega_{A,nk})] \operatorname{Im}\boldsymbol{\mathcal{G}}(\mathbf{r}_A,\mathbf{r}_A,\omega_{A,nk}) \\ &+ \Theta(\omega_{A,kn})n(\omega_{A,kn}) \operatorname{Im}\boldsymbol{\mathcal{G}}(\mathbf{r}_A,\mathbf{r}_A,\omega_{A,kn})\Bigg\} \mathbf{d}_{A^{kn}_{\kappa\delta}}.\end{aligned} \tag{2.98}$$

Here, $\xi_j = \frac{2\pi k_B T}{\hbar} j$ denotes the Matsubara frequencies and $\sum_{j=0}^{\infty}{}' = \sum_{j=0}^{\infty}\left(1-\frac{1}{2}\delta_{j0}\right)$. The Matsubara sum originates from the poles of the Bose–Einstein distribution on the imaginary axis. At zero temperature, it becomes an integral over the imaginary frequencies, see App. B.5.

We first consider the coefficients (2.97) and (2.98) with $\nu = \delta$. The terms describe the shift $\omega^{\mathrm{CP}}_{A^{n}_{\nu\nu}}$ and the broadening $\Gamma_{A^{n}_{\nu\nu}}$ of the n, ν state. Such a shift was first computed by Casimir and Polder [53] and is referred to as Casimir–Polder (CP) shift [51, 52]. As a limiting case the broadening contains the free-space rate at zero temperature (2.26). It also accounts for the modifications of the local density of states due to the presence of the cavity. This can lead to an enhanced decay rate, an effect first predicted by Purcell [117, 118].

Let us set aside the substates for a moment and focus on the energy levels n and k to interpret Eq. (2.97). The expression $\mathbf{d}_{A,nk} \cdot \operatorname{Re}\boldsymbol{\mathcal{G}}_{\mathrm{cav}}(\mathbf{r}_A,\mathbf{r}_A,\omega_{A,nk})\mathbf{d}_{A,kn}$ read from right to left says that atom A transitions from state n to state k realizing a photon with frequency $\omega_{A,nk}$ that travels from the atom to the cavity[12] and back to the atom where it is reabsorbed such that the atom transitions back from k to n as sketched in Fig. 2.4 a. The transitions are either triggered by the stimulated emission and absorption of a thermal photon ($n(\omega_{A,nk})$ and $n(\omega_{A,kn})$ terms) or by the stimulated emission due to vacuum fluctuations (1 term). The expression $-\frac{2}{\hbar}\sum_k \frac{\omega_{A,nk}\mathbf{d}_{A,nk}\otimes\mathbf{d}_{A,kn}}{\xi_j^2+(\omega_{A,nk})^2}$ can be identified as the polarizability of the atom A for a virtual photon of frequency $i\xi_j$ [51, 52]. Hence, the second line of Eq. (2.97) says that the atom is spontaneously polarized, releasing an off-resonant virtual photon that travels from the atom to the body and back ($\boldsymbol{\mathcal{G}}_{\mathrm{cav}}(\mathbf{r}_A,\mathbf{r}_A,i\xi_j)$ term) and restores the atom's original state.

Mathematically the shift (2.97) should contain the full Green's tensor like the broadening (2.98). But we have replaced it with the Green's tensor of the cavity environment following [51, 52]. The missing free space part of the Green's tensor formally gives an infinite result. But it can be renormalized and then gives the Lamb shift [51], here complemented by an AC Stark shift caused by the finite temperature [76]. The Casimir–Polder shift is the Lamb shift in media. The free space Lamb shift is naturally independent of the macroscopic environment and the position of the atoms. Starting from Eq. (2.95), we take it to be incorporated into the atomic transition frequency $\omega_{A,ge}$. A more elaborate discussion of the free space Lamb shift and the renormalization process can be found in Refs. [51, 76, 107] and the references therein.

---

[12] Take Fig. 2.1 b and put source and probe point on the same spot to visualize $\boldsymbol{\mathcal{G}}_{\mathrm{cav}}(\mathbf{r}_A,\mathbf{r}_A,\omega_{A,nk})$.

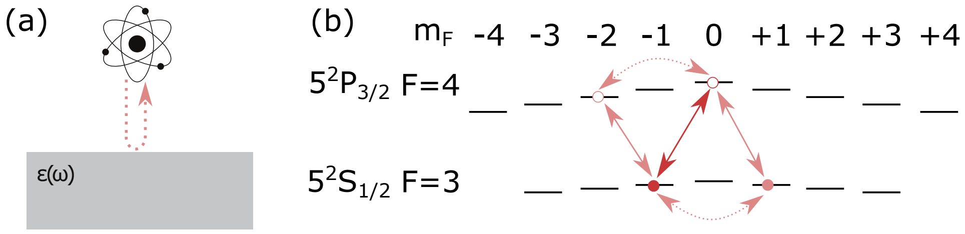

Figure 2.4: (a) Schematic illustration of the Casimir–Polder interaction: a spontaneously generated atomic transition releases a photon that is reflected upon the macroscopic environment and reabsorbed by the atom. (b) The ^{85}Rb ground state and an excited state from Fig. 2.3 in presence of a macroscopic body. The atom-wall interaction lifts the degeneracy of the m_F substates. Furthermore, it may cause a substate interaction (light red dashed arrow) that couples a coherence (dark red solid line) other others with the same initial or final state (light red solid line).

Let us now consider the coefficients (2.97) and (2.98) with $\nu \neq \delta$. When a photon is reflected upon a macroscopic body, it may change its spin. When a photon with altered spin is reabsorbed as part of the atom-wall interaction, the atom ends up in a different substate than the one in which it started. In Eq. (2.95) this substate interaction couples coherences that start from the same ground state or end up in the same excited state, see Fig. 2.4 b.

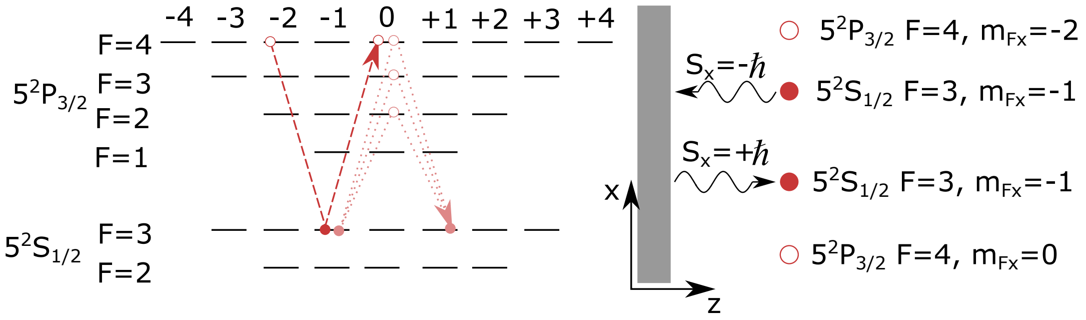

Figure 2.5: Left: Overview of dipole allowed transitions connecting the states $5^2\mathrm{P}_{3/2} F = 4, m_{Fx} = -2$ and $5^2\mathrm{P}_{3/2} F = 4, m_{Fx} = 0$ (dashed, dark red lines) and $5^2\mathrm{S}_{1/2} F = 3, m_{Fx} = -1$ and $5^2\mathrm{S}_{1/2} F = 3, m_{Fx} = +1$ (pointed, light red lines) through intermediate states on the $5^2\mathrm{P}_{3/2}$ and $5^2\mathrm{S}_{1/2}$ manifolds. Right: The transitions are accomplished by a photon that is emitted, has its spin changed upon reflection, and is then reabsorbed.

Let us consider an example where our laser drives a ^{85}Rb atom from the ground state $5^2\mathrm{S}_{1/2} F = 3$ to the excited state $5^2\mathrm{P}_{3/2} F = 4$ in front of a flat surface. We consider sublevels with respect to a quantization axis in the x-direction, see Fig. 2.5. The one-point Green's tensor of our system, $\boldsymbol{G}(\mathbf{r}, \mathbf{r}, \omega) = \mathrm{diag}(G^{\parallel}(\mathbf{r}, \mathbf{r}, \omega), G^{\parallel}(\mathbf{r}, \mathbf{r}, \omega), G^{\perp}(\mathbf{r}, \mathbf{r}, \omega))$, features different components parallel (x and y) and perpendicular (z) to the surface. A $\Delta m_{Fx} = 1$ transition emits a photon whose electric field components E_y and E_z are treated differently by the surface such that the spin of the photon may change from $S_x = -\hbar$ to $S_x = +\hbar$, see Fig. 2.5. An atom that starts an excited $m_{e,Fx} = -2$ state ends a $m_{e,Fx} = 0$, the coefficient $\omega^{\mathrm{CP}}_{A^{e}_{0,-2},x}$ is nonzero. This causes two coherences, which both start from a $m_{g,Fx} = -1$ ground state but end in the excited substates $m_{e,Fx} = 0$ and $m_{e,Fx} = -2$, to interact.

To get a quantitative impression, we used Eq. (2.97) to compute[13] the usual Casimir–Polder shift $\omega^{\mathrm{CP}}_{A^{e}_{0,0},x}$ and the interaction term $\omega^{\mathrm{CP}}_{A^{e}_{0,-2},x}$ 10 nm away from a perfect mirror. The interaction term is about 6% of the shift.

This stands in stark contrast to the ground state where the substate interaction is basically zero. As an example, we consider $\omega^{\mathrm{CP}}_{A^{g}_{-1,+1},x}$. A series of transitions exist between $m_{g,Fx} = -1$ and $m_{g,Fx} = +1$ that are shown in Fig. 2.5. Their dipole moments cancel each other out exactly, $\sum_\kappa \mathbf{d}_{A^{ge}_{\nu\kappa}} \otimes \mathbf{d}_{A^{eg}_{\kappa\mu}} = \mathbf{0}$. The cancellation is not exact if one takes into account the small energy differences between the hyperfine states as in Ref. [119]. However, the interaction term is then still eight orders of magnitude smaller than the Casimir–Polder shift between the ground and excited state [119]. The behavior is not specific to this example. The substate interaction term is also negligible (at least for a planar geometry) for other ground state sublevels and when other excited states in the $n^2P_{1/2}$ and $n^2P_{3/2}$ manifolds are included as intermediate states.

For our planar geometry, we have the rare opportunity to evade the sublevel interaction terms altogether by choosing an atomic basis with the quantization axis in the z-direction. The reason is that photons released through a $\Delta m_{Fz} = \pm 1$ transition only have electric field components in the x-y plane, which are treated equally by the surface. Therefore, their spin cannot change upon reflection and we can further simplify our equation of motion. Since the substate interaction is present in one atomic basis set and absent in the other, one might fear that the physics changes depending on which scenario is investigated. However, in Sec. 3.1.3, we will find that the atomic polarizability is the same for both scenarios precisely because of the presence of the substate interaction in one case and its absence in the other.

After this excursion into the atom-wall interaction, we continue with the third approximation that follows the decorrelation and the rotating-wave approximations. We assume the atoms to start with and remain in an incoherent classical mixture of sublevels [116], i.e. $\langle \hat\sigma_{A^{gg}_{\mu\nu}} \rangle = \delta_{\mu\nu} f_{A^{g}_{\mu}}$ with occupation numbers $f_{A^{g}_{\mu}}$. In thermal equilibrium, the occupation number of an energy level, $f_{A,g} = \sum_\mu f_{A^{g}_{\mu}}$, is given by a Maxwell–Boltzmann distribution $f_{A,n} = e^{-E_{A,n}\beta}/(\sum_k e^{-E_{A,k}\beta})$. For a rubidium atom at $T = 300\,\mathrm{K}$, the first two excited states $5\mathrm{P}_{1/2}$ and $5\mathrm{P}_{3/2}$ feature thermal population probabilities $< 10^{-26}$. Thus, for the scope of this thesis, we can assume that only the ground state is initially populated.

As the fourth approximation, we assume that the incident field is weak enough that the excited state population remains negligible, i.e. $\langle \hat\sigma_{A,kk} \rangle \approx 0$ if $k \neq g$. Then our unsaturated, coherence-free atoms follow the equation of motion

---

[13] For this we must not only take into account the states shown in Fig. 2.5 but all possible intermediate states in $n^2S_{1/2}$, $n^2D_{3/2}$ and $n^2D_{5/2}$ manifolds.

$$\begin{aligned}\frac{d}{dt}\left\langle\hat{\hat{\sigma}}_{A^{ge}_{\mu\nu}}(t)\right\rangle &= i(\omega_{A,ge}+\omega_L)\left\langle\hat{\hat{\sigma}}_{A^{ge}_{\mu\nu}}(t)\right\rangle + \frac{i}{\hbar}f_{A^{g}_{\mu}}\mathbf{d}_{A^{eg}_{\nu\mu}}\cdot\mathbf{E}_{\mathrm{inc}}(\mathbf{r}_A)\\ &+\frac{i}{\hbar}f_{A^{g}_{\mu}}\mathbf{d}_{A^{eg}_{\nu\mu}}\cdot\sum_{B\neq A}\boldsymbol{\mathcal{G}}(\mathbf{r}_A,\mathbf{r}_B,\omega_{B,eg})\sum_{\delta\epsilon}\mathbf{d}_{B^{ge}_{\delta\epsilon}}\left\langle\hat{\hat{\sigma}}_{B^{ge}_{\delta\epsilon}}(t)\right\rangle\\ &+i\sum_{\epsilon}\left(-\omega^{\mathrm{CP}}_{A^{e}_{\nu\epsilon}}+\frac{i}{2}\Gamma_{A^{e}_{\nu\epsilon}}\right)\left\langle\hat{\hat{\sigma}}_{A^{ge}_{\mu\epsilon}}(t)\right\rangle + i\sum_{\epsilon}\left(\omega^{\mathrm{CP}}_{A^{g}_{\mu\epsilon}}+\frac{i}{2}\Gamma_{A^{g}_{\mu\epsilon}}\right)\left\langle\hat{\hat{\sigma}}_{D^{ge}_{\epsilon\nu}}(t)\right\rangle. \end{aligned} \tag{2.99}$$

The first term of Eq. (2.99) describes the free time evolution, the second the contribution of driving laser field, the third the resonant interactions with the other atomic dipoles, and the last two terms contain the fluctuation-induced shifts and broadenings of ground and excited states. Remarkably, the finite temperature only impacts shifts and broadenings but does not contribute to the resonant dipole-dipole interaction. To the best of my knowledge, this derivation is the first to showcase this fact.

Finally, we take the quantization axis of our atoms in z-direction such that the substate interaction terms are zero. We introduce the detuning δ_A between the vacuum transition frequency and the laser field, the Casimir–Polder shift of the transition line $\omega^{\mathrm{CP}}_{A^{eg}_{\nu\mu}}$, and the natural broadening of the line $\gamma_{A^{eg}_{\nu\mu}}$,

$$\delta_A \equiv \omega_L - \omega_{A,eg}, \quad \omega^{\mathrm{CP}}_{A^{eg}_{\nu\mu}} = \omega^{\mathrm{CP}}_{A^{e}_{\nu\nu}} - \omega^{\mathrm{CP}}_{A^{g}_{\mu\mu}}, \quad \gamma_{A^{eg}_{\nu\mu}} = \left(\Gamma_{A^{e}_{\nu\nu}} + \Gamma_{A^{g}_{\mu\mu}}\right)/2. \tag{2.100}$$

Hence, the coupled dipole model in a planar geometry takes the compact form

$$\begin{aligned}\frac{d}{dt}\left\langle\hat{\hat{\sigma}}_{A^{ge}_{\mu\nu}}(t)\right\rangle =& i\left(\delta_A - \omega^{\mathrm{CP}}_{A^{eg}_{\nu\mu}}(\mathbf{r}_A) + i\gamma_{A^{eg}_{\nu\mu}}(\mathbf{r}_A)\right)\left\langle\hat{\hat{\sigma}}_{A^{ge}_{\mu\nu}}(t)\right\rangle + \frac{i}{\hbar}f_{A^{g}_{\mu}}\mathbf{d}_{A^{eg}_{\nu\mu}}\cdot\mathbf{E}_{\mathrm{inc}}(\mathbf{r}_A)\\ &+\frac{i}{\hbar}f_{A^{g}_{\mu}}\mathbf{d}_{A^{eg}_{\nu\mu}}\cdot\sum_{B\neq A}\boldsymbol{\mathcal{G}}(\mathbf{r}_A,\mathbf{r}_B,\omega_{B,eg})\sum_{\delta\epsilon}\mathbf{d}_{B^{ge}_{\delta\epsilon}}\left\langle\hat{\hat{\sigma}}_{B^{ge}_{\delta\epsilon}}(t)\right\rangle, \end{aligned} \tag{2.101}$$

In our planar geometries, the incident field generally consists of forward and backward propagating planar waves components

$$\mathbf{E}_{\mathrm{inc}}(\mathbf{r}) = \mathbf{E}^{+}_{\mathrm{inc}}e^{ikz} + \mathbf{E}^{-}_{\mathrm{inc}}e^{-ikz}. \tag{2.102}$$

Due to our assumption of an unsaturated vapor, the linear superposition principle applies. The total atomic response $\langle\hat{\hat{\sigma}}_{A^{ge}_{\mu\nu}}\rangle$ can be written as the sum of two independent responses to the fields $\mathbf{E}^{+}_{\mathrm{inc}}e^{ikz}$ and $\mathbf{E}^{-}_{\mathrm{inc}}e^{-ikz}$, which each fulfill their own coupled dipole model, respectively.

Due to the thermal motion, the vapor can change locally or due to influx from other positions. This is captured by the hydrodynamic derivative

$$\frac{d}{dt}\left\langle\hat{\hat{\sigma}}_{A^{ge}_{\mu\nu}}\right\rangle = \frac{\partial}{\partial t}\left\langle\hat{\hat{\sigma}}_{A^{ge}_{\mu\nu}}\right\rangle + \mathbf{v}_A\cdot\boldsymbol{\nabla}\left\langle\hat{\hat{\sigma}}_{A^{ge}_{\mu\nu}}\right\rangle, \tag{2.103}$$

which results from the chain rule. The term $\mathbf{v}_A \cdot \boldsymbol{\nabla} \langle \hat{\tilde{\sigma}}_{A_{\mu\nu}^{ge}} \rangle$ encodes two effects: First the Doppler shift and second a nonlocal behavior because a moving atom can be excited in one place but radiate at another. Both will be elucidated in more detail in Chapter 3. In the following, we will study the stationary state of the vapor, where the explicit time dependence vanishes,

$$\begin{aligned}\mathbf{v}_A \cdot \boldsymbol{\nabla} \langle \hat{\tilde{\sigma}}_{A_{\mu\nu}^{ge}} \rangle = {} & i\left(\delta_A - \omega^{\mathrm{CP}}_{A_{\nu\mu}^{eg}}(\mathbf{r}_A) + i\gamma_{A_{\nu\mu}^{eg}}(\mathbf{r}_A)\right) \langle \hat{\tilde{\sigma}}_{A_{\mu\nu}^{ge}}(t) \rangle + \frac{i}{\hbar} f_{A_\mu^g} \mathbf{d}_{A_{\nu\mu}^{eg}} \cdot \mathbf{E}_{\mathrm{inc}}(\mathbf{r}_A) \\ & + \frac{i}{\hbar} f_{A_\mu^g} \mathbf{d}_{A_{\nu\mu}^{eg}} \cdot \sum_{B \neq A} \boldsymbol{\mathcal{G}}(\mathbf{r}_A, \mathbf{r}_B, \omega_{B,eg}) \sum_{\delta\epsilon} \mathbf{d}_{B_{\delta\epsilon}^{ge}} \langle \hat{\tilde{\sigma}}_{B_{\delta\epsilon}^{ge}}(t) \rangle \, . \qquad (2.104)\end{aligned}$$

2.3.4. Limitations of the coupled dipole model

It is helpful to review the approximations that have been used to derive the coupled dipole (2.104) to clarify their robustness and their restrictions. We also sketch how these limitations may be overcome.

We have assumed that the incident field is so weak that the population of the excited state is negligible. As a result, the atoms can always absorb a photon, i.e. they do not saturate. The atomic response is linear and follows the superposition principle, which immensely facilitates the modeling and the numerical evaluation. However, in an experiment, it might be necessary to use stronger incident fields to get a better signal-to-noise ratio. Additionally, the field enhancement in a cavity environment can lead to a violation of the weak-field limit. To include saturation, one has to consider Eq. (2.95) instead of Eq. (2.101). Equations of motion for the populations $\langle \hat{\tilde{\sigma}}_{A_{\epsilon\delta}^{ee}}(t) \rangle$ and $\langle \hat{\tilde{\sigma}}_{A_{\epsilon\delta}^{gg}}(t) \rangle$ need to be set up. Subsequently, the coupled equation system of diagonal and off-diagonal density matrix elements has to be solved.

In our Hamiltonian, we have only included the dipole terms arguing that higher-order multipoles present only small corrections in the far field. However, a random ensemble will inevitably include atoms that are so close to each other that higher-order multipole terms do play a role and even exceed the dipole contribution in the total interaction potential. Ironically, at the smallest of distances where these deviations are most pronounced, they do not affect the atomic spectra. The strong interactions shift the atomic lines so far away from their original resonance that the external laser field can no longer couple to the atom. The atom pairs are literally left in the dark and the dipole term alone suffices to cause that effect. Higher-order multipoles can only affect the spectra in an intermediate distance regime. In this thesis, we study the ground state and the few first excited states whose wave functions have a small spatial extend. As a result, the dipole approximation still holds for relatively small distances and no significant distance window is opened for contributions from higher-order multipoles. However, one could also study excited states with very high principal quantum numbers, i.e. Rydberg states, which possess much larger wave functions [8]. Then deviations from the dipole approximation occur at a much wider range of distances and the next-order multipole terms, i.e. electric quadrupole and magnetic dipole, should be included to provide a more reliable description.

Rydberg states are characterized by enormous polarizabilities, large transition dipole moments, and small transition frequencies between adjacent states [8]. They feature strong atom-wall interactions. The resulting line shifts may no longer be perturbatively small compared to the atomic transition frequencies. In this case, Casimir–Polder and Purcell have to be obtained from a self-consistent iterative treatment [102, 120] or by exact diagonalization [121]. In a dense vapor, a self-consistent treatment must also include the other vapor atoms. For example, it is known that the Casimir–Polder shifts and Purcell rates are modified when emitters are placed in a continuous medium of refractive index n [122–124]. However, as we will show in Chapter 4, the atomic vapor does not behave like one would expect from continuous medium theory because it is a granular medium. Here, a perturbative treatment of the atom-wall interaction suffices because we consider only the first few excited states that feature weaker interactions.

Furthermore, we have assumed that our interactions take place in the weak coupling regime, which enabled us to use the Born–Markov approximation. There are, however, cavity and waveguide structures whose Green's tensors feature sharp peaks at the frequencies of the guided modes. In photonic crystal cavities, such resonances can be tailored to the user's needs [125]. If the resonance matches one of the relevant atomic transition frequencies, a coherent exchange of energy between atoms and field occurs. The time scales of atoms and field can no longer be separated and the density matrix can no longer be factorized: the Born–Markov approximation breaks down. In some simple situations, such a strong coupling can be accounted for by an exact analytic solution of the Heisenberg equation of motion [52, 120]. In general, no analytic solution is available. In this case, one can systematically include non-Markovian dynamics with the time-convolutionless projection operator technique [76]. It offers a perturbative expansion that in second order is identical to our master equation in Born–Markov approximation [76]. The simple planar dielectric cavities considered in this thesis do not possess sharp resonances at the atomic frequencies such that the inclusion of non-Markovian terms is not necessary.

The higher-order terms of the perturbation series also contain other physical effects. The fourth order reveals the van der Waals (vdW) interaction, the fluctuation-induced interaction between two atoms [47, 51, 52, 126]. Van der Waals and Casimir–Polder theories transition into one another when one replaces the macroscopic body with a dilute collection of atoms. The vdW interaction involves the exchange of two virtual photons between the atoms and therefore contains two Green's tensors [47, 51, 52, 126]. In free space and at nonretarded distances the vdW interaction decays accordingly as C_6/r^6, much faster than resonant dipole-dipole interactions proportional to $1/r^3$. For the ground state and the first few excited states studied in this thesis, the C_6 coefficient is relatively small such that vdW interactions are neglected in this thesis. However, vdW interactions can become important for Rydberg atoms because the interaction coefficient $C_6 \propto (n^*)^{11}$ features an extremely strong scaling with the effective principal quantum number n^* [8] [14].

---

[14] The effective principal quantum number n^* is the principal quantum number minus the quantum defect [8].

Another approximation that requires closer examination concerns our atomic model that only includes the transitions of the valence electron. This is a standard assumption as the laser photons, due to their limited energy, do not excite the core electrons. However, quantum fluctuations occur at all frequencies and therefore induce virtual transitions to the core electrons too. The core polarizability accounts for 16% of the Casimir–Polder shift in ground-state sodium atoms and for 50% in ground-state francium atoms [127] that possess more core electrons and protons. The core polarizability weakly depends on the atomic state due to the Pauli exclusion principle, which prevents transitions of the core electrons to the state occupied by the valence electron [128, 129]. But this concerns only a small fraction of all possible transitions such that the state dependence can usually be neglected. Our model only includes the difference of the Casimir–Polder shifts of the lower and upper level such that the core polarizability contributions approximately cancel. Therefore, we can only consider the transitions of the valence electron. However, the Casimir–Polder interaction also introduces a force that has to be computed for ground and excited state separately. Then the core electron contribution has to be taken into account[15] as experiments showed [130]. Tabulated values for the core polarizability of alkali atoms can be found in Ref. [129]. In this thesis, we neglect the Casimir–Polder force because the relevant Casimir–Polder potentials are much smaller than the kinetic energy of the thermal atoms[16].

For our model, we assumed that the external laser field is nearly resonant with one atomic transition and far detuned from all others. While this assumption is robust for fine structure states that are well separated, it can become an issue when hyperfine transitions are included, which are usually Gigahertz or less apart from one another. If the interaction potentials of the atoms remain smaller than these separations and the assumption of an unsaturated vapor holds, one can simply use the linear superposition principle and add the responses of the individual hyperfine transitions. However, when the transitions overlap due to large atom-atom interactions, i.e. in a dense vapor, the model needs to include the couplings between the different hyperfine ground and excited states and diagonalize the resulting system of equations. In the following chapters, we perform numerical computations only using the fine structure of the atoms because this already represents the realistic size of the expected effects. However, an optimal model of a specific experiment should include the hyperfine structure and, if necessary, consider the coupling of the hyperfine components.

Finally, it should be noted that we have neglected the possibility that the atom-atom interactions constitute coherences between different ground states [116]. Although we start from a classical mixture of sublevels, coherences can be built up over time. When internal-level many-body quantum correlations are present, the effects covered by our model still occur, but are augmented by others. Quantum correlations complicate the model considerably. Their treatment is, unfortunately, beyond the scope of this thesis. More details on the topic can be found in Ref. [116].

---

[15] The higher the excited state, the lower the relative contribution of the core electrons to the shift. Therefore this is mainly relevant for the ground state and the first few excited states.

[16] Let us estimate that Casimir–Polder shift should be smaller than 100 GHz so that the atom can still be excited. This corresponds to an energy of 0.4 meV, whereas the thermal energy at room temperate is around 25 meV. The work that the Casimir–Polder effect can do cannot significantly accelerate the system.

2.3.5. Polarizability and atom-atom interactions at zero temperature

The close correspondence of our coupled dipole model (2.104) to classical physics can be illustrated at zero temperature[17]. By introducing the near-resonant atomic polarizability

$$\boldsymbol{\alpha}_{A,ge} = -\frac{1}{\hbar}\sum_{\mu,\nu}\frac{f_{A^g_\mu}\mathbf{d}_{A^{ge}_{\mu\nu}}\otimes\mathbf{d}_{A^{eg}_{\nu\mu}}}{\delta_A - \omega^{\mathrm{CP}}_{A^{eg}_{\nu\mu}}(\mathbf{r}_A) + i\gamma_{A^{eg}_{\nu\mu}}(\mathbf{r}_A)}, \tag{2.105}$$

the coupled dipole model (2.104) can be recast in the compact form

$$\mathbf{p}_{A,ge} = \boldsymbol{\alpha}_{A,ge}\left[\mathbf{E}_{\mathrm{inc}}(\mathbf{r}_A) + \sum_{B\neq A}\boldsymbol{\mathcal{G}}(\mathbf{r}_A,\mathbf{r}_B,\omega_{B,eg})\mathbf{p}_{B,ge}\right], \tag{2.106}$$

where $\mathbf{p}_{A,ge} \equiv \sum_{\mu,\nu}\mathbf{d}_{A^{ge}_{\mu\nu}}\langle\hat{\tilde{\sigma}}_{A^{ge}_{\mu\nu}}\rangle$ is the atomic dipole moment. According to Eq. (2.106), the dipole moment of atom A is proportional to the electric field acting on atom A, which consists of the contribution of the external field and the field scattered by all other atoms onto A. The proportionality constants are the components of the polarizability tensor (2.105). Let us consider the solution of the problem with two atoms A and B. Using the block matrix inversion presented in App. B.8, we find the dipole moment of atom A to be

$$\begin{aligned}\mathbf{p}_{A,ge} &= \left[\boldsymbol{I} - \boldsymbol{\alpha}_{A,ge}\boldsymbol{\mathcal{G}}(\mathbf{r}_A,\mathbf{r}_B,\omega_{B,eg})\boldsymbol{\alpha}_{B,ge}\boldsymbol{\mathcal{G}}(\mathbf{r}_B,\mathbf{r}_A,\omega_{B,eg})\right]^{-1}\\ &\quad\times\left\{\mathbf{E}_{\mathrm{inc}}(\mathbf{r}_A) + \boldsymbol{\alpha}_{A,ge}\boldsymbol{\mathcal{G}}(\mathbf{r}_A,\mathbf{r}_B,\omega_{A,eg})\mathbf{E}_{\mathrm{inc}}(\mathbf{r}_B)\right\} \qquad (2.107)\\ &= \sum_{n=0}^{\infty}\left\{\boldsymbol{\alpha}_{A,ge}\boldsymbol{\mathcal{G}}(\mathbf{r}_A,\mathbf{r}_B,\omega_{B,eg})\boldsymbol{\alpha}_{B,ge}\boldsymbol{\mathcal{G}}(\mathbf{r}_B,\mathbf{r}_A,\omega_{B,eg})\right\}^n\\ &\quad\times\left\{\mathbf{E}_{\mathrm{inc}}(\mathbf{r}_A) + \boldsymbol{\alpha}_{A,ge}\boldsymbol{\mathcal{G}}(\mathbf{r}_A,\mathbf{r}_B,\omega_{A,eg})\mathbf{E}_{\mathrm{inc}}(\mathbf{r}_B)\right\}. \qquad (2.108)\end{aligned}$$

For the second equality, we used the Neumann series[18], which is the matrix analog to the geometric series. Our result can be immediately understood as the Born series summed up to infinite order, as illustrated and elaborated in Fig. 2.6.

Finally, a few remarks on the polarizability (2.105) should be made. Due to our assumption of a near-resonant incident field, it contains only a single resonant denominator with detuning $\delta_A = \omega_L - \omega_{A,eg}$ and not a second term with an anti-resonant denominator containing $\omega_L + \omega_{A,eg}$. An exact expression for the polarizability is cumbersome to obtain. It must fulfill the reflection principle, $\alpha(-\omega) = \alpha^*(\omega)$, and the optical theorem that connects the imaginary part of $\alpha(\omega)$

---

[17] In Sec. 3.2.2, we also showcase a polarizability expression at finite temperature in a local, continuous medium.

[18] We assume that the infinite series converges for the chosen Green's tensors and atomic polarizabilities.

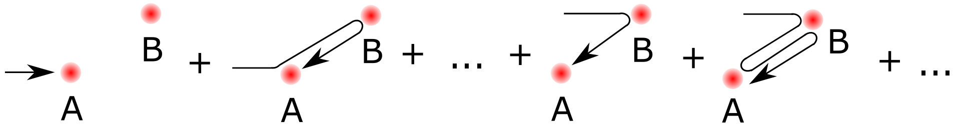

Figure 2.6: Illustration of the Born series in Eq. (2.108). The total field acting on atom A originally steams from two sources: The incident field on atom A (left) and the incident field on B that is scattered on atom A (right to the first dots). A dipole moment in A produces an additional dipole moment B that acts back on A. The repetition of this process induces the higher-order terms abbreviated by dots.

to the scattering cross section $\sigma_{\mathrm{sc}}(\omega)$[19] as [131, 132]

$$\frac{\omega}{\epsilon_0 c}\mathrm{Im}\,\alpha(\omega) = \frac{\omega^4}{2\pi\epsilon_0^2 c^4}|\alpha(\omega)|^2 = \sigma_{\mathrm{sc}}(\omega). \tag{2.109}$$

The optical theorem states energy conservation, i.e. the energy that the atom absorbs from the incidence beam has to be scattered from it at the same rate. Off resonance, both demands can only be met by a frequency-dependent linewidth that can be derived either in a calculation beyond rotating wave and Markov approximations [131–133] or through a special unitary transformation method [134]. In this thesis, we restrict ourselves to the near-resonant case, where detuning and homogeneous broadening are much smaller than the resonance frequency and such approaches are not necessary.

2.4. The scattered light field

Experiments usually detect the light fields that are scattered by the atomic dipole moments [135, 136]. We now derive the relation between the two. Since our interaction picture master equation has been formulated only for atomic operators, we now take a complementary path and consider Heisenberg equations of motion. In the Heisenberg picture, the photonic ladder operator obeys the equation of motion

$$\begin{aligned}\partial_t\hat{\mathbf{f}}(\mathbf{r},\omega,t) &= \frac{1}{i\hbar}[\hat{\mathbf{f}}(\mathbf{r},\omega,t),\hat{H}(t)] && (2.110)\\ &= -i\omega\hat{\mathbf{f}}(\mathbf{r},\omega,t) + \sum_A\sqrt{\frac{\mathrm{Im}\,\epsilon(\mathbf{r},\omega)}{\pi\epsilon_0\hbar}}\frac{\omega^2}{c^2}\boldsymbol{G}^{+}(\mathbf{r}_A,\mathbf{r},\omega)\hat{\mathbf{d}}_A(t), && (2.111)\end{aligned}$$

where $\boldsymbol{G}^{+} = \boldsymbol{G}^{*T}$ denotes the conjugate transpose. The solution takes the form[20]

$$\hat{\mathbf{f}}(\mathbf{r},\omega,t) = e^{-i\omega t}\hat{\mathbf{f}}(\mathbf{r},\omega,0) + \sum_A\sqrt{\frac{\mathrm{Im}\,\epsilon(\mathbf{r},\omega)}{\pi\epsilon_0\hbar}}\frac{\omega^2}{c^2}\int_0^t dt'\,e^{-i\omega(t-t')}\boldsymbol{G}^{+}(\mathbf{r}_A(t'),\mathbf{r},\omega)\hat{\mathbf{d}}_A(t'). \tag{2.112}$$

---

[19] There is a very well-known limiting case for the scattering cross section when the light frequency is much smaller than the atomic resonance frequency such that the polarizability is constant. The given equation then shows $\sigma_{\mathrm{sc}}(\omega) \propto \omega^4$, i.e. the Rayleigh scattering's $1/\lambda^4$ dependence that explains the blue color of the sky.

[20] The initial value problem $\dot{a} = \Omega a + f(t)$ has the unique solution $a(t) = a(0)e^{\Omega t} + \int_0^t dt' e^{\Omega(t-t')}f(t')$.

We now insert this result into Eq. (2.46) and use Green's tensor identity (2.30) to obtain the positive frequency component of the electric field operator

$$\begin{aligned}\hat{\mathbf{E}}(\mathbf{r},\omega,t) &= e^{-i\omega t}\hat{\mathbf{E}}(\mathbf{r},\omega,0) + \frac{i\mu_0\omega^2}{\pi}\sum_A\int_0^t dt'\, e^{-i\omega(t-t')}\mathrm{Im}\,\boldsymbol{G}(\mathbf{r},\mathbf{r}_A(t'),\omega)\hat{\mathbf{d}}_A(t') && (2.113)\\ &\approx e^{-i\omega t}\hat{\mathbf{E}}(\mathbf{r},\omega,0) + \frac{i\mu_0\omega^2}{\pi}\sum_A\int_0^t dt'\, e^{-i\omega(t-t')}\mathrm{Im}\,\boldsymbol{G}(\mathbf{r},\mathbf{r}_A(t),\omega)\hat{\mathbf{d}}_A(t'). && (2.114)\end{aligned}$$

In the last line, we neglected velocity-dependent corrections as in Eq. (2.82) and App. (B.4). The complete electric field operator (2.48) takes the form

$$\begin{aligned}\hat{\mathbf{E}}(\mathbf{r}) = &\int_0^\infty d\omega\left[\hat{\mathbf{E}}(\mathbf{r},\omega)e^{-i\omega t} + \hat{\mathbf{E}}^*(\mathbf{r},\omega)e^{i\omega t}\right]\\ &+\frac{i\mu_0}{\pi}\sum_A\int_0^\infty d\omega\int_0^t dt'\left[e^{-i\omega(t-t')} - e^{i\omega(t-t')}\right]\omega^2\mathrm{Im}\,\boldsymbol{G}(\mathbf{r},\mathbf{r}_A,\omega)\hat{\mathbf{d}}_A(t'). \qquad (2.115)\end{aligned}$$

For our weak coupling case, this relation can be simplified by Born–Markov approximations. First, we perform a field averaging and retrieve the incident electric field as in Eq. (2.78). Next, we rewrite the integral $\int_0^t dt' f(t') = \int_0^t ds f(t-s)$ as for Eq. (2.69)

$$\begin{aligned}\langle\hat{\mathbf{E}}(\mathbf{r})\rangle = &\,\mathbf{E}_{\mathrm{inc}}(\mathbf{r})e^{-i\omega_L t} + \frac{i\mu_0}{\pi}\sum_A\sum_{m,n}\sum_{\mu,\nu}\int_0^\infty d\omega\int_0^t ds\,\omega^2\mathrm{Im}\,\boldsymbol{G}(\mathbf{r},\mathbf{r}_A,\omega)\mathbf{d}_{A^{mn}_{\mu\nu}}\\ &\times\left[e^{-i\omega s} - e^{i\omega s}\right]\langle\hat{\sigma}_{A^{mn}_{\mu\nu}}(t-s)\rangle\,. \qquad (2.116)\end{aligned}$$

In Markov approximation, the field only depends on atomic operators at the same time t. We can achieve that by assuming that the atomic time evolution under the integral is approximately harmonic

$$\hat{\sigma}_{A^{mn}_{\mu\nu}}(t-s) \simeq e^{-i\omega_{A,mn}s}\hat{\sigma}_{A^{mn}_{\mu\nu}}(t). \qquad (2.117)$$

As in Section 2.3.3, we take the laser to be far detuned from all transitions other than $g \to e$. As a result, the free time evolution ($e^{it\omega_{A,mn}}$) and the laser time evolution ($e^{i\omega_L t}$), lead to fast-rotating terms that can be neglected except when $m = g$ and $n = e$. Denoting the variables in the laser frame by $\langle\hat{\hat{\mathbf{E}}}(\mathbf{r})\rangle = \langle\hat{\mathbf{E}}(\mathbf{r})\rangle\, e^{i\omega_L t}$, we have

$$\begin{aligned}\langle\hat{\hat{\mathbf{E}}}(\mathbf{r})\rangle = &\,\mathbf{E}_{\mathrm{inc}}(\mathbf{r}) + \frac{i\mu_0}{\pi}\sum_A\sum_{\mu,\nu}\int_0^\infty d\omega\int_0^t ds\,\omega^2\mathrm{Im}\,\boldsymbol{G}(\mathbf{r},\mathbf{r}_A,\omega)\mathbf{d}_{A^{ge}_{\mu\nu}}\\ &\times\left[e^{-i(\omega+\omega_{A,ge})s} - e^{-i(-\omega+\omega_{A,ge})s}\right]\langle\hat{\sigma}_{A^{ge}_{\mu\nu}}(t)\rangle\, e^{i\omega_L t}. \qquad (2.118)\end{aligned}$$

Next, we extend the upper limit of the time integral to infinity as in Eq. (2.69) and use the distribution identity (2.84) to conduct the time and frequency integrals. We obtain

$$\begin{aligned}\langle\hat{\hat{\mathbf{E}}}(\mathbf{r})\rangle =& \mathbf{E}_{\mathrm{inc}}(\mathbf{r}) + \Bigg\{\frac{\mu_0}{\pi}\mathcal{P}\int_0^\infty d\omega\left[\frac{1}{\omega+\omega_{A,ge}}+\frac{1}{\omega-\omega_{A,ge}}\right]\omega^2\mathrm{Im}\,\boldsymbol{G}(\mathbf{r},\mathbf{r}_A,\omega)\\ &+ i\mu_0\omega^2\mathrm{Im}\,\boldsymbol{G}(\mathbf{r},\mathbf{r}_A,\omega_{A,eg})\Bigg\}\mathbf{d}_{A^{ge}_{\mu\nu}}\,\langle\hat{\sigma}_{A^{ge}_{\mu\nu}}(t)\rangle\,e^{i\omega_L t}. \end{aligned} \tag{2.119}$$

This can be further simplified using the Kramers–Kronig relation[21] for the Green's tensor [52],

$$\begin{aligned}\omega^2\mathrm{Re}\,\boldsymbol{G}(\mathbf{r},\mathbf{r}',\omega) &= \frac{1}{\pi}\mathcal{P}\int_{-\infty}^{\infty}d\omega'\frac{(\omega')^2\mathrm{Im}\,\boldsymbol{G}(\mathbf{r},\mathbf{r}',\omega')}{\omega'-\omega} &(2.120)\\ &= \frac{1}{\pi}\mathcal{P}\int_0^\infty d\omega'\frac{(\omega')^2\mathrm{Im}\,\boldsymbol{G}(\mathbf{r},\mathbf{r}',\omega')}{\omega'-\omega}+\frac{1}{\pi}\mathcal{P}\int_0^\infty d\omega'\frac{(\omega')^2\mathrm{Im}\,\boldsymbol{G}(\mathbf{r},\mathbf{r}',\omega')}{\omega'+\omega}. &(2.121)\end{aligned}$$

With $\mathbf{p}_{A,ge}=\sum_{\mu,\nu}\mathbf{d}_{A^{ge}_{\mu\nu}}\,\langle\hat{\hat{\sigma}}_{A^{ge}_{\mu\nu}}\rangle$, the expectation value of the electric field becomes

$$\langle\hat{\hat{\mathbf{E}}}(\mathbf{r})\rangle = \mathbf{E}_{\mathrm{inc}}(\mathbf{r}) + \mu_0\omega^2\sum_A\boldsymbol{G}(\mathbf{r},\mathbf{r}_A,\omega_{A,eg})\mathbf{p}_{A,ge}, \tag{2.122}$$

as expected from the superposition principle and Eq. (2.20). Since we made no assumption on the atomic population, Eq. (2.122) holds for both saturated and unsaturated atoms.

2.4.1. Light transmission and reflection of an atomic ensemble

The scattered field patterns of a random atomic ensemble, which result from Eq. (2.122), are spatially very complex [72]. However, in practice, one collects light from a spatial region over which the field can be integrated. To this end, we assume that a lens right behind the vapor focuses all scattered light onto a single point where it is detected [137], see Fig. 2.7. As a result, transmission and reflection can be expressed by a single number, respectively. Assuming that the focal point is so far away that the far field or Fraunhofer approximation applies, the field at the detector is given by [138]

$$\mathbf{E}(f) = \frac{-ie^{ikn_1f}}{\lambda_1 f}\int_{\mathrm{lens}} dA\,\mathbf{E}(\mathbf{r}). \tag{2.123}$$

Inserting Eq. (2.122), we have to integrate the Green's tensor over the lens area. This can be done analytically if the lens area is assumed to be effectively infinite, see App. (A.5). We end up with the Green's functions of the 1-D Helmholtz equation

$$\int dA'\boldsymbol{G}(\mathbf{r},\mathbf{r}',\omega) = \mathrm{diag}(G^{\mathrm{1D}}(z,z',\omega),G^{\mathrm{1D}}(z,z',\omega),0), \quad z\neq z'. \tag{2.124}$$

---

[21] The KK relation is a general consequence of the analyticity of $\omega^2\boldsymbol{G}(\mathbf{r},\mathbf{r}',\omega)$ in the upper half of the complex plane. It can be derived using the same contour integration techniques as those utilized in App. B.5.

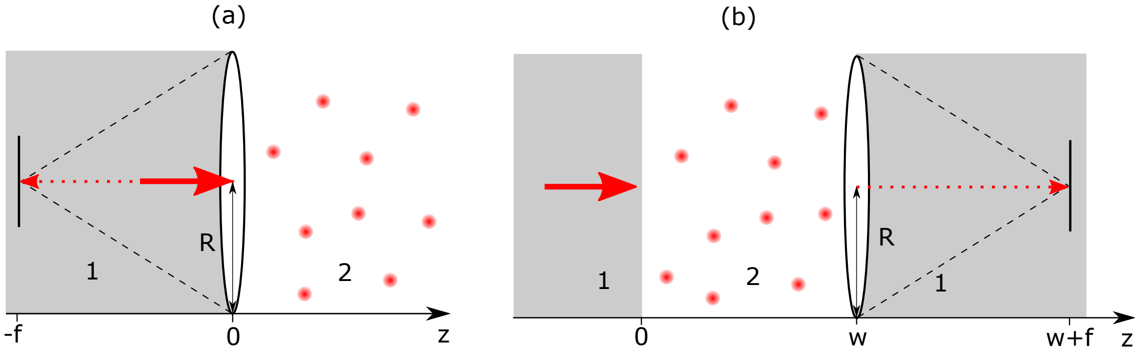

Figure 2.7: A lens collects the backward (a) or forward (b) scattered light and focuses it onto a single point where it is detected. Reflection and transmission can be described by a single number instead through a complex scattering pattern that changes rapidly as the atoms move around.

The above shows that only the transverse field components are propagated. The 1-D Green's function of the surface and the cavity geometry in Fig. 2.7 with z in region 1 and z' in region 2 are

$$G^{\mathrm{1D}}_{\mathrm{surf,out}}(z,z',\omega_{eg}) = \frac{i}{2k} t_{21}\, e^{ikn_1|z|+ikz'}, \tag{2.125}$$

$$G^{\mathrm{1D}}_{\mathrm{cav,out}}(z,z',\omega_{eg}) = \frac{i}{2k} t_{21}\, e^{ikn_1(z-w)} \frac{e^{ik(w-z')} + r_{21}e^{ik(w+z')}}{1-r_{21}^2 e^{2ikw}}, \tag{2.126}$$

with the standard Fresnel coefficients (see Ref. [138] and App. A.3.2) of the macroscopic geometry with vacuum instead of the atomic vapor

$$r_{21} = \frac{1-n_1}{1+n_1}, \quad r_{12} = \frac{n_1-1}{n_1+1}, \quad t_{21} = \frac{2}{1+n_1}, \quad t_{12} = \frac{2n_1}{1+n_1}. \tag{2.127}$$

The 1-D Green's function (2.125) is intuitive to read when keeping the geometry in Fig. 2.7a in mind. The function describes a plane wave running from the right (z' in region 2) to the left (z in region 1). First, it propagates in vacuum ($e^{ikz'}$) then it passes from region 2 to region 1 (t_{21}) and finally propagates to z in region 1 ($e^{ikn_1|z|}$). An analogous reasoning applies to the cavity Green's function (2.126) where additionally a geometric sum appears $\sum_{n=0}^{\infty}[r_{21}^2\exp(2ikw)]^n = 1/(1-r_{21}^2\exp(2ikw))$ due to the multiple reflections inside of the cavity.

Throughout this thesis, we will assume that the incident field is polarized in x-direction. This is without loss of generality because we consider atoms with equally populated ground state sublevels that do not distinguish any polarization direction. The scattered field is then also x-polarized. The reflection coefficient of a dielectric-vapor interface becomes

$$r = r_{12} + \frac{\frac{k^2}{\epsilon_0}\sum_A G^{\mathrm{1D}}_{\mathrm{surf,out}}(0, z', \omega_{eg}) p_{x,A,ge}}{\int_{\mathrm{lens}} dA E_0} \tag{2.128}$$

$$= r_{12} + \frac{ikt_{21}}{2\epsilon_0 \mathcal{A}} \sum_A e^{ikz_A} \frac{p_{x,A,ge}}{E_0}, \tag{2.129}$$

where $\mathcal{A}$ is the lens area and E_0 is the amplitude of the incident field before the interface. Analogously, one finds the transmission coefficient of the vapor-filled cavity to be

$$t = t_0 + \frac{ikt_{21}e^{ikw(1-n_1)}}{2\epsilon_0 \mathcal{A}} \sum_A \frac{e^{-ikz_A} + r_{21}e^{ikz_A}}{1 - r_{21}^2 e^{2ikw}} \frac{p_{x,A,ge}}{E_0}, \tag{2.130}$$

where $t_0 = (t_{12}t_{21}e^{ikw(1-n_1)})/(1 - r_{21}^2 e^{2ikw})$.

The atomic dipole moments are determined by the coupled dipole model (2.104) and the corresponding spectra by Eqs. (2.129) and (2.130). Equipped with these foundations, we can now study the atom-wall interactions in Chapter 3 and the atom-atom interactions in a nanocavity in Chapter 4.

3. The Casimir–Polder effect in spectroscopy

In this chapter, we show how the atom-wall interaction via the Casimir–Polder (CP) effect alters the spectroscopic response of atoms and how this fact can be used to determine the Casimir–Polder effect in vapor cells. In general, there are two main classes of approaches to measure the CP effect. The first group investigates the impact of the CP force on atomic motion, while the second probes the CP line shift.

The first group includes experiments that determine the strength of the CP interaction from the center-of-mass oscillations of an atomic cloud that is optically trapped above a surface [139–141]. Furthermore, there are matter-wave diffraction experiments that record the interference patterns of atoms and molecules when they pass a nanograting. Some particles cannot pass the grating as the attractive CP force deflects them onto the surface, which impacts the intensity pattern [130, 142–144]. Additionally, the force imprints a phase on the particles that do pass [145, 146]. Other experiments utilize an evanescent laser field emanating from the surface with which the atoms interact. The field produces a repulsive dipole force that counteracts the CP attraction such that its strength can be inferred from the height of the energy barrier [147, 148]. Furthermore, in quantum mechanics, an atom can be reflected from a purely attractive CP potential that increases sharply near the surface. This type of quantum reflection has been used to determine the CP force on metastable neon atoms [149]. Other experiments measured the deflection of ground-state sodium atoms traveling through a micron-sized parallel-plate cavity [150] or performed spectroscopy on an atomic beam of Rydberg atoms passing through a gold cavity [151, 152].

This leads to the second group of spectroscopic methods that investigate the Casimir–Polder line shift. While force-based methods work well for long-lived states such as ground or highly excited Rydberg states, spectroscopic techniques can also access short-lived excited states. In this thesis, we focus on two relatively simple but very powerful methods based on thermal vapor cells: Selective reflection spectroscopy [57, 60, 153–155] that measures the reflection from a planar dielectric-vapor interface depending on the detuning from the atomic resonance and thin cell spectroscopy [54, 156–158] where transmission spectra can be recorded through vapor layers of nanometer thickness. Selective reflection produces high resolution, sub-Doppler spectra [57, 60]. It was used to demonstrate a repulsive Casimir–Polder potential for atomic states whose transition frequencies coincide with resonances of the dielectric surface [159, 160] and to showcase the temperature dependence of atom-surface interactions [161]. The spectrum originates from atoms with a wide variety of distances to the surface. Nanocells, on the other hand, cap the maximal atom-surface distance. Wedged nanocells specifically allow probing vapor layers of different thicknesses by shining light through different positions of the wedge [54]. A recent work has extracted Casimir–Polder coefficients from the transmission spectra of wedged nanocells [158]. The experimental progress in the field invites a refined theoretical description. Since selective reflection and thin cell spectroscopy integrate over atoms with different atom-surface distances, a fit model is required to extract the value of the Casimir–Polder shift. Most experimental studies utilize approximate models that neglect the interactions between the atoms, the anisotropy of the atomic polarisability, the Purcell effect, as well as the retardation of the Casimir–Polder potential. In this chapter, we explore the consequences of these simplifications for the determination of the Casimir–Polder effect.

We first compute and discuss numerical Casimir–Polder line shifts and Purcell line widths. We transfer our coupled dipole model of interacting particles to the description of the atomic vapor as a continuous medium. This allows us to theoretically calculate selective reflection and thin cell spectra both with and without the usual simplifications. We demonstrate that the exact spectra can be fitted with the simplified models which, however, leads to altered Casimir–Polder interaction coefficients. This finding has important implications for the quantitative comparison of theoretical and experimental results.

3.1. Computation of Casimir–Polder shifts

Before we calculate Casimir–Polder shifts, it is appropriate to point out that there are two different uses of the term “Casimir–Polder interaction”. A short excursion into science history helps to understand them. Casimir and Polder determined the dispersion interaction between an atom and a perfect conductor in 1948 [53] using second-order perturbation theory. This served as preparation to study atom-atom dispersion interactions over long distances, which requires at least fourth-order perturbation theory. As a consequence, older works in quantum optics and atomic physics use “Casimir–Polder interaction” to describe the long-distance limit of a dispersion interaction where retardation due to the finite speed of light is essential. The opposite, nonretarded or static interaction regime, which has been known prior, is then called “van der Waals interaction”. Since critical parts of the atom-wall interaction take place in a regime where neither extreme strictly applies, we adopt the more practical, modern naming scheme of macroscopic QED. It distinguishes which types of objects interact: The interaction of two microscopic objects (e.g. two atoms) is referred to as van der Waals interaction, the interaction of a microscopic and a macroscopic object (e.g. an atom and a surface) as Casimir–Polder interaction and the interaction of two macroscopic objects (e.g. two surfaces) as Casimir interaction. Each is named after the scientists who first prominently tackled the respective case [47, 51, 52]. The different names reflect that the Casimir–Polder interaction of an atom and a surface is not the same as independently summing up the van der Waals interactions of the atom with each individual surface molecule[1]. The presence of the surrounding molecules modifies the interactions of each van der Waals pair [51, 52] which the expression for the Casimir–Polder shift elegantly incorporates by using the Green’s tensor.

---

[1] Although such a pairwise summation serves as an approximation known as the Hamaker approach [51].

3.1.1. The nonretarded limit

As a first step, we show that the Casimir–Polder shift in front of a surface can be expressed as C_3/z^3 if the atom-surface distance z is sufficiently small. This nonretarded or static limit is the most common way to describe Casimir–Polder interactions in atomic physics and has a very illustrative explanation as we will see. To perform the quantitative derivation, we split the exact Casimir–Polder shift (2.97) into a resonant and an off-resonant contribution [52], $\omega^{\mathrm{CP}}_{A\substack{n\\ \nu\nu}} = \omega^{\mathrm{offres}}_{\substack{n\\ \nu}}(\mathbf{r}_A) + \omega^{\mathrm{res}}_{\substack{n\\ \nu}}(\mathbf{r}_A)$,

$$\omega^{\mathrm{offres}}_{\substack{n\\ \nu}}(\mathbf{r}_A) = \frac{1}{\hbar}\sum_{\substack{k\\ \kappa}} \mathbf{d}_{A\substack{nk\\ \nu\kappa}} \cdot \frac{2k_BT}{\hbar}\sum_{j=0}^{\infty}{}' \frac{\omega_{A,nk}\boldsymbol{\mathcal{G}}_{\mathrm{surf}}(\mathbf{r}_A,\mathbf{r}_A,i\xi_j)}{\xi_j^2+(\omega_{A,nk})^2}\mathbf{d}_{A\substack{kn\\ \kappa\nu}}, \tag{3.1}$$

$$\omega^{\mathrm{res}}_{\substack{n\\ \nu}}(\mathbf{r}_A) = \frac{1}{\hbar}\sum_{\substack{k\\ \kappa}} n(\omega_{A,kn})\mathbf{d}_{A\substack{nk\\ \nu\kappa}} \cdot \mathrm{Re}\,\boldsymbol{\mathcal{G}}_{\mathrm{surf}}(\mathbf{r}_A,\mathbf{r}_A,\omega_{A,nk})\mathbf{d}_{A\substack{kn\\ \kappa\nu}}. \tag{3.2}$$

The former involves the Green's tensors with real frequency arguments, which propagate real photons, and the latter Green's tensors with imaginary frequency arguments which propagate virtual photons. To express the resonant contribution in the above form, we rewrite the Bose–Einstein distribution as $n(-\omega) = -[n(\omega)+1]$.

At nonretarded distances, $z\omega/c \ll 1$, and for a surface with permittivity $\epsilon_1(\omega)$, the surface part of the one-point Green's tensor becomes (see App. A.2)

$$\boldsymbol{\mathcal{G}}^{\mathrm{nr}}_{\mathrm{surf}}(\mathbf{r},\mathbf{r},\omega) = \frac{\epsilon_1(\omega)-1}{\epsilon_1(\omega)+1}\frac{\mathrm{diag}(1,1,2)}{32\pi\epsilon_0 z^3}. \tag{3.3}$$

For the resonant contribution, the nonretarded approximation requires the atom-wall distance to be small compared to the atomic transition wavelength, $z \ll c/|\omega_{A,nk}|$. For the off-resonant contribution, the atom-wall distance has to be small compared the reduced wavelength[2] of a thermal photon, $z \ll c/\xi_j = \lambda_{\mathrm{th}}/(2\pi j)$. Ultimately, $z \ll \lambda_{\mathrm{th}}/(2\pi j)$ cannot be fulfilled when j becomes infinitely large. But since $z \ll c/|\omega_{A,nk}|$, the nonretarded approximation is still valid when $\xi_j \approx |\omega_{A,nk}|$, while terms with $\xi_j \gg |\omega_{A,nk}|$ barely influence the sum due to the prefactor $1/[\xi_j^2+(\omega_{A,nk})^2]$.

Under the above conditions, we can insert the nonretarded Green's tensor (3.3) and immediately obtain a Casimir–Polder potential $\omega^{\mathrm{CP}}_{A\substack{n\\ \nu\nu}} = C_3/z^3$ with

$$\begin{aligned} C_3 = \frac{1}{32\pi\epsilon_0\hbar}\sum_{\substack{k\\ \kappa}} \mathbf{d}_{A\substack{nk\\ \nu\kappa}} \cdot \mathrm{diag}(1,1,2)\mathbf{d}_{A\substack{kn\\ \kappa\nu}} \Bigg(& n(\omega_{A,kn})\frac{\epsilon_1(\omega_{A,kn})-1}{\epsilon_1(\omega_{A,kn})+1} \\ & + \frac{2k_BT}{\hbar}\sum_{j=0}^{\infty}{}' \frac{\omega_{A,nk}}{\xi_j^2+(\omega_{A,nk})^2}\frac{\epsilon_1(i\xi_j)-1}{\epsilon_1(i\xi_j)+1}\Bigg). \end{aligned} \tag{3.4}$$

---

[2] The reduced wavelength is $\lambdabar \equiv \lambda/(2\pi)$. At room temperature $\lambda_{\mathrm{th}} = \hbar c/(k_BT) \approx 8\,\mu\mathrm{m}$.

The C_3 coefficient can be significantly simplified if we neglect dispersion, i.e. set $\epsilon_1(\omega) \approx \epsilon_1$. Then, the Matsubara sum can be carried out analytically using [52]

$$\sum_{j=0}^{\infty}{}' \frac{1}{a^2 + j^2} = \frac{\pi}{2a} \coth(\pi a), \quad \coth\left(\frac{\hbar\omega_{A,nk}}{2k_B T}\right) = -2n(\omega_{A,kn}) - 1, \tag{3.5}$$

and the Casimir–Polder shift takes the compact form [52]

$$\omega^{\text{CP}}_{A\substack{n\\ \nu\nu}} = -\frac{1}{64\pi\hbar\epsilon_0 z_A^3}\frac{\epsilon_1 - 1}{\epsilon_1 + 1}\sum_{\substack{k\\ \kappa}} \mathbf{d}_{A\substack{nk\\ \nu\kappa}} \cdot \text{diag}(1,1,2)\mathbf{d}_{A\substack{kn\\ \kappa\nu}} \tag{3.6}$$

$$= -\frac{1}{2\hbar}\sum_{\substack{k\\ \kappa}} \mathbf{d}_{A\substack{nk\\ \nu\kappa}} \cdot \boldsymbol{\mathcal{G}}_{\text{surf}}(\mathbf{r}_A, \mathbf{r}_A, 0)\mathbf{d}_{A\substack{kn\\ \kappa\nu}}. \tag{3.7}$$

This result can be intuitively understood with the help of the image-dipole construction of electrostatics. In this approach, one considers an electric charge in front of a dielectric surface and seeks the electric field. It can be shown [101] that the field is the same as in a replacement system where no surface exists but a mirror charge of a certain magnitude is placed on the opposite side of the former interface[3].

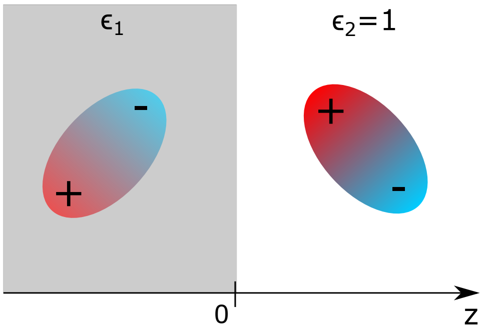

Figure 3.1: The mirror dipole picture of the nonretarded Casimir–Polder interactions. An atomic dipole that is spontaneously produced by atomic or field fluctuations induces a mirror dipole on the other side of the surface. The interaction of the original and the mirror dipole gives rise to the Casimir–Polder line shift.

According to Eq. (3.7), the Casimir–Polder interaction can be pictured as in Fig. 3.1: Fluctuations spontaneously create a dipole moment in the atom that induces a mirror dipole on the opposite side of the surface. This mirror dipole exerts the field $\boldsymbol{\mathcal{G}}_{\text{mirror}}(\mathbf{r}_A, \mathbf{r}_A, 0)\mathbf{d}_{A\substack{kn\\ \kappa\nu}}$ on the atomic dipole $\mathbf{d}_{A\substack{nk\\ \nu\kappa}}$. The potential energy of this dipole-dipole interaction causes the Casimir–Polder line shift. We get a prefactor of $1/2$ because some of the energy is already used up to induce the mirror dipole [162]. The minus sign indicates that dipole and mirror dipole by default are orientated such that they attract one another as in Fig. 3.1. In the next section, we investigate the accuracy of the C_3 approximation via exact numerical computation.

---

[3] In App. A.2 we use this reasoning to derive the nonretarded surface Green's tensor (3.3).

3.1.2. Rigorous computations for the rubidium D_2 line

We evaluate the Casimir–Polder shift (2.97) and the Purcell line broadening (2.98) with the exact surface Green's tensor (A.54) derived in App. A.3 for the rubidium D_2 line, i.e. the transition from the ground state $5S_{1/2}$ to the second excited state $5P_{3/2}$.

First, we consider a perfectly reflecting surface, that is an idealization of a metal or a superconductor, at zero temperature. This is the most minimalist example, and the results solely depend on the properties of the atoms. Fig. 3.2 shows the atomic transitions that dominate the CP shift. The nonretarded limit can be expected for $z \ll 780\,\mathrm{nm}/(2\pi) \approx 125\,\mathrm{nm}$, the smallest reduced wavelength of an important transition.

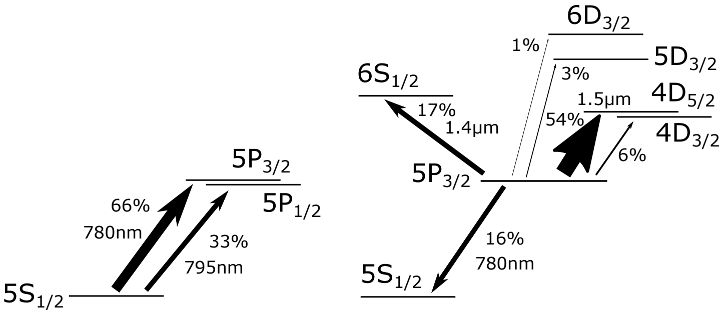

Figure 3.2: Selected transitions from the energy level diagram of rubidium which dominate the Casimir–Polder potential in front of a perfect reflector at $T = 0\,\mathrm{K}$. The percent values alongside the arrows indicate the relative contribution of the transition to the total C_3 coefficient of a rubidium atom in the $5S_{1/2}$ state (left) or the $5P_{3/2}$ state (right). The lengths refer to the transition wavelength in vacuum.

The line shifts and broadenings are shown in Fig. 3.3. The $m_j = \pm 3/2$ and $m_j = \pm 1/2$ sublevels of the excited state experience different Casimir–Polder effects, recall Fig. 2.4 b, such that two different line shifts and linewidths exist depending on the excited state sublevel. The C_3 panel in Fig. 3.3 shows that the exact shift follows a $C_3(z)/z^3$ behavior. The effective $C_3(z)$ changes up to 50% between $z = 1\,\mathrm{nm}$ and $z = 100\,\mathrm{nm}$. For larger distances, the potential approaches the retarded regime and oscillates [52], see right side of Fig. 3.3. This originates from the resonant part of the potential, more precisely from the propagation of the real photons emitted from the $5P_{3/2} \rightarrow 5S_{1/2}$ downward transition that go to the surface and are reabsorbed by the atom that restores its original excited state, recall Fig. 2.4 a. Since the photon travels a distance $2z$, the oscillation period in Fig. 3.3 is $780\,\mathrm{nm}/2 = 390\,\mathrm{nm}$. The oscillation amplitude decreases as $1/z$, recall Eq. (2.24), such that the shift vanishes at infinity. Analogous oscillations appear in the long distances limit of the excited state linewidth, which approaches its free space value at an infinite distance to the surface. In Fig. 3.3 the free space linewidth is indicated by the dashed line in the lower panel. At short distances, the linewidth of the excited states with $m_j = \pm 1/2$ is nearly constant but it is larger than in free space as the surface enhances the local density of states. In contrast, the surface prohibits the decay of the $m_j = \pm 3/2$ excited states as the atom-surface distance approaches zero. Consequently, the linewidth

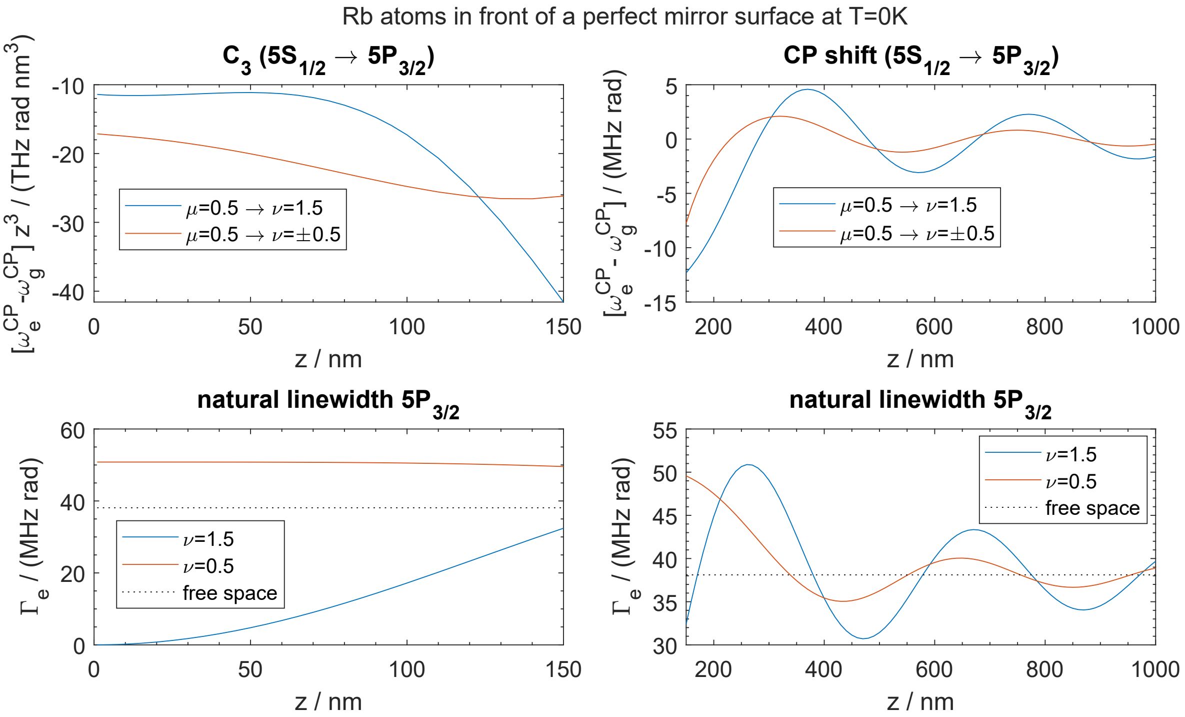

Figure 3.3: Casimir–Polder shift of the D_2 line (upper part) and Purcell line broadening (lower part) over the distance z between the rubidium atom and a perfect reflector at zero temperature. They are given for the m_j sublevel of the lower state (μ) and upper state (ν). The results are the same if the signs of μ and ν are reversed, e.g. from $\mu = 0.5 \to \nu = 1.5$ to $\mu = -0.5 \to \nu = -1.5$. At short distances, the potential is multiplied by z^3 to obtain an effective C_3 interaction coefficient. The natural linewidth of the transition is the same as the linewidth of the excited state because the ground state cannot decay any further.

vanishes. The $m_j = \pm 3/2$ states can only decay into $m_j = \pm 1/2$ states, thus releasing circularly polarized photons whose electric field components would lie parallel to the surface. However, the tangential electric field components on the surface of a perfect electric conductor are zero such that these photons cannot be emitted.

Next, we consider a dielectric sapphire surface. Sapphire is frequently used in the construction of vapor cells because it withstands chemically aggressive alkali atoms and relatively high temperatures [56]. It is also birefringent. We assume that its optical axis is aligned normal to the surface and report the corresponding Green's tensor in App. A.4. The resulting Casimir–Polder line shift and width are shown in Fig. 3.4. It turns out that the results are only marginally different from an isotropic surface whose permittivity is the geometric mean of the permittivities for the ordinary and extraordinary rays[4]. The permittivity function of sapphire was taken from Ref. [163]. The modeling of many other real materials is discussed in App. D.

---

[4] In the nonretarded limit, the geometric mean description is exact, see App. A.4. For optical frequencies, the ordinary and extraordinary permittivity of sapphire only deviate by around 3%, which translates into a change of around 1% in the Casimir–Polder potential at larger (retarded) distances when one compares the simplified isotropic description against the exact birefringent result.

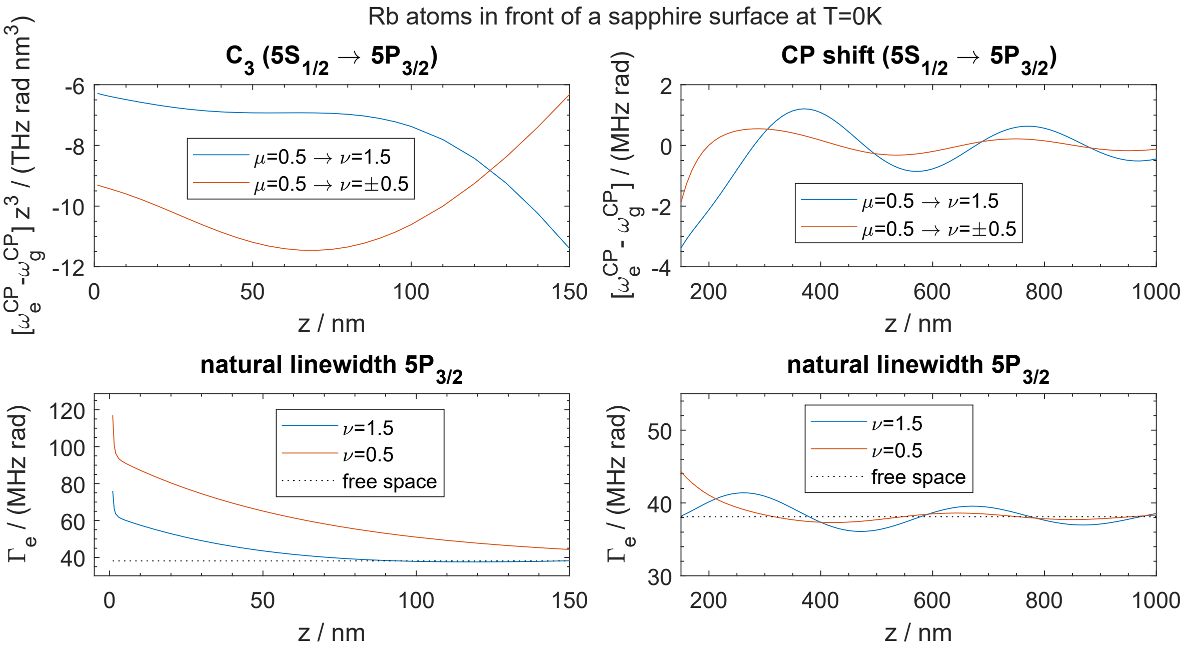

Figure 3.4: Casimir–Polder shift of the D_2 line (upper part) and Purcell line broadening (lower part) over the distance z between the rubidium atom and a sapphire surface at zero temperature, analogous to Fig. 3.3.

The sapphire surface produces weaker image dipoles than the perfect reflector and features a smaller effective $C_3(z)$ coefficient. On the other hand, close to the surface, the linewidth reaches even larger values than before. In the immediate vicinity to the surface ($z \leq 3\,\text{nm}$) it even diverges as Γ_3/z^3, following the nonretarded Green's tensor (3.3). However, due to the low absorption of sapphire at the atomic transition frequency, the imaginary part of the nonretarded approximation in Eq. (3.3) becomes quickly negligible for any distance more than a few nanometers away from the surface. The change in the local density of states and hence the linewidth is then governed by small propagating wave terms (see Ref. [52]) that are included in the exact Green's tensor. The linewidth declines slowly with increasing z. At larger distances, it follows the same oscillatory behavior as before but with a smaller amplitude.

Next, we investigate the impact of finite temperature on the Casimir–Polder shift and Purcell linewidth. The atom-surface separations that we are interested in are much smaller than the reduced wavelength of room temperature photons of $8\,\mu\text{m}$. The atomic transitions that are relevant for the rubidium D_2 line have transition wavelengths between 780 nm and $1.5\,\mu\text{m}$, see Fig. 3.2. Room temperature is not enough to excite these transitions, i.e. the Bose-Einstein distribution factors $n(\omega_{A,nm})$ are almost the same as at zero temperature. The two comparisons above show us that we are both geometrically and spectroscopically in a low-temperature regime, such that only small changes to the zero temperature result can be expected. Unfortunately, a spectroscopically small temperature implies that a large number of Matsubara frequencies must be considered for the Casimir–Polder shift (2.97) to converge. To make the numerics fast and accurate nonetheless, we apply a convergence accelerating method from Ref. [164] to the Matsubara sum. At 300 K, the Casimir–Polder shift changes by less than 1% and at 900 K by less than 5% for all distances $z \leq 1\,\mu\mathrm{m}$ where the Casimir–Polder shift is not close to zero. The changes to the linewidth are negligible in both cases. Thus the zero-temperature results shown in Fig. 3.4 remain a good approximation for a thermal vapor.

Still, this does not mean that temperature can be neglected in general when computing Casimir–Polder shifts. In App. E.3, we investigate a $5\mathrm{P}_{3/2} \to 6\mathrm{D}_{3/2}$ transition where adjacent states are separated by much smaller energy gaps. Then the room temperature is no longer spectroscopically low and can cause significant changes. The $6\mathrm{D}_{3/2}$ state of rubidium features at transition whose frequency matches a resonance of the dielectric surface. This results in a CP shift that is repulsive instead of attractive in the immediate vicinity of the surface.

3.1.3. The polarizability of the rubidium D_2 line

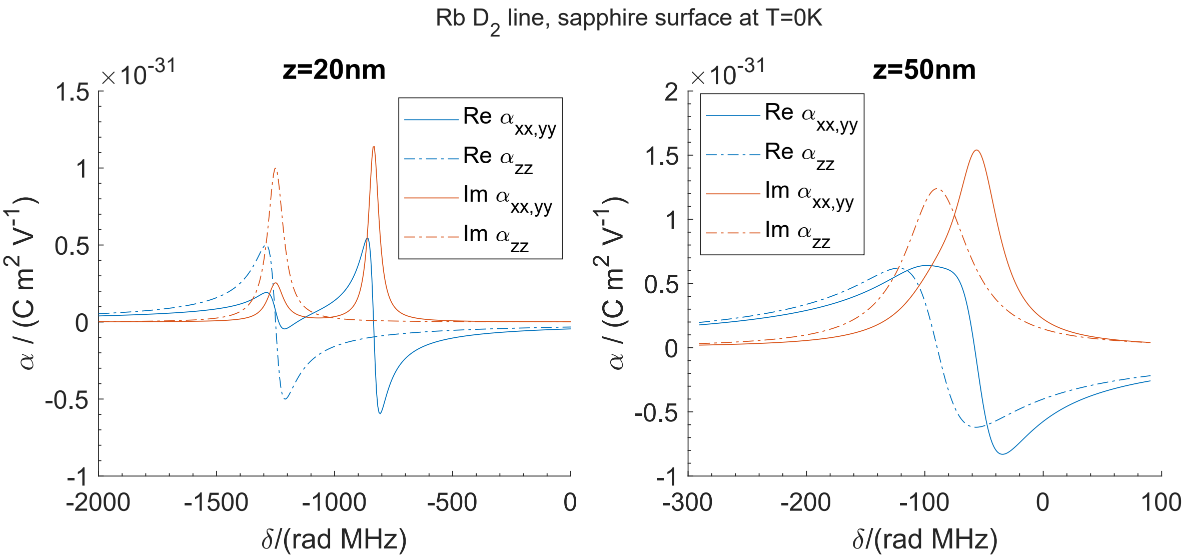

Figure 3.5: Components of the polarizability tensor of a rubidium ground state atom over the detuning δ from its free space D_2 line resonance. The atom is located $z = 20\,\mathrm{nm}$ (left) or $z = 50\,\mathrm{nm}$ (right) away from a sapphire surface and influenced by the Casimir–Polder interaction and Purcell effect shown in Fig. 3.4. The polarizability tensor $\boldsymbol{\alpha}_{A,ge} = \mathrm{diag}(\alpha_{xx}, \alpha_{yy}, \alpha_{zz})$ is diagonal but not isotropic $\alpha_{xx} = \alpha_{yy} \neq \alpha_{zz}$.

We can now examine the impact of the atom-wall interactions on the properties of the atoms. For this, we determine the atomic polarizability (2.105) for near-resonant excitation of the D_2 line of a single rubidium atom in front of a sapphire surface at zero temperature. Fig. 3.5 shows the polarizability over the detuning from the free space resonance for two different atom-surface distances, $z = 20\,\mathrm{nm}$ and $z = 50\,\mathrm{nm}$. We have assumed that the two ground-state sublevels $5\mathrm{S}_{1/2}, m_j = \pm 1/2$ are populated with equal probability. As a result, the polarizability tensor is diagonal, $\boldsymbol{\alpha}_{A,ge} = \mathrm{diag}(\alpha_{xx}, \alpha_{yy}, \alpha_{zz})$, but anisotropic, $\alpha_{xx} = \alpha_{yy} \neq \alpha_{zz}$, due to the lifted degeneracy between the $m_j = \pm 1/2$ and $m_j = \pm 3/2$ sublevels of the excited state. The Casimir–Polder effect shifts the atomic resonance to the red.

The polarizability components parallel to the surface $\alpha_{xx,yy}$ exhibit two peaks[5] that merge into one as the atom-surface distance increases from $z = 20\,\text{nm}$ to $z = 50\,\text{nm}$. This indicates that a phenomenological description of one polarizability component with a single peak can be successful, especially when additional broadenings due to temperature or atom-atom interactions come into play. On the other hand, Fig. 3.5 contradicts the use of a single isotropic polarizability for both $\alpha_{xx,yy}$ and α_{zz}.

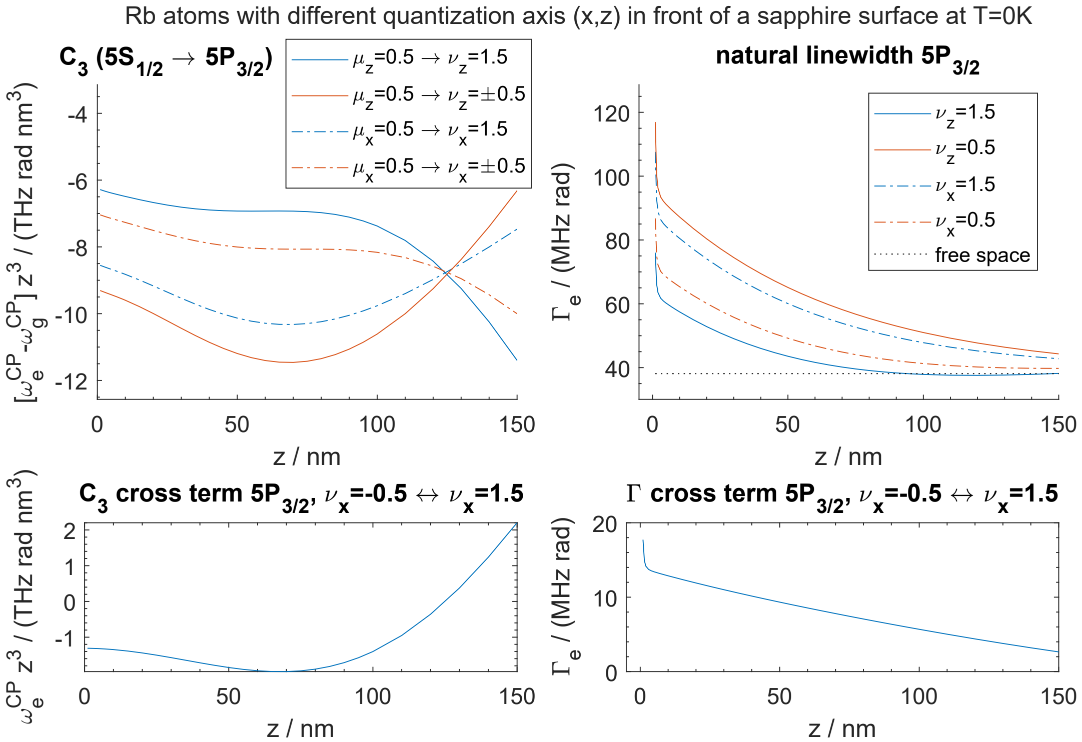

Figure 3.6: Upper panel: Casimir–Polder shift of the D_2 line and Purcell broadening over the distance z between the rubidium atom and a sapphire surface at zero temperature. μ_z and μ_x refer to m_j sublevels of the ground state with quantization axes perpendicular (z) or parallel (x) to the surface. In the former case the curves are the same as in Fig. 3.4. Lower panel: Sublevel interaction terms (recall Eqs. (2.97) and (2.98)) between excited state sublevels with a quantization axes parallel to the surface over the atom-surface distance z. They cause coherences from the $\mu = 1/2$ ground state to the $\nu = 3/2$ and $\nu = -1/2$ excited substate to depend on one another. Before a polarizability can be computed, the coupled equation system of the coherences has to be solved first.

Our atoms could also start as a statistical mixture of $m_j = \pm 1/2$ states that are quantized along an axis that is parallel, not perpendicular to the surface. We then obtain different Casimir–Polder shifts and Purcell linewidths, as shown in Fig. 3.6. In addition, we encounter non-zero sublevel coupling terms (recall Fig. 2.5), namely $\omega^{\text{CP}}_{A^{\ e}_{0.5,-1.5},x}$ and $\Gamma_{A^{\ e}_{0.5,-1.5},x}$ that are also shown in Fig. 3.6. They cause the coherences $\langle \hat{\tilde{\sigma}}_{A^{g\ \ e}_{0.5,1.5}}, x\rangle$ and $\langle \hat{\tilde{\sigma}}_{A^{g\ \ e}_{0.5,-0.5}}, x\rangle$ to depend on one another. For a single atom, we solve the coupled equation system (2.99). Subsequently, we compute the polarizability, which turns out to be the same as before. The coupling terms compensate for the different line shifts and linewidth. This highlights the significance of the sublevel coupling terms and shows that our choice of initial states does not affect the spectroscopic properties of the atoms. Having calculated and understood the Casimir–Polder and Purcell effects, we can now set up a theory to determine their impact in spectroscopy.

---

[5] The large peak is caused by $5\text{S}_{1/2}, m_j = \pm 1/2 \to 5\text{P}_{3/2}, m_j = \pm 3/2$ transitions and the smaller by $5\text{S}_{1/2}, m_j = \pm 1/2 \to 5\text{P}_{3/2}, m_j = \mp 1/2$ transitions. The α_{zz} component is governed by the $5\text{S}_{1/2}, m_j = \pm 1/2 \to 5\text{P}_{3/2}, m_j = \pm 1/2$ transitions.

3.2. The continuous medium approximation

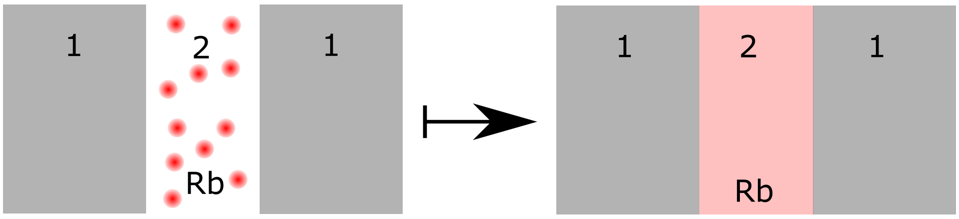

Figure 3.7: In standard electrodynamics, an atomic vapor is thought of as a continuous medium.

Selective reflection and thin cell spectroscopy are based on the description of an atomic vapor as a continuous medium as shown in Fig. 3.7. In the following, we transfer our coupled dipole model (2.104) to this perspective. As a result, certain microscopic effects such as atomic collisions are no longer explicitly considered. Instead, they are expressed as effective contributions to the line widths, line shifts, and atomic transition rates. We make the simplest possible assumption and add a line shift and a broadening that are both spatially independent and equal for all atoms. Thus, the new linewidth and shift become

$$\bar{\Delta}_{\substack{eg\\ \nu\mu}}(z) = \omega^{\mathrm{CP}}_{\substack{eg\\ \nu\mu}}(z) + \Delta^{\mathrm{col}}_{\substack{eg\\ \nu\mu}}, \quad \bar{\gamma}_{\substack{eg\\ \nu\mu}}(z) = \gamma_{\substack{eg\\ \nu\mu}}(z) + \gamma^{\mathrm{col}}_{\substack{eg\\ \nu\mu}}. \tag{3.8}$$

In the following, we drop the e, g subscript of these quantities for a more compact notation. The exact form of the new terms is considered in Sec. 3.2.4.

For the sake of simplicity, we assume that the incident field is normal to the interface[6]. Thus, the expectation values of the atomic flip operators become continuous functions

$$\langle \hat{\tilde{\sigma}}_{A^{ge}_{\mu\nu}} \rangle \mapsto \sigma_{\substack{ge\\ \mu\nu}}(z, v_z), \tag{3.9}$$

that only depend on z and v_z due to the overall cylindrical symmetry. Consequently, $\sigma_{\substack{ge\\ \mu\nu}}(z, v_z)$ carries the unit of an inverse velocity. Additionally, we assume the same sublevel population numbers $f_{\substack{g\\ \mu}}$ for all atoms and assert a velocity distribution $W(v_z)$,

$$f_{A,\substack{g\\ \mu}}(v_z) \mapsto W(v_z) f_{\substack{g\\ \mu}}, \tag{3.10}$$

---

[6] Oblique incidence has two main effects: It adds a Doppler broadening originating from the motion in x and y direction [60] and the CP shift perpendicular to the surface, not only the one parallel to it, takes effect.

that is usually assumed to be a Maxwell–Boltzmann distribution

$$W(v) = \frac{1}{v_{\text{th}}\sqrt{\pi}} e^{-v^2/v_{\text{th}}^2}, \quad v_{\text{th}} = \sqrt{\frac{2k_BT}{m}}, \tag{3.11}$$

where v_{th} is the most probable speed $|\mathbf{v}|$ of an atom. The use of the Maxwell–Boltzmann distribution for atoms in front of a surface is further discussed in Sec. 3.2.5.

To describe the atomic interactions, the sum over all atoms in Eq. (2.104) is replaced by an integral featuring the atomic number density $N = n_{\text{Atoms}}/V$,

$$\sum_{B\neq A} f(\mathbf{r}_A, \mathbf{r}_B) \mapsto N \int dV' \, f(\mathbf{r}, \mathbf{r}') - N \int_{\delta V'} dV' \, f(\mathbf{r}, \mathbf{r}'). \tag{3.12}$$

Since $B = A$ is excluded from the sum, an integral over an exclusion volume $\delta V'$ around $\mathbf{r}' = \mathbf{r}$ is subtracted. Its contribution is determined by the delta distribution term of the Green's tensor. For a cube or spherical exclusion volume, see Eq. (A.8) or Ref. [165], one finds

$$\int_{\delta V'} dV' \, \boldsymbol{G}(\mathbf{r}, \mathbf{r}', \omega_{eg}) \sigma_{\substack{ge \\ \delta\epsilon}}(z', v_z') = -\frac{\boldsymbol{I}}{3k^2} \sigma_{\substack{ge \\ \delta\epsilon}}(z, v_z'). \tag{3.13}$$

The remaining integral can be decomposed as $\int dV' = \int_0^w dz' \int dA'$. We know from Eq. (2.124) and App. (A.5) that the integral over A' results in a 1-D Green's function. When z and z' are both in the vapor region, the Green's functions for a cavity or surface geometry read

$$G^{\text{1D}}_{\text{surf}}(z, z', \omega_{eg}) = \frac{i}{2k} \left(e^{ik|z-z'|} + r_{21} e^{ik(z+z')} \right), \tag{3.14}$$

$$G^{\text{1D}}_{\text{cav}}(z, z', \omega_{eg}) = \frac{i}{2k} \frac{e^{ik|z-z'|} + r_{21} e^{ik(z+z')} + r_{21} e^{ik(2w-z-z')} + r_{21}^2 e^{ik(2w-|z-z'|)}}{1 - r_{21}^2 e^{2ikw}}. \tag{3.15}$$

As in Sec. 2.4.1, we take our incident field to be x-polarized. Due to the cylindrical symmetry, the system retains the polarization so that only the x component of field and dipole moment must be considered. We write our coupled dipole model for the continuous medium as a set of two coupled equations, one for the atomic polarization

$$v_z \partial_z \sigma_{\substack{ge \\ \mu\nu}}(z, v_z) = i \left[\delta - \bar{\Delta}_{\nu\mu}(z) + i\bar{\gamma}_{\nu\mu}(z) \right] \sigma_{\substack{ge \\ \mu\nu}}(z, v_z) + \frac{i}{\hbar} W(v_z) f_\mu d_{x, \substack{eg \\ \nu\mu}} E_x^{\text{loc}}(z), \tag{3.16}$$

and one for the electric field

$$E_x^{\text{loc}}(z) = E_x(z) + \frac{N}{3\epsilon_0} \left\langle p_x(z) \right\rangle_v, \tag{3.17}$$

$$E_x(z) = E_{x,\text{inc}}(z) + N \frac{k^2}{\epsilon_0} \int_0^w dz' \, G^{\text{1D}}(z, z', \omega_{eg}) \left\langle p_x(z') \right\rangle_v. \tag{3.18}$$

Here $E_x^{\text{loc}}(z)$ denotes the local field, the effective electric field perceived by an atom that is modified due to the polarization of the surrounding continuous vapor. We postpone the discussion of the local field effect to Sec. 3.2.3 because its best-known form requires the refractive index of the vapor to be derived first. Our target quantity, the atomic dipole moment, results from an ensemble average over the velocity as

$$\langle p_x(z)\rangle_v = \sum_{\delta\epsilon} d_{x,\substack{ge\\ \delta\epsilon}} \int_{-\infty}^{\infty} dv'_z \, \sigma_{\substack{ge\\ \delta\epsilon}}(z, v'_z). \tag{3.19}$$

3.2.1. Formal solution and nonlocal response

To solve Eq. (3.16), we introduce a helper function following Refs. [60, 166]

$$L_{\nu\mu}(z) = \int_{z_0}^{z} dz' \left(-i\left[\delta - \bar{\Delta}_{\nu\mu}(z')\right] + \bar{\gamma}_{\nu\mu}(z')\right), \tag{3.20}$$

with whom Eq. (3.16) can be recast as

$$v_z \partial_z \sigma_{\substack{ge\\ \mu\nu}}(z, v_z) = -\,\partial_z L_{\nu\mu}(z) \sigma_{\substack{ge\\ \mu\nu}}(z, v_z) + \frac{i}{\hbar} W(v_z) f_{\substack{g\\ \mu}} d_{x,\substack{eg\\ \nu\mu}} E_x^{\mathrm{loc}}(z). \tag{3.21}$$

We assume quenching collisions with the cell walls, which ensure that the atoms are unpolarized when they depart from a surface,

$$\sigma_{\substack{ge\\ \mu\nu}}(z = 0, v_z > 0) = \sigma_{\substack{ge\\ \mu\nu}}(z = w, v_z < 0) = 0. \tag{3.22}$$

For a surface geometry, we take $w = \infty$ and likewise assume that the atoms arriving from far away are unpolarized. We find the formal solutions

$$\sigma_{\substack{ge\\ \mu\nu}}(z, v_z > 0) = \frac{i}{\hbar} \frac{W(v_z)}{v_z} f_{\substack{g\\ \mu}} d_{x,\substack{eg\\ \nu\mu}} \int_0^z dz' \, E_x^{\mathrm{loc}}(z') \exp\left[\Lambda_{\nu\mu}(z', z)/v_z\right], \tag{3.23}$$

$$\sigma_{\substack{ge\\ \mu\nu}}(z, v_z < 0) = \frac{i}{\hbar} \frac{W(v_z)}{v_z} f_{\substack{g\\ \mu}} d_{x,\substack{eg\\ \nu\mu}} \int_w^z dz' \, E_x^{\mathrm{loc}}(z') \exp\left[\Lambda_{\nu\mu}(z', z)/v_z\right], \tag{3.24}$$

$$\sigma_{\substack{ge\\ \mu\nu}}(z, v_z = 0) = \frac{i}{\hbar} \frac{W(0)}{(-i\delta + i\bar{\Delta}_{\nu\mu}(z) + \bar{\gamma}_{\nu\mu}(z))} f_{\mu} d_{x,\substack{eg\\ \nu\mu}} E_x^{\mathrm{loc}}(z), \tag{3.25}$$

where

$$\Lambda_{\nu\mu}(z', z) \equiv L_{\nu\mu}(z') - L_{\nu\mu}(z) \tag{3.26}$$

$$= \underbrace{\left(-i\delta_{\nu\mu} + \bar{\gamma}_{\nu\mu}^{\mathrm{vac}}\right)(z' - z)}_{=\Lambda_{\nu\mu}^{\mathrm{vac}}(z',z)} + \underbrace{\int_z^{z'} dz'' \left(i\omega_{\nu\mu}^{\mathrm{CP}}(z'') + \bar{\gamma}_{\nu\mu}(z'') - \bar{\gamma}_{\nu\mu}^{\mathrm{vac}}\right)}_{=\Lambda_{\nu\mu}^{\mathrm{AW}}(z',z)}. \tag{3.27}$$

Here $\bar{\gamma}_{\nu\mu}^{\mathrm{vac}} = \gamma_{\nu\mu}^{\mathrm{vac}} + \gamma_{\nu\mu}^{\mathrm{col}}$ is the sum of the natural and the collisional linewidth in free space and $\delta_{\nu\mu} \equiv [\delta - \Delta_{\nu\mu}^{\mathrm{col}}]$.

The integration in Eqs. (3.23) and (3.24) indicates that a thermal atomic vapor is a nonlocal medium. The atomic response at z depends on field values $E_x^{\mathrm{loc}}(z')$ at other positions z' because a moving atom that is excited at z' travels to position z. To get a better understanding, let us consider an atomic cloud with the extend of about one wavelength, $w \sim \lambda$, and neglect the atom-surface interactions such that $\Lambda_{\nu\mu}(z', z) \approx \Lambda^{\mathrm{vac}}_{\nu\mu}(z', z)$ as shown in Fig. (3.8). The integration range in Eqs. (3.23) and (3.24) is then determined by the exponential function $\exp(-\bar{\gamma}^{\mathrm{vac}}_{\nu\mu}|z - z'|/|v_z|)$. The function shows that the distance between the spot where the atom is excited z' and the spot z where it contributes to the polarization cannot be much larger than the average distance $|v_z|/\bar{\gamma}^{\mathrm{vac}}_{\nu\mu}$ that an excited atom with a lifetime of $1/\bar{\gamma}^{\mathrm{vac}}_{\nu\mu}$ travels before it decays. A small broadening implies that a large region such as the orange one in Fig. 3.8 contributes to the atomic response. However, if the broadening is very large and the atoms decay quickly, the system response only depends on field values $E(z') \approx E(z)$ very close to the spot excitation. Such a situation is depicted by the blue region in Fig. 3.8 and means that the atomic vapor behaves approximately as an ordinary local medium.

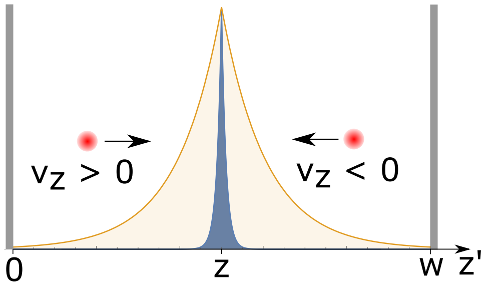

Figure 3.8: Illustration of the regions from which polarized atoms of velocity $\pm v_z$ arrive at a probe point z to contribute to the atomic response, compare Ref. [167]. We consider a cavity of length $w \sim \lambda$ and neglect Casimir–Polder and Purcell interactions. In case of a large homogeneous broadening ($\xi(v_z) = |v_z|/\bar{\gamma}^{\mathrm{vac}}_{\nu\mu} = 0.01\,w$), shown in blue, the atomic polarization originates from a small spatial region around z within which $E(z') \approx E(z)$. The atomic response is approximately local. A smaller homogeneous broadening ($\xi(v_z) = 0.1\,w$) shown in light orange leads to a strongly nonlocal scenario, where atomic polarizations that were originally created at almost any point in the cavity contribute to the polarization in the center.

3.2.2. Local limit in absence of atom-wall interactions

When the homogeneous broadening is large enough to reach the local limit, we can retrieve the familiar results from standard electrodynamics where the atomic vapor is described by a refractive index n_g. To facilitate this task, we again neglect the Casimir–Polder interactions and take $\Lambda_{\nu\mu}(z', z) \approx \Lambda^{\mathrm{vac}}_{\nu\mu}(z', z)$. This only makes sense as long as the focus is on the link between microscopic dipole-dipole interactions and standard continuous electrodynamics and not on an accurate description of a nanometer-sized vapor cell.

We start with an ansatz for the local field

$$E^{\mathrm{loc}}_x(z) = E^+ e^{ikn_g z} + E^- e^{-ikn_g z}, \tag{3.28}$$

with a yet unknown constant n_g. Inserting into Eqs. (3.23), (3.24) gives

$$
\begin{aligned}
\sigma_{\substack{ge\\ \mu\nu}}(z, v_z > 0) &= \frac{-W(v_z) f_{\substack{g\\ \mu}} d_{\substack{x,eg\\ \nu\mu}}}{\hbar} \sum_{\eta=+,-} \frac{E^\eta \left(e^{\eta i k n_g z} - e^{\left(i\delta_{\nu\mu} - \bar{\gamma}^{\text{vac}}_{\nu\mu}\right) z/v_z}\right)}{\delta_{\nu\mu} - \eta k n_g v_z + i\bar{\gamma}^{\text{vac}}_{\nu\mu}} && (3.29)\\
&\approx \frac{-W(v_z) f_{\substack{g\\ \mu}} d_{\substack{x,eg\\ \nu\mu}}}{\hbar} \left[\frac{e^{i k n_g z} E^+}{\delta_{\nu\mu} - k n_g v_z + i\bar{\gamma}^{\text{vac}}_{\nu\mu}} + \frac{e^{-i k n_g z} E^-}{\delta_{\nu\mu} + k n_g v_z + i\bar{\gamma}^{\text{vac}}_{\nu\mu}}\right], && (3.30)\\
\sigma_{\substack{ge\\ \mu\nu}}(z, v_z < 0) &= \frac{-W(v_z) f_{\substack{g\\ \mu}} d_{\substack{x,eg\\ \nu\mu}}}{\hbar} \sum_{\eta=+,-} \frac{E^\eta e^{\eta i k n_g z} \left(1 - e^{\left(i\delta_{\nu\mu} - \bar{\gamma}^{\text{vac}}_{\nu\mu}\right)(w-z)/|v_z|}\right)}{\delta_{\nu\mu} - \eta k n_g v_z + i\bar{\gamma}^{\text{vac}}_{\nu\mu}} && (3.31)\\
&\approx \frac{-W(v_z) f_{\substack{g\\ \mu}} d_{\substack{x,eg\\ \nu\mu}}}{\hbar} \left[\frac{e^{i k n_g z} E^+}{\delta_{\nu\mu} - k n_g v_z + i\bar{\gamma}^{\text{vac}}_{\nu\mu}} + \frac{e^{-i k n_g z} E^-}{\delta_{\nu\mu} + k n_g v_z + i\bar{\gamma}^{\text{vac}}_{\nu\mu}}\right]. && (3.32)
\end{aligned}
$$

As part of our local approximation, we assume a large homogeneous broadening with $\bar{\gamma}^{\text{vac}}_{\nu\mu} \frac{|z|}{|v_z|} \gg 1$ and $\bar{\gamma}^{\text{vac}}_{\nu\mu} \frac{|w-z|}{|v_z|} \gg 1$. Clearly, these inequalities cannot hold in the immediate vicinity to the walls where $z = 0$ or $z = w$ and the atomic response is determined by quenching collisions. However, we can assume that the affected areas are small enough to have no significant effect on the transmission and reflection spectra such that the deviations that occur there can be neglected. The above expressions explicitly feature the Doppler shift $\pm k n_g v_z$, whose sign depends on the relative orientation between the wave vector of the incoming light field and the velocity vector of the atom. The dipole moment (3.19) takes the compact form

$$
\langle p_x(z)\rangle_v = \underbrace{-\frac{1}{\hbar}\sum_{\mu,\nu} f_{\substack{g\\ \mu}} \left|d_{\substack{x,eg\\ \nu\mu}}\right|^2 \int_{-\infty}^{\infty} dv_z \, \frac{W(v_z)}{\delta_{\nu\mu} - k n_g v_z + i\bar{\gamma}^{\text{vac}}_{\nu\mu}}}_{=\alpha} E^{\text{loc}}_x(z). \tag{3.33}
$$

When integrating over all velocities, the sign of the Doppler shift makes no difference because of the even symmetry of the Maxwell–Boltzmann distribution $W(v_z) = W(-v_z)$. As a result, the same polarizability applies to both forward and backward running wave components. Inserting Eq. (3.33) into Eq. (3.17), we can relate the ordinary and the local electric field (3.17) as

$$
E^{\text{loc}}_x(z) = \frac{1}{1 - \frac{N}{3\epsilon_0}\alpha} E_x(z). \tag{3.34}
$$

With wise foresight, we introduce the abbreviation

$$
(\epsilon - 1) \equiv \frac{N\alpha}{\epsilon_0} / \left(1 - \frac{N}{3\epsilon_0}\alpha\right). \tag{3.35}
$$

By inserting the above in Eq. (3.18), the electric field is shown to obey

$$
E_x(z) = E_{x,\text{inc}}(z) + \frac{ik}{2}(\epsilon - 1) N \int_0^w dz' \frac{2k}{i} G^{1\text{D}}(z, z', \omega_{eg}) E_x(z'). \tag{3.36}
$$

The incident field for a surface or a cavity geometry is

$$E_{x,\mathrm{inc}}^{\mathrm{surf}} = t_{12}E_0 e^{ikz}, \quad E_{x,\mathrm{inc}}^{\mathrm{cav}} = t_{12}E_0 \frac{e^{ikz} + r_{21}e^{ik(2w-z)}}{1 - r_{21}^2 e^{2ikw}}, \tag{3.37}$$

respectively, while the corresponding 1-D Green's function is given by Eq. (3.14) or (3.15). We can convert Eq. (3.36) into a differential equation by differentiating[7] two times by z and replacing the integral with the help of the original expression. The result is a common harmonic oscillator,

$$E_x''(z) + k^2\epsilon E_x(z) = 0. \tag{3.38}$$

Hence, we insert the ansatz $E_x(z) = Ae^{ikn_g z} + Be^{-ikn_g z}$ with $n_g = \sqrt{\epsilon}$ and $\mathrm{Im}\, n_g \geq 0$ into Eq. (3.36). By comparing coefficients, we find the electric field in a surface or a cavity geometry

$$E_x^{\mathrm{surf}}(z) = \tilde{t}_{12}E_0 e^{ikn_g z}, \quad E_x^{\mathrm{cav}}(z) = \tilde{t}_{12}E_0 \frac{e^{ikn_g z} + \tilde{r}_{21}e^{ikn_g(2w-z)}}{1 - \tilde{r}_{21}^2 e^{2ikn_g w}}, \tag{3.39}$$

respectively, which feature new Fresnel coefficients

$$\tilde{t}_{12} = \frac{2n_1}{n_1 + n_g}, \quad \tilde{t}_{21} = \frac{2n_g}{n_1 + n_g}, \quad \tilde{r}_{21} = \frac{n_g - n_1}{n_g + n_1}, \tag{3.40}$$

between a wall with index n_1 and the vapor with index n_g. This result shows the self-consistency with our ansatz function (3.28) that is now seen to be

$$E_x^{\mathrm{loc}}(z) = \underbrace{\frac{1}{1 - \frac{N}{3\epsilon_0}\alpha} \frac{\tilde{t}_{12}E_0}{1 - \tilde{r}_{21}^2 e^{2ikn_g w}}}_{=E^+} e^{ikn_g z} + \underbrace{\frac{1}{1 - \frac{N}{3\epsilon_0}\alpha} \frac{\tilde{t}_{12}E_0\tilde{r}_{21}e^{2ikn_g w}}{1 - \tilde{r}_{21}^2 e^{2ikn_g w}}}_{=E^-} e^{-ikn_g z}. \tag{3.41}$$

The cavity field contains two summands and a geometric sum denominator, which can be

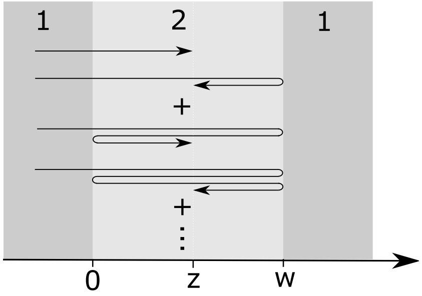

Figure 3.9: Photon pathways that determine the field acting inside of a cavity. The two fundamental paths are followed by multiple internal reflections leading to a geometric sum, $\sum_{n=0}^{\infty}[(r^{21})^2 e^{2iwk_2}]^n$.

---

[7] Either split the integral into two to remove the absolute value function and recall the Leibniz integral rule $\frac{d}{dx}\left(\int_{a(x)}^{b(x)} dy\, f(x,y)\right) = f(x,b)b'(x) - f(x,a)a'(x) + \int_{a(x)}^{b(x)} dy\, \partial_x f(x,y)$ or use the identity $\partial_x^2|x| = 2\delta(x)$.

intuitively understood by comparison with the photon pathways shown in Fig. 3.9. By solving the self-consistent scattering problem (3.36), we have transformed the incident fields (3.37) featuring the refractive index of vacuum into the acting fields (3.39) featuring a refractive index $n_g = \sqrt{\epsilon}$ for the atomic vapor.

Of course, we can retrieve not only the fields from standard optics, but also the reflection coefficient of the dielectric-vapor interface and the transmission coefficient of the vapor-filled cavity. In a continuous vapor, the relations for reflection (2.129) and transmission coefficient (2.130) become

$$r^{\mathrm{surf}} = r_{12} + t_{21}\frac{ik}{2}\frac{N}{\epsilon_0}\int_0^\infty dz\, e^{ikz}\frac{\langle p_x(z)\rangle_v}{E_0}, \tag{3.42}$$

$$t^{\mathrm{cav}} = t_0 + \frac{ikt_{21}e^{ikw(1-n_1)}N}{2\epsilon_0}\int_0^w dz\, \frac{e^{-ikz}+r_{21}e^{ikz}}{1-r_{21}^2e^{2ikw}}\frac{\langle p_x(z)\rangle_v}{E_0}. \tag{3.43}$$

Inserting the fields (3.39), we find

$$r^{\mathrm{surf}} = \tilde{r}_{12}, \quad t^{\mathrm{cav}} = \frac{\tilde{t}_{12}\tilde{t}_{21}e^{iw(kn_g-k_1)}}{1-\tilde{r}_{21}^2e^{2in_gkw}}, \tag{3.44}$$

the familiar Fresnel reflection coefficient and the Fabry–Pérot transmission profile. The refractive index n_g is not given directly by the above relations. Eq. (3.33), Eq. (3.35), and $n_g = \sqrt{\epsilon}$ show that the Doppler shift within the polarizability depends on the refractive index and that the refractive index depends on the polarizability. An iterative approach can be used to obtain a self-consistent result. Close to resonance, where $\operatorname{Im} n_g$ is appreciably larger than zero, another particularity occurs: In addition to the usual Doppler shift $kv_z \operatorname{Re} n_g$, there is also a contribution of $kv_z \operatorname{Im} n_g$ to the linewidth. However, reaching the local limit in a cavity of size $w \sim 1/k$ with atoms whose velocities can reach v_{th} implies that $\bar{\gamma}_{\nu\mu}^{\mathrm{vac}} \gtrsim v_{\mathrm{th}}k$. Therefore, the changes to the small Doppler effect can not drastically alter the vapor's properties.

3.2.3. Lorentz–Lorenz relation

Now that we have established the link between the polarizability and the refractive index, Eq. (3.35), we can rearrange it in the form of a famous result

$$\frac{\alpha N}{3\epsilon_0} = \frac{\epsilon-1}{\epsilon+2} = \frac{n^2-1}{n^2+2}. \tag{3.45}$$

When the right-hand side denotes (static) permittivities, this equation is known as Clausius–Mossotti relation and when the right-hand side denotes a refractive index (at optical frequencies) it is called Lorentz–Lorenz (LL) relation [101, 168]. The LL relation shows that the microscopic polarizability is not directly proportional to macroscopic susceptibility $\epsilon - 1$, but to the fraction[8]

---

[8] Heating liquids like water or carbon disulfide, Ludvig Lorenz showed that the ratio $[(n^2-1)/(n^2+2)]/N$ remains unchanged even as the liquids become vapors and their density changes by orders of magnitude [70]. For vapors with low density where $n \approx 1$, one often uses $(n^2-1)/(n^2+2) \approx 2/3(n-1)$.

$(\epsilon-1)/(\epsilon+2)$. It results from the local field correction that we introduced in Eq. (3.17) and which stems from the volume integral over the singularity of the Green's tensor in a continuous environment, Eq. (3.13). Physically, it expresses the fact that the field perceived by an atom in a medium is not the same as in vacuum due to the polarization of the surrounding. The effect was discovered independently by Hendrik Lorentz [69] and Ludvig Lorenz [70] and is named after both of them. For once, this saves us from doubts about how Loren(t)z is spelled correctly[9]. One can also define an effective polarizability, $\alpha^{\mathrm{loc}} = \alpha/\left(1 - N\alpha/(3\epsilon_0)\right)$, that includes the local field correction and features a direct proportionality $(\epsilon-1) = N\alpha^{\mathrm{loc}}/\epsilon_0$.

Let us consider a vapor that is dominated by homogeneous broadening, e.g., an ultracold vapor or a thermal vapor with a large collisional broadening, such that the Doppler shift and nonlocal effects can be neglected. Let us further assume that all atomic sublevels feature the same broadening, the same Casimir–Polder and the same collisional shifts that we write as $\bar{\Delta}_{\nu\mu}(z) = \bar{\Delta}_{eg}(z)$ and $\bar{\gamma}_{\nu\mu}(z) = \bar{\gamma}_{eg}(z)$. Further, all atomic substates shall be populated equally, i.e. $f_{\underset{\mu}{g}} = 1/(2J_g+1)$ in case of a fine structure basis. Together with the abbreviation[10] $\sum_{\mu,\nu}\left|d_{x,\nu\mu}^{\;eg}\right|^2 = (2J_e+1)|d_{x,eg}|^2$, the effective polarizability can then be written as

$$\alpha^{\mathrm{loc}} = -\frac{1}{\hbar}\frac{(2J_e+1)}{(2J_g+1)}\frac{|d_{x,eg}|^2}{\delta - \Delta_{eg}^{\mathrm{LL}} - \bar{\Delta}_{eg}(z) + i\bar{\gamma}_{eg}(z)}. \tag{3.46}$$

It is the same as the ordinary single atom polarizability except for the shift

$$\Delta_{eg}^{\mathrm{LL}} = -\frac{(2J_e+1)}{(2J_g+1)}\frac{N|d_{x,eg}|^2}{3\epsilon_0\hbar}, \tag{3.47}$$

which is called the Lorentz–Lorenz shift. In this form, the local field correction presents itself as an attractive ($-$ sign) dipole-dipole interaction ($\propto |d_{x,eg}|^2$) between the atom and the atoms surrounding it that shifts the atomic resonance to the red. Let us further consider a transition from the ground state to an excited state that can only decay back to the ground state, e.g., the alkali D-line transitions. Then, one can rewrite the LL shift in terms of the decay rate in free space[11] as

$$\Delta_{eg}^{\mathrm{LL}} = -\frac{(2J_e+1)}{(2J_g+1)}\frac{\pi N}{3k^3}\Gamma_e^{\mathrm{vac}}. \tag{3.48}$$

The local field correction cannot be rewritten into a simple line shift if the atomic sublevels possess different Casimir–Polder shifts or when the Doppler shift plays an important role.

---

[9] Among others the Lorentz force, the Lorentz transformation, the Lorentzian distribution and the Drude–Lorentz model are named after Hendrik Lorentz while the Lorenz gauge and the Lorenz factor (the proportionalty constant of the Wiedemann–Franz law) are named after Ludvig Lorenz.

[10] We drag out the factor $(2J_e+1)$ to clarify the relation to the quantity $|d_{x,eg}|^2 = \sum_\mu \left|d_{x,\nu\mu}^{\;eg}\right|^2$ that governs the linewidth.

[11] Often a transition $J_g = 0 \rightarrow J_e = 1$ is considered, such that $\Delta_{eg}^{\mathrm{LL}} = -\pi(N/k^3)\Gamma_e^{\mathrm{vac}}$. Bear in mind that $|d_{x,eg}|^2 = |\mathbf{d}_{eg}|^2/3$.

3.2.4. Atomic collisions

The Lorentz-–Lorenz relation describes an isotropic dipole-dipole interaction between an atom and all atoms surrounding it. However, in the immediate vicinity of an atom, the isotropy gets repeatedly broken by temporary close encounters with individual other atoms, i.e. collisions. In this section, we elaborate on the theory behind the collisional broadening and shift added in Eq. (3.8). In general, one can distinguish between inelastic collisions, which change the atomic states and elastic collisions, which only change the phase of the atomic wavefunction and result in line broadenings and shifts [169]. For many problems in atomic physics, one can neglect inelastic collisions (adiabatic approximation) [135]. While unifying semi-classical and quantum theories exist for elastic collisions, they are most conveniently studied within one of two opposite limits, the quasi-static or the impact limit, both of which lead to a homogeneous line broadening [135, 136, 170–172]. This line broadening is proportional to the atomic density, which in an ideal gas, where $p = Nk_BT$, is proportional to the gas pressure. Hence, the effect is also known as pressure broadening. In our case, where the two colliding atoms are identical, it is also called self-broadening.

The first of the two common approximations, the quasi-static approximation, assumes the duration of the collision τ_C to be much larger than other relevant time scales, such as the time between two collisions [136]. Then, the interaction potential between the atoms translates into a line shift that is taken to be constant over the time τ_C. In an ensemble average over various atomic distances and orientations, the line shift becomes a line broadening [135]. The quasi-static approximation is favored when the temperature is low, i.e. τ_C is long, because of the slow movement of the atoms, or when the atomic density is high, i.e. the time between collisions becomes short [136]. The opposite impact approximation assumes that the collision occurs almost instantaneously compared to the time between collisions. Usually, one considers only two atoms (binary approximation) moving on classical, straight trajectories. The smallest distance between the two atoms is called the impact parameter ρ. During the collision, i.e. over the time τ_C, the wave train of the emitting atom acquires a phase shift [135]. After averaging over all impact parameters, this phase shift translates to a line broadening and shift [135, 136]. The impact parameter that results in a phase shift of unity is called the Weisskopf radius ρ_W and provides a typical length scale for the collision [135, 136]. Taking it as a rough estimate for the section of the trajectory where significant interactions occur, one can estimate the collision time as $\tau_C \approx \rho_W/\bar{v}_r$ [135]. Here $\bar{v}_r = \sqrt{8k_BT/(\pi\mu)}$ with the reduced mass $\mu = m_Am_B/(m_A + m_B)$ of the colliding pair is the mean relative velocity of the two particles, assuming that both follow a Maxwell–Boltzmann distribution[12]. The impact approximation is favored at low densities, when the time between collisions becomes long, and at high temperatures, when the collision duration is short.

---

[12] To compute $\bar{v}_r = \int d^3\mathbf{v}_1 \int d^3\mathbf{v}_2 W(\mathbf{v}_1)W(\mathbf{v}_2)v_r$ one can conveniently use the relative velocity $\mathbf{v}_r = \mathbf{v}_1 - \mathbf{v}_2$ and the center of mass $\mathbf{U} = (m_1\mathbf{v}_1 + m_2\mathbf{v}_2)/(m_1 + m_2)$ coordinates because $d^3\mathbf{v}_1 d^3\mathbf{v}_2 = d^3\mathbf{v}_r d^3\mathbf{U}$ and $m_1v_1^2 + m_2v_2^2 = (m_1 + m_2)U^2 + \mu v_r^2$.

Thermal vapors are often treated in the impact approximation. Experiments in a bulk vapor (see Ref. [173] and the references therein) show that the collisional broadening $\Gamma^{\mathrm{col}} = 2\gamma^{\mathrm{col}}$ of the sodium, rubidium, and cesium D-lines, averaged over the degenerate sublevels, follows the simple form

$$\Gamma^{\mathrm{col}} = \beta N \approx 2\pi \sqrt{\frac{(2J_e+1)}{(2J_g+1)}} \Gamma_{\mathrm{e}}^{\mathrm{vac}} \frac{N}{k^3}, \tag{3.49}$$

where the degeneracy prefactor $\sqrt{(2J_e+1)/(2J_g+1)}$ is 1 for the D_1 and $\sqrt{2}$ for the D_2 line. The approximate sign in Eq. (3.49) refers to the theoretical prediction of Lewis [171] that involves an additional prefactor, which also depends on the angular momentum structure of the lower and upper state of the colliding atoms. Usually, this prefactor can be approximated by unity considering the experimental error bounds. The Weisskopf radius $\rho_W = \sqrt{\beta/(2\pi\bar{v}_r)}$ of the rubidium D_2 line at 360°C is on the order of $10\,\mathrm{nm}$ [17]. The binary approximation can be reformulated into the requirement that only one other atom resides within a sphere with the Weisskopf radius around the emitting atom. For the rubidium D_2 line, this is fulfilled for fairly large densities $N < (4\pi\rho_W^3/3)^{-1} \approx 180k^3$.

However, the conditions of the impact approximation are not always fulfilled, especially at the wings of the spectrum. At these large detunings, the spectrum is impacted by short time scales $1/(\omega - \omega_{eg})$, e.g., atomic states that are much shorter-lived than the average [136]. Then the duration of the atomic collision is no longer short and the quasi-static limit usually offers a better description [135, 136]. Practically, this results in a similar line broadening. Nonetheless, this regime shift contributes to the many difficulties associated with predicting a collisional line shift. A variety of qualitatively different results exist depending on the exact conditions and the exact assumptions made. While some works obtain no shift for an $1/r^3$ potential [171], others predict a blueshift [170], while experiments often extract a small redshift [174]. A complete discussion of the topic and an exact expression for the collisional line shift is, unfortunately, beyond the scope of this thesis. A more extensive quantitative treatment of collision processes can be found in the reviews of Lewis [171] and Allard and Kielkopf [172].

The works cited in this section study atomic collisions in free space. We know, however, that when the distance between the colliding atoms is similar to their distance to a macroscopic surface, modifications through the surface Green's tensor must occur. This happens both directly through the modified dipole-dipole interaction potential and indirectly through the spatially varying atomic properties that originate from the Casimir–Polder and Purcell effects. It goes beyond the scope of the present thesis to rederive the theory of collisions in the framework of macroscopic QED, although such results would be very desirable. When qualitative expressions for the collisional broadening are needed in this chapter, we utilize the free space result (3.49) as a rough approximation.

3.2.5. The velocity distribution in front of a surface

Finally, we discuss the velocity distribution of the atoms. While a free-space vapor in thermal equilibrium obeys the Maxwell–Boltzmann distribution, our problem involves a surface with which the atoms constantly collide. In this situation, the Maxwell–Boltzmann distribution arises when the flux of atoms from and to the surface[13] is proportional to the cosine of the angle between the flux direction and the surface normal [175]. In kinetic gas theory, this is known as Knudsen's cosine law [176]. The flux is composed of elastic scattering (specular reflection or diffraction), inelastic scattering (associated with the creation or annihilation of phonons), and desorption (following adsorption by the surface) [175]. The cosine law considers only the sum of these contributions so that individual components can show a different behavior. For example, multiple works have suggested sharper distributions $\propto \cos^n \theta$ with $n > 1$ for surface desorption, see Ref. [175] and the references therein. The cosine law presumes rectilinear and classical atomic trajectories. These assumptions may be questionable in close vicinity to the surface, where a strongly spatially varying Casimir–Polder potential is present and quantum reflection could play a role. The Casimir–Polder effect could have a significant impact on the trajectories of atoms that move nearly parallel to the wall. Such atoms dominate the signal in some types of selective reflection experiments, as we will see in the next sections. Therefore, a recent experiment [177] investigated atoms leaving the surface at grazing angles of $85^\circ - 88.5^\circ$. But no deviations from the Maxwell–Boltzmann behavior were found, similarly to an older experiment [178] which used a low-density thermal Na vapor in a long cylindrical glass cell. While there is no rigorous microscopic justification for an isotropic Maxwell–Boltzmann velocity distribution in front of a surface, there is also no experimental evidence towards another distribution. Therefore, the isotropic Maxwell–Boltzmann distribution is our working hypothesis. Because our theoretical framework remains applicable for other velocity distributions, it can be updated in the future if necessary.

3.3. Theoretical description of spectroscopic techniques

Utilizing the continuous medium model, we can now present the theory of the spectroscopic techniques that are used to determine the Casimir–Polder shift in vapor cells.

3.3.1. Selective reflection spectroscopy

The reflectance of the dielectric-vapor interface at the cell wall undergoes characteristic changes when the light frequency is tuned over the atomic resonance, recall Fig. 1.2 a. The observation of these changes is termed selective reflection (SR) spectroscopy. Inserting the velocity averaged dipole moment (3.19) into Eq. (3.42), the amplitude reflection coefficient of a cell wall can be written as

---

[13] We assume thermal equilibrium, such that the particle flux from the surface equals the flux from the surface.

$$r^{\text{surf}} = r_{12} + \underbrace{N \sum_{\mu,\nu} \frac{ikt_{21}}{2\epsilon_0} \int_{-\infty}^{\infty} dv_z \int_0^{\infty} dz \, \frac{e^{ikz}}{E_0} d_{x,\mu\nu}^{\,ge} \sigma_{\mu\nu}^{ge}(z, v_z)}_{=\zeta(\omega_L)} . \tag{3.50}$$

The measured intensity reflection coefficient $R_{\text{SR}} = |r^{\text{surf}}|^2$ is

$$\begin{aligned} R_{\text{SR}} &= |r_{12}|^2 + N\left(r_{12}\zeta^*(\omega_L) + r_{12}^*\zeta(\omega_L)\right) + N^2|\zeta(\omega_L)|^2 && (3.51) \\ &\approx r_{12}^2 + 2Nr_{12}\text{Re}\,\zeta(\omega_L), && (3.52) \end{aligned}$$

assuming that the atomic vapor is thin enough that the vapor induced changes are small compared to the reflection coefficient against vacuum. Usually, one investigates situations where the dielectric features very low losses[14] at the ground to excited state transition frequency such that we can take $r_{12} \in \mathbb{R}$. Further, one often assumes that the atomic vapor is so thin that atom-atom interactions can be neglected altogether, such that the electric field is unchanged by the presence of the atomic vapor, $E_x^{\text{loc}}(z) \approx E_{x,\text{inc}}(z)$ [60]. Inserting this in Eqs. (3.23) and (3.24), the atomic contribution $\zeta(\omega_L)$ becomes

$$\begin{aligned} \zeta(\omega_L) \approx &- \sum_{\mu,\nu} \frac{k\, t_{12}\, t_{21}}{2\epsilon_0\hbar} |d_{x,\mu\nu}^{\,ge}|^2 f_\mu^g \int_0^\infty dz \left\{ \int_0^z dz'\, e^{ik(z'+z)} \int_0^\infty dv_z \, \frac{W(v_z)}{v_z} \exp\left(\frac{\Lambda_{\nu\mu}(z',z)}{v_z}\right) \right. \\ &\left. + \int_\infty^z dz'\, e^{ik(z'+z)} \int_{-\infty}^0 dv_z \, \frac{W(v_z)}{v_z} \exp\left(\frac{\Lambda_{\nu\mu}(z',z)}{v_z}\right) \right\} && (3.53) \\ = &- \sum_{\mu,\nu} \frac{k\, t_{12}\, t_{21}}{\epsilon_0\hbar} |d_{x,\mu\nu}^{\,ge}|^2 f_\mu^g \int_0^\infty dz \int_0^z dz'\, e^{ik(z'+z)} \int_0^\infty dv_z \, \frac{W(v_z)}{v_z} \exp\left(\frac{\Lambda_{\nu\mu}(z',z)}{v_z}\right) . && (3.54) \end{aligned}$$

For the second equality, we transformed the velocity integral, $\int_{-\infty}^0 dv f(v) = \int_0^\infty dv f(-v)$, and the spatial integral,

$$\int_0^a dz \int_a^z dz'\, f(z',z) = -\int_0^a dz' \int_{z'}^a dz\, f(z,z') = -\int_0^a dz \int_0^z dz'\, f(z,z'). \tag{3.55}$$

Physically, this means that the atoms departing from and arriving at the surface contribute equally to the change in reflectance [60, 179]. This peculiarity occurs for a single surface, a thin atomic vapor with negligible atom-atom interactions and negligible saturation. It is not valid in general.

---

[14] This assumption does not affect the possibility that the surface is resonant with one of the transitions that enter the Casimir–Polder interaction coefficient.

3.3.2. Frequency-modulated selective reflection spectroscopy

Selective reflection spectroscopy can be refined by frequency modulation techniques which allow removing the impact of Doppler broadening. In this approach, sidebands are added to the optical frequency of the excitation laser field and a beating signal is detected [180–182], see Fig. 3.10. The sidebands are produced by an electro-optic modulator (EOM) which generates periodic phase changes with a modulation frequency ω_m and of a magnitude that is given by the modulation index M. Thus, the laser field acquires a time dependence

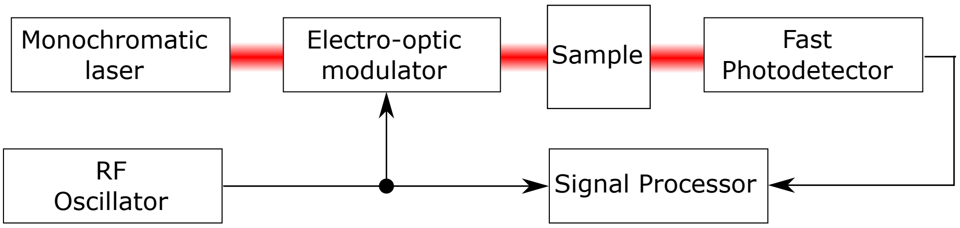

Figure 3.10: General scheme of frequency-modulated spectroscopy following Ref. [182].

$$E_{\text{inc}}(t) = E_0\, e^{-i[\omega_L t + M\sin(\omega_m t)]} = E_0\, e^{-i\omega_L t} \sum_{n=-\infty}^{\infty} J_n(M) e^{-in\omega_m t}. \tag{3.56}$$

The second equality is the Jacobi–Anger expansion[15] for the cylindrical Bessel functions $J_n(M)$ [183]. In practice, the modulation index is weak, $M \ll 1$, such that one can use the Taylor expansion

$$J_n(M) = \frac{M^n}{2^n n!} + \mathcal{O}(M^{n+2}), \quad \text{for } n \in \mathbb{N}_0. \tag{3.57}$$

The Bessel functions of negative n are obtained via $J_{-n}(M) = (-1)^n J_n(M)$. Weak modulation effectively limits the infinite sum in Eq. (3.56) to the first terms from $n = -1$ to $n = +1$. Since our unsaturated vapor obeys the superposition principle, we can calculate and add up the atomic responses to each frequency component of the incident field. The intensity reflection coefficient is

$$R_{\text{FM}} = \left| \frac{E_r(t) e^{-i\omega_L t}}{E_0 e^{-i\omega_L t}} \right|^2 = \left| \sum_{n=-1}^{1} \{ r_{12} + N\zeta(\omega_L + n\omega_m) \} J_n(M) e^{-in\omega_m t} \right|^2 + \mathcal{O}(M^2). \tag{3.58}$$

Let us further assume that the atomic vapor is so thin that changes to the reflectance on the order of $\mathcal{O}(N^2)$ can be discarded. Neglecting also the terms $\mathcal{O}(M^2)$, the reflection signal becomes

---

[15] Taking the $J_n(M)$ as Fourier expansion coefficients, one can use the Jacobi–Anger relation to obtain the Bessel function definition (A.43).

$$
\begin{aligned}
R_{\mathrm{FM}} &\approx R_{\mathrm{SR}} + N r_{12} \frac{M}{2} \Big[\zeta(\omega_L + \omega_m) - \zeta^*(\omega_L - \omega_m) + \zeta^*(\omega_L) - \zeta(\omega_L) \Big] e^{-i\omega_m t} + \text{c.c.} && (3.59) \\
&= R_{\mathrm{SR}} + N r_{12} \frac{M}{2} \Bigg\{ \mathrm{Re}\, \left[\zeta(\omega_L + \omega_m) - \zeta(\omega_L - \omega_m) \right] \cos(\omega_m t) \\
&\qquad + \mathrm{Im}\, \left[\zeta(\omega_L + \omega_m) - 2\zeta(\omega_L) + (\omega_L - \omega_m) \right] \sin(\omega_m t) \Bigg\} && (3.60) \\
&\approx R_{\mathrm{SR}} + N r_{12} M \Bigg\{ \omega_m \mathrm{Re}\, \left[\zeta'_{\mu\nu}(\omega_L) \right] \cos(\omega_m t) + \frac{\omega_m^2}{2} \mathrm{Im}\, \left[\zeta''_{\mu\nu}(\omega_L) \right] \sin(\omega_m t) \Bigg\}. && (3.61)
\end{aligned}
$$

In the last line, we approximated the difference quotients by the corresponding derivatives assuming that the modulation frequency ω_m is sufficiently small. Locking onto the in-phase component ($\propto \cos(\omega_m t)$) provides access to the first derivative of the real part atomic response, while the out-of-phase component ($\propto \sin(\omega_m t)$) is proportional to the second derivative of the imaginary part of the atomic contribution. Sometimes the real and imaginary parts of the atomic signal contribution are referred to as dispersive and absorptive response functions [60].

As in the previous subsection, we consider a low-density limit in which atom-atom interactions are neglected. Then, the first derivative of Eq. (3.54) takes the form

$$
\zeta'(\omega_L) = \sum_{\mu,\nu} \frac{ik\, t_{12} t_{21}}{\epsilon_0 \hbar} |d_{x,\mu\nu}^{\,ge}|^2 f_\mu^g \int_0^\infty dz \int_0^z dz'\, e^{ik(z'+z)} (z' - z) \int_0^\infty dv_z\, \frac{W(v_z)}{v_z^2} \exp\left(\frac{\Lambda_{\nu\mu}(z', z)}{v_z} \right). \tag{3.62}
$$

Let us consider the high temperature or Doppler limit where the Doppler width $v_{\mathrm{th}} k$ is much larger than the detuning, the linewidth, and the Casimir–Polder shift. Then, we can approximate $W(v_z) \approx W(0)$ and conduct the velocity integral analytically,

$$
\begin{aligned}
\zeta'(\omega_L) &\approx - \sum_{\mu,\nu} \frac{ik\, t_{12} t_{21}}{\epsilon_0 \hbar} |d_{x,\mu\nu}^{\,ge}|^2 f_\mu^g \int_0^\infty dz \int_0^z dz'\, e^{ik(z'+z)} \frac{(z' - z) W(0)}{\Lambda_{\nu\mu}(z', z)} && (3.63) \\
&= \frac{t_{12} t_{21} W(0)}{2k\epsilon_0} \left(-\frac{1}{\hbar} \sum_{\mu,\nu} f_\mu^g \frac{|d_{x,\mu\nu}^{\,ge}|^2}{\left(\delta_{\nu\mu} + i\bar{\gamma}_{\nu\mu}^{\mathrm{vac}} \right)} \right) \left(1 + 2k^2 \int_0^\infty dz \int_0^z dz'\, e^{ik(z'+z)} \frac{\Lambda_{\nu\mu}^{\mathrm{AW}}(z', z)}{\Lambda_{\nu\mu}(z', z)} \right). && (3.64)
\end{aligned}
$$

The last line is found by expanding with $\left(-i\delta_{\nu\mu} + \bar{\gamma}_{\nu\mu}^{\mathrm{vac}} \right)$, adding a zero in the numerator, $0 = \Lambda_{\nu\mu}^{\mathrm{AW}}(z', z) - \Lambda_{\nu\mu}^{\mathrm{AW}}(z', z)$, and conducting the double integral over $e^{ik(z'+z)}$. The term in parenthesis is the atomic polarizability without any Doppler shift. Thus the in-phase component of the frequency-modulated selective reflection (FMSR), Eq. (3.64), is created by atoms with $v_z = 0$ that are flying parallel to the wall. This elimination of the Doppler shift in the thermal vapor is possible because of the nonlocal character of the atomic emission and the access to the first derivative via the frequency-modulated incident field. In absence of atom-wall interactions, where $\Lambda^{\mathrm{AW}}_{\nu\mu}(z', z) = 0$, only the first part of Eq. (3.64) remains. One can use this to estimate that the out-of-phase component of the reflectance (3.61), which includes a second derivative, is suppressed roughly by a factor of $\omega_m/\bar{\gamma}^{\mathrm{vac}}_{\nu\mu}$ compared to the in-phase component [60].

3.3.3. Thin cell spectroscopy

In contrast to a single wall, or equivalently a large vapor cell, nanocells confine atoms to very narrow spaces. This limits the maximum atom-wall distance and enables relatively strong transmission signals despite the resonant interaction due to the short pathway in the vapor. The amplitude transmission coefficient (3.43) of the cavity geometry can be written as

$$
\begin{aligned}
t^{\mathrm{cav}} &= t_0 + N \sum_{\mu,\nu} \frac{ikt_{21}e^{iwk(1-n_1)}}{2\epsilon_0 E_0} \int_{-\infty}^{\infty} dv_z \int_0^w dz\, \frac{e^{-ikz} + r_{21}e^{ikz}}{1 - r_{21}^2 e^{2ikw}} d_{x,\mu\nu}^{\;ge} \sigma_{\mu\nu}^{ge}(z, v_z) && (3.65)\\
&= t_0 + N\zeta_{\mathrm{cav}}(\omega_L). && (3.66)
\end{aligned}
$$

The measured quantity is the intensity transmission coefficient

$$
T^{\mathrm{NC}} = t_0^2 + N\left[t_0\zeta^*_{\mathrm{cav}}(\omega_L) + t_0^*\zeta_{\mathrm{cav}}(\omega_L)\right] + N^2 \left|\zeta_{\mathrm{cav}}(\omega_L)\right|^2 . \tag{3.67}
$$

For a sufficiently thin vapor, we may again neglect the atom-atom interactions such that $E^{\mathrm{loc}}_x(z) \approx E_{x,\mathrm{inc}}(z)$. Utilizing the transformations of the velocity and spatial integrals (3.55), the atomic response can then be cast into

$$
\begin{aligned}
\zeta_{\mathrm{cav}}(\omega_L) = &-\sum_{\mu,\nu} f^g_\mu |d_{x,\mu\nu}^{\;ge}|^2 \frac{ke^{iwk(1-n_1)}}{\epsilon_0\hbar} \frac{t_{12}t_{21}}{(1 - r_{21}^2 e^{2ikw})^2} \int_0^\infty dv_z\, \frac{W(v_z)}{v_z} \int_0^w dz \int_0^z dz' \\
&\times \exp\left(\frac{\Lambda_{\nu\mu}(z', z)}{v_z}\right) \left(r_{21}\left[e^{ik(z_1+z_2)} + e^{ik(2w-z_1-z_2)}\right] + \left(1 + r_{21}^2 e^{2ikw}\right)\cos[k(z - z')]\right).
\end{aligned}
\tag{3.68}
$$

Thin cell spectra can show sub-Doppler features [184–186] that are phenomenologically reminiscent of a work by Robert Dicke [187] and therefore referred to as Dicke-type narrowing. However, the observations do not seem to be directly related to Dicke's theory. They result from the nonlocal response of the vapor and the quenching boundary conditions [188], which are taken into account by our treatment.

3.4. Calculation of spectra

Finally, we utilize the low-density limits presented in the previous section to compute FMSR and thin cell spectra based on exact Casimir–Polder shifts, Purcell effect, and sublevel splittings. Subsequently, we fit the resulting spectra with a single constant C_3 coefficient. This establishes a link between the exact treatment in theory and the simplified treatment often used in experiments.

Some experiments exceed the limits for which the low-density approximation strictly holds to get a stronger signal and a better signal-to-noise ratio. Inspired by a recent experiment [158], we investigate such a situation in the last subsection. Instead of using the low-density approximation, we self-consistently compute thin cell transmission spectra at moderate densities in the continuous medium model. The C_3 coefficients are usually negative. Bear in mind that whenever we compare them in the following, larger and smaller refer to the absolute values of the coefficients.

3.4.1. Low-density frequency-modulated selective reflection spectra

Using Eqs. (3.52) and (3.64), we compute the FMSR spectra of the rubidium D_1 and D_2 lines for a sapphire surface at $T = 300\,\mathrm{K}$. The density of $N = 0.01k^3$ is small enough to neglect vapor-induced changes to the incident field. We also disregard the collisional broadening, which is smaller than 9% of the vacuum linewidth, such that the only density dependence of our spectrum is in the prefactor $2Nr_{12}$.

For the numerical evaluation, the upper bound of the z integral in Eq. (3.64) needs to be truncated to a finite value w. However, the result obtained this way oscillates with w and very large values of w may be required to obtain convergence. We cope with this challenge through an averaging scheme that is presented in Sec. E.1. It allows us to include only distances up to two transition wavelengths for the D-lines[16]. Of course, this only works because the FMSR signal is determined by the atoms close to the surface.

The computed spectra are shown in Fig. 3.11 together with a fit model that replaces the exact atom-wall interaction[17] with a simple C_3 expression[18] and additionally adjusts the vacuum linewidth and a prefactor. The simple model provides an excellent phenomenological description. The fitted prefactor of the D_2 (D_1) line is only 3% (5%) smaller than in the exact computation and the fitted linewidth is only 5% (9%) larger than its vacuum value. The uncertainty of all fitted parameters is on the order of 1% or smaller. The fitted C_3 coefficients are roughly 40% larger[19] than the exact results in immediate vicinity to the surface, see Fig. 3.11. This larger value compensates for the Purcell effect and the CP shift at larger distances that exceed what one would expect from a pure C_3/z^3 potential, recall Fig. 3.4. These results conform with the findings on cesium in Ref. [189], which is the only other work known to the author that incorporates the exact CP shift and Purcell effect in vapor cell spectra. Ref. [189] adds a fourth parameter to its model, a collisional shift, that is also used to fit experimental spectra. In our calculation, it has no physical motivation, is not required to reach a good match, and has only

---

[16] For the D line spectra, we apply the oscillation correction from Sec. E.1 to a distance of $\lambda/2$ subsequently to two oscillation periods of λ and $\lambda/2$.

[17] $\Lambda^{\mathrm{AW}}_{\nu\mu}(z', z) = L^{\mathrm{AW}}_{\nu\mu}(z') - L^{\mathrm{AW}}_{\nu\mu}(z)$ is efficiently computed by interpolating precalculated integrals $L^{\mathrm{AW}}_{\nu\mu}(z_i)$.

[18] $\Lambda^{\mathrm{AW}}_{\nu\mu}(z', z) \mapsto iC_3/2 \times (1/z^2 - 1/z'^2)$ where the same C_3 is used for all ν, μ pairs.

[19] For the D_2 line, we compare the fitted value with the result for the $\mu = 1/2 \to \nu = 1.5$ transition that dominates the signal in the exact computation because its squared dipole moment is three times as large as for the $\mu = 1/2 \to \nu = \pm 0.5$ transition.

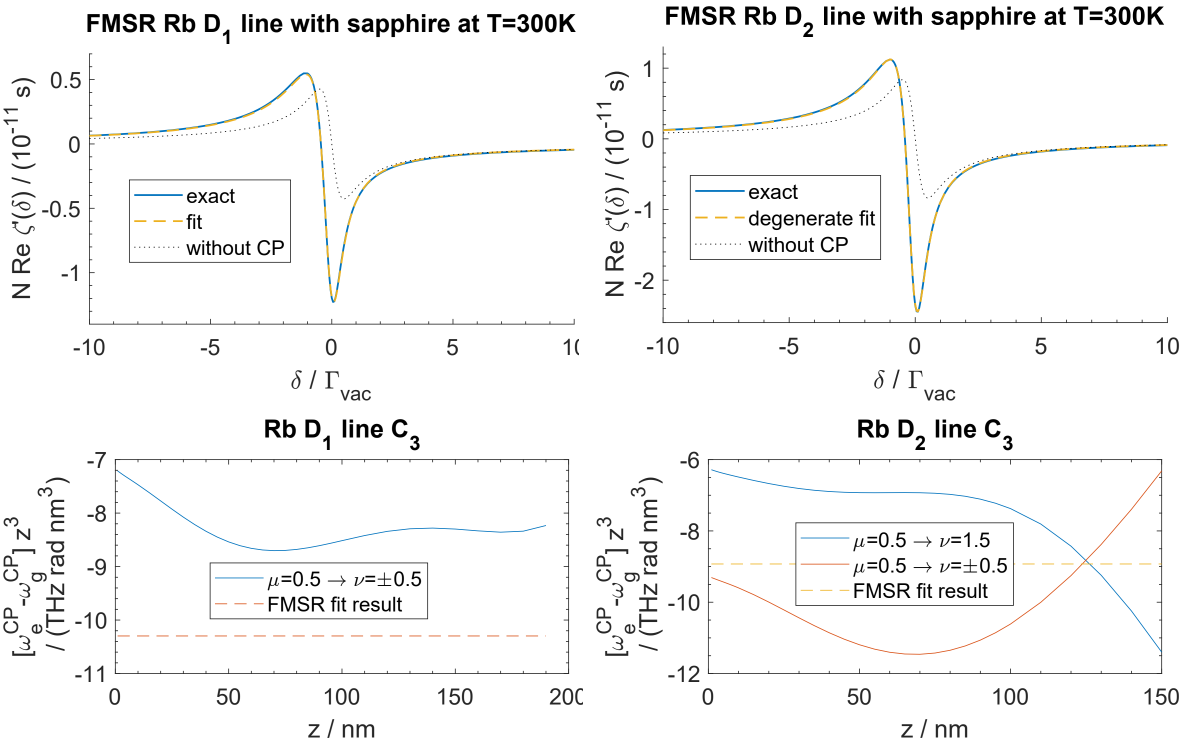

Figure 3.11: Upper panel: FMSR spectra of the rubidium D_1 and D_2 line, respectively, for a sapphire surface at $T = 300\,\mathrm{K}$ and a density of $N = 0.01k^3$. The dotted line indicates the result one would obtain if no atom-wall interaction was present. The exact result largely overlaps with a three-parameter fit that includes a prefactor, a constant linewidth, and a constant C_3 coefficient that are equal for all substates. Lower panel: C_3 coefficient from the fit together with the effective C_3 from the exact computation.

a small impact on the other parameters[20] when included. In addition, Ref. [189] appears to have used the same (isotropically averaged) Casimir–Polder shifts and Purcell broadenings for all substate pairs μ, ν. Our D_2 line result in Fig. 3.4 shows that a fit with a single C_3 coefficient can still be applicable even when the exact CP shifts differ between the substates pairs.

Furthermore, Ref. [189] suggested that the fitted C_3 coefficient can change as the homogeneous linewidth increases through atomic collisions. Conceptually, this is plausible. A larger homogeneous linewidth allows exciting atoms with larger Casimir–Polder shifts which occur when atoms are closer to the surface. The effective C_3 coefficient differs as one approaches the surface, recall Fig. 3.4. This should impact the fitted C_3 coefficient. However, a considerable change in the collisional broadening implies a considerably large density. In general, it is therefore not compatible with the low-density approximation used in Ref. [189]. Instead, a self-consistent treatment, which we will discuss in Sec. 3.4.3, is required to avoid a bias.

Finally, we should address the limits of the flat velocity distribution $W(v_z) \approx W(0)$ used to obtain Eq. (3.64). Without this assumption, the velocity integral requires an expensive numerical computation. The flat velocity distribution suffices for D-line FMSR spectra in Fig. 3.11. But in App. E.3.1, we also consider a $5\mathrm{P}_{3/2} \to 6\mathrm{D}_{3/2}$ transition that features a much larger Casimir–Polder shift and much larger Purcell line broadening. Both are no longer small compared to the Doppler shift kv_{th}, which is the condition for the approximation $W(v_z) \approx W(0)$. If one conducts the approximation nonetheless and calculates an FMSR spectrum with Eq. (3.64), the result will contain artifacts, as shown in App. E.3.1. In general, it is therefore necessary to perform the integral over the full velocity distribution instead of using Eq. (3.64). This is, however, left to future work.

---

[20] The fitted C_3 and linewidth become roughly 1% [4%] smaller for the D_2 [D_1] line.

3.4.2. Low-density thin cell transmission spectra

We have seen that at a single surface, the fitted C_3 coefficient turns out to be larger than the nonretarded C_3 in the $z \to 0$ limit because of the long-range behavior of the shift that is underestimated by C_3/z^3 law. In a nanocavity with a small width w, however, all atoms approximately follow a C_3 law as the atom surface distance can never be larger than $w/2$. This makes it interesting to perform a C_3 fit in cavity geometry and compare the results with those for a surface from the previous subsection.

For this purpose, we must first compute the exact Casimir–Polder shift and Purcell broadening of the rubidium D-lines in a cavity with two sapphire walls using the exact Green's tensor (A.46) derived in App. A.3. They are shown in Fig. 3.12 and Fig. 3.13. Since the cavities are mirror-symmetric, it is sufficient to present the results only for z smaller or equal to half of the cavity width w. The effective C_3 coefficient is computed by dividing the shift with $(1/z^3 + 1/(w-z)^3)$, i.e. the proportionality factor one would expect if the cavity shift was the sum of the two surface shifts[21]. The most striking difference between cavity and surface geometries is, as one would expect, the strong increase of the Purcell effect for some m_j. We will see the consequences of this down below.

With the exact atom-interactions known, we compute the corresponding thin cell transmission spectra (3.67) at $T = 300\,\mathrm{K}$. Analogously to the previous subsection, the density is $N = 0.01k^3$ and thus small enough to use the low-density approximation of Eq. (3.68). The velocity integration in Eq. (3.68) poses a challenge in presence of atom-wall interactions as the integrand becomes highly oscillatory in close vicinity to the surfaces[22]. Standard adaptive quadrature schemes can still cope with the spectra in this subsection, presuming that suitable adjustments to the upper and lower boundaries of the velocity integral are made. In more general scenarios, it is most likely necessary to use specialized integrators such as Levin's rule [190, 191] which is also implemented in Wolfram Mathematica's NIntegrate command.

As an example, we show the spectra for one cavity width in Fig. 3.14 together with a simplified fit model. Analogously to the previous section, the fit parameters are the C_3

---

[21] Generally, the two surfaces impact one another, as a mirror dipole produced in one surface also induces one on the other and so on. In the nonretarded limit, however, this effect would only cause a few percent deviation from $C_3(1/z^3 + 1/(w-z)^3)$ [158]. The distance dependence of the effective $C_3(z)$ occurs mainly because the nonretarded limit is not strictly adhered to at nonzero distances from the surfaces.

[22] The exponential $\exp\left[\Lambda_{\nu\mu}(z', z)/v_z\right]$ involves terms similar or equal to $\exp\left(iC_3/(2z^2 v)\right)$, whose oscillation frequency becomes infinitely large as $z \to 0$.

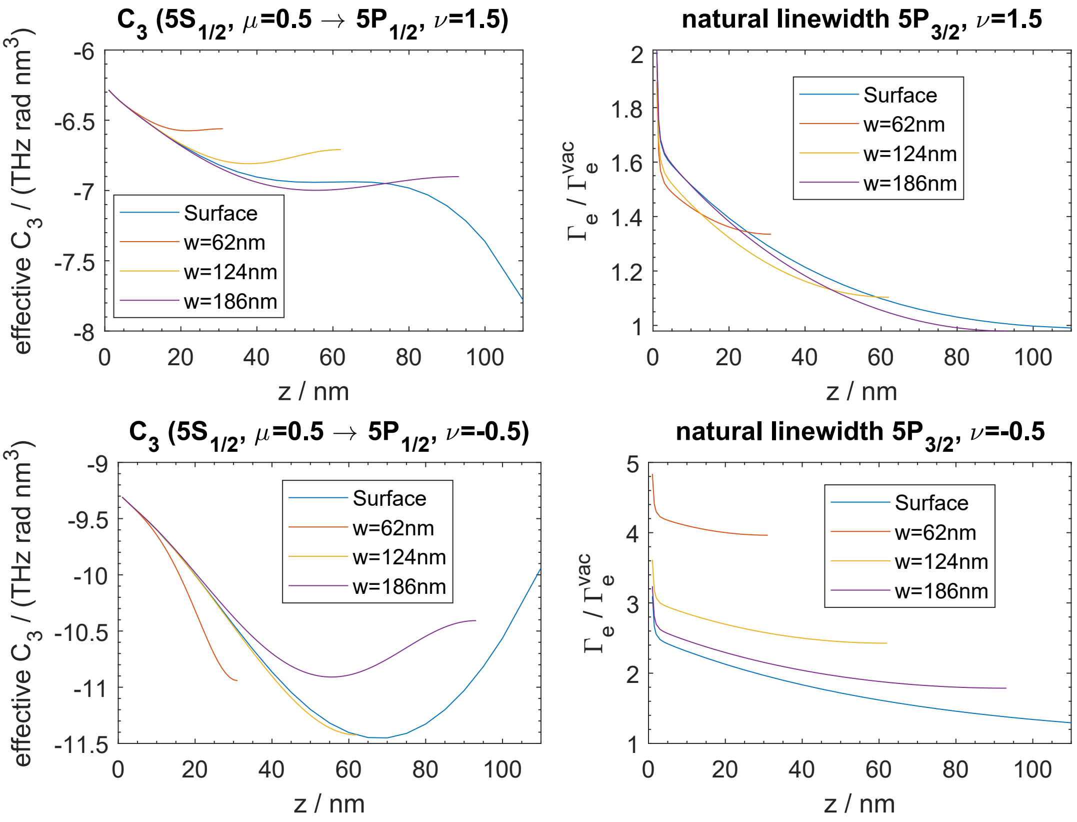

Figure 3.12: Casimir–Polder shift and Purcell broadening of the rubidium D_2 line at a sapphire surface and in sapphire cavities of different width w at $T = 300\,\mathrm{K}$. The upper and lower panel correspond to transitions with different m_j sublevels. The effective C_3 is computed by dividing the shift by $1/z^3$ for the surface and by $1/z^3 + 1/(w-z)^3$ for the cavities. The cavity results are only shown up to a distance of $w/2$ since they are mirror-symmetric for the remaining z values.

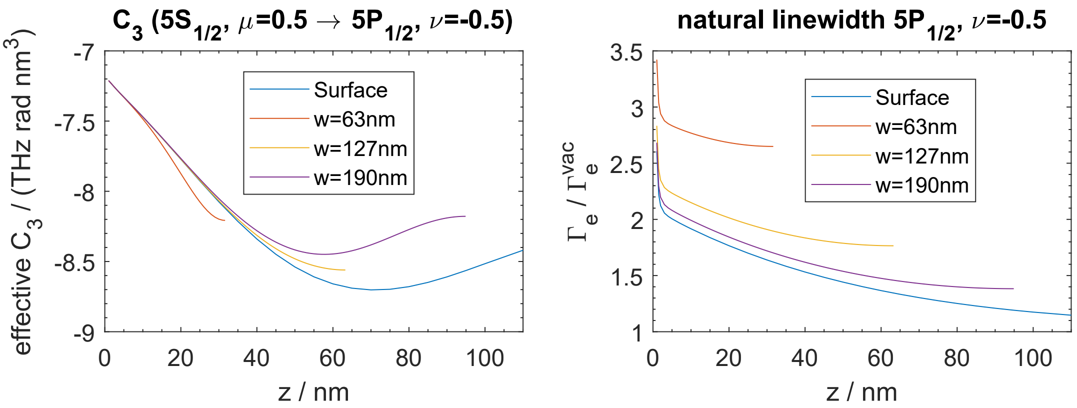

Figure 3.13: Casimir–Polder shift and Purcell broadening at a sapphire surface and in sapphire cavities of different width w analogously to Fig. 3.12 but for the rubidium D_1 line.

coefficient, the linewidth, and a prefactor. The phenomenological description with the fit is again excellent. The fitted prefactor is always close to one[23]. The fitted shift and linewidth are shown in Fig. 3.15. The fitted linewidth grows as the cavity width shrinks because of the stronger Purcell effect demonstrated in Fig. 3.12 and Fig. 3.13. The fitted C_3 coefficient, on the other hand, changes by less than 5% for different w and can therefore be considered roughly constant. This matches the observations in a recent experiment [158] that found a fitted C_3 that is constant for different cavity widths within the error bars. Furthermore, the absolute value of the fitted C_3 is smaller for the nanocell than for the surface, as expected based on the lack of long-range contributions. Nonetheless, the fitted C_3 coefficients are still around 15% to 18% larger than the nonretarded C_3 for $z \to 0$ that is often used for comparison. The reason is that even in thin cavities, whose width is smaller than the reduced transition wavelength, the effective C_3 can still be 20% larger at the center than at the border of the cavity, see Fig. 3.12 and Fig. 3.13.

---

[23] The largest deviation is only 1.4%.

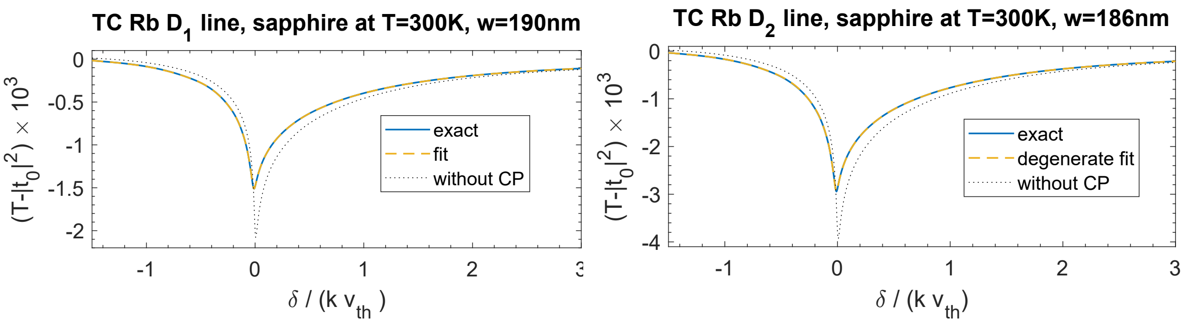

Figure 3.14: FMSR spectra of the rubidium D_1 and D_2 line for a sapphire cavity of width $w = 190\,\mathrm{nm}$ and $w = 186\,\mathrm{nm}$ at $T = 300\,\mathrm{K}$ and a density of $N = 0.01k^3$. The dotted line indicates the result one would obtain if no atom-wall interaction was present. The exact result largely overlaps with a three-parameter fit that includes a prefactor, a constant linewidth, and a constant C_3 coefficient that are equal for all substates.

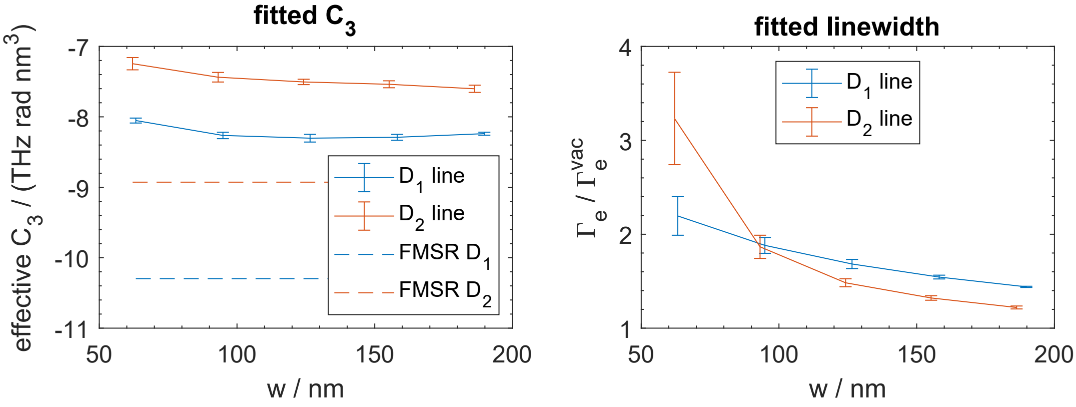

Figure 3.15: Fitted effective C_3 coefficient and linewidth over the width w of the sapphire cavity for the rubidium D_1 and D_2 line. The corresponding spectra for the largest w are shown in Fig. 3.14. The dashed lines indicate the FMSR results from the previous subsection that were obtained for a surface geometry.

In conclusion, we have shown that in the low-density limit, FMSR spectra from a surface and thin cell transmission spectra can be excellently described by fitting to a model with a simple

C_3 coefficient. However, this fitted C_3 varies between methods as different spatial regions are integrated. In our examples, it is 20% to 40% larger than the result of a nonretarded calculation. Often a fitted C_3 from an experiment is compared to a nonretarded C_3 from a theoretical calculation. This comparison may not be very significant in quantitative terms. Instead, one should compute the exact shift and use the same fit function as for the experimental data to obtain a theoretical fitted C_3 that could be compared against the experimental result.

Furthermore, the theoretical prediction should include the sublevel splitting and the induced anisotropy. Often, however, only isotropically averaged values are used for theoretical predictions. In the following, we will use the example of the D_2 line to demonstrate how this can lead to erroneous conclusions. Out of the two types of sublevel transitions ($\pm 1/2 \to \pm 3/2$ and $\pm 1/2 \to \mp 1/2$) that enter into the transmission spectrum, the $\pm 1/2 \to \pm 3/2$ transitions dominate due to their larger dipole moment. This is reflected by the fitted C_3 shown in Fig. 3.15 that is much closer to the effective C_3 of the $\pm 1/2 \to \pm 3/2$ transitions than the effective C_3 of the $\pm 1/2 \to \mp 1/2$ transitions. The latter is roughly 30% larger than the former, see Fig. 3.12 and Fig. 3.13. An isotropic average leads to a value of $C_3 = -7.8\,\mathrm{THz\,rad\,nm}^3$ that is larger than the $C_3(z \to 0) = -6.3\,\mathrm{THz\,rad\,nm}^3$ of the dominant $\pm 1/2 \to \pm 3/2$ transition. The increase of static C_3 by isotropic averaging brings it close to the fitted of $C_3 \approx -7.5\,\mathrm{THz\,rad\,nm}^3$. If one would not further evaluate the actual distance dependence, this could create the impression of a quantitative match within 4%, although it is pure coincidence.

Finally, we should state that an optimal theoretical description of an experiment accounts for the hyperfine structure of the atoms. The corresponding dipole moments are given in App. C and have been implemented in the context of this work. The main reason for using the fine structure instead was to avoid a confusingly large amount of sublevel transitions that would have obscured the fundamental points of this chapter.

3.4.3. Atom-atom interactions in thin cell spectra

At low atomic densities, like $N = 0.01\,k^3$, there are only small changes in the transmission as can be seen in Fig. 3.14. In an experiment, it may be difficult to distinguish them from background noise. Therefore, a recent experiment in thin cells [158] has been conducted at a much higher density $N \approx 17\,k^3$ [188] [24] that may no longer comply with the low-density approximation that we have used so far.

To investigate the matter, we need to solve the equations for atomic polarization (3.23), (3.24) and field (3.17), (3.18) in a self-consistent fashion. First, we compute the atomic response (starting with $E_x^{\mathrm{loc}}(z) \approx E_{x,\mathrm{inc}}(z)$ in the first step) and infer the electric field inside the cavity. This new field is then used to compute a new atomic response and the process is repeated until a convergent result is found. Here we also include the collisional broadening (3.49). Fig. 3.16 shows the thin cell transmission spectra for two cavity widths, $\lambda/(4\pi) \approx 62\,\mathrm{nm}$ and $186\,\mathrm{nm}$,

---

[24] The experiments have been conducted on the cesium D_1 line where $\lambda = 895\,\mathrm{nm}$. The k in $N \approx 17\,k^3$ corresponds to this wavelength.

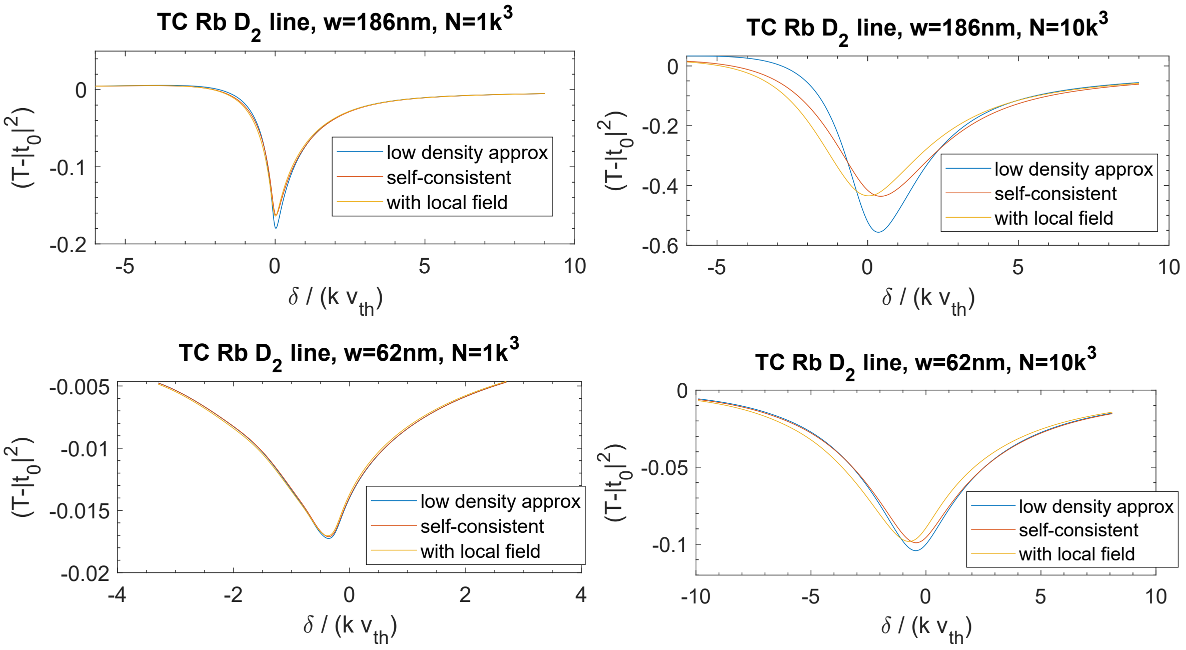

Figure 3.16: Thin cell transmission spectra of the rubidium D_2 line in sapphire cavities at $T = 300\,\mathrm{K}$. We consider two different cavity widths $w = 62\,\mathrm{nm}$ and $w = 186\,\mathrm{nm}$ and at two different densities $N = 1\,k^3$ and $N = 10\,k^3$. Three different continuous medium models have been used: a low-density approximation, a self-consistent treatment but without the local field correction, and a self-consistent treatment with the traditional local field correction. The typical Doppler shift is roughly $v_{\mathrm{th}}k \approx 2\,\mathrm{GHz\,rad}$.

at densities of $N = 1\,k^3$ and $N = 10\,k^3$. Three different models are shown. The first is the low density approximation with $E_x^{\mathrm{loc}}(z) \approx E_{x,\mathrm{inc}}(z)$. The other two are self-consistent spectra, one of which includes the local field correction (3.17) and the other disregards it, setting $E_x^{\mathrm{loc}}(z) \approx E_x(z)$. The spectra for $w = 186\,\mathrm{nm}$ and $N = 1\,k^3$ show differences mainly very close to the resonance. This is where the atomic polarization is the strongest and therefore fosters the most pronounced change to the electric field inside the cavity. Naturally, the three models feature much more pronounced differences at $N = 10\,k^3$ where also a wider frequency range is affected. It is striking that the differences between the models are much smaller in the smaller cavity with $w = 62\,\mathrm{nm}$. In the small cavity, all atoms are strongly influenced by the Casimir–Polder shift, whereas the larger cavity includes atoms further away from the surface that are only mildly affected. The CP interactions decrease the atomic polarization, suppress changes in the field, and weaken the role of atom-atom interactions. Despite the high density of $N \approx 17\,k^3$, Ref. [158] was able to fit experimental spectra with a model that ignores atom-atom interactions. This may be attributed to the dominant role of the Casimir–Polder effect for the small cavities with $w \leq 100\,\mathrm{nm}$ under the conditions in Ref. [158]. However, even if that is the case, a self-consistent model should still be consulted to check whether the omission of the atom-atom interaction biases the extracted C_3 coefficient in any way.

Previous works have investigated the impact of atom-atom interactions on standard selective reflection spectroscopy at a single surface [153, 192]. However, the model with atom-atom interactions was not used for the evaluation of experimental results [155] published by partly the same authors due to the "excessive computation time" [155] that would have been required at the time. Other works that presented a self-consistent treatment for a cavity, e.g., Ref. [193] ignored the Casimir–Polder interaction.

Fig. 3.16 shows that when a self-consistent treatment leads to differences, local field corrections also play an important role. However, the validity of the Lorentz–Lorenz treatment of local field corrections has been called into question by a series of recent experimental [44, 73] and theoretical findings [71, 72, 194] when it comes to the near-resonant excitation of atomic vapors. The reason is that an atomic vapor is granular and behaves differently from a continuous medium for which the Lorentz–Lorenz relation has been derived. Since the spectra in Fig. 3.16, as well as older works like Refs. [153, 192], are based on the assumption of a continuous medium, they cannot be considered exact in the light of these new facts. Instead, it is necessary to uncover the role of the granular nature of atomic gas on the atom-atom interactions in a nanocavity. This is the subject of Chapter 4.

4. Atom-atom interactions in nanocavities

In this chapter, we show how a macroscopic environment shapes the light-induced atom-atom interactions. As a first step, we demonstrate that the response of dense atomic ensembles deviates from the established continuous medium theory. In particular, we address the so-called collective Lamb shift. Then, we present a granular simulation approach and use it to compute the near-resonant transmission of light through a thermal rubidium vapor in a planar nanocavity. We find density-dependent line shifts and broadenings beyond continuous electrodynamics models that oscillate with the cavity width and compare them with similar observations that have been made in a recent experiment [44]. Furthermore, we predict that the amplitudes of the oscillations can be controlled by coatings that modify the cavity's finesse. Future experiments can probe this prediction and assess the validity of our theory. These findings have also been published in Ref. [194]. Finally, we address cold atomic gases in free space and showcase the differences to thermal gases. We briefly review a new approach to solve the coupled dipole model [195] that might contribute to a computationally more efficient treatment of thermal gases in the future.

4.1. The collective Lamb shift

In Chapter 3, we treated the atomic vapor as a continuous medium, although it is actually a random ensemble of atomic particles. In the latter case, there is no explicit local field correction (3.17) or a Lorentz–Lorenz shift (3.48) because only vacuum exists in the immediate vicinity of each atom. Adopting the granular perspective on the atomic vapor, we can utilize ergodicity and compute its time average by performing an ensemble average. To that end, we solve the coupled dipole model (2.104) for many different random atomic configurations. One could expect that the Lorentz–Lorenz effect emerges again as a consequence of the averaged atom-atom interactions.

To test this, we consider a slab of rubidium atoms in free space with a thickness of $w = 1.5/k \approx 186\,\mathrm{nm}$ at zero temperature. Fig. 4.1 shows the transmission for the near-resonant excitation of the D_2 line for different atomic densities N that have been computed by an average over thousands of random atomic configurations[1]. According to the continuous medium theory, one expects a red shift of the transmission minimum with increasing density. This shift is not given directly by the Lorentz–Lorenz expression (3.48) as it also depends on the sample geometry. In 1973 Friedberg, Hartman, and Manassah [170] derived the so-called "collective Lamb shift" (CLS) that incorporates the geometry dependence. For a slab of width w, it reads

$$\Delta_{\mathrm{CLS}} = \Delta_{\mathrm{LL}} - \frac{3\Delta_{\mathrm{LL}}}{4}\left(1 - \frac{\sin(2kw)}{2kw}\right). \tag{4.1}$$

---

[1] The simulation method is detailed in Sec. 4.2.3.

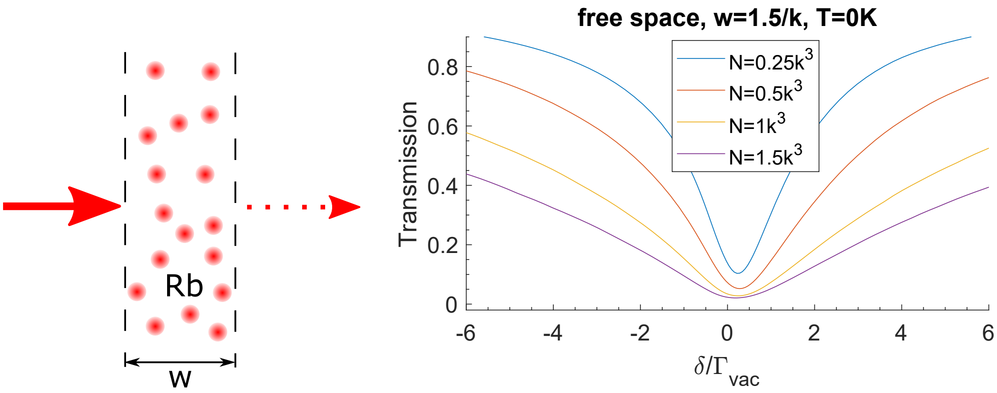

Figure 4.1: Left: Light transmission through a slab of rubidium atoms with width w in free space. Right: Corresponding spectra for the near-resonant excitation of the D_2 line for different atomic densities N at zero temperature.

In our example, this suggests a minimum at $-0.9\,\Gamma_{\text{vac}}$ for a density of $N = 1.5\,k^3$ where $\Delta_{\text{LL}} = -\pi\Gamma_{\text{vac}}$. But in Fig. 4.1, no shift can be seen. This absence of a density-dependent shift in the simulation of an interacting cold atomic ensemble was first reported by Javanainen et al. [71] in 2014. Experiments followed that confined varying numbers of cold atoms in ellipsoid [73, 196] and disc-shaped potentials [75]. While some experiments confirmed the absence of the shift [73–75], others agreed with the CLS prediction for the respective geometry [196].

The theoretical study of Javanainen et al. [71] also predicted that the CLS is partially restored in a thermal vapor due to the inhomogeneous broadening by the Doppler effect. Wedged cells that confine thermal vapor layers with nanometer thicknesses are the ideal platform to probe predictions across different densities and thicknesses. The first experiment in wedged nanocells was published in 2012 [18] and seemed to agree with the CLS shift (4.1). However, inspired by the cold atom debate, a new measurement partly by the same authors was published in 2018 [44]. Although the experimental results were equivalent, the new evaluation assessed the initial agreement with the CLS prediction to be fortuitous [44]. In addition, theoretical arguments were raised [44, 72] against applying Eq. (4.1) to vapor cells. To elucidate these unusual developments and the physics behind them, we must first rederive the CLS expression (4.1) from our coupled dipole model.

4.1.1. Derivation and discussion

We consider a slab of atoms of thickness w that is dominated by homogeneous broadening such that the coupled dipole model is given by Eq. (2.105) and Eq. (2.106). We transform the model for a continuous medium as in Sec. 3.2 and find

$$p_x(z) = \alpha_{xx}^{\text{loc}}\, E_0 e^{ikz} + \frac{N\alpha_{xx}^{\text{loc}}\, k^2}{\epsilon_0} \int_0^w dz'\, G_{\text{free}}^{\text{1D}}(z, z', \omega_{eg}) p_x(z'). \tag{4.2}$$

The polarizability $\alpha_{xx}^{\mathrm{loc}}$ incorporates the local field correction as discussed in Sec. (3.2.3). The calculation of a CLS usually includes the atom-atom interactions only to first order in the Green's tensor, see, e.g., Refs. [170] and [196]. This constitutes a single scattering or first Born approximation. To conduct it here, we insert the zeroth-order solution $p_x(z) \approx \alpha^{\mathrm{loc}} E_{x,\mathrm{inc}}(z)$ in the integral and find

$$p_x(z) \approx \alpha_{xx}^{\mathrm{loc}}\, E_0 \left(e^{ikz} + \chi k^2 \int_0^w dz'\, G_{\mathrm{free}}^{\mathrm{1D}}(z, z', \omega_{eg}) e^{ikz'} \right), \tag{4.3}$$

where $\chi(z) = N\alpha_{xx}^{\mathrm{loc}}(z)/\epsilon_0$ denotes the susceptibility. The transmission (3.43) through the vapor slab is then given by

$$t = 1 + \frac{ik\chi w}{2}(1 + \chi\xi) \quad \text{with} \quad \xi = \frac{k^2}{w} \int_0^w dz \int_0^w dz'\, G_{\mathrm{free}}^{\mathrm{1D}}(z, z', \omega_{eg}) e^{ik(z'-z)}. \tag{4.4}$$

We assume the same population of all substates, $f_{i_\mu^g} = 1/(2J_g + 1)$, and express the susceptibility $\chi = 3\Delta_{\mathrm{LL}}/(\delta - \Delta_{\mathrm{LL}} + i\gamma_0)$ in terms of the Lorentz–Lorenz shift Δ_{LL}. Since the first Born approximation takes χ to be small, we can use $1 + x \approx \frac{1}{1-x}$ for $x \ll 1$ and approximate the transmission profile by a Lorentz curve

$$t \approx 1 - \frac{kw\chi}{2i} \frac{1}{1 - \chi\xi} = 1 - \frac{3\Delta_{\mathrm{LL}} kw}{2i(\delta - \Delta_{\mathrm{LL}} - 3\Delta_{\mathrm{LL}} \mathrm{Re}\,\xi) + 6\Delta_{\mathrm{LL}} \mathrm{Im}\,\xi - 2\gamma_0}. \tag{4.5}$$

The shift of the Lorentz profile is the CLS. The integral we have to solve is the same[2] as Eq. (4.1) in the work of Friedberg, Hartman, and Manassah [170],

$$\Delta_{\mathrm{CLS}} = \Delta_{\mathrm{LL}} + 3\Delta_{\mathrm{LL}}\, \mathrm{Re}\,\xi = \Delta_{\mathrm{LL}} + \frac{3\Delta_{\mathrm{LL}} k^2}{w} \mathrm{Re} \int_0^w dz \int_0^w dz'\, \frac{i}{2k} e^{ik|z'-z|} e^{ik(z'-z)} \tag{4.6}$$

$$= \Delta_{\mathrm{LL}} - \frac{3\Delta_{\mathrm{LL}}}{4} \left(1 - \frac{\sin(2kw)}{2kw} \right). \tag{4.7}$$

The above derivation of the "collective Lamb shift" requires only classical physics, whereas the Lamb shift has its origin in the quantum fluctuations of matter and fields. The name "collective Lamb shift" is therefore misleading. While some works on the CLS adopt the continuous medium approximation, e.g., Ref. [170], others retain the granular nature of the vapor [196]. But all works known to me adopt the first Born approximation, which is intrinsically problematic[3] for a density-dependent effect. As the density increases and the effect should become more distinct, the truncation of the Born series to the first-order term ceases to be a reliable approximation. Fig. 4.2 compares the CLS against the minimum position in the Fabry–Pérot profile of a cavity with vacuum "walls" that constitutes the exact all order solution in a continuous medium, recall Sec. 3.2.2. At very small densities $N \sim 0.01\,k^3$, the exact result approaches the CLS (4.1) [72].

---

[2] The only difference is that we have already conducted the area integral over the 3-D Green's tensor that led to the 1-D Green's function and that we have already included the bulk shift Δ_{LL}.

[3] Another problematic approximation is the use of the far-field Green's tensor. It may be justifiable in Ref. [196] specifically because of the low densities $N \leq k^3/80$ considered there. But larger densities around $1\,k^3$ imply that the distance between neighboring atoms is only a fraction of the transition wavelength such that the exact Green's tensor has to be used.

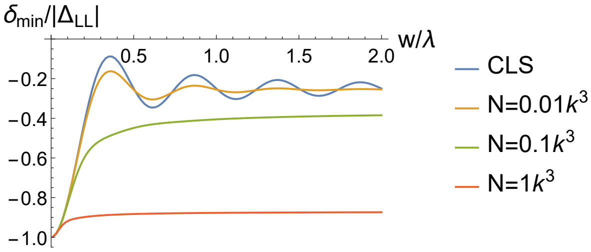

Figure 4.2: Detuning with minimal transmission through a Fabry–Pérot cavity with vacuum "walls" filled a vapor of two-level atoms plotted against the cavity size, compare Ref. [72].

This density is similar to the maximum density of around $k^3/90$ used in the experiment [196] that agreed with a CLS prediction. It is also much smaller than the $N \sim 1\,k^3$ investigated in the experiment [73] that disagreed with the CLS prediction. This is not necessarily a contradiction: Due to the smaller density, the first Born approximation or CLS may be sufficient for the first experiment but not for the second, while both can be explained by a coupled dipole model. The shift observed in Ref. [196] is likely attributed to the global geometry of the sample[4] and not to a local field correction effect.

The CLS has also been successfully probed with x-rays in solid targets, namely iron and tantalum nuclei sandwiched between nanometer-thin, solid layers of other materials [197, 198]. It is possible that the parameters of these experiments also justify the use of the first Born approximation. This is speculative, though, and a precise investigation of these very different systems is beyond the scope of this thesis.

The above analysis shows that the CLS (4.1) only holds when a vacuum surrounds the vapor and the density is small $N \sim 0.01\,k^3$. Both of these conditions are not fulfilled in the nanocell experiment from 2012 [18] that involved sapphire walls and densities $N \sim 50\,k^3$. In Ref. [18], the shift was extracted based on a fit model that partly accounted for cavity effects to produce the correct line shape. A closer inspection shows that this model, which is detailed in Ref. [17] and the supplemental of Ref. [44], was not designed in a physically correct manner. In particular, it does not comply with the Fabry–Pérot formula (3.44) [44]. Curiously, this mistake resulted in a shift that closely resembled Eq. (4.1), although there is no physical connection between the two. The new study from 2018 [44] was able to fit the observed transmission spectra by a Fabry–Pérot lineshape with an additional density-dependent broadening and shift. Surprisingly, these two parameters still showed an oscillatory dependence on the thickness of the vapor layer [44]. This could not be explained by the theories at that time, which had only been conducted in free space, see Ref. [72]. Our coupled dipole model includes the influence of the cavity on the atom-atom interaction and our simulation leads to broadenings and shifts that are similar to the observations in Ref. [44] as we show in the next section.

---

[4] In the same way that a Fabry–Pérot profile has a shifted transmission minimum.

4.2. Atom-atom interactions in sapphire nanocavities

We first present the necessary equations to simulate the transmission through discrete atomic ensembles in a nanocavity. Then, we develop a continuous reference model with two fit parameters, an additional broadening and an additional shift. Finally, we present our simulation procedure and fit our theoretical spectra with the continuous reference model, which allows a comparison with recent experimental results [44, 194].

4.2.1. Granular model

The spatial dependence of the incident field, $\mathbf{E}_{\text{inc}}(z) = \mathbf{E}_{\text{inc}}^{+}\, e^{ikz} + \mathbf{E}_{\text{inc}}^{-}\, e^{-ikz}$, imprints a distance dependence on the atomic response that can be captured by an ansatz

$$\langle \hat{\tilde{\sigma}}_{A^{ge}_{\mu\nu}}(z)\rangle = \langle \hat{\tilde{\sigma}}^{+}_{A^{ge}_{\mu\nu}}\rangle\, e^{ikz} + \langle \hat{\tilde{\sigma}}^{-}_{A^{ge}_{\mu\nu}}\rangle\, e^{-ikz}. \tag{4.8}$$

The coupled dipole model (2.104) can be rewritten as two independent equations for the atomic responses $\langle \hat{\tilde{\sigma}}^{+}_{A^{ge}_{\mu\nu}}\rangle$ and $\langle \hat{\tilde{\sigma}}^{-}_{A^{ge}_{\mu\nu}}\rangle$ to each of the incident field components. This reflects the linear superposition principle and leads to

$$\begin{aligned}\mathbf{v}_A \cdot \boldsymbol{\nabla}\, \langle \hat{\tilde{\sigma}}^{\pm}_{A^{ge}_{\mu\nu}}\rangle\, e^{\pm ikz_A} &= i\left(\delta - \left[\omega^{\text{CP}}_{A^{eg}_{\nu\mu}}(\mathbf{r}_A) \pm kv_{A,z}\right] + i\gamma_{A^{eg}_{\nu\mu}}(z_A)\right) \langle \hat{\tilde{\sigma}}^{\pm}_{A^{ge}_{\mu\nu}}\rangle\, e^{\pm ikz_A} \\ &+ \frac{i}{\hbar} f_{A^{g}_{\mu}}\, \mathbf{d}_{A^{eg}_{\nu\mu}} \cdot \left(\mathbf{E}^{\pm}_{\text{inc}}\, e^{\pm ikz_A} + \sum_{B\neq A} \boldsymbol{\mathcal{G}}(\mathbf{r}_A, \mathbf{r}_B, \omega_{B,eg}) \sum_{\delta\epsilon} \mathbf{d}_{B^{ge}_{\delta\epsilon}}\, \langle \hat{\tilde{\sigma}}^{\pm}_{B^{ge}_{\delta\epsilon}}\rangle\, e^{\pm ikz_B}\right).\end{aligned} \tag{4.9}$$

The ansatz has made the zeroth-order Doppler shift $kv_{A,z}$ explicit. Finally, we perform a local approximation and take $\boldsymbol{\nabla}\, \langle \hat{\tilde{\sigma}}^{\pm}_{A^{ge}_{\mu\nu}}\rangle \approx \mathbf{0}$. The physical justification is that the atom-atom interactions in a dense vapor effectively give rise to a large homogeneous broadening that suppresses the nonlocal character of the thermal vapor, recall Sec. 3.2.1. The approximation also neglects the changes to the Doppler shift $kv_{A,z}$ when the effective wavenumber in the vapor changes with increasing density, recall Sec. 3.2.2. Physically, it would be desirable to waive the approximation, especially for moderate densities $N \sim 1\, k^3$. Practically though, it is indispensable because of the high computational requirements of the discrete coupled dipole model which we encounter in the next sections. Neglecting the spatial derivative, we can rewrite the coupled dipole model in a compact form, analogously to Sec. 2.3.5. For the dipole moment $\mathbf{p}_A = \mathbf{p}_A^{+}\, e^{ikz} + \mathbf{p}_A^{-}\, e^{-ikz}$, we find the two equation sets

$$\mathbf{p}_A^{\pm}\, e^{\pm ikz_A} = \boldsymbol{\alpha}^{\pm}_{A,ge} \left[\mathbf{E}^{\pm}_{\text{inc}}(\mathbf{r}_A) e^{\pm ikz_A} + \sum_{B\neq A} \boldsymbol{\mathcal{G}}(\mathbf{r}_A, \mathbf{r}_B, \omega_{B,eg}) \mathbf{p}_B^{\pm}\, e^{\pm ikz_B}\right], \tag{4.10}$$

$$\boldsymbol{\alpha}^{\pm}_{A,ge} = -\frac{1}{\hbar} \sum_{\mu,\nu} \frac{f_{A^{g}_{\mu}}\, \mathbf{d}_{A^{ge}_{\mu\nu}} \otimes \mathbf{d}_{A^{eg}_{\nu\mu}}}{\delta - \omega^{\text{CP}}_{A^{eg}_{\nu\mu}}(\mathbf{r}_A) \mp kv_{A,z} + i\gamma_{A^{eg}_{\nu\mu}}(\mathbf{r}_A)}. \tag{4.11}$$

When the dipole moments $\mathbf{p}_A$ are known, the transmission can be computed via Eq. (2.130).

4.2.2. Continuous fit model

Next, we construct a continuous version of Eq. (4.10). It includes an additional broadening Γ_p and a shift Δ_p which phenomenologically account for the missing effects from the discrete model. We assume that all atomic substates are equally populated and introduce the helper expressions

$$\langle \boldsymbol{\alpha}(z)\rangle_v = \frac{1}{(2J_g+1)}\sum_{\mu,\nu}\langle \boldsymbol{\alpha}_{\substack{ge\\ \mu\nu}}(z)\rangle_v, \quad B_{\mu\nu}(z) = \delta - \omega^{\mathrm{CP}}_{\substack{eg\\ \nu\mu}}(z) - \Delta_p + i\left[\gamma_{\substack{eg\\ \nu\mu}}(z) + \gamma_p\right]. \tag{4.12}$$

For the polarizability (4.11), we conduct the ensemble average over the velocity distribution

$$\begin{aligned}\langle \boldsymbol{\alpha}_{\substack{ge\\ \mu\nu}}(z)\rangle_v &= \frac{-1}{\sqrt{\pi}\hbar v_{\mathrm{th}}}\mathbf{d}_{\substack{ge\\ \mu\nu}} \otimes \mathbf{d}_{\substack{eg\\ \nu\mu}} \int_{-\infty}^{\infty} dv\, \frac{1}{B_{\mu\nu}(z) \mp kv} e^{-v^2/v_{\mathrm{th}}^2} \\ &= \frac{-\sqrt{\pi}}{\hbar\omega_D}\mathbf{d}_{\substack{ge\\ \mu\nu}} \otimes \mathbf{d}_{\substack{eg\\ \nu\mu}} \left[D\left(\frac{B_{\mu\nu}(z)}{\omega_D}\right) - i\,\exp\left(-\frac{B_{\mu\nu}^2(z)}{\omega_D^2}\right)\mathrm{sign}\left(\frac{\mathrm{Im}\, B_{\mu\nu}(z)}{\omega_D}\right)\right]. \end{aligned} \tag{4.13}$$

Here $\omega_D = kv_{\mathrm{th}}$ and $D(x) = e^{x^2}\int_0^x dt\, e^{-t^2}$ denotes the Dawson function for which stable numerical implementations are available [199]. Due to the velocity integration, the same polarizability applies for both components of the incident field. A division into ± components for forward and backward running waves is no longer necessary. The coupled dipole model (4.10) can be mapped to its continuous counterpart using the techniques from Sec. 3.2. The result can be cast into the form

$$E_{x,\mathrm{inc}}(z) = \frac{1}{\langle \alpha_{xx}(z)\rangle_v}\langle p_x(z)\rangle_v - N\frac{k^2}{\epsilon_0}\int_0^w dz'\, G^{\mathrm{1D}}_{\mathrm{cav}}(z,z',\omega_{eg})\,\langle p_x(z')\rangle_v\,. \tag{4.14}$$

Unlike in Sec. 3.2.2, Eq. (4.14) cannot be solved analytically because of the spatial dependence of the Casimir–Polder and Purcell effects. The integral in Eq. (4.14) is replaced by a sum using a Gauss–Legendre quadrature rule. The resulting linear equation system can be solved numerically. Subsequently, the transmission (3.43) can be computed using the same quadrature knots. Eq. (4.14) does not include the local field correction. It can be easily added by replacing the prefactor $1/\langle \alpha_{xx}(z)\rangle_v$ with $[1/\langle \alpha_{xx}(z)\rangle_v - N/(3\epsilon_0)]$.

4.2.3. Simulation procedure

Our simulations are conducted for ^{85}Rb atoms at room temperature whose Doppler width (FWHM) is roughly $85\,\Gamma_{\mathrm{vac}}$ that are confined in sapphire nanocavities as depicted in Fig. 1.2 b and Fig. 2.7 b. The transmission spectra are computed for the near-resonant excitation of the D_2 line ($5\mathrm{S}_{1/2} \to 5\mathrm{P}_{3/2}$ transition), whose Casimir–Polder shift and Purcell broadening have been discussed in Chapter 3. For the numerical implementation, we truncate the slab of atoms to a cylinder of radius $R = \sqrt{256\pi}/k$ [72]. In each simulation run, we assign random positions, ground-state populations ($m_j = +1/2$ or $m_j = -1/2$ state) and Doppler shifts sampled from the Maxwell–Boltzmann distribution[5] to the otherwise static atoms. Then, we solve the two coupled dipole models (4.10) for the two incident field components for various detunings δ and infer the transmission using Eq. (2.130). We compute the mean value of the intensity transmission over thousands of random atomic realizations until the transmission profile converges. These steps are performed for various atomic number densities N and cavity width w. An exemplary result is shown on the left side of Fig. 4.3.

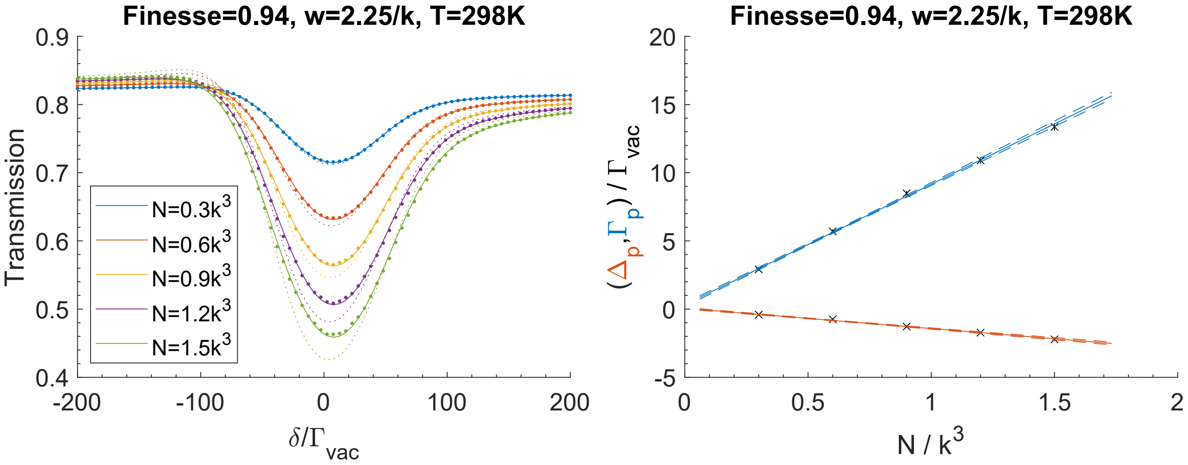

Figure 4.3: Left: Transmission spectra through a sapphire nanocavity filled with rubidium vapors with different densities N at room temperature. They are plotted against the detuning δ from the D_2 line resonance in a vacuum. The dots are obtained from the microscopic simulation with the coupled dipole model, the dashed lines from standard continuous medium theory with a local field correction. The straight lines show a fit of a continuous medium model without local field correction but with an additional shift Δ_p and a broadening Γ_p to the dotted simulation results. Right: The fit parameters Δ_p and Γ_p from the spectra on the left are plotted against the corresponding vapor density. The lines show a linear fit.

The simulation results (dots) differ significantly from the standard continuous medium theory (dashed lines), especially when the atomic number density N becomes larger. They are well described by fitting an additional shift Δ_p and an additional broadening Γ_p with our continuous medium model (4.14) (straight lines). On the right side of Fig. 4.3, the fit parameters are plotted against the corresponding atomic densities. The relation can be very well described by a linear fit with gives constant slopes $\partial_N \Delta_p$ and $\partial_N \Gamma_p$ as in the experiment [44]. The density is directly proportional to the number of interaction partners available to each atom. Thus, the linear increase with density is expected for a shift and a broadening caused by atom-atom interactions. The slopes describe the collective atom-atom interactions that are present in a granular vapor but are not accounted for in the standard continuous medium theory. The fit parameters Δ_p and Γ_p feature statistical uncertainties that we estimate from the fit to the continuous medium model. We propagate these errors in the linear fit by utilizing the estimation method of York et al. [200] instead of a simple polynomial regression.

---

[5] The velocities, $v_{z,A} = \sqrt{k_B T/m}\,\mathcal{N}(0,1)$, are random numbers drawn from a normal distribution $\mathcal{N}(\mu, \sigma^2)$ with variance $\sigma^2 = k_B T/m$ and mean $\mu = 0$.

It should be emphasized that the additional homogeneous broadening and the additional homogeneous shift pose an effective phenomenological description. In chapter 3, we were able to fit spectra with a simple C_3 interaction coefficient, although the underlying Casimir–Polder shift effect had a much more complex spatial dependence. Analogously, it is plausible that the "real" broadening and shift in the cavity also feature a more complex spatial dependence, an inhomogeneity between atoms, etc. Nonetheless, the fitted values for C_3, Γ_p, and Δ_p quantify the (averaged) strength of the atom-wall or atom-atom interaction, respectively. They can be determined and compared in theory and experiment, which is sufficient for the purpose of this chapter.

Atom-atom interactions become significant at a density on the order of $N \sim 1\,k^3 \approx 5 \times 10^{20}\,\mathrm{m}^{-3}$. That is also the regime considered in Fig. 4.3. For $N \sim 1\,k^3$ the Lorentz–Lorenz shift (3.48) and the collisional broadening (3.49) become comparable to or larger than the natural linewidth in vacuum. Yet, even a rubidium vapor with $N = 100\,k^3 \approx 5 \times 10^{22}\,\mathrm{m}^{-3}$ has a much smaller density than air under normal conditions, $N_{\mathrm{air}} = 2.5 \times 10^{25}\,\mathrm{m}^{-3}$. Due to the strong interaction at resonance, a rubidium vapor with a density of $N \leq 5 \times 10^{22}\,\mathrm{m}^{-3}$ reaches a refractive index of 1.31 [17], which is comparable to the refractive index of liquid water of 1.33, although water's atomic number density, $N \approx 3 \times 10^{28}\,\mathrm{m}^{-3}$, is almost a million times larger. It would be very desirable to simulate densities like $N \sim 50\,k^3$ that are reached in nanocell experiments [18, 44]. However, this is not practical due to the high computational cost of coupled dipole model for which large linear equation systems have to be solved. The effort scales with the number of atoms cubed. This limits our simulations to less than 1500 atoms and caps the densities on the order of $1\,k^3$ when larger cavity widths up to $w \sim \lambda$ are also to be investigated. Our simulation model does not account for the nonlocal response of the vapor that still plays a role at the moderate densities $\sim 1\,k^3$. An experimental investigation at $N = 1\,k^3$ would likely result in spectra that are different from Fig. 4.3. Still, we want to compare against experiments that took place at densities of $N \sim 50\,k^3$ and obey the local limit. For this purpose, it is consistent to use our local theory when we assume that the extracted slopes $\partial_N \Delta_p$ and $\partial_N \Gamma_p$ also apply to larger densities. The radius $R = \sqrt{256\pi}/k$ to which we have truncated our computational domain is also a compromise between accuracy and numerical effort. We have checked in sample computations that the influence of the finite radius on the slopes is well within our statistical error. However, if these error bars are to be improved by higher statistics, a larger radius may also be required, which will increase the numerical effort considerably.

Our continuous fit model incorporates the atom-wall interactions via the Casimir–Polder and Purcell effect. These interactions create inert vapor layers at the surfaces because they detune the resonances to such an extent that the atoms can no longer be excited by the laser field. Approximately 60 nm away from the surface, the Casimir–Polder shift is weak enough to be comparable to the natural linewidth. Then, the atomic response approaches the value that

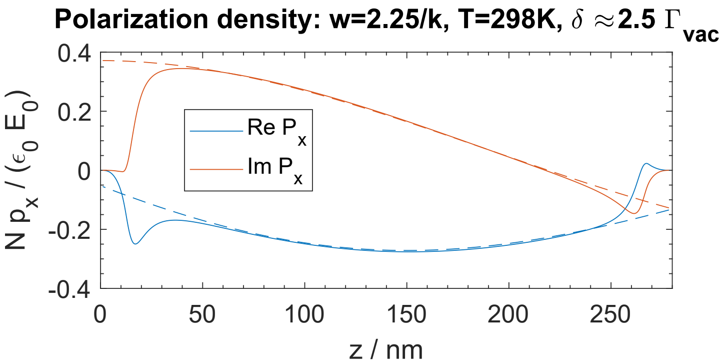

Figure 4.4: Polarization density of a rubidium vapor in a sapphire cavity of width $w \approx 280\,\text{nm}$ plotted against the location z in the cavity for one specific detuning δ from the D_2 line resonance. The straight lines show the spatial profile from the fitted continuous medium model. By integrating this profile according to Eq. (3.43), one obtains the data point for the transmission at $\delta = 2.5\,\Gamma_{\text{vac}}$ in Fig. 4.3. The same model was used for the dashed lines except that the Casimir–Polder and Purcell effects have been omitted.

would be obtained if there was no atom-wall interaction as shown in Fig. 4.4. Furthermore, we have conducted simulations without including atom-wall interactions. For cavities of width $w \geq 1/k$ that are not dominated by atom-wall interactions, we find the same collective atom-atom interaction parameters $\partial_N \Delta_p$ and $\partial_N \Gamma_p$ within the statistical uncertainty. This means that the two parameters are solely determined by the two-level transition $5S_{1/2} \rightarrow 5P_{3/2}$, which can be fully characterized just by the transition wavelength and the transition dipole moment. We can express our cavity width w in terms of the wavelength and the slopes $\partial_N \Delta_p$ and $\partial_N \Gamma_p$ in terms of the slope of the Lorentz–Lorenz shift $\partial_N \Delta_{\text{LL}}$. These dimensionless quantities apply to any effective two-level system, i.e. any of the D lines of any of the alkali vapors.

4.2.4. Theory vs. experiment

The first experiment with dense atomic vapors in wedged nanocells in 2012 was conducted with rubidium atoms [18], like our simulations. The second experiment in 2018 used potassium atoms[6] [44]. Using our dimensionless units, we can perform a cross-species comparison and plot the experimental findings of Ref. [44] against our simulation results in Fig. 4.5. The experimental data points end at a certain cavity thickness because the absorption becomes too strong to obtain a transmission signal.

Theoretical and experimental collective shifts both show an oscillatory behavior with a similar period and amplitude. The experimentally observed shift could be represented by a cosine function with a period of $(0.50 \pm 0.02)\,\lambda$ for a cavity size between $0.1\,\lambda$ to $0.75\,\lambda$ [44]. This period approximately matches the series of dips and peaks in the simulation located at $0.52\,\lambda$, $0.80\,\lambda$ and $1.06\,\lambda$. However, the shift does not follow a simple analytic function like a cosine in regions

---

[6] Potassium atoms feature a particularly small hyperfine splitting. While rubidium atoms produce a series of transmission dips caused by the transitions between the various hyperfine states, these dips virtually merge in a thermal potassium vapor. Dealing with a single line is more convenient in the experiment.

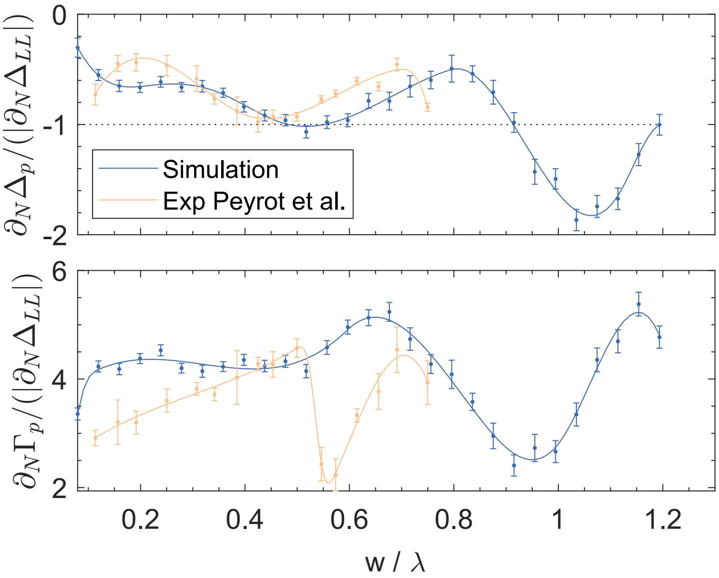

Figure 4.5: Slope of collective shift (top) and broadening (bottom) over width w of a vapor-filled sapphire cavity in simulation (^{85}Rb, room temperature, density $\simeq 1\,k^3$) and experiment [44] (^{39}K, temperature varied up to 600 K, density up to $100\,k^3$). In textbook electrodynamics, a constant Lorentz–Lorenz shift (dotted line) is expected. Simulation error bars correspond to 1σ, solid lines are spline interpolations. The figure is also published in Ref. [194].

larger than 0.75λ. The first dip for the shift is displaced between simulation and experiment by about 0.1λ but features the same minimum of $\partial_N \Delta_p = (-1.0 \pm 0.1)\partial_N \Delta_{LL}$ in the experiment and $\partial_N \Delta_p = (-1.1 \pm 0.1)\partial_N \Delta_{LL}$ in the simulation. The simulated collective broadening oscillates similarly to the shift and partially overlaps with the experimental broadening around $0.4\,\lambda$ and $0.5\,\lambda$ and around a cavity width of $0.7\,\lambda$. As a major difference, the experiment shows a pronounced dip in the broadening around $0.55\,\lambda$ that is not present in the simulation.

The experiment (N up to $100\,k^3$ [44]) and the simulations (N up to $1.5\,k^3$) have been conducted at very different densities, such that the comparison relies on the extrapolation of a linear trend. Another difference is that all simulations have run at the same temperature ($T \approx 300\,\mathrm{K}$), while in the experiment different temperatures are used to reach different vapor densities[7]. The experiment reaches substantially higher temperatures (up to $T = 600\,\mathrm{K}$) while using lighter ^{39}K atoms. In order to determine the influence of the temperature, we have carried out some example calculations at higher temperatures but found no significant changes to our collective shifts and broadenings. Furthermore, three effects could influence the experiment that are not covered by the theoretical model.

First, atom-wall collisions may change the atomic velocity distribution away from a Maxwell–Boltzmann shape. As we discussed in Sec. 3.2.5, the Maxwell–Boltzmann distribution is a working hypothesis that can and should be replaced when new evidence hints towards another distribution. Second, the simulation does not fully account for atomic collisions. We average interaction over different static configurations, which resembles the treatment of the quasi-static regime in collision theories, recall Sec. 3.2.4. In thermal vapors, however, the collisions take place in the impact regime, for which the trajectories and the motion of the atoms must be included. Both collisional effects and static interaction effects like the Lorentz–Lorenz shift scale linearly with density. This makes them hard to distinguish in the experiment[8]. Interestingly, the collisional broadening (3.49) differs between D_1 and D_2 line by a factor of $\sqrt{2}$. For the Lorentz–Lorenz shift (3.48) and the collective broadening Γ_p the ratio is 2. Therefore, conducting experiments on D_1 and D_2 lines might help to distinguish the effects. Third, we neglect temporal and spatial derivatives in a simplistic manner. As a result, the Doppler shift is approximated to the "zeroth order" [72] by the vacuum shift. Deviations can be caused, e.g., by the effective refractive index of the gas, recall Sec. 3.2.2. In addition, the finite spectrum of the laser field and the light emitted by the atoms are not taken into account. Instead, we conduct our simulations in a monochromatic approximation that treats each frequency component of the light field independently. To overcome these limitations, one could solve the interaction problem of moving atoms in the time domain and conduct the average there. But this increases the numerical effort tremendously, and no successful implementation of such an approach for an interacting dense vapor is known to me at the time of writing.

---

[7] The vapor density is controlled by heating the metallic deposit in the reservoir to a particular temperature. In the nanocell experiments, this temperature also applies to the cell.

Collisions are the most likely cause for the discrepancies between theory and simulation because they also scale linearly with density and have a profound impact on thermal vapors. The similarity between simulation and experiment in Fig. 4.5 suggests that the collective shift and broadening observed in the experiments are caused by the granular nature of the atomic gas and the modified atom-atom interactions in the nanocavity environment. To test this conjecture, we suggest a series of new experiments in coated cavities.

4.3. Atom-atom interactions in coated nanocavities

The atom-atom interactions in the cavity depend on the reflectance of the cavity walls. Cavity coatings adjust this reflectance and should be able to change the collective broadening and shift.

An increase can be accomplished by equipping the cavities with distributed Bragg reflectors (DBR) made out of $\lambda/4$ stacks, see Fig. 4.6 c and 4.6 d. We use alternating layers of silica ($n = 1.45$) and sapphire ($n = 1.77$). The topmost layer is always sapphire. Therefore, unknown effects connected to the surface, such as possible deviations from the Maxwell–Boltzmann velocity distribution, should occur in the same way in different cavities. In an experiment, this might help to segregate their impact. The transmission and reflection coefficients of the cavity coatings are calculated with the matrix input-output formalism presented in App. E.2. We label the cavities by their finesse $\mathcal{F} = \pi|r_{21}|/(1 - |r_{21}|^2)$ [138], a figure of merit that increases

---

[8] The experiment in Ref. [174] distinguished the effects using the third-order nonlinear optical response. However, the work relies on the assumption of a continuous medium and ignores the granular character of the vapor.

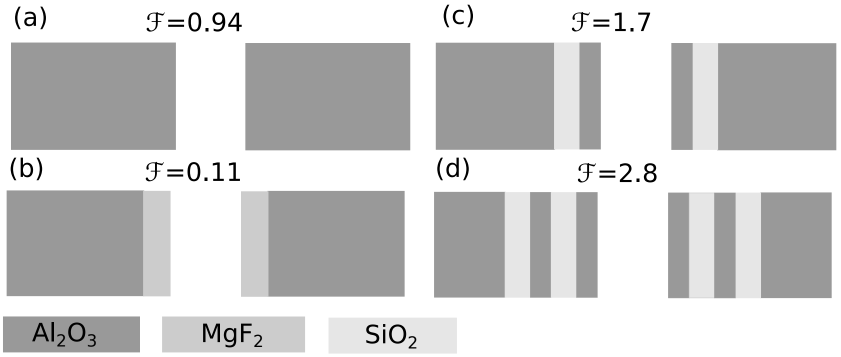

Figure 4.6: Cavity designs of finesse $\mathcal{F}$ with (a) no, (b) anti-reflection, or (c,d) Bragg mirror coating with $\lambda/(4n)$ layers. Figure also published in Ref. [194].

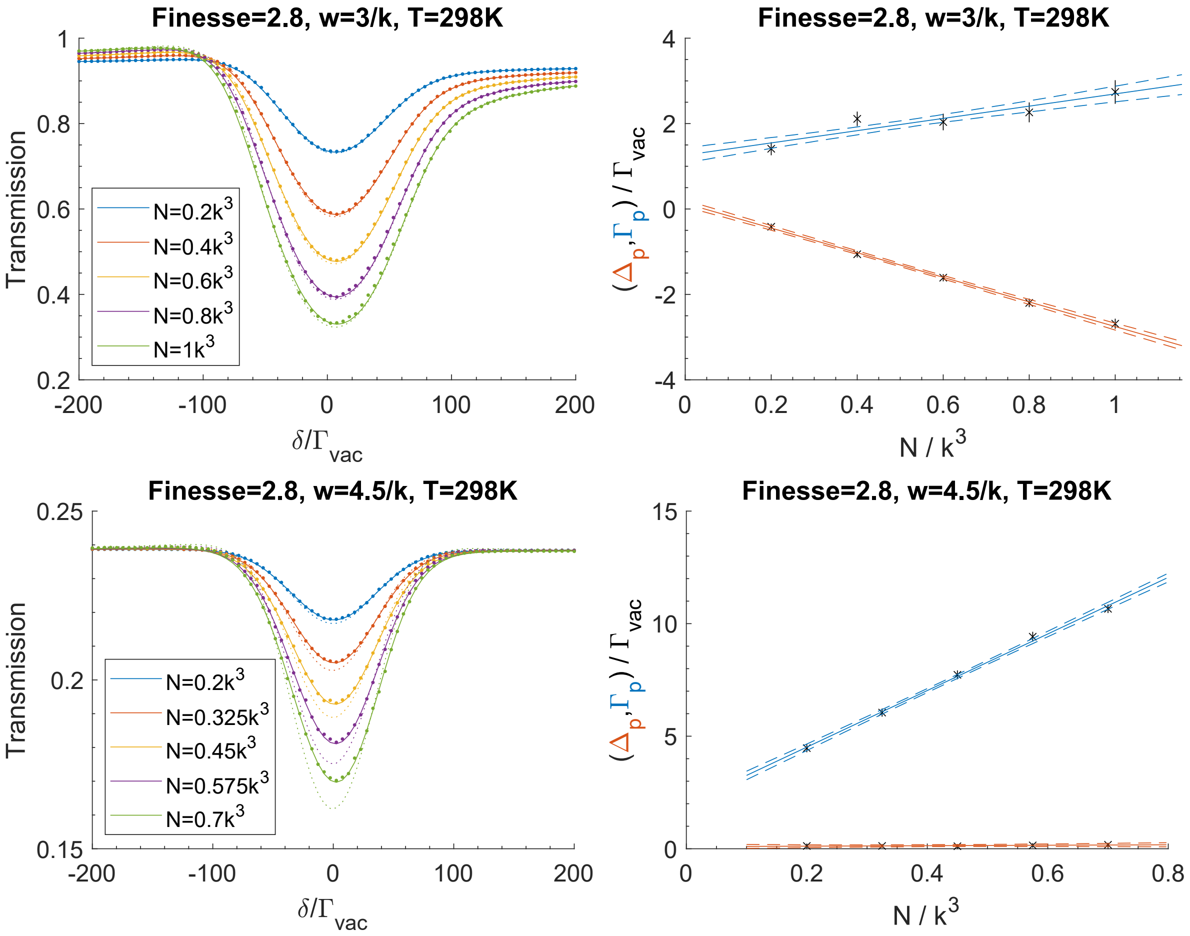

Figure 4.7: Left: Transmission spectra through a nanocavity filled with rubidium vapor for two different cavity width w. Right: Fitted collective broadening and shift Δ_p, Γ_p plotted against the vapor density. The graphs are analogous to Fig. 4.3 but for a coated cavity with Finesse 2.8, see Fig. 4.6 d.

monotonically with reflectance. Although our finesses are small[9], they are sufficient to cause prominent changes.

---

[9] Good cavities can reach finesses above 10^5. But high finesses would not be helpful to us because they allow transmission only for specific cavity thicknesses and vapor densities.

Exemplary spectra for the cavity design with finesse 2.8 are shown in Fig. 4.7. We immediately see stark differences in the slopes of the collective broadening and shift depending on the cavity width. Coincidentally, the standard local field correction works very well for $w = 3/k$. This is an exception, though, and not true for almost any other cavity widths, see also Fig. E.6 in the appendix. Furthermore, Fig. 4.7 shows that the linear fits do not generally extrapolate to a shift and broadening of zero at zero density. Such a small offset also occurs for the uncoated sapphire cavities for some thicknesses. It reminds us that the description with a homogeneous shift and broadening is only phenomenological and not exact. Furthermore, a higher finesse also raises the asymmetries in the transmission spectrum that occur for some cavity widths, see Fig. E.6 in the appendix.

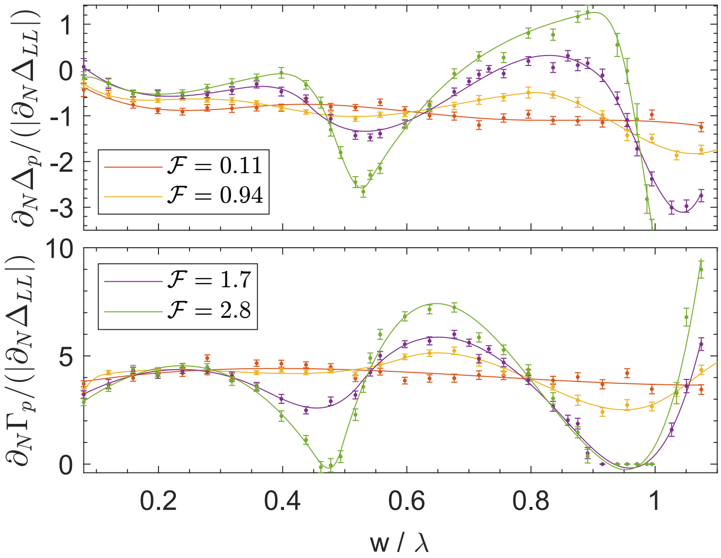

Figure 4.8: Slope of the collective shift (top) and broadening (bottom) over width d of the atomic layer. The atoms are in free space or in the coated cavities depicted in Fig. 4.6, respectively. Error bars correspond to 1σ, solid lines are spline interpolations. Compare Ref. [194].

In Fig. 4.8, we plot the slops of the collective shift and broadening against the cavity width for all cavity designs from Fig. 4.6. This also includes a cavity with smaller finesse due to an anti-reflection (AR) coating shown in Fig. 4.6 b. For this, we use a $\lambda/4$ magnesium fluoride ($n = 1.38$ [201]) layer, which provides a decent reflection suppression ($R \approx 0.1\%$). For the sake of simplicity, we have not included a thin sapphire layer on top ($\sim 10\,\text{nm}$) that would likely be required in an experiment to protect the AR coating against the chemically aggressive alkali vapor. With increasing cavity finesse, we get a prominent enhancement of the amplitudes of the oscillatory features in the collective shift and broadening as depicted in Fig. 4.8. At the same time, the oscillations are strongly suppressed in the AR-coated cavity. We attribute the oscillatory dependence to the constructive or destructive interference of the photons that mediate the atom-atom interactions inside the cavity. Because a higher finesse sharpens these interferences, it is plausible that the shift and broadening can be enhanced with higher finesse and suppressed with lower finesse. The collective shift and broadening in an AR-coated cavity are similar but not identical to those in free space, as shown in the appendix in Fig. E.7. The AR coating only suppresses reflection at normal incidence, whereas the light fields scattered between atoms also hit the cavity walls under oblique angles. In conclusion, we have shown that the density- and width-dependent shifts and broadenings in a nanocavity can be tuned by adjusting the cavity's reflectance with coatings. The systematic changes predicted in Fig. 4.8 can be tested in future experiments.

4.4. Cold gases in free space

Although the coupled dipole model applies to all temperatures, the effective description in continuous medium models differs between hot and cold vapors. In Fig. 4.9, we show the transmission spectrum of a cold rubidium vapor in free space (dots), analogously to Fig. 4.1. It features significant deviations from a fit attempt with a Fabry–Pérot profile with an additional homogeneous line broadening and shift (straight lines) as we have used it for the thermal vapors.

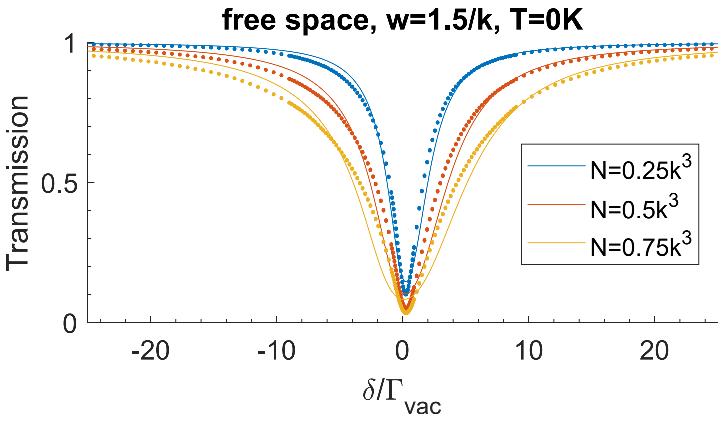

Figure 4.9: Transmission spectra through a slab of rubidium atoms in free space at zero temperature excited near-resonantly to the D_2 line for different atomic densities N. The coupled dipole simulation results (dots) are shown together with a fit attempt based on a Fabry–Pérot profile with an additional homogeneous broadening and a homogeneous shift.

Yet, a very recent work by Andreoli et al. [195] found an excellent continuous medium description for a cold vapor. Instead of using two parameters for the entire spectrum, the authors of Ref. [195] fitted the real and imaginary part of the vapor's refractive index for each detuning individually. Such an approach is only possible in free space, where no atom-wall interactions exist and the refractive does not vary spatially. To facilitate a refractive index fit for our simulation results, we compute not only the ensemble average of the intensity transmission coefficient but also of the amplitude transmission coefficient like Ref. [195]. In an ensemble of moving atoms, each atomic configuration corresponds to a different point in time. Each configuration scatters a different light intensity onto the detector which effectively averages the intensity over its finite response time. We mimic this by computing the average of the intensity transmission coefficient. An average over the amplitude transmission coefficient, on the other hand, causes scattered light fields originating from different atomic configurations to interfere. Therefore, the two averages are not identical. However, in our examples, the results of both approaches are so close to each other that the amplitude coefficient can be used too. Instead of a single real number $|t|^2$, we get a complex value t that can be converted into a complex refractive index by using Eq. (3.43). In Fig. 4.10, we fit the transmission profiles of different cavity widths w with the same complex refractive index n.

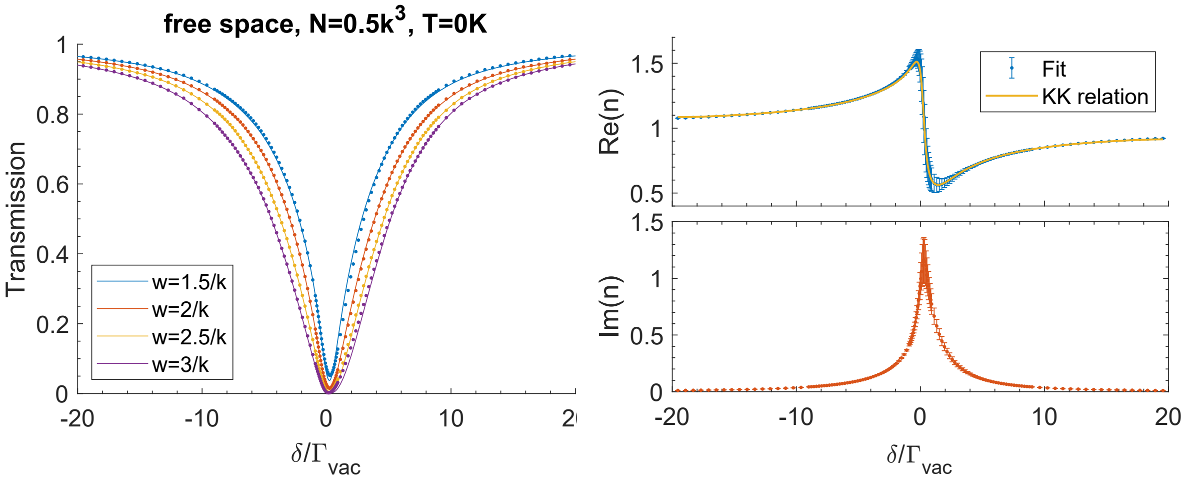

Figure 4.10: Left: Transmission spectra through slabs of rubidium atoms of different thicknesses w in free space at zero temperature excited near-resonantly to the D_2 line. The coupled dipole simulation results (dots) are shown together with a fit to a Fabry–Pérot profile with the real and imaginary part of the vapor's refractive index as parameters. Right: Fitted real and imaginary part of the vapor's refractive index plotted against the detuning. They are shown as points with error bars that largely overlap close to resonance. The straight yellow line indicates the result of a Kronig–Kramers transformation (4.15) of the fitted imaginary part of the refractive index.

It might seem inappropriate to compute an average over random atomic positions at absolute zero where atoms do not move. However, we find results that are analogous to those shown in Fig. 4.9 and Fig. 4.10 also for small temperatures like $T = 0.1\,\mathrm{K}$ where atomic velocities of $v_{\mathrm{th}} \approx 4\,\mathrm{m/s}$ enforce a time or configurational average. It is noteworthy that a single[10] refractive index in a Fabry–Pérot profile (3.43) can explain the spectra at different cavity widths. However, it is not very conclusive to fit just eight numbers (real and imaginary parts of the transmission coefficient for four different cavity widths) with two parameters.

If the fitted values for $\mathrm{Re}\, n(\delta)$ and $\mathrm{Im}\, n(\delta)$ are proper physical quantities, they must obey Kronig–Kramers relations analogously to Eqs. (2.10) and (2.11). Using the results from App. D and the fact that the detuning is small compared to the resonance frequency, $|\delta| \ll \omega_{eg}$, the Kronig–Kramers relation for the real part of the refractive index can be written as

$$\mathrm{Re}\, n(\delta) \approx 1 + \frac{1}{\pi}\mathcal{P}\int_{\delta_a}^{\delta_b} d\delta' \,\frac{\mathrm{Im}\, n(\delta') - \mathrm{Im}\, n(\delta)}{\delta' - \delta} + \frac{\mathrm{Im}\, n(\delta)}{\pi} \ln\left(\frac{\delta_b - \delta}{\delta - \delta_a}\right), \tag{4.15}$$

---

[10] Within a certain error bound indicated in Fig. 4.10.

where $\delta_a < \delta < \delta_b$. Here δ_a and δ_b border the interval where $\operatorname{Im} n(\delta)$ is appreciable larger than zero. Using Eq. (4.15), we have computed the real part of the refractive index from the fitted $\operatorname{Im} n(\delta)$ and have indicated the result by a straight yellow line in Fig. 4.10. We find that the Kronig–Kramers relations are fulfilled. The fact that a physical description with refractive indices is possible but a fit with a homogeneous broadening and line shift fails means that we must have an inhomogeneous broadening in the vapor. Ref. [195] presents a new path to solve the coupled dipole model that elucidates the physical mechanism behind this inhomogeneity.

4.4.1. Renormalization group approach

The renormalization group (RG) approach of Andreoli et al. [195] solves the coupled dipole model by approximately diagonalizing the many-body interaction matrix in terms of pairwise blocks. Let us consider two atoms close to one another, i.e. $k|\mathbf{r}_1 - \mathbf{r}_2| \to 0$. Their interactions matrix has two eigenstates shifted as ω_- and ω_+ [195]. These shifts diverge as $1/r_{21}^3$ which leads to two well-separated resonances with broadenings[11] of $\Gamma_+ \approx 2\Gamma_{\mathrm{vac}}$ and $\Gamma_- \approx 0$ [195], respectively. In the renormalization group (RG) approach, the two interacting atoms are replaced with an optically equivalent pair of noninteracting but shifted atoms that show the same scattering behavior.

Initially, the RG algorithm of Ref. [195] allows all atoms to interact. After the first step it discards the interaction potential of the strongest interacting pair and instead randomly assigns them the shifts ω_- and ω_+ that are obtained from the exact solution of their two-body problem. Importantly, the line broadening is left unchanged. Unlike the shift, the broadening does not diverge and therefore cannot be approximated pairwise [195]. If the modified broadenings Γ_+ and Γ_- are included, the scheme leads to nonphysical solutions [195]. The algorithm continues to replace the pair with the strongest effective interaction with a shifted noninteracting pair until the strongest effective interaction drops below a certain threshold, see Fig 4.11. A single atom can gather multiple shifts when it is part of multiple pairs, but each pair is only replaced once. As in the coupled dipole model, the RG approach is applied for various detunings and the resulting transmission is averaged over sets of random positions. The algorithm accomplishes a transition from a microscopic perspective that involves complex interactions to a self-similar system with renormalized resonance frequencies where complex details must no longer be considered. Therefore it is referred to as a renormalization group approach.

The new effective resonance frequencies can be characterized by a smooth probability function $P(\omega_{\mathrm{eff}})$ [195]. The distribution can also be obtained from the exact diagonalization of the coupled dipole model for each atomic configuration. Both results are reported to agree very well, demonstrating the validity of the RG approach [195]. Microscopically, the vapor is a random arrangement of atoms whose different distances from each other lead to different effective resonance frequencies. Therefore, the macroscopic description of the vapor with a refractive index n includes an inhomogeneous broadening given by $P(\omega_{\mathrm{eff}})$. This inhomogeneous

---

[11] These broadenings are also known from Dicke superradiance [61].

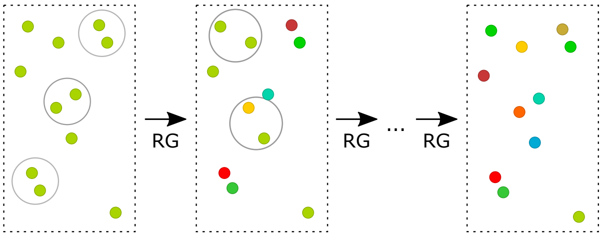

Figure 4.11: Concept of the renormalization group (RG) approach, compare Ref. [195]. In each step, the strongest interacting pair of atoms is replaced by an optically equivalent non-interacting pair with shifted resonance frequencies. The procedure is repeated until all strongly interacting pairs are replaced.

broadening prevents the refractive index of the vapor from exceeding a certain maximum value no matter how large the atomic density becomes. This is the central finding of Ref. [195] and stands in stark contrast to the homogeneous Lorentz–Lorenz shift (3.48) from standard continuous electrodynamics that allows an arbitrary high refractive index. The cause of a maximum value for $\mathrm{Re}\, n$ is the limited number of near-resonant atoms for light to interact with. At some point, adding more atoms merely shifts the same amount of preexisting atoms out of resonance. In Ref. [195] there are approximately 0.3 near-resonant atoms in a volume of $1/k^3$ regardless of how large the atomic density becomes.

The treatment in Ref. [195] involves a few approximations: It uses the nonretarded version of the free-space Green's tensor and takes fields and dipoles to be scalar quantities such that only the xx component of the Green's tensor enters the interaction matrix. The latter decreases the number of rows and columns in the interaction matrix by a factor of three and greatly reduces the computational cost. This also facilitates certain improvements compared to our treatment. Andreoli et al. simulated atomic samples with a significantly wider radius, used a Gaussian beam profile for the incident field, and integrated the scattered light fields over a hemispherical surface far from the atomic ensemble. From our cold vapor spectra, we could not straightforwardly extract reasonable refractive indices for some larger cavity widths and densities. The larger computational domain in Ref. [195] might help to reduce such issues. Furthermore, we have extracted[12] the refractive index data from Ref. [195] and found them to comply excellently with Kramers–Kronig relations. It would be very desirable to extend Ref. [195] to the exact 3-D Green's tensor, to include Doppler shifts and macroscopic environments. A (semi-)analytical solution to the RG approach could greatly reduce the computational complexity. In this way, the RG approach could have a great potential for thermal gases as it could allow investigating higher atomic densities, nonlocal effects, or any other effect whose study is limited by the high computational cost of the model.

---

[12] A useful tool for this is the WebPlotDigitizer [202].

5. Conclusion and outlook

This work investigated the interactions of thermal atomic vapors at a planar surface and in planar nanocavities that are subjected to near-resonant laser light. In Chapter 2, we revisited the formalism of macroscopic quantum electrodynamics and showed how the quantized electromagnetic field could be expressed in the presence of linearly absorbing and dispersing media utilizing the classical electromagnetic Green's tensor. Our system included thermal and electromagnetic ground state fluctuations. Starting from a Hamiltonian with an atom-field coupling, we derived an equation of motion for the atomic coherence between the ground and an excited state that includes atom-wall (Casimir–Polder and Purcell effects) and resonant atom-atom interactions up to second order in perturbation theory. We considered the often overlooked role of the magnetic atomic sublevels m_j in the atom-wall interaction, especially the sublevel splitting and coupling. The stationary limit of the atomic equation of motion led to the coupled dipole model that has been used in the remainder of this thesis. By solving the coupled dipole model, one obtains the light-induced dipole moments from which the scattered light fields, the reflection spectra at a surface, and the transmission spectra through a nanocavity can be computed.

Chapter 3 investigated how the strength of Casimir–Polder interactions can be inferred from reflection and transmission spectra of thermal vapor cells and nanocavities, respectively. First, we determined the Casimir–Polder and Purcell effects at a planar surface. In the nonretarded limit, the shift follows a C_3/z^3 law. But we showed numerically that the C_3 coefficient starts to change just 10 nm away from the surface. As a prerequisite for understanding the theories commonly used to evaluate experimental spectra, we transferred the coupled dipole model to a continuous medium description of the atomic vapor. As a cross-check, we demonstrated how the well-known Fabry–Pérot transmission profile could be retrieved from our theory. Furthermore, we discussed the local field correction that arises in a continuous medium and that in a homogeneously broadened system can be rewritten into a homogeneous shift, the Lorentz–Lorenz shift. Assuming low atomic densities, we derived theoretical reflection spectra of a vapor cell (selective reflection and frequency modulated selective reflection spectroscopy) and the transmission spectra of a nanocell. We computed spectra based on the exact Casimir–Polder shifts and Purcell line broadenings and subsequently fitted them with a simplified model containing a constant C_3 coefficient. The phenomenological description was excellent, but the fitted C_3 coefficient was 20% to 40% larger than one would expect from nonretarded theory. Many works compare a C_3 from nonretarded theory with a fitted C_3 from an experiment. In quantitative terms, this may not be very meaningful. Instead, one could attempt a comparison with an effective C_3 that is computed from a theoretical spectrum without the nonretarded approximation.

Chapter 4 studied the atom-atom interactions of dense vapors in nanocavities. We reviewed recent theoretical and experimental evidence that resonantly excited atomic vapors deviate from the expectations from standard continuous electrodynamics. Specifically, the Lorentz–Lorenz shift does not apply or is modified because an atomic vapor is a granular and not a continuous medium. We aimed to develop a theoretical model for a recent experiment with a dense thermal vapor in a wedged nanocell by Peyrot et al. [44]. For this, we simulated the light scattering of random atomic ensembles in a sapphire nanocavity. Like the experimental spectra, our simulated spectra could only be described by continuous medium models when an additional shift and broadening were included. Both of them grow linearly with density. Their slops featured a similar oscillatory dependence on the cavity width w in both theory and experiment. However, the high computational cost constrains the simulations to moderated atomic densities around $1\,k^3$ while the experiments reach densities up to $100\,k^3$. Furthermore, we conducted simulations in nanocavities that were equipped with coatings to increase or decrease the reflectance of the cavity walls. We found that a higher reflectance massively increases the amplitudes of the oscillations of the additional broadening and shift while an anti-reflection coating suppresses the oscillations. These systematic changes can be probed in future experiments to test the validity of our theory. Finally, we showed that in a cold vapor the atom-atom interactions lead to an inhomogeneous broadening. This finding is part of a recent work by Andreoli et al. [195] who developed a new approach to approximate the solution of the coupled dipole model using renormalization group theory.

Our theoretical description of thermal vapors in macroscopic environments is by no means complete and leaves many open questions for future works. It would be very desirable to solve the coupled dipole model for densities as high as in the experiment and to solve the model for atoms that move over a period of time. The latter helps to account for nonlocal effects, changes to the Doppler shifts, atomic collisions, and much more. The main obstacle standing in the way of these advancements is the high numerical cost of finding exact solutions to the coupled dipole model. Only recently, the renormalization group approach has offered a new way of approximating solutions. This could help to decrease the numerical effort, especially if (semi-)analytical solutions for the process would be found. The first step is to see if the scheme can be extended to include the exact 3-D Green's tensor, randomly assigned Doppler shifts, and Green's tensors of a macroscopic geometry.

Furthermore, our three-dimensional coupled dipole model could be applied to other macroscopic geometries. So far, (cold) atom-atom interactions have been explored in one- and two-dimensional photonic crystals [203–206]. But hot or cold atoms have also been interfaced with microresonators [207], nanofibers [208], hollow-core fibers [209], superconducting chips [210], or atomic cladding waveguides [16, 45]. The dipole-dipole interactions in these systems can be studied by inserting the Green's tensor for the respective geometry into our scheme. Nonetheless, in some systems, the model must be extended by the transit time broadening when dealing with thermal atoms. When fields are strongly localized, e.g. around a waveguide, thermal atoms enter and leave the field region. As a result, they only interact for a finite amount of time which leads to the transit time broadening.

In many experiments, atom-atom interactions have not been a concern because the atomic densities used were too low for them to have a significant impact. However, that can change when the atoms are excited to higher levels, especially to Rydberg states. The transitions between Rydberg levels have much smaller wavenumbers k such that much fewer atoms are needed to reach the critical density of $1\,k^3$. To study Rydberg atoms, the present coupled dipole model should be extended by two aspects. First, coherences between multiple levels should be considered because Rydberg atoms are usually produced by two excitation steps. Second, atom-wall and atom-atom interactions should be treated self-consistently. Rydberg atoms feature strong interactions and small energy gaps between adjacent states. Therefore, it is likely that the effect of interactions is no longer perturbatively small. Works on both of these points exist but there is no unified model that can be applied to dense thermal vapors in arbitrary geometries.

Another related line of research is the inclusion of atomic saturation, i.e. that there is a significant excited state population when the light intensity rises. In essence, this means extending the work of Lehmberg [211, 212] to a macroscopic environment. This advance is particularly important for cavities and waveguides because they feature local field enhancements which promote saturation. The next step is to drop the weak-coupling approximation. This can be done, e.g., by including fourth-order terms with the time-convolutionless projection operator technique [76]. A theory in a macroscopic environment beyond weak coupling would be beneficial to experimental proposals [125] that aim to produce strong atom-photon coupling in a thermal vapor via a photonic crystal cavity. This proposal reflects the key concept of quantum optics with thermal vapors: The short interaction and coherence times are overcome by a much stronger atom-photon coupling.

Once all the crucial effects of a system are described, the macroscopic QED formalism can show its greatest strength: A macroscopic environment, i.e. the Green's tensor, can be designed such that the system follows a particular behavior. First works on such an inverse design approach have recently been presented [213, 214]. In the long term, an inverse design has the potential to improve existing applications such as vapor-based single-photon sources and quantum memories and to enable completely new ones. In this way, further development of the concepts presented in this thesis might one day contribute to the "second quantum revolution".

A. Electromagnetic Green's tensors

A.1. The Green's tensor of bulk media

We derive the electromagnetic Green's tensor for a homogeneous medium of permittivity $\epsilon(\omega)$ following Refs. [51, 126]. We need to solve the Helmholtz equation

$$[\boldsymbol{\nabla} \times \boldsymbol{\nabla} \times -k^2]\, \boldsymbol{G}_{\text{bulk}}(\mathbf{r}, \mathbf{r}', \omega) = \boldsymbol{I}\delta(\mathbf{r} - \mathbf{r}'), \tag{A.1}$$

where $k^2 = \epsilon(\omega)\frac{\omega^2}{c^2}$. Using the identity $\boldsymbol{\nabla} \times \boldsymbol{\nabla}\times = \boldsymbol{\nabla} \otimes \boldsymbol{\nabla} - \Delta\boldsymbol{I}$, we obtain

$$[\Delta + k^2]\, \boldsymbol{G}_{\text{bulk}}(\mathbf{r}, \mathbf{r}', \omega) = \boldsymbol{\nabla}[\boldsymbol{\nabla} \cdot \boldsymbol{G}_{\text{bulk}}(\mathbf{r}, \mathbf{r}', \omega)] - \boldsymbol{I}\delta(\mathbf{r} - \mathbf{r}'). \tag{A.2}$$

Applying the divergence operator on (A.1), we find

$$\boldsymbol{\nabla} \cdot \boldsymbol{G}_{\text{bulk}}(\mathbf{r}, \mathbf{r}', \omega) = -\frac{\boldsymbol{\nabla} \cdot \boldsymbol{I}\delta(\mathbf{r} - \mathbf{r}')}{k^2}. \tag{A.3}$$

Combining the above relations,

$$[\Delta + k^2]\, \boldsymbol{G}_{\text{bulk}}(\mathbf{r}, \mathbf{r}', \omega) = -\left[\boldsymbol{I} + \frac{1}{k^2}\boldsymbol{\nabla} \otimes \boldsymbol{\nabla}\right] \delta(\mathbf{r} - \mathbf{r}'). \tag{A.4}$$

This equation can be solved by an ansatz

$$\boldsymbol{G}_{\text{bulk}}(\mathbf{r}, \mathbf{r}', \omega) = \left[\boldsymbol{I} + \frac{1}{k^2}\boldsymbol{\nabla} \otimes \boldsymbol{\nabla}\right] g(\mathbf{r}, \mathbf{r}', \omega), \tag{A.5}$$

where $g(\mathbf{r}, \mathbf{r}', \omega)$ is the well-known (retarded) solution of the scalar Helmholtz equation

$$[\Delta + k^2]\, g(\mathbf{r}, \mathbf{r}', \omega) = -\delta(\mathbf{r} - \mathbf{r}') \quad \Rightarrow \quad g(\mathbf{r}, \mathbf{r}', \omega) = \frac{\exp(ik|\mathbf{r} - \mathbf{r}'|)}{4\pi|\mathbf{r} - \mathbf{r}'|}. \tag{A.6}$$

Thus, the bulk Green's tensor with a spherical exclusion volume around $\mathbf{r} = \mathbf{r}'$ [165] is

$$\begin{aligned} \boldsymbol{G}_{\text{bulk}}(\mathbf{r}, \mathbf{r}', \omega) &= \left[\boldsymbol{I} + \frac{1}{k^2}\boldsymbol{\nabla} \otimes \boldsymbol{\nabla}\right] \frac{\exp(ik|\mathbf{r} - \mathbf{r}'|)}{4\pi|\mathbf{r} - \mathbf{r}'|} && \text{(A.7)} \\ &= -\frac{\delta(\boldsymbol{\rho})\boldsymbol{I}}{3k^2} - \frac{e^{ik\rho}}{4\pi k^2\rho^3}\left([1 - ik\rho - (k\rho)^2]\, \boldsymbol{I} - [3 - 3ik\rho - (k\rho)^2]\, \mathbf{e}_\rho \otimes \mathbf{e}_\rho \right). && \text{(A.8)} \end{aligned}$$

where $\boldsymbol{\rho} = \mathbf{r} - \mathbf{r}'$, $\rho = |\boldsymbol{\rho}|$, and $\mathbf{e}_\rho = \boldsymbol{\rho}/\rho$.

A.2. The image dipole method

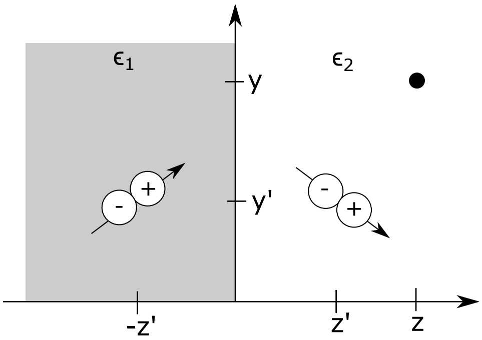

Figure A.1: A dipole in front of a surface located at $(x', y', z')^T$ produces a mirror dipole at $(x', y', -z')^T$ emitting light to a probe point $(x, y, z)^T$. Probe and source point are taken to located in region 2.

With the image dipole technique, one can easily construct the Green's tensor of a planar interface in short-distance approximation, see, e.g., Ref. [215]. At short or nonretarded distances, the source dipole is effectively static and produces a mirror dipole inside the surface, see Fig. A.1. The surface contribution to the Green's tensor is the field emitted by that artificial dipole computed through the nonretarded limit ($\rho k \ll 1$) of the bulk Green's tensor, Eq. (A.8),

$$\mu_0\omega^2 \boldsymbol{G}^{\mathrm{nr}}_{\mathrm{bulk}}(\mathbf{r},\mathbf{r}',\omega) = -\frac{\delta(\boldsymbol{\rho})\boldsymbol{I}}{3\epsilon_0\epsilon_2(\omega)} - \frac{[\boldsymbol{I} - 3\mathbf{e}_\rho \otimes \mathbf{e}_\rho]}{4\pi\epsilon_0\epsilon_2(\omega)\rho^3}, \tag{A.9}$$

with $\boldsymbol{\rho} = (x - x', y - y', z - z')^T$. We assume that the probe and source point of the surface Green's tensor lie in front of the interface. The magnitude of the image charges is given by the ratio $\frac{\epsilon_1(\omega)-\epsilon_2(\omega)}{\epsilon_1(\omega)+\epsilon_2(\omega)}$ [101] and the orientation of the image dipole is flipped in the xy-plane, so that

$$\begin{aligned}\mu_0\omega^2 \boldsymbol{G}^{\mathrm{nr}}_{\mathrm{surf}}(\mathbf{r},\mathbf{r}',\omega) &= \frac{\epsilon_1(\omega)-\epsilon_2(\omega)}{\epsilon_1(\omega)+\epsilon_2(\omega)}\mu_0\omega^2 \boldsymbol{G}^{\mathrm{nr}}_{\mathrm{bulk}}(\mathbf{r},(x',y',-z'),\omega)\,\mathrm{diag}(-1,-1,1) &\text{(A.10)}\\ &= \frac{\epsilon_1(\omega)-\epsilon_2(\omega)}{\epsilon_1(\omega)+\epsilon_2(\omega)}\frac{[\boldsymbol{I} - 3\mathbf{e}_{\tilde\rho} \otimes \mathbf{e}_{\tilde\rho}]}{4\pi\epsilon_0\epsilon_2(\omega)\tilde\rho^3}\,\mathrm{diag}(1,1,-1), &\text{(A.11)}\end{aligned}$$

with $\tilde{\boldsymbol{\rho}} = (x - x', y - y', z + z')^T$. If probe and source points coincide, the surface Green's tensor takes the simple form

$$\mu_0\omega^2 \boldsymbol{G}^{\mathrm{nr}}_{\mathrm{surf}}(\mathbf{r},\mathbf{r},\omega) = \frac{\epsilon_1(\omega)-\epsilon_2(\omega)}{\epsilon_1(\omega)+\epsilon_2(\omega)}\frac{\mathrm{diag}(1,1,2)}{32\pi\epsilon_0\epsilon_2(\omega)z^3}. \tag{A.12}$$

In the limit of non-absorbing media, $\mathrm{Im}\,\epsilon_2(\omega), \mathrm{Im}\,\epsilon_1(\omega) \to 0$, the above expressions are only valid for the absolute value and the real part of the Green's function. The imaginary part has to be computed from the exact expression of the surface Green's tensor presented in Appendix A.3. For a perfect mirror, we can obtain an exact result from the image dipole technique if we use the exact bulk Green's tensor instead of the nonretarded approximation.

A.3. Construction of surface and cavity Green's tensors

We derive the Green's tensor in planar layered media following the treatment in Ref. [51].

A.3.1. Vector wave functions

To construct the scattering contribution of the Green's tensor, see Eq. (2.31), we make use of so-called vector wave functions (VWF) that derive from a scalar function $\psi^j_\lambda(\mathbf{r})$ as [86]

$$\mathbf{L}^j_\lambda(\mathbf{r}) = \boldsymbol{\nabla}\psi^j_\lambda(\mathbf{r}), \quad \mathbf{M}^j_\lambda(\mathbf{r}) = \boldsymbol{\nabla} \times \mathbf{c}(\mathbf{r})\,\psi^j_\lambda(\mathbf{r}), \quad \mathbf{N}^j_\lambda(\mathbf{r}) = \frac{1}{k_j}\boldsymbol{\nabla} \times \mathbf{M}^j_\lambda(\mathbf{r}), \tag{A.13}$$

with pilot vector $\mathbf{c}(\mathbf{r})$ and mode label λ. $\mathbf{M}^j_\lambda(\mathbf{r})$ and $\mathbf{N}^j_\lambda(\mathbf{r})$ represent the (divergence-free) curl part of the field, whereas $\mathbf{L}^j_\lambda(\mathbf{r})$ contains the (curl-free) source part. The VWFs form a complete orthogonal basis [86]. The functions $\psi^j_\lambda(\mathbf{r})$ obey the scalar Helmholtz equation in layer j

$$[\Delta + k_j^2]\psi^j_\lambda(\mathbf{r}) = 0. \tag{A.14}$$

where $k_j = \sqrt{\epsilon_j(\omega)}\omega/c$ with $\operatorname{Im} k_j \geq 0$. As a result, the VWFs fulfill the vector Helmholtz equation (2.33) [86] and transfer this property to a Green's tensor that is constructed as linear superposition of VWFs as

$$\boldsymbol{G}_{\mathrm{sc}}(\mathbf{r},\mathbf{r}',\omega) = \mathop{\sum\!\!\!\!\!\!\!\int}_{\lambda} \left[\mathbf{L}^j_\lambda(\mathbf{r}) \otimes \mathbf{c}_{L,\lambda}(\mathbf{r}') + \mathbf{M}^j_\lambda(\mathbf{r}) \otimes \mathbf{c}_{M,\lambda}(\mathbf{r}') + \mathbf{N}^j_\lambda(\mathbf{r}) \otimes \mathbf{c}_{N,\lambda}(\mathbf{r}')\right]. \tag{A.15}$$

Finally, we must determine expansion coefficients $\mathbf{c}_{L/N/M,\lambda}(\mathbf{r})$ such that $\boldsymbol{G}(\mathbf{r},\mathbf{r}',\omega)$ obeys the boundary conditions to obtain the unique solution of the vector Helmholtz equation.

In our planar geometry, the scalar Helmholtz equation is solved by plane waves

$$\psi^j_{\mathbf{k}\pm}(\mathbf{r}) = e^{i\mathbf{k}_{j,\pm}\cdot\mathbf{r}} = e^{i\mathbf{k}^{\|}\cdot\mathbf{r}\pm k_j^{\perp}z}. \tag{A.16}$$

We decompose the wave vector into components parallel and orthogonal to the surface, $\mathbf{k}_j = \mathbf{k}^{\|} + \mathbf{k}_j^{\perp}$, and distinguish forward and backward propagating waves, $\psi^j_{\mathbf{k}+}(\mathbf{r})$ and $\psi^j_{\mathbf{k}-}(\mathbf{r})$, respectively. Next, we introduce a basis of s (perpendicular = German "senkrecht") and p (parallel = German "parallel") polarized plane waves

$$\mathbf{e}^j_{s\pm} = \mathbf{e}_{k^{\|}} \times \mathbf{e}_z, \quad \mathbf{e}^j_{p\pm} = \frac{1}{k_j}(k^{\|}\mathbf{e}_z \mp k_j^{\perp}\mathbf{e}_{k^{\|}}). \tag{A.17}$$

Together with the vector $\mathbf{e}^j_{\mathbf{k}\pm} = (k^{\|}\mathbf{e}_{k^{\|}} \pm k_j^{\perp}\mathbf{e}_z)/k_j$, the vectors $(\mathbf{e}^j_{p\pm}, \mathbf{e}^j_{s\pm}, \mathbf{e}^j_{\mathbf{k}\pm})$ form an orthogonal right-handed coordinate system (see Fig. A.2). Choosing the pilot vector as $\mathbf{c} = \mathbf{e}_z$ [86],

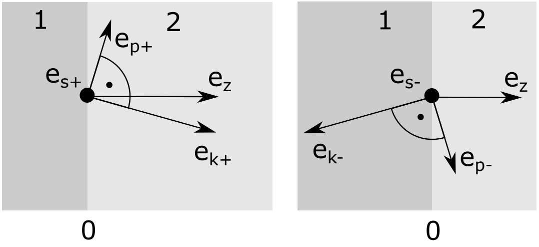

Figure A.2: Right-handed coordinate system of $(\mathbf{e}^j_{p+}, \mathbf{e}^j_{s+}, \mathbf{e}^j_{\mathbf{k}+})$ and $(\mathbf{e}^j_{p-}, \mathbf{e}^j_{s-}, \mathbf{e}^j_{\mathbf{k}-})$.

the VWFs (A.13) become [51]

$$\mathbf{M}^j_{\mathbf{k}\pm}(\mathbf{r}) = ik^{\parallel}\mathbf{e}^j_{s\pm}e^{i\mathbf{k}^{\parallel}\cdot\mathbf{r}\pm k^{\perp}_j z} = ik^{\parallel}\tilde{\mathbf{M}}^j_{\mathbf{k}\pm}(\mathbf{r}), \tag{A.18}$$

$$\mathbf{N}^j_{\mathbf{k}\pm}(\mathbf{r}) = k^{\parallel}\mathbf{e}^j_{p\pm}e^{i\mathbf{k}^{\parallel}\cdot\mathbf{r}\pm k^{\perp}_j z} = k^{\parallel}\tilde{\mathbf{N}}^j_{\mathbf{k}\pm}(\mathbf{r}). \tag{A.19}$$

It is convenient to switch to renormalized VWFs $\tilde{\mathbf{M}}^j_{\mathbf{k}\pm}(\mathbf{r})$, $\tilde{\mathbf{N}}^j_{\mathbf{k}\pm}(\mathbf{r})$ with renormalized expansion coefficients $\tilde{\mathbf{c}}_{M/N,\lambda}(\mathbf{r})$ [51]. Here we do not require the $\mathbf{L}^j_{\lambda}(\mathbf{r})$ functions as there are no external sources and currents in our problem that would produce curl-free fields.

Next, we express the bulk Green's tensor with VWFs. Invoking a Fourier transformation, the scalar Green's function of the bulk medium, Eq. (A.6), can be rewritten as [51]

$$g(\mathbf{r},\mathbf{r}',\omega) = \frac{1}{8\pi^3}\int d^3\mathbf{k}'\frac{e^{i\mathbf{k}'\cdot(\mathbf{r}-\mathbf{r}')}}{k'^2 - k_j^2} = \frac{i}{8\pi^2}\int d^2\mathbf{k}^{\parallel}\frac{e^{i\mathbf{k}^{\parallel}\cdot(\mathbf{r}-\mathbf{r}')+ik^{\perp}_j|z-z'|}}{k^{\perp}_j}. \tag{A.20}$$

Since $\partial_z|z| = \Theta(z) - \Theta(-z)$ and $\partial_z^2|z| = 2\delta(z)$, the bulk Green's tensor (A.5) becomes [51, 216]

$$\begin{aligned}\boldsymbol{G}_{\text{bulk}}(\mathbf{r},\mathbf{r}',\omega) = &-\frac{\mathbf{e}_z\otimes\mathbf{e}_z}{k_j^2}\delta(\mathbf{r}-\mathbf{r}') + \frac{i}{8\pi^2}\int d^2\mathbf{k}^{\parallel}\frac{e^{i\mathbf{k}^{\parallel}\cdot(\mathbf{r}-\mathbf{r}')}}{k^{\perp}_j}\\ &\times\sum_{\sigma=s,p}\Big\{\mathbf{e}^j_{\sigma+}\otimes\mathbf{e}^j_{\sigma+}e^{ik^{\perp}_j(z-z')}\Theta(z-z') + \mathbf{e}^j_{\sigma-}\otimes\mathbf{e}^j_{\sigma-}e^{-ik^{\perp}_j(z-z')}\Theta(z'-z)\Big\}.\end{aligned} \tag{A.21}$$

The singular term corresponds to the one for a disk-shaped exclusion volume [86, 165]. It differs from the singular term in Eq. (A.8) that applies to a spherical exclusion volume. However, the trace is the same in both cases, as it is independent of the shape of the exclusion volume [165]. We can read off the expansion coefficients from Eq. (A.21)

$$\tilde{\mathbf{c}}_{M/N,\mathbf{k}\pm}(\mathbf{r}') = \frac{i}{8\pi^2 k^{\perp}_j}\mathbf{e}^j_{s/p\pm}e^{-(i\mathbf{k}^{\parallel}\cdot\mathbf{r}'\pm k^{\perp}_j z')}. \tag{A.22}$$

Eq. (A.21) has a straightforward interpretation: When $z > z'$ ($z < z'$), a forward (backward) propagating s- or p-polarized plane wave is leaving from $\mathbf{r}'$ and arriving at $\mathbf{r}$ as a forward (backward) propagating s- or p-polarized wave. With this physical intuition and the known form of the expansion coefficients, we can infer Green's tensor for a surface with $z' > 0$, $z' > z$

from the possible photon paths in Fig. A.4 a [51]

$$\boldsymbol{G}_{\mathrm{surf}}(\mathbf{r},\mathbf{r}',\omega)=\begin{cases}\frac{i}{8\pi^2}\int d^2\mathbf{k}^{\parallel}\frac{e^{i\mathbf{k}^{\parallel}\cdot(\mathbf{r}-\mathbf{r}')}}{k_2^{\perp}}\sum_{\sigma=s,p}r_\sigma^{21}\mathbf{e}^2_{\sigma+}\otimes\mathbf{e}^2_{\sigma-}e^{ik_2^{\perp}(z+z')}, & z>0,\\ \frac{i}{8\pi^2}\int d^2\mathbf{k}^{\parallel}\frac{e^{i\mathbf{k}^{\parallel}\cdot(\mathbf{r}-\mathbf{r}')}}{k_2^{\perp}}\sum_{\sigma=s,p}t_\sigma^{21}\mathbf{e}^1_{\sigma-}\otimes\mathbf{e}^2_{\sigma-}e^{-ik_1^{\perp}z+ik_2^{\perp}z'}, & z<0.\end{cases}\tag{A.23}$$

The coefficients r_σ^{21} and t_σ^{21} describe reflection and transmission. The total Green's tensor for the surface geometry is

$$\boldsymbol{G}(\mathbf{r},\mathbf{r}',\omega)=\boldsymbol{G}_{\mathrm{surf}}(\mathbf{r},\mathbf{r}',\omega)+\Theta(z)\frac{i}{8\pi^2}\int d^2\mathbf{k}^{\parallel}\frac{e^{i\mathbf{k}^{\parallel}\cdot(\mathbf{r}-\mathbf{r}')}}{k_2^{\perp}}\sum_{\sigma=s,p}\mathbf{e}^2_{\sigma-}\otimes\mathbf{e}^2_{\sigma-}e^{ik_2^{\perp}(-z+z')}.\tag{A.24}$$

A.3.2. Boundary conditions and Fresnel reflection coefficients

We can now determine reflection and transmission coefficients through boundary conditions. Let us consider a point $\mathbf{r}$ at the boundary between layers 1 and 2 in a surface geometry, see Fig. A.4 a. We define $\mathbf{r}_{1,2}=\lim_{h\to 0}\mathbf{r}\pm h\mathbf{e}_\perp$ and $\mathbf{e}_{\parallel}$ ($\mathbf{e}_\perp$) as a unit vector parallel (perpendicular) to the interface of layers 1 and 2. Also, we assume that the source point of the Green's tensor is not on the boundary. At the interface, the tangential components of $\mathbf{E}(\mathbf{r})$ and $\mathbf{B}(\mathbf{r})$ and (in absence of external sources and currents) the normal components of $\mathbf{D}(\mathbf{r})$ and $\mathbf{H}(\mathbf{r})$ must be steady. Therefore, the Green's tensor must obey [51]:

$$\mathbf{e}_{\parallel}\cdot\left[\boldsymbol{G}(\mathbf{r}_1,\mathbf{r}',\omega)-\boldsymbol{G}(\mathbf{r}_2,\mathbf{r}',\omega)\right]=\mathbf{0}^T,\tag{A.25}$$

$$\mathbf{e}_{\parallel}\cdot\left[\boldsymbol{\nabla}\times\boldsymbol{G}(\mathbf{r}_1,\mathbf{r}',\omega)-\boldsymbol{\nabla}\times\boldsymbol{G}(\mathbf{r}_2,\mathbf{r}',\omega)\right]=\mathbf{0}^T,\tag{A.26}$$

$$\mathbf{e}_{\perp}\cdot\left[\epsilon_1(\omega)\boldsymbol{G}(\mathbf{r}_1,\mathbf{r}',\omega)-\epsilon_2(\omega)\boldsymbol{G}(\mathbf{r}_2,\mathbf{r}',\omega)\right]=\mathbf{0}^T,\tag{A.27}$$

$$\mathbf{e}_{\perp}\cdot\left[\boldsymbol{\nabla}\times\boldsymbol{G}(\mathbf{r}_1,\mathbf{r}',\omega)-\boldsymbol{\nabla}\times\boldsymbol{G}(\mathbf{r}_2,\mathbf{r}',\omega)\right]=\mathbf{0}^T.\tag{A.28}$$

Using $\boldsymbol{\nabla}\times\tilde{\mathbf{M}}^j_{\mathbf{k}\pm}(\mathbf{r})=-ik_j\tilde{\mathbf{N}}^j_{\mathbf{k}\pm}(\mathbf{r})$ and $\boldsymbol{\nabla}\times\tilde{\mathbf{N}}^j_{\mathbf{k}\pm}(\mathbf{r})=ik_j\tilde{\mathbf{M}}^j_{\mathbf{k}\pm}(\mathbf{r})$, we obtain six conditions [51]:

$$\text{Eq. (A.25) with } \mathbf{e}_{\parallel}=\mathbf{e}_s: \quad 1+r_s^{21}=t_s^{21},\tag{A.29}$$

$$\text{Eq. (A.25) with } \mathbf{e}_{\parallel}=\mathbf{e}_{\mathbf{k}^{\parallel}}: \quad \frac{k_2^{\perp}}{k_2}(1-r_p^{21})=\frac{k_1^{\perp}}{k_1}t_p^{21},\tag{A.30}$$

$$\text{Eq. (A.26) with } \mathbf{e}_{\parallel}=\mathbf{e}_s: \quad k_2(1+r_p^{21})=k_1t_p^{21},\tag{A.31}$$

$$\text{Eq. (A.26) with } \mathbf{e}_{\parallel}=\mathbf{e}_{\mathbf{k}^{\parallel}}: \quad k_2^{\perp}(1-r_s^{21})=k_1^{\perp}t_p^{21},\tag{A.32}$$

$$\text{Eq. (A.27) with } \mathbf{e}_{\perp}=\mathbf{e}_z: \quad \frac{\epsilon_2}{k_2}(1+r_p^{21})=\frac{\epsilon_1}{k_1}t_p^{21},\tag{A.33}$$

$$\text{Eq. (A.28) with } \mathbf{e}_{\perp}=\mathbf{e}_z: \quad 1+r_s^{21}=t_s^{21}.\tag{A.34}$$

They are simultaneously fulfilled by the standard Fresnel coefficients [51, 138]

$$r_s^{21} = \frac{k_2^\perp - k_1^\perp}{k_2^\perp + k_1^\perp}, \quad r_p^{21} = \frac{\epsilon_1 k_2^\perp - \epsilon_2 k_1^\perp}{\epsilon_1 k_2^\perp + \epsilon_2 k_1^\perp}, \tag{A.35}$$

$$t_s^{21} = \frac{2k_2^\perp}{k_2^\perp + k_1^\perp}, \quad t_p^{21} = \frac{k_1}{k_2}\frac{2\epsilon_2 k_2^\perp}{\epsilon_1 k_2^\perp + \epsilon_2 k_1^\perp}. \tag{A.36}$$

In the main text, we also require coefficients for multilayer interfaces. We can infer them from the two-layer coefficients, that will now be denoted $\tilde{r}_\sigma^{j+1,j}$ and $\tilde{t}_\sigma^{j+1,j}$ by means of a recursion relation [51]. By summing up the multiple reflection photon pathways in Fig. A.3, we obtain the reflection coefficient between layers $j+1$ and j, $r_\sigma^{j+1,j}$, from the reflection coefficient of previous interface $r_\sigma^{j,j-1}$ as

$$\begin{aligned} r_\sigma^{j+1,j} &= \tilde{r}_\sigma^{j+1,j} + \tilde{t}_\sigma^{j+1,j} e^{ik_j^\perp w_j} r_\sigma^{j,j-1} e^{ik_j^\perp w_j} \tilde{t}_\sigma^{j,j+1} \sum_{k=0}^{\infty} \left(\tilde{r}_\sigma^{j,j+1} r_\sigma^{j,j-1} e^{2ik_j^\perp w_j}\right)^k \\ &= \frac{\tilde{r}_\sigma^{j+1,j} + \left(\tilde{t}_\sigma^{j+1,j}\tilde{t}_\sigma^{j,j+1} - \tilde{r}_\sigma^{j+1,j}\tilde{r}_\sigma^{j,j+1}\right) r_\sigma^{j,j-1} e^{2ik_j^\perp w_j}}{1 - \tilde{r}_\sigma^{j,j+1} r_\sigma^{j,j-1} e^{2ik_j^\perp w_j}} = \frac{\tilde{r}_\sigma^{j+1,j} + r_\sigma^{j,j-1} e^{2ik_j^\perp w_j}}{1 - \tilde{r}_\sigma^{j,j+1} r_\sigma^{j,j-1} e^{2ik_j^\perp w_j}}. \end{aligned} \tag{A.37}$$

.

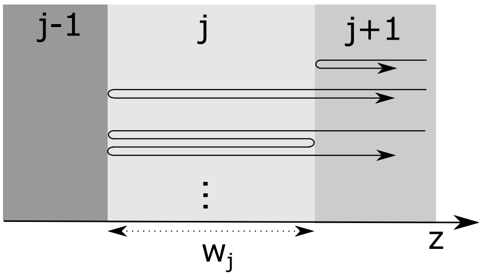

Figure A.3: Photon pathways to determine the effective reflection coefficient of a multilayer interface. Multiple internal reflections lead to a geometric sum.

A.3.3. Surface and cavity Green's tensors

The Green's tensor for the cavity in Fig. A.4 b can be constructed analogously to Eq. (A.23). With $0 \leq z, z' \leq w$ we find [51]

$$\begin{aligned} \boldsymbol{G}_{\mathrm{cav}}(\mathbf{r}, \mathbf{r}', \omega) &= \frac{i}{8\pi^2} \int d^2\mathbf{k}^\parallel \, \frac{e^{i\mathbf{k}^\parallel \cdot (\mathbf{r}-\mathbf{r}')}}{k_2^\perp} \sum_{\sigma=s,p} \Bigg(\frac{(r_\sigma^{21})^2 e^{ik_2^\perp (2w+z-z')}}{D_\sigma} \mathbf{e}_{\sigma+}^2 \otimes \mathbf{e}_{\sigma+}^2 + \mathbf{e}_{\sigma-}^2 \otimes \mathbf{e}_{\sigma+}^2 \\ &\times \frac{r_\sigma^{21} e^{ik_2^\perp (2w-z-z')}}{D_\sigma} + \frac{r_\sigma^{21} e^{ik_2^\perp (z'+z)}}{D_\sigma} \mathbf{e}_{\sigma+}^2 \otimes \mathbf{e}_{\sigma-}^2 + \frac{(r_\sigma^{21})^2 e^{ik_2^\perp (2w-z+z')}}{D_\sigma} \mathbf{e}_{\sigma-}^2 \otimes \mathbf{e}_{\sigma-}^2 \Bigg), \end{aligned} \tag{A.38}$$

where $D_\sigma = 1 - (r_\sigma^{21})^2 e^{2iwk_2^\perp}$. To evaluate this expression, we transform into a convenient coordinate system in which the source is located at $\mathbf{r}_2 = (0, 0, z_2)$ and the receiver at $\mathbf{r}_1 = (x, 0, z_1)$.

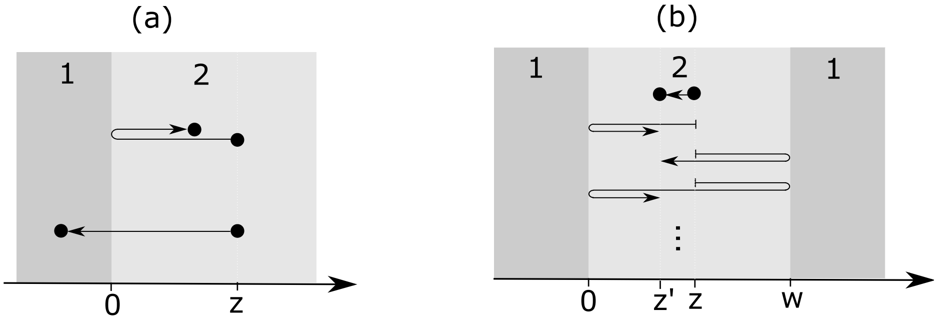

Figure A.4: Photon pathways in (a) a surface and (b) a cavity geometry. The Green's tensor can be constructed by examining the direction of the outgoing and incoming waves at the source point and the receiver point, respectively. Reflections and transmissions give rise to factors of r_σ^{21} and t_σ^{21}, respectively. The four pathways in the cavity are followed by multiple internal reflections leading to a geometric sum, $\sum_{n=0}^{\infty}[(r_\sigma^{21})^2 e^{2iwk_2^\perp}]^n$.

We define the distance $x=\sqrt{(x_1-x_2)^2+(y_1-y_2)^2}$ and the angle $\cos\varphi=(x_1-x_2)/x$ to the x-axis. Using the cylindrical symmetry of our planar geometry, we can express the Green's tensor $\boldsymbol{G}_{\text{cav}}(\mathbf{r}_1,\mathbf{r}_2,\omega)$ by the Green's tensor in our new coordinate system $\boldsymbol{G}_{\text{cav}}(x,z_1,z_2,\omega)$ through a rotation

$$\boldsymbol{G}_{\text{cav}}(\mathbf{r}_1,\mathbf{r}_2,\omega)=\boldsymbol{G}_{\text{cav}}(x,\varphi,z_1,z_2,\omega)=\boldsymbol{R}^T(\varphi)\boldsymbol{G}_{\text{cav}}(x,z_1,z_2,\omega)\boldsymbol{R}(\varphi), \tag{A.39}$$

$$\boldsymbol{R}(\varphi)=\begin{pmatrix}\cos\varphi & -\sin\varphi & 0\\ \sin\varphi & \cos\varphi & 0\\ 0 & 0 & 1\end{pmatrix}. \tag{A.40}$$

Using cylindrical coordinates for the wave vector $\mathbf{k}^{\|}=k^{\|}(\cos\varphi_k,\sin\varphi_k,0)^T$, the $\mathbf{e}_{\sigma\pm}^j$ basis vectors according to Eq. (A.17) become

$$\mathbf{e}_{s\pm}^j=(\sin\varphi_k,-\cos\varphi_k,0)^T,\quad \mathbf{e}_{p\pm}^j=\frac{1}{k_j}(\mp k_j^\perp\cos\varphi_k,\mp k_j^\perp\sin\varphi_k,k^{\|})^T. \tag{A.41}$$

Hence, the Green's tensor $\boldsymbol{G}_{\text{cav}}(x,z_1,z_2,\omega)$ is

$$\begin{aligned}&\boldsymbol{G}_{\text{cav}}(x,z_1,z_2,\omega)\\&=\frac{i}{8\pi^2}\int_0^\infty dk^{\|}\,\frac{k^{\|}}{k_2^\perp}\int_0^{2\pi}d\varphi_k\,e^{ik^{\|}x\cos\varphi_k}\sum_{\sigma=s,p}\left(\frac{(r_\sigma^{21})^2e^{ik_2^\perp(2w+z_1-z_2)}}{D_\sigma}\mathbf{e}_{\sigma+}^2\otimes\mathbf{e}_{\sigma+}^2+\mathbf{e}_{\sigma-}^2\otimes\mathbf{e}_{\sigma+}^2\right.\\&\left.\times\frac{r_\sigma^{21}e^{ik_2^\perp(2w-z_1-z_2)}}{D_\sigma}+\frac{r_\sigma^{21}e^{ik_2^\perp(z_2+z_1)}}{D_\sigma}\mathbf{e}_{\sigma+}^2\otimes\mathbf{e}_{\sigma-}^2+\frac{(r_\sigma^{21})^2e^{ik_2^\perp(2w-z_1+z_2)}}{D_\sigma}\mathbf{e}_{\sigma-}^2\otimes\mathbf{e}_{\sigma-}^2\right),\end{aligned} \tag{A.42}$$

The integral over φ_k leads to the cylindrical Bessel functions [183]

$$J_n(x) = \frac{1}{2\pi i^n}\int_0^{2\pi} d\varphi\, e^{ix\cos\varphi}\cos(n\varphi). \tag{A.43}$$

Eventually, the cavity Green's tensor takes the form

$$\boldsymbol{G}_{\text{cav}}(x,z_1,z_2,\omega) = \int_0^\infty dk^{\|}\,\frac{ik^{\|}}{8\pi k_2^{\perp}}\begin{pmatrix} I_{1+} & 0 & I_{3+} \\ 0 & I_{1-} & 0 \\ I_{3-} & 0 & I_2 \end{pmatrix}, \tag{A.44}$$

$$I_{1\pm} = \left[J_0(xk^{\|}) \pm J_2(xk^{\|})\right] T_1 + \left[J_0(xk^{\|}) \mp J_2(xk^{\|})\right][T_2 - T_4], \tag{A.45}$$

$$I_2 = 2\left(\frac{k^{\|}}{k_2^{\perp}}\right)^2 J_0(xk^{\|})\,[T_2 + T_4], \quad I_{3\pm} = -2iJ_1(xk^{\|})\,[T_3 \pm T_5], \tag{A.46}$$

where

$$T_1 = \frac{r_s^{21}}{D_s}\left[r_s^{21}\left(e^{i(2d+z_1-z_2)k_2^{\perp}} + e^{i(2d-z_1+z_2)k_2^{\perp}}\right) + \left(e^{i(z_1+z_2)k_2^{\perp}} + e^{i(2d-z_1-z_2)k_2^{\perp}}\right)\right], \tag{A.47}$$

$$T_2 = \frac{(k_2^{\perp} r_p^{21})^2}{k_2^2 D_p}\left(e^{i(2d+z_1-z_2)k_2^{\perp}} + e^{i(2d-z_1+z_2)k_2^{\perp}}\right), \tag{A.48}$$

$$T_3 = \frac{k_2^{\perp}k^{\|}(r_p^{21})^2}{k_2^2 D_p}\left(e^{i(2d+z_1-z_2)k_2^{\perp}} - e^{i(2d-z_1+z_2)k_2^{\perp}}\right), \tag{A.49}$$

$$T_4 = \frac{(k_2^{\perp})^2 r_p^{21}}{k_2^2 D_p}\left(e^{i(z_1+z_2)k_2^{\perp}} + e^{i(2d-z_1-z_2)k_2^{\perp}}\right), \tag{A.50}$$

$$T_5 = \frac{k_2^{\perp}k^{\|} r_p^{21}}{k_2^2 D_p}\left(e^{i(z_1+z_2)k_2^{\perp}} - e^{i(2d-z_1-z_2)k_2^{\perp}}\right). \tag{A.51}$$

Analogously, we obtain the surface Green's tensor as

$$\boldsymbol{G}_{\text{surf}}(x,z_1+z_2,\omega) = \int_0^\infty dk^{\|}\,\frac{ik^{\|}}{8\pi k_2^{\perp}}e^{ik_2^{\perp}(z_1+z_2)}\begin{pmatrix} I_{1+} & 0 & I_3 \\ 0 & I_{1-} & 0 \\ -I_3 & 0 & I_2 \end{pmatrix}, \tag{A.52}$$

$$I_{1\pm} = \left[J_0(xk^{\|}) \pm J_2(xk^{\|})\right] r_s^{21} - \frac{r_p^{21}(k_2^{\perp})^2}{k_2^2}\left[J_0(xk^{\|}) \mp J_2(xk^{\|})\right], \tag{A.53}$$

$$I_2 = 2\frac{r_p^{21}(k^{\|})^2}{k_2^2}J_0(xk^{\|}), \quad I_3 = -2i\frac{k^{\|}k_2^{\perp}r_p^{21}}{k_2^2}J_1(xk^{\|}). \tag{A.54}$$

In general, the remaining integral over $k^{\|}$ can only be solved numerically. For purely imaginary frequencies, the numerical integration is straightforward. For real frequencies, however, a complex integration contour must be used to avoid poles between $0 \leq k^{\|} \leq \max_j \operatorname{Re}(k_j)$ that lie close to the real axis [217]. For this purpose, we utilize a simple third order polynomial in the range between $0 \leq k^{\|} \leq k^R$

$$\tilde{k}^{\|} = k^{\|} - ik^I \frac{8}{3}\left[\frac{k^{\|}}{k^R} - \left(\frac{k^{\|}}{k^R}\right)^3\right], \quad k^R = \frac{\omega}{c} + \max_j \mathrm{Re}\,(k_j), \quad k^I = \min\left(\frac{k^R}{10}, \frac{10}{x}\right), \tag{A.55}$$

whose imaginary part reaches a minimum of around $-ik^I$. The expression for k^R includes a safety margin of ω/c [217]. The value of k^I must be capped for large x because the exponential behavior of Bessel functions $J_n(\pm ik^I x)$ with imaginary arguments. Optionally, for $k^{\|} \geq k^R$, one can use another integration contour with a positive imaginary part or even a contour parallel to the imaginary axis [217] to speed up convergence.

A.4. The uniaxial birefringent surface

We give the Green's tensor for a uniaxial birefringent surface interfaced with a vacuum. Assuming that probe and source points are located in the vacuum region ($z, z' > 0$), the Green's tensor, analogously to Eq. (A.23), takes the form

$$\boldsymbol{G}_{\mathrm{bisurf}}(\mathbf{r}, \mathbf{r}', \omega) = \frac{i}{8\pi^2}\int d^2\mathbf{k}^{\|}\,\frac{e^{i\mathbf{k}^{\|}\cdot(\mathbf{r}-\mathbf{r}')}}{k_2^{\perp}} \sum_{\sigma_1=s,p}\;\sum_{\sigma_2=s,p} r^{21}_{\sigma_1\sigma_2}\mathbf{e}^2_{\sigma_1+} \otimes \mathbf{e}^2_{\sigma_2-} e^{ik_2^{\perp}(z+z')}. \tag{A.56}$$

We assume that the optical axis is perpendicular to the surface, which implies a permittivity tensor $\boldsymbol{\epsilon}_1 = \mathrm{diag}(\epsilon^{\|}, \epsilon^{\|}, \epsilon^{\perp})$ where $\epsilon^{\|}$ is the permittivity of the ordinary and $\epsilon^{\perp}$ the permittivity of the extraordinary ray. Since our permittivity tensor is diagonal, the plane waves do not change their polarization upon reflection and $r^{21}_{ps} = r^{21}_{sp} = 0$ [218]. As a result, the Green's tensor of the birefringent surface is almost the same as for the isotropic surface except for the new reflection coefficients [218, 219]

$$r^{21}_{ss} = \frac{k^{\perp}_{s,2} - k^{\perp}_{s,1}}{k^{\perp}_{s,2} - k^{\perp}_{s,1}}, \quad r^{21}_{pp} = \frac{k^{\perp}_{p,2}\epsilon^{\|}_1 - k^{\perp}_{p,1}\epsilon^{\|}_2}{k^{\perp}_{p,2}\epsilon^{\|}_1 + k^{\perp}_{p,1}\epsilon^{\|}_2}, \tag{A.57}$$

where the z components of wave vectors for the p and s waves are given by

$$k^{\perp}_{s,i} = \sqrt{\frac{\omega^2}{c^2}\epsilon^{\|}_i - \left(k^{\|}\right)^2}, \quad k^{\perp}_{p,i} = \sqrt{\frac{\omega^2}{c^2}\epsilon^{\|}_i - \frac{\epsilon^{\|}_i}{\epsilon^{\perp}_i}\left(k^{\|}\right)^2}. \tag{A.58}$$

Naturally, for vacuum $k^{\perp}_{s,2} = k^{\perp}_{p,2} = k^{\perp}_2 = \sqrt{\omega^2/c^2 - (k^{\|})^2}$. For a dielectric surface in the static limit $\omega \to 0$, we have $k^{\perp}_2, k^{\perp}_{s,1} \to ik^{\|}$ and $k^{\perp}_{s,1} \to i\sqrt{\epsilon^{\|}_i/\epsilon^{\perp}_i}k^{\|}$ such that the reflection coefficients become

$$r^{21}_{ss} \to 0, \quad r^{21}_{pp} \to \frac{\sqrt{\epsilon^{\|}_1\epsilon^{\perp}_1} - 1}{\sqrt{\epsilon^{\|}_1\epsilon^{\perp}_1} + 1}. \tag{A.59}$$

This is the image dipole factor (see App. A.2) of an interface between vacuum and an isotropic surface whose permittivity is the geometric mean $\sqrt{\epsilon_1^{\|}\epsilon_1^{\perp}}$ of the ordinary and extraordinary permittivity. The static Green's tensor of a birefringent surface is therefore same as the static Green's tensor of an isotropic surface with permittivity $\sqrt{\epsilon_1^{\|}\epsilon_1^{\perp}}$ [163, 218].

A.5. Cylindrical symmetry and 1-D Green's function

We compute integrals of type $\int dA' \boldsymbol{G}(\mathbf{r}, \mathbf{r}', \omega)$ where A' is an infinite plane parallel to our planar interfaces. We start by applying the integral to the Helmholtz equation (2.18),

$$\int dA' \left[\Delta \boldsymbol{I} - \boldsymbol{\nabla} \otimes \boldsymbol{\nabla} + k^2(z)\right] \boldsymbol{G}(\mathbf{r}, \mathbf{r}', \omega) = -\int dA' \boldsymbol{I} \delta(\mathbf{r} - \mathbf{r}') = -\boldsymbol{I} \delta(z - z'), \tag{A.60}$$

where $k^2(z) = \epsilon(z, \omega)\omega^2/c^2$. Because of the cylindrical symmetry, the Green's tensor can be written in cylindrical coordinates as

$$\boldsymbol{G}(\mathbf{r}, \mathbf{r}', \omega) = \boldsymbol{R}^T(\varphi) \begin{pmatrix} G_{xx}(0, \rho, z, z', \omega) & 0 & G_{xz}(0, \rho, z, z', \omega) \\ 0 & G_{yy}(0, \rho, z, z', \omega) & 0 \\ G_{zx}(0, \rho, z, z', \omega) & 0 & G_{zz}(0, \rho, z, z', \omega) \end{pmatrix} \boldsymbol{R}(\varphi), \tag{A.61}$$

where the rotation matrix is given by Eq. (A.40). We can conduct the ρ and φ integrals of Eq. (A.60) by recalling that $\boldsymbol{\nabla} = \mathbf{e}_\rho \partial_\rho + \frac{1}{\rho}\mathbf{e}_\varphi \partial_\varphi + \mathbf{e}_z \partial_z$ and by using the radiation boundary condition that the Green's tensor vanishes for $\rho \to \infty$. We find that the integrated tensor is of diagonal form

$$\int dA' \boldsymbol{G}(\mathbf{r}, \mathbf{r}', \omega) = \mathrm{diag}(G^{1\mathrm{D}}(z, z', \omega), G^{1\mathrm{D}}(z, z', \omega), G^{\perp}(z, z', \omega)). \tag{A.62}$$

The scalar entries are the solution of the 1-D Helmholtz equation

$$[\partial_z^2 + k^2(z)] G^{1\mathrm{D}}(z, z', \omega) = -\delta(z - z'), \tag{A.63}$$

and a rescaled delta function $G^{\perp}(z, z', \omega) = -\delta(z - z')/k^2(z)$. In a bulk medium, the 1-D Green's function is

$$G^{1\mathrm{D}}_{\mathrm{bulk}}(z, z', \omega) = \frac{i}{2k} e^{ik|z - z'|}, \tag{A.64}$$

as one can quickly validate by inserting into Eq. (A.63). The 1-D Green's functions are simple planar waves propagators. Using the Fresnel reflection and transmission coefficients for normal incidence, one can infer the 1-D Green's function from a sketch of the wave's propagation path. In Fig. A.5, we show the pathways out of the cavity and can immediately specify the

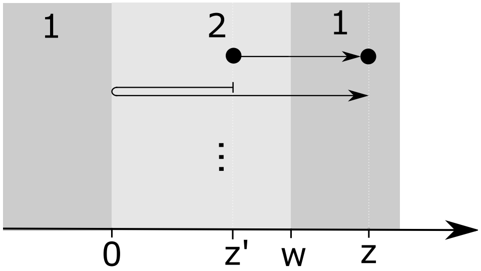

Figure A.5: Photon pathways starting inside and ending outside of the cavity. The two pathways are followed by multiple internal reflections leading to a geometric sum, $\sum_{n=0}^{\infty}[(r^{21})^2 e^{2iwk_2}]^n$.

corresponding Green's function as

$$G^{\mathrm{1D}}_{\mathrm{cav,out}}(z,z',\omega) = \frac{it_{21}}{2k_2}\frac{e^{ik_2(w-z')+ik_1(z-w)} + r_{21}e^{ik_2(w+z')+ik_1(z-w)}}{1-r_{21}^2 e^{2ik_2 w}}. \tag{A.65}$$

For two points inside of the cavity (see Fig. A.4 b), we have a total Green's function of

$$G^{\mathrm{1D}}_{\mathrm{in}}(z,z',\omega) = G^{\mathrm{1D}}_{\mathrm{bulk}}(z,z',\omega) + G^{\mathrm{1D}}_{\mathrm{cav}}(z,z',\omega) \tag{A.66}$$

$$= \frac{i}{2k_2}\frac{e^{ik_2|z-z'|} + r_{21}e^{ik_2(z+z')} + r_{21}e^{ik_2(2w-z-z')} + r_{21}^2 e^{ik_2(2w-|z-z'|)}}{1-r_{21}^2 e^{2ik_2 w}}. \tag{A.67}$$

Instead of starting over from the Helmholtz equation, one can also integrate an explicit expression for the Green's tensor. Ref. [220] follows that path to derive Eq. (A.64) from Eq. (A.8). However, this approach is often more cumbersome and less general.

A.6. The discrete dipole approximation

In this section, we present the discrete dipole approximation (DDA) [87] in more detail. In the following, we drop the frequency argument ω for brevity. We discretize Eq. (2.36) and set the permittivity χ_j to the volume average within the respective cell j

$$\boldsymbol{G}(\mathbf{r}_i,\mathbf{r}') = \bar{\boldsymbol{G}}(\mathbf{r}_i,\mathbf{r}') + \sum_j^N \left(\int_{V_j} \mathrm{d}^3\mathbf{s}\,\bar{\boldsymbol{G}}(\mathbf{r}_i,\mathbf{s})\right)\frac{\omega^2}{c^2}\chi_j \boldsymbol{G}(\mathbf{r}_j,\mathbf{r}'). \tag{A.68}$$

Our background Green's tensor decomposes into the bulk and scattering contribution, $\bar{\boldsymbol{G}}(\mathbf{r},\mathbf{r}') = \bar{\boldsymbol{G}}_{\mathrm{bulk}}(\mathbf{r},\mathbf{r}') + \bar{\boldsymbol{G}}_{\mathrm{sc}}(\mathbf{r},\mathbf{r}')$. We treat the volume integral by a point-like approximation[1] and obtain

$$\int_{V_j} \mathrm{d}^3\mathbf{r}'\,\frac{\omega^2}{c^2}\bar{\boldsymbol{G}}(\mathbf{r}_i,\mathbf{r}') \approx \begin{cases} V_j\frac{\omega^2}{c^2}\bar{\boldsymbol{G}}(\mathbf{r}_i,\mathbf{r}_j), & i\neq j \\ (\boldsymbol{M}_i - \boldsymbol{L}_i) + V_i\frac{\omega^2}{c^2}\bar{\boldsymbol{G}}_{\mathrm{sc}}(\mathbf{r}_i,\mathbf{r}_i), & i=j \end{cases}. \tag{A.69}$$

---

[1] A more precise but also more complex treatment of the volume integral is given in Ref. [221].

The terms $\boldsymbol{L}_i$ and $\boldsymbol{M}_i$ account for the singularity in the Green's tensor and describe finite-size effects of the unit cells [87]. For cubes with edge length w, one can find simple analytic expressions for $\boldsymbol{L}_i$ [165] and $\boldsymbol{M}_i$ [222, 223], leading to the so-called LAK model [87]

$$\boldsymbol{L}_i = \frac{1}{3}\boldsymbol{I}, \quad \boldsymbol{M}_i = \frac{2}{3}\boldsymbol{I}\left[(1 - i\bar{k}_i a)e^{i\bar{k}_i a} - 1\right], \tag{A.70}$$

where $\bar{k}_i = \frac{\omega^2}{c^2}\bar{\epsilon}(\mathbf{r}_i)$ and $a = w\left(\frac{3}{4\pi}\right)^{1/3}$ is the equivalent radius of a sphere. Next, we introduce the local-field corrected Green's tensor and a pseudo-polarizability

$$\boldsymbol{G}^{\mathrm{loc}}(\mathbf{r}_i, \mathbf{r}') = \left[\boldsymbol{I} + (\boldsymbol{L}_{\boldsymbol{i}} - \boldsymbol{M}_{\boldsymbol{i}})\chi_i\right]\boldsymbol{G}(\mathbf{r}_i, \mathbf{r}'), \tag{A.71}$$

$$\boldsymbol{\alpha}_i = \chi_i V_i \left[\boldsymbol{I} + (\boldsymbol{L}_{\boldsymbol{i}} - \boldsymbol{M}_{\boldsymbol{i}})\chi_i\right]^{-1}. \tag{A.72}$$

An important special case arises when finite size effects can be neglected, $\boldsymbol{M}_{\boldsymbol{i}} = \boldsymbol{0}$, and we replace $\chi_i \to \tilde{\epsilon}_i - 1$. The pseudo-polarizability, $\boldsymbol{\alpha}_i = 3V_i\frac{\epsilon_i - 1}{\epsilon_i + 2}$, transitions to the well-known Clausius–Mossotti relation [101]. For the local fields, we obtain the linear equation system

$$\boldsymbol{G}^{\mathrm{loc}}(\mathbf{r}_i, \mathbf{r}') = \bar{\boldsymbol{G}}(\mathbf{r}_i, \mathbf{r}') + \frac{\omega^2}{c^2}\bar{\boldsymbol{G}}_{\mathrm{sc}}(\mathbf{r}_i, \mathbf{r}_i)\boldsymbol{\alpha}_i\boldsymbol{G}^{\mathrm{loc}}(\mathbf{r}_i, \mathbf{r}') + \sum_{j \neq i}^{N} \frac{\omega^2}{c^2}\bar{\boldsymbol{G}}(\mathbf{r}_i, \mathbf{r}_j)\boldsymbol{\alpha}_j\boldsymbol{G}^{\mathrm{loc}}(\mathbf{r}_j, \mathbf{r}'). \tag{A.73}$$

Once we have computed the $\boldsymbol{G}^{\mathrm{loc}}(\mathbf{r}_i, \mathbf{r}')$ for a given source point $\mathbf{r}'$, we can infer the Green's tensor to any probe point $\mathbf{r}$ by

$$\boldsymbol{G}(\mathbf{r}, \mathbf{r}') = \bar{\boldsymbol{G}}(\mathbf{r}, \mathbf{r}') + \frac{\omega^2}{c^2}\sum_{i}^{N}\bar{\boldsymbol{G}}(\mathbf{r}, \mathbf{r}_i)\boldsymbol{\alpha}_i\boldsymbol{G}^{\mathrm{loc}}(\mathbf{r}_i, \mathbf{r}'). \tag{A.74}$$

Instead of solving Eq. (A.73) directly, one often introduces a polarization like tensor (compare Ref. [87]), $\boldsymbol{P}(\mathbf{r}_i, \mathbf{r}') \equiv \boldsymbol{\alpha}_i\boldsymbol{G}^{\mathrm{loc}}(\mathbf{r}_i, \mathbf{r}')$, and implements

$$\bar{\boldsymbol{G}}(\mathbf{r}_i, \mathbf{r}') = \left[\boldsymbol{\alpha}_i^{-1} - \frac{\omega^2}{c^2}\bar{\boldsymbol{G}}_{\mathrm{sc}}(\mathbf{r}_i, \mathbf{r}_i)\right]\boldsymbol{P}(\mathbf{r}_i, \mathbf{r}') - \sum_{j \neq i}^{N}\frac{\omega^2}{c^2}\bar{\boldsymbol{G}}(\mathbf{r}_i, \mathbf{r}_j)\boldsymbol{P}(\mathbf{r}_j, \mathbf{r}'). \tag{A.75}$$

This brings the advantage that the terms under the sum do not depend on the material composition of each dipole scatterer. With known values for $\boldsymbol{P}(\mathbf{r}_j, \mathbf{r}')$, the Green's tensor to the probe point is

$$\boldsymbol{G}(\mathbf{r}, \mathbf{r}') = \bar{\boldsymbol{G}}(\mathbf{r}, \mathbf{r}') + \sum_{i}^{N}\frac{\omega^2}{c^2}\bar{\boldsymbol{G}}(\mathbf{r}, \mathbf{r}_i)\boldsymbol{P}(\mathbf{r}_i, \mathbf{r}'). \tag{A.76}$$

A.6.1. Block Toeplitz matrices

Our Eq. (A.75) can be cast into a matrix form as

$$(\boldsymbol{B}+\boldsymbol{A}+\boldsymbol{R})\,\tilde{\boldsymbol{P}}=\tilde{\bar{\boldsymbol{G}}}. \tag{A.77}$$

The known $\tilde{\bar{\boldsymbol{G}}}$ and the unknown $\tilde{\boldsymbol{P}}$ are composed of N 3×3 matrices

$$\tilde{\boldsymbol{P}}=\left[\boldsymbol{P}(\mathbf{r}_1,\mathbf{r});\ldots;\boldsymbol{P}(\mathbf{r}_N,\mathbf{r})\right],\quad \tilde{\bar{\boldsymbol{G}}}=\left[\bar{\boldsymbol{G}}(\mathbf{r}_1,\mathbf{r});\ldots;\bar{\boldsymbol{G}}(\mathbf{r}_N,\mathbf{r})\right]. \tag{A.78}$$

The matrix $\boldsymbol{B}$ is a diagonal matrix that contains the inverse pseudo-polarizabilities of the discrete dipoles

$$\boldsymbol{B}=\operatorname{diag}\left(\alpha_{1x}^{-1},\alpha_{1y}^{-1},\alpha_{1z}^{-1},\ldots,\alpha_{Nx}^{-1},\alpha_{Ny}^{-1},\alpha_{Nz}^{-1}\right). \tag{A.79}$$

The $3N\times 3N$ matrices $\boldsymbol{A}$ and $\boldsymbol{R}$ account for direct ($\boldsymbol{A}$) and body assisted ($\boldsymbol{R}$) interactions between the discrete dipoles

$$\boldsymbol{A}=\begin{bmatrix}\boldsymbol{A}_{11} & \ldots & \boldsymbol{A}_{1N}\\ \vdots & & \vdots\\ \boldsymbol{A}_{N1} & \ldots & \boldsymbol{A}_{NN}\end{bmatrix}\quad\text{where}\quad \boldsymbol{A}_{ij}=\begin{cases}\mathbf{0} & \text{for } i=j\\ -\bar{\boldsymbol{G}}_{\text{bulk}}(\mathbf{r}_i,\mathbf{r}_j) & \text{for } i\neq j\end{cases}, \tag{A.80}$$

$$\boldsymbol{R}=\begin{bmatrix}\boldsymbol{R}_{11} & \ldots & \boldsymbol{R}_{1N}\\ \vdots & & \vdots\\ \boldsymbol{R}_{N1} & \ldots & \boldsymbol{R}_{NN}\end{bmatrix}\quad\text{where}\quad \boldsymbol{R}_{ij}=-\bar{\boldsymbol{G}}_{\text{sc}}(\mathbf{r}_i,\mathbf{r}_j). \tag{A.81}$$

The equation system (A.77) is usually solved iteratively [87]. We employ the BiCGSTAB algorithm [224] together with a Jacobi preconditioner.

When the background is a planar surface and one discretizes on a regular grid, the interaction matrices $\boldsymbol{A}$ and $\boldsymbol{R}$ have a special form that allows for a great reduction of the computational costs of the DDA. The direct part of the Green's tensor $\bar{\boldsymbol{G}}_{\text{bulk}}(\mathbf{r},\mathbf{r}',\omega)$ only depends on the distance $\mathbf{r}-\mathbf{r}'$. The scattering part of a surface $\bar{\boldsymbol{G}}_{\text{surf}}(\mathbf{r},\mathbf{r}',\omega)$ only depends on the distance between the mirror dipole of the source point $\mathbf{r}'$ and the probe point $\mathbf{r}$, assuming that both points lie above the substrate. Thus,

$$\boldsymbol{G}_{\text{bulk}}(\mathbf{r},\mathbf{r}',\omega)=\boldsymbol{G}_{\text{bulk}}(x-x',y-y',z-z',\omega), \tag{A.82}$$

$$\boldsymbol{G}_{\text{surf}}(\mathbf{r},\mathbf{r}',\omega)=\boldsymbol{G}_{\text{surf}}(x-x',y-y',z+z',\omega). \tag{A.83}$$

Therefore, only a fraction of the entries inside the interaction matrices is unique. One can sort the equally sized discrete dipoles by rows, columns, and lines. Wherever necessary, artificial dipoles with a small $\chi_i=10^{-6}$ are added such that one obtains a rectangular parallelepiped of dipoles that encloses the entire geometry. This way, the interaction matrices inherit the symmetries of the background Green's tensor and acquire a block Toeplitz (BT) structure, where $\boldsymbol{M}_{ij} = \boldsymbol{M}_{j-i}$, e.g. for n rows

$$\boldsymbol{M} = \begin{bmatrix} \boldsymbol{m}_0 & \boldsymbol{m}_1 & \dots & \boldsymbol{m}_n \\ \boldsymbol{m}_{-1} & \boldsymbol{m}_0 & \ddots & \vdots \\ \vdots & \ddots & \ddots & \boldsymbol{m}_1 \\ \boldsymbol{m}_{-n} & \dots & \boldsymbol{m}_{-1} & \boldsymbol{m}_0 \end{bmatrix}. \tag{A.84}$$

The pattern repeats itself within the $\boldsymbol{m}_i$ such that $\boldsymbol{R}$ becomes a 2-level BT matrix and $\boldsymbol{A}$ a 3-level BT matrix [90, 91]. For each matrix, only the unique building blocks need to be stored. The iterative solver is based on products between the interaction matrices and arbitrary vectors that usually have $\mathcal{O}(n^2)$ complexity. For BT matrices, however, the products can be seen as discrete convolutions and thereby be replaced by simple $\mathcal{O}(n)$ vector-vector products in the Fourier domain. This provides an enormous speed-up, see, e.g., [225], as we are now limited by fast Fourier transformations (FFT) with a complexity of only $\mathcal{O}(n\log(n))$.

We have implemented the scheme by Barrowes *et al.* [91] which allows for 3D Fourier acceleration for products with $\boldsymbol{A}$ and 2D Fourier acceleration for products with $\boldsymbol{R}$. Recent approaches [226] also enable a 3D Fourier acceleration for $\boldsymbol{R}$, although the symmetry in z-direction is broken in the presence of a surface. The remaining diagonal matrix $\boldsymbol{B}$ is stored as a vector. Its contribution can be computed by a cheap vector-vector product.

It can be helpful to reduce the number of points for which the Green's tensor has to be computed. Especially for one-point Green's tensors at imaginary frequencies, one can do so by interpolating correction factors $\boldsymbol{G}^{\mathrm{DDA}}(\mathbf{r},\mathbf{r})/\boldsymbol{G}^{\mathrm{1stBorn}}(\mathbf{r},\mathbf{r})$ between points where the full DDA computation was conducted. Compared to the Green's tensor, these correction factors do not vary as strongly with surface distance or frequency, and the interpolation can be reasonably accurate (usually much better than 5%). The tensors in first Born approximation $\boldsymbol{G}^{\mathrm{1stBorn}}(\mathbf{r},\mathbf{r})$ can usually be computed very fast.

B. Auxiliary calculations on atom-light interactions

B.1. Field quantization in homogeneous media

Following Ref. [49], we present the quantized electric field in a homogeneous medium, which includes free space as a limiting case. First, we conduct the replacement $\hat{\mathbf{f}}(\mathbf{r},\omega) \to \hat{\mathbf{f}}(z,\omega)/\sqrt{\mathcal{A}}$, where $\mathcal{A}$ is the normalization area perpendicular to the propagation direction that we assume to be along the z-axis. Invoking the shorthand notations $\sqrt{\epsilon(\omega)} = n(\omega) = n_R(\omega) + i n_I(\omega)$, $\epsilon(\omega) = \epsilon(\omega) + i\epsilon(\omega)$ and Eqs. (A.8) and (2.46), the electric field operator in a bulk material reads

$$
\begin{aligned}
\hat{\mathbf{E}}_{\text{bulk}}(\mathbf{r},\omega) &= i\sqrt{\frac{\hbar}{\pi\epsilon_0\mathcal{A}}}\frac{\omega^2}{c^2}\int_{-\infty}^{\infty} dz' \int dA' \sqrt{\operatorname{Im}\epsilon(\omega)}\boldsymbol{G}_{\text{bulk}}(\mathbf{r},\mathbf{r}',\omega)\hat{\mathbf{f}}(z',\omega) \\
&= i\sqrt{\frac{\hbar}{\pi\epsilon_0\mathcal{A}}}\frac{\omega^2}{c^2}\int_{-\infty}^{\infty} dz' \frac{ic}{2n(\omega)\omega} e^{in(\omega)\frac{\omega}{c}|z-z'|}\operatorname{diag}(1,1,0)\sqrt{\operatorname{Im}\epsilon(\omega)}\,\hat{\mathbf{f}}(z',\omega). \qquad \text{(B.1)}
\end{aligned}
$$

Since $\int_{-\infty}^{\infty} dz' f(z') = \int_{-\infty}^{z} dz' f(z') + \int_{-\infty}^{-z} dz' f(-z')$, we can rewrite the field with new operators

$$
\hat{\mathbf{E}}_{\text{bulk}}(z,\omega) = \sqrt{\frac{\hbar\omega n_R(\omega)}{4\pi\epsilon_0 c\mathcal{A}}}\frac{i}{n(\omega)}\left(\hat{\mathbf{a}}_+(z,\omega)e^{n_R(\omega)\frac{\omega}{c}z} + \hat{\mathbf{a}}_-(z,\omega)e^{-n_R(\omega)\frac{\omega}{c}z}\right), \qquad \text{(B.2)}
$$

$$
\hat{\mathbf{a}}_\pm(z,\omega) = i\sqrt{2n_I(\omega)\frac{\omega}{c}}e^{\mp n_I(\omega)\frac{\omega}{c}z}\int_{-\infty}^{\pm z} dz' e^{-i\frac{\omega}{c}n(\omega)z'}\boldsymbol{I}^\perp\hat{\mathbf{f}}(\pm z',\omega), \qquad \text{(B.3)}
$$

where $\boldsymbol{I}^\perp = \operatorname{diag}(1,1,0)$ and we applied $\epsilon_I = \operatorname{Im} n^2 = 2n_R n_I$. We compute the commutator of the new ladder operators using Eq. (2.44)

$$
\begin{aligned}
\left[\hat{\mathbf{a}}_\pm(z,\omega), \hat{\mathbf{a}}_\pm^\dagger(z',\omega')\right] &= 2n_I(\omega)\frac{\omega}{c}e^{\mp n_I(\omega)\frac{\omega}{c}(z+z')}\int_{-\infty}^{\pm z} d\alpha\, e^{-in(\omega)\frac{\omega}{c}\alpha} \\
&\quad\times \int_{-\infty}^{\pm z'} d\alpha'\, e^{in^*(\omega)\frac{\omega}{c}\alpha'}\boldsymbol{I}^\perp\delta(\alpha-\alpha')\delta(\omega-\omega') \\
&= 2n_I(\omega)\frac{\omega}{c}e^{\mp n_I(\omega)\frac{\omega}{c}(z+z')}\int_{-\infty}^{\pm z} d\alpha\, e^{2n_I(\omega)\frac{\omega}{c}\alpha}\Theta(\pm z'-\alpha)\boldsymbol{I}^\perp\delta(\omega-\omega') \\
&= e^{-n_I(\omega)\frac{\omega}{c}|z-z'|}\boldsymbol{I}^\perp\delta(\omega-\omega'). \qquad \text{(B.4)}
\end{aligned}
$$

The definitions of $\hat{\mathbf{a}}_\pm(z,\omega)$ have different signs than in Ref. [49]. This originates from the sign on the right-hand side of the one dimensional Helmholtz equation, i.e. $-\delta(z-z')$ here and $+\delta(z-z')$ in Ref. [49].

B.2. Commutation rules of partial atom and field operators

The equal-time commutation rules between field and atomic operators apply to complete operators [227] but not necessarily to partial contributions. In the Heisenberg picture, Eq. (2.114), one can decompose the electric field operator into an external field and an atomic part

$$\hat{\mathbf{E}}(\mathbf{r},\omega,t) = \underbrace{\hat{\mathbf{E}}(\mathbf{r},\omega,0)e^{-i\omega t}}_{=\hat{\mathbf{E}}_{\text{free}}(\mathbf{r},\omega,t)} + \underbrace{\frac{i\mu_0\omega^2}{\pi}\sum_A\int_0^t dt' e^{-i\omega(t-t')}\mathrm{Im}\,\boldsymbol{G}(\mathbf{r},\mathbf{r}_A(t'),\omega)\hat{\mathbf{d}}_A(t')}_{=\hat{\mathbf{E}}_{\text{atoms}}(\mathbf{r},\omega,t)} . \tag{B.5}$$

Due to $[\hat{\mathbf{E}}(\mathbf{r},\omega,t),\hat{\sigma}_{A,mn}(t)] = \hat{\mathbf{0}}$, we can have nonzero commutators for the partial fields

$$\left[\hat{\mathbf{E}}_{\text{free}}(\mathbf{r},\omega,t),\hat{\sigma}_{A,mn}(t)\right] = -\left[\hat{\mathbf{E}}_{\text{atoms}}(\mathbf{r},\omega,t),\hat{\sigma}_{A,mn}(t)\right] \neq \hat{\mathbf{0}}, \tag{B.6}$$

because $[\hat{\mathbf{d}}_A(t'),\hat{\sigma}_{A,mn}(t)]$ does not always vanish. There are situations where Eq. (B.6) is zero but this should be shown explicitly [227].

B.3. Expectation values of thermal fields

In this section, we compute the electric field expectation values of a thermal field. The density matrix of the thermal field reads [52, 113]

$$\rho_T = \frac{e^{-\hat{H}_F/(k_BT)}}{Z}, \quad Z = \mathrm{Tr}\left(e^{-\hat{H}_F/(k_BT)}\right). \tag{B.7}$$

Since the thermal state is diagonal in the photon number, the expectation values of unequal numbers of creation and annihilation operators vanish

$$\langle\hat{\mathbf{E}}^\dagger(\mathbf{r},\omega)\rangle_T = \langle\hat{\mathbf{E}}(\mathbf{r},\omega)\rangle_T = \langle\hat{\mathbf{E}}^\dagger(\mathbf{r},\omega)\otimes\hat{\mathbf{E}}^\dagger(\mathbf{r}',\omega')\rangle_T = \langle\hat{\mathbf{E}}(\mathbf{r},\omega)\otimes\hat{\mathbf{E}}(\mathbf{r}',\omega')\rangle_T = \mathbf{0}. \tag{B.8}$$

Nonzero results are expected for $\langle\hat{\mathbf{E}}^\dagger(\mathbf{r},\omega)\otimes\hat{\mathbf{E}}(\mathbf{r}',\omega')\rangle_T$ and

$$\varphi \equiv \langle\hat{\mathbf{f}}^\dagger(\mathbf{r},\omega)\otimes\hat{\mathbf{f}}(\mathbf{r}',\omega')\rangle_T = \mathrm{Tr}\left\{\hat{\mathbf{f}}^\dagger(\mathbf{r},\omega)\otimes\hat{\mathbf{f}}(\mathbf{r}',\omega')\rho_T\right\}, \tag{B.9}$$

if $\mathbf{r}=\mathbf{r}'$ and $\omega=\omega'$. In order to evaluate the trace, it is sufficient to consider the single-mode subset of the Hilbert space, $\sum_{j=0}^{\infty}|\mathbf{j}(\mathbf{r},\omega)\rangle\langle\mathbf{j}(\mathbf{r},\omega)|$, that contributes to nonzero values of φ. The corresponding normalization constant is

$$\begin{aligned}
Z =& \sum_{j=0}^{\infty} \langle \mathbf{j}(\mathbf{r},\omega)| \exp\left[-\int d^3\mathbf{r}' \int_0^\infty d\omega' \, \hat{\mathbf{f}}^\dagger(\mathbf{r}',\omega') \cdot \hat{\mathbf{f}}(\mathbf{r}',\omega') \frac{\hbar\omega'}{k_B T}\right] |\mathbf{j}(\mathbf{r},\omega)\rangle && \text{(B.10)}\\
=& \sum_{j=0}^{\infty} \langle \mathbf{j}(\mathbf{r},\omega)| \exp\left[-\int d^3\mathbf{r}' \int_0^\infty d\omega' \, j\delta(\omega-\omega')\delta(\mathbf{r}-\mathbf{r}') \frac{\hbar\omega'}{k_B T}\right] |\mathbf{j}(\mathbf{r},\omega)\rangle && \text{(B.11)}\\
=& \sum_{j=0}^{\infty} e^{-j\hbar\omega/(k_B T)} = \frac{1}{1-e^{-\hbar\omega/(k_B T)}}, && \text{(B.12)}
\end{aligned}$$

and the expectation value of ladder operators

$$\begin{aligned}
\varphi =& \frac{1}{Z} \sum_{j=0}^{\infty} \langle \mathbf{j}(\mathbf{r},\omega)| \, \hat{\mathbf{f}}^\dagger(\mathbf{r},\omega) \otimes \hat{\mathbf{f}}(\mathbf{r}',\omega') \exp\left[-\int d^3\mathbf{r}_2 \int_0^\infty d\omega_2 \, \hat{\mathbf{f}}^\dagger(\mathbf{r}_2,\omega_2) \cdot \hat{\mathbf{f}}(\mathbf{r}_2,\omega_2) \frac{\hbar\omega_2}{k_B T}\right] |\mathbf{j}(\mathbf{r},\omega)\rangle \\
=& \frac{1}{Z} \sum_{j=0}^{\infty} \langle \mathbf{j}(\mathbf{r},\omega)| \, \hat{\mathbf{f}}^\dagger(\mathbf{r},\omega) \otimes \hat{\mathbf{f}}(\mathbf{r}',\omega') e^{-j\hbar\omega/(k_B T)} \, |\mathbf{j}(\mathbf{r},\omega)\rangle && \text{(B.13)}\\
=& \frac{1}{Z} \sum_{j=0}^{\infty} j e^{-j\hbar\omega/(k_B T)} \boldsymbol{I} \delta(\mathbf{r}-\mathbf{r}')\delta(\omega-\omega') = n(\omega) \boldsymbol{I} \delta(\mathbf{r}-\mathbf{r}')\delta(\omega-\omega'), && \text{(B.14)}
\end{aligned}$$

where we use the geometric sum $\sum_{j=0}^{\infty} j q^j = q\partial_q \sum_{j=0}^{\infty} q^j = \frac{q}{(1-q)^2}$ and the Bose-Einstein distribution (2.67). Combing the above with Eqs. (2.30) and (2.46), we obtain $\langle \hat{\mathbf{E}}^\dagger(\mathbf{r},\omega) \otimes \hat{\mathbf{E}}(\mathbf{r}',\omega') \rangle_T$, i.e. Eq. (2.65) of the main text. Using Eqs. (2.44), (2.46), and (2.30), we compute the commutator

$$\int_0^\infty d\omega' \left[\hat{\mathbf{E}}(\mathbf{r},\omega), \hat{\mathbf{E}}^\dagger(\mathbf{r}',\omega')\right] = \frac{\hbar\mu_0}{\pi} \omega^2 \mathrm{Im}\, \boldsymbol{G}(\mathbf{r},\mathbf{r}',\omega), \tag{B.15}$$

and infer $\langle \hat{\mathbf{E}}(\mathbf{r},\omega) \otimes \hat{\mathbf{E}}^\dagger(\mathbf{r}',\omega') \rangle_T$ from $\langle \hat{\mathbf{E}}^\dagger(\mathbf{r},\omega) \otimes \hat{\mathbf{E}}(\mathbf{r}',\omega') \rangle_T$.

B.4. Position memory of the Green's tensor

We aim to simplify the coefficient

$$\Xi_{CD}(t,s) = \frac{\mu_0}{\pi\hbar} \int_0^\infty d\omega \, \left\{ [1+n(\omega)] \, e^{-is\omega} + n(\omega) e^{is\omega} \right\} \omega^2 \mathrm{Im}\, \boldsymbol{G}(\mathbf{r}_C(t), \mathbf{r}_D(t-s), \omega), \tag{B.16}$$

through a Taylor series expansion in the time argument within the Green's tensor. We can approximate the position $\mathbf{r}_D(t-s) \approx \mathbf{r}_D(t) - s\mathbf{v}_D(t)$ and the Green's tensor as [52]

$$\boldsymbol{G}(\mathbf{r}_C, \mathbf{r}_D(t-s), \omega) \approx \boldsymbol{G}(\mathbf{r}_C, \mathbf{r}_D(t), \omega) + \boldsymbol{G}(\mathbf{r}_C, \mathbf{r}_D(t), \omega) [\boldsymbol{\nabla}_{\mathbf{r}_D} \cdot \mathbf{v}_D](-s). \tag{B.17}$$

With $-se^{\pm is\omega} = \pm i \frac{d}{d\omega} e^{\pm is\omega}$, we find

$$\begin{aligned}\Xi_{CD}(t,s) &\approx \frac{\mu_0}{\pi\hbar}\int_0^\infty d\omega\,\left\{[1+n(\omega)]\,e^{-is\omega}+n(\omega)e^{is\omega}\right\}\omega^2 \mathrm{Im}\,\boldsymbol{G}(\mathbf{r}_C(t),\mathbf{r}_D(t),\omega)\\ &+\frac{i\mu_0}{\pi\hbar}\int_0^\infty d\omega\,\frac{d}{d\omega}\left\{-[1+n(\omega)]\,e^{-is\omega}+n(\omega)e^{is\omega}\right\}\omega^2 \mathrm{Im}\,\boldsymbol{G}(\mathbf{r}_C(t),\mathbf{r}_D(t),\omega)[\boldsymbol{\nabla}_{\mathbf{r}_D}\cdot\mathbf{v}_D].\end{aligned} \tag{B.18}$$

We can transform the above expression through integration by parts. Due to the high frequency limit (2.28) and the reflection principle (2.27), the Green's tensor is purely real at the integration boundaries

$$\lim_{\omega\to 0}\omega^2 \mathrm{Im}\,\boldsymbol{G}(\mathbf{r}_1,\mathbf{r}_2,\omega) = \lim_{\omega\to\infty}\omega^2 \mathrm{Im}\,\boldsymbol{G}(\mathbf{r}_1,\mathbf{r}_2,\omega) = \mathbf{0}. \tag{B.19}$$

Thus,

$$\begin{aligned}\Xi_{CD}(t,s) &= \frac{\mu_0}{\pi\hbar}\int_0^\infty d\omega\,\left\{[1+n(\omega)]\,e^{-is\omega}+n(\omega)e^{is\omega}\right\}\omega^2 \mathrm{Im}\,\boldsymbol{G}(\mathbf{r}_C(t),\mathbf{r}_D(t),\omega)\\ &-\frac{i\mu_0}{\pi\hbar}\int_0^\infty d\omega\,\left\{-[1+n(\omega)]\,e^{-is\omega}+n(\omega)e^{is\omega}\right\}\frac{d}{d\omega}\left[\omega^2 \mathrm{Im}\,\boldsymbol{G}(\mathbf{r}_C(t),\mathbf{r}_D(t),\omega)\right][\boldsymbol{\nabla}_{\mathbf{r}_D}\cdot\mathbf{v}_D].\end{aligned} \tag{B.20}$$

The importance of the second term is reflected by the ratio

$$\frac{d}{d\omega}\left[\omega^2 \mathrm{Im}\,\boldsymbol{G}_{ij}(\mathbf{r}_C,\mathbf{r}_D,\omega)\right][\boldsymbol{\nabla}_{\mathbf{r}_D}\cdot\mathbf{v}_D]/\left(\omega^2 \mathrm{Im}\,\boldsymbol{G}_{ij}(\mathbf{r}_C,\mathbf{r}_D,\omega)\right), \tag{B.21}$$

which becomes considerable if the velocity of the atom is large and/or the imaginary part of the Green's tensor is strongly peaked in the frequency domain. The latter usually implies a strong atom-field coupling and is therefore not compatible with the Born–Markov approximation [52] which is used to obtain the integral in the first place. A peak of the Green's tensor has two common causes: a resonance in the permittivity or a narrow mode in a waveguide geometry. The first case occurs for basically all macroscopic bodies and is most important to our study. We investigated the above ratio for atoms with a thermal velocity of $v = 100\,\mathrm{m/s}$ and a flat sapphire surface. Even under ideal conditions, i.e. at a resonance frequency ($\approx 17\,\mathrm{THz}$) and with probe and source point 1 nm away from the surface, the ratio only reaches $\sim 1\%$. At 10 nm it is only $\sim 10^{-3}$. Away from the resonance, e.g., at optical frequencies, larger ratios are found at larger distances from the surface, e.g., 10^{-6} at 10 nm distance and 10^{-5} at 1 μm distance. Overall, the ratios remain small, so it is sufficient to consider only the first term of Eq. (B.20) in this thesis. However, the correction term deserves a closer look when faster atoms and/or structures and materials with stronger resonances are studied.

B.5. Green's tensor contour integration

In this section, we transform the real frequency integrals of $\boldsymbol{\mathcal{B}}_{A,nm}(\mathbf{r},\mathbf{r}')$ and $\boldsymbol{\mathcal{F}}_{A,nm}(\mathbf{r},\mathbf{r}')$, Eqs. (2.90) and (2.88), into a form feasible for numerical evaluation following Ref. [52]. For $\boldsymbol{\mathcal{B}}_{A,nm}(\mathbf{r},\mathbf{r}')$, we first split our expression into two integrals using $\mathrm{Im}\,\boldsymbol{G}(\omega) = [\boldsymbol{G}(\omega) - \boldsymbol{G}(-\omega)]/(2i)$. We utilize the analyticity of the Green's tensor and the residue theorem to reformulate the frequency integrals on closed integration contours along the imaginary axis, see $T = 0\,\mathrm{K}$ case of Fig. B.1. We circumvent the poles along the real axis by semi-circles and obtain

$$\begin{aligned}\boldsymbol{\mathcal{B}}_{A,nm}(\mathbf{r},\mathbf{r}') =& -\frac{\mu_0}{\hbar\pi 2i}\mathcal{P}\int_0^\infty d\omega\,\frac{\omega^2\boldsymbol{G}(\mathbf{r},\mathbf{r}',\omega)}{\omega-\omega_{A,nm}} + \frac{\mu_0}{\hbar\pi 2i}\mathcal{P}\int_0^{-\infty} d\omega\,\frac{\omega^2\boldsymbol{G}(\mathbf{r},\mathbf{r}',\omega)}{\omega+\omega_{A,nm}}\\ =& -\frac{\mu_0}{\hbar\pi 2i}\left(-\int_\infty^0 d\xi\, i\frac{(i\xi)^2\boldsymbol{G}(\mathbf{r},\mathbf{r}',i\xi)}{i\xi-\omega_{A,nm}} + i\pi\Theta(\omega_{A,nm})\omega_{A,nm}^2\boldsymbol{G}(\mathbf{r},\mathbf{r}',\omega_{A,nm})\right)\\ &+\frac{\mu_0}{\hbar\pi 2i}\left(-\int_\infty^0 d\xi\, i\frac{(i\xi)^2\boldsymbol{G}(\mathbf{r},\mathbf{r}',i\xi)}{i\xi+\omega_{A,nm}} - i\pi\Theta(\omega_{A,nm})\omega_{A,nm}^2\boldsymbol{G}(\mathbf{r},\mathbf{r}',-\omega_{A,nm})\right)\\ =& -\frac{\mu_0}{\hbar}\Theta(\omega_{A,nm})\omega_{A,nm}^2\mathrm{Re}\,\boldsymbol{G}(\mathbf{r},\mathbf{r}',\omega_{A,nm}) - \frac{\mu_0}{\hbar\pi}\int_0^\infty d\xi\,\frac{\omega_{A,nm}}{\omega_{A,nm}^2+\xi^2}\xi^2\boldsymbol{G}(\mathbf{r},\mathbf{r}',i\xi).\end{aligned} \tag{B.22}$$

Analogously, we tackle $\boldsymbol{\mathcal{D}}_{A,nm}(\mathbf{r},\mathbf{r}')$ that includes finite temperature contributions. The Bose-Einstein distribution exhibits poles on the imaginary axis (see $T > 0\,\mathrm{K}$ case of Fig. B.1) at the so-called Matsubara frequencies [52], $\xi_j = \frac{2\pi k_B T}{\hbar} j$ with $j \in \mathbb{N}_0$. In their vicinity, we may use a Taylor expansion on the Bose-Einstein function (2.67), $n(\omega) \simeq k_B T/[\hbar(\omega - i\xi_j)]$, to read off the residue $k_B T/\hbar$. The pole at $j = 0$ is surrounded by a semicircle and thereby carries half weight. It is useful to introduce the shorthand notation $\sum_{j=0}^{\infty}{}' f(\xi_j) = \frac{1}{2}f(\xi_0) + \sum_{j=1}^{\infty} f(\xi_j)$.

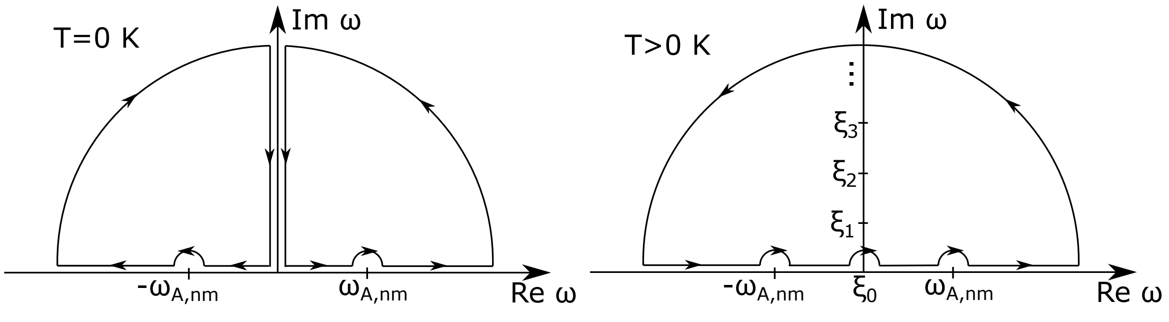

Figure B.1: Integration contours used for evaluating the real frequency integrals of $\boldsymbol{\mathcal{B}}_{A,nm}(\mathbf{r},\mathbf{r}')$ ($T = 0\,\mathrm{K}$ case) and $\boldsymbol{\mathcal{F}}_{A,nm}(\mathbf{r},\mathbf{r}')$ ($T > 0\,\mathrm{K}$ case) following Ref. [52].

Recalling that $n(-\omega) = -[n(\omega)+1]$, we find

$$
\begin{aligned}
\boldsymbol{\mathcal{F}}_{A,nm}(\mathbf{r},\mathbf{r}') =& \frac{\mu_0}{\hbar\pi}\mathcal{P}\int_0^\infty d\omega\,\omega^2 \mathrm{Im}\,\boldsymbol{G}(\mathbf{r},\mathbf{r}',\omega)\left[-\frac{[n(\omega)+1]}{\omega-\omega_{A,nm}}+\frac{n(\omega)}{\omega_{A,nm}+\omega}\right]\\
=& \frac{\mu_0}{2i\hbar\pi}\mathcal{P}\int_{-\infty}^\infty d\omega\,\omega^2 \boldsymbol{G}(\mathbf{r},\mathbf{r}',\omega)\left[-\frac{[n(\omega)+1]}{\omega-\omega_{A,nm}}+\frac{n(\omega)}{\omega_{A,nm}+\omega}\right]\\
=& 2\pi i\frac{\mu_0}{2i\hbar\pi}\frac{k_BT}{\hbar}\sum_{j=0}^{\infty}{}'(i\xi_j)^2\boldsymbol{G}(\mathbf{r},\mathbf{r}',i\xi_j)\left[\frac{1}{-i\xi_j+\omega_{A,nm}}+\frac{1}{\omega_{A,nm}+i\xi_j}\right]\\
&+\pi i\frac{\mu_0}{2i\hbar\pi}\Big([-n(\omega_{A,nm})-1]\boldsymbol{G}(\mathbf{r},\mathbf{r}',\omega_{A,nm})+n(-\omega_{A,nm})\boldsymbol{G}(\mathbf{r},\mathbf{r}',-\omega_{A,nm})\Big)\\
=& -\frac{\mu_0}{\hbar}\left(\Theta(\omega_{A,nm})[n(\omega_{A,nm})+1]-\Theta(\omega_{A,mn})n(\omega_{A,mn})\right)\mathrm{Re}\,\boldsymbol{G}(\mathbf{r},\mathbf{r}',\omega_{A,nm})\\
&-\frac{2\mu_0k_BT}{\hbar^2}\sum_{j=0}^{\infty}{}'\frac{\omega_{A,nm}\xi_j^2\boldsymbol{G}(\mathbf{r},\mathbf{r}',i\xi_j)}{\xi_j^2+(\omega_{A,nm})^2}.
\end{aligned}
\tag{B.23}
$$

The coefficient $\boldsymbol{\mathcal{B}}_{A,nm}(\mathbf{r},\mathbf{r}')$ is the zero-temperature limit of $\boldsymbol{\mathcal{F}}_{A,nm}(\mathbf{r},\mathbf{r}')$. The transition of the Matsubara sum to the zero frequency integral can be accomplished by means of the Abel–Plana relation [52].

B.6. Transformation between quantum mechanical pictures

In this section, we detail the transformation of the master equation in the interaction picture, Eq. (2.85), to the master equation in the Schrödinger picture, Eq. (2.93), and finally to the equation of motion of an operator $\hat{O}(t)$ in the Heisenberg picture, Eq. (2.94). First, we replace the density matrix in the interaction picture by the corresponding Schrödinger picture density matrix, $\hat{\rho}_A^I(t) = \hat{U}_A^\dagger(t)\rho_A^S(t)\hat{U}_A(t)$, where $\hat{U}_A(t) = \exp\left(-\frac{i}{\hbar}\hat{H}_At\right)$. The left-hand side derivative in Eq. (2.85) becomes

$$
\frac{d}{dt}\hat{\rho}_A^I(t) = \frac{d}{dt}\left(\hat{U}_A^\dagger(t)\rho_A^S(t)\hat{U}_A(t)\right) = \hat{U}_A^\dagger(t)\frac{d\rho_A^S(t)}{dt}\hat{U}_A(t) + \frac{i}{\hbar}\hat{U}_A^\dagger(t)\left[\hat{H}_A,\rho_A^S(t)\right]\hat{U}_A(t). \tag{B.24}
$$

We then remove the outer time evolution operators by applying $\hat{U}_A(t)$ from left and $\hat{U}_A^\dagger(t)$ from the right on both sides of the equation. For the operator expressions on the right-hand side of Eq. (2.85) we find, e.g.,

$$
\begin{aligned}
&\hat{U}_A(t)\hat{\sigma}_{C,mn}\hat{\sigma}_{D,ij}\hat{U}_A^\dagger(t)\rho_A^S(t)\hat{U}_A(t)\hat{U}_A^\dagger(t)e^{it(\omega_{C,mn}+\omega_{D,ij})}\\
=&\underbrace{\hat{U}_A(t)\hat{\sigma}_{C,mn}\hat{U}_A^\dagger(t)}_{=\hat{\sigma}_{C,mn}e^{-it\omega_{C,mn}}}\underbrace{\hat{U}_A(t)\hat{\sigma}_{D,ij}\hat{U}_A^\dagger(t)}_{=\hat{\sigma}_{D,ij}e^{-it\omega_{D,ij}}}\rho_A^S(t)e^{it(\omega_{C,mn}+\omega_{D,ij})} = \hat{\sigma}_{C,mn}\hat{\sigma}_{D,ij}\rho_A^S(t).
\end{aligned}
\tag{B.25}
$$

We treat all other terms analogously and arrive at Eq. (2.93), the master equation in the Schrödinger picture.

Next, we use our result to compute the expectation value of an arbitrary operator $\langle \hat{O}(t) \rangle = \mathrm{Tr}\left\{ \hat{\rho}(t)\hat{O}(0) \right\}$. Utilizing the cyclic properties of the trace, we factor out the density matrix in the operator expressions on the right-hand side, e.g.,

$$\mathrm{Tr}\left\{ \left[\hat{H}_A, \rho_A^S(t) \right] \hat{O} \right\} = \mathrm{Tr}\left\{ - \left[\hat{H}_A, \hat{O} \right] \rho_A^S(t) \right\}, \tag{B.26}$$

$$\mathrm{Tr}\left\{ \hat{\sigma}_{C,mn}\hat{\sigma}_{D,ij}\rho_A^S(t)\hat{O} \right\} = \mathrm{Tr}\left\{ \hat{O}\hat{\sigma}_{C,mn}\hat{\sigma}_{D,ij}\rho_A^S(t) \right\}. \tag{B.27}$$

Because $\mathrm{Tr}\left\{ \hat{\rho}(t)\hat{O}(0) \right\} = \mathrm{Tr}\left\{ \hat{O}(t)\hat{\rho}(0) \right\}$, we can now easily transform into the Heisenberg picture, e.g.,

$$\mathrm{Tr}\left\{ \hat{O}\hat{\sigma}_{C,mn}\hat{\sigma}_{D,ij}\rho_A^S(t) \right\} = \mathrm{Tr}\left\{ \hat{O}^H(t)\hat{\sigma}^H_{C,mn}(t)\hat{\sigma}^H_{D,ij}(t)\rho_A(0) \right\}. \tag{B.28}$$

Analogously, we utilize $\mathrm{Tr}\left\{ \frac{d\hat{\rho}(t)}{dt}\hat{O}(0) \right\} = \mathrm{Tr}\left\{ \hat{\rho}(0)\frac{d\hat{O}(t)}{dt} \right\}$ for the derivative on the left-hand side. Since the resulting equation must hold for arbitrary density matrices $\rho_A(0)$, we can read off the equation of motion of the operator $\langle \hat{O}(t) \rangle$ and arrive at Eq. (2.94) in the main text.

B.7. Conducting the rotating wave approximation

We present the intermediate steps taken to conduct the rotating wave approximation, which result in Eq. (2.95). First of all, we insert $\hat{O} = \hat{\sigma}_{A^{ge}_{\mu\nu}}(t)$ into the Heisenberg equation of motion, Eq. (2.94), and find

$$\begin{aligned}
\frac{d}{dt}\left\langle \hat{\sigma}_{A^{ge}_{\mu\nu}}(t) \right\rangle &= i\omega_{A,ge}\left\langle \hat{\sigma}_{A^{ge}_{\mu\nu}}(t) \right\rangle + \frac{i}{\hbar}\sum_{\substack{k\\ \kappa}}\left(\left\langle \hat{\sigma}_{A^{gk}_{\mu\kappa}}(t) \right\rangle \mathbf{d}_{A^{ek}_{\nu\kappa}} - \left\langle \hat{\sigma}_{A^{ke}_{\kappa\nu}}(t) \right\rangle \mathbf{d}_{A^{kg}_{\kappa\mu}} \right) \cdot \mathbf{E}_{\mathrm{inc}}(\mathbf{r}_A, t) \\
&+ \sum_{D}\sum_{\substack{ijk\\ \delta\epsilon\kappa}}\Bigg\{ \mathbf{d}_{A^{ek}_{\nu\kappa}} \cdot \boldsymbol{\mathcal{H}}_{D,ji}(\mathbf{r}_A, \mathbf{r}_D)\left\langle \hat{\sigma}_{A^{gk}_{\mu\kappa}}(t)\hat{\sigma}_{D^{ij}_{\delta\epsilon}}(t) \right\rangle - \mathbf{d}_{A^{kg}_{\kappa\mu}} \cdot \boldsymbol{\mathcal{H}}_{D,ji}(\mathbf{r}_A, \mathbf{r}_D)\left\langle \hat{\sigma}_{A^{ke}_{\kappa\nu}}(t)\hat{\sigma}_{D^{ij}_{\delta\epsilon}}(t) \right\rangle \\
&- \mathbf{d}_{A^{ek}_{\nu\kappa}} \cdot \boldsymbol{\mathcal{H}}^*_{D,ij}(\mathbf{r}_A, \mathbf{r}_D)\left\langle \hat{\sigma}_{D^{ij}_{\delta\epsilon}}(t)\hat{\sigma}_{A^{gk}_{\mu\kappa}}(t) \right\rangle + \mathbf{d}_{A^{kg}_{\kappa\mu}} \cdot \boldsymbol{\mathcal{H}}^*_{D,ij}(\mathbf{r}_A, \mathbf{r}_D)\left\langle \hat{\sigma}_{D^{ij}_{\delta\epsilon}}(t)\hat{\sigma}_{A^{ke}_{\kappa\nu}}(t) \right\rangle \Bigg\}\mathbf{d}_{D^{ij}_{\delta\epsilon}}.
\end{aligned} \tag{B.29}$$

Note that the sum over C reduces to the $C = A$ term. When $C \neq A$, the atomic operators of atoms A and C commute and the corresponding terms mutually cancel. Next, we split the sum into terms $B = A$ and $B \neq A$, and factorize the operator product of two different atoms according to the decorrelation approximation presented in the main text

$$\begin{aligned}
\frac{d}{dt}\left\langle \hat{\sigma}_{A^{ge}_{\mu\nu}}(t)\right\rangle &= i\omega_{A,ge}\left\langle \hat{\sigma}_{A^{ge}_{\mu\nu}}(t)\right\rangle + \frac{i}{\hbar}\sum_{\substack{k\\ \kappa}}\left(\left\langle \hat{\sigma}_{A^{gk}_{\mu\kappa}}(t)\right\rangle \mathbf{d}_{A^{ek}_{\nu\kappa}} - \left\langle \hat{\sigma}_{A^{ke}_{\kappa\nu}}(t)\right\rangle \mathbf{d}_{A^{kg}_{\kappa\mu}}\right)\cdot \mathbf{E}_{\mathrm{inc}}(\mathbf{r}_A,t)\\
&+\sum_{B\neq A}\sum_{\substack{ijk\\ \delta\epsilon\kappa}}\Bigg\{\mathbf{d}_{A^{ek}_{\nu\kappa}}\cdot \boldsymbol{\mathcal{H}}_{B,ji}(\mathbf{r}_A,\mathbf{r}_B)\left\langle \hat{\sigma}_{A^{gk}_{\mu\kappa}}(t)\right\rangle \left\langle \hat{\sigma}_{B^{ij}_{\delta\epsilon}}(t)\right\rangle - \mathbf{d}_{A^{kg}_{\kappa\mu}}\cdot \boldsymbol{\mathcal{H}}_{B,ji}(\mathbf{r}_A,\mathbf{r}_B)\left\langle \hat{\sigma}_{A^{ke}_{\kappa\nu}}(t)\right\rangle \left\langle \hat{\sigma}_{B^{ij}_{\delta\epsilon}}(t)\right\rangle\\
&-\mathbf{d}_{A^{ek}_{\nu\kappa}}\cdot \boldsymbol{\mathcal{H}}^{*}_{B,ij}(\mathbf{r}_A,\mathbf{r}_B)\left\langle \hat{\sigma}_{B^{ij}_{\delta\epsilon}}(t)\right\rangle \left\langle \hat{\sigma}_{A^{gk}_{\mu\kappa}}(t)\right\rangle + \mathbf{d}_{A^{kg}_{\kappa\mu}}\cdot \boldsymbol{\mathcal{H}}^{*}_{B,ij}(\mathbf{r}_A,\mathbf{r}_B)\left\langle \hat{\sigma}_{B^{ij}_{\delta\epsilon}}(t)\right\rangle \left\langle \hat{\sigma}_{A^{ke}_{\kappa\nu}}(t)\right\rangle\Bigg\}\mathbf{d}_{B^{ij}_{\delta\epsilon}}\\
&+\sum_{\substack{jk\\ \epsilon\kappa}}\Bigg\{\mathbf{d}_{A^{ek}_{\nu\kappa}}\cdot \boldsymbol{\mathcal{H}}_{A,jk}(\mathbf{r}_A,\mathbf{r}_A)\mathbf{d}_{A^{kj}_{\kappa\epsilon}}\left\langle \hat{\sigma}_{A^{gj}_{\mu\epsilon}}(t)\right\rangle - \mathbf{d}_{A^{kg}_{\kappa\mu}}\cdot \boldsymbol{\mathcal{H}}_{A,je}(\mathbf{r}_A,\mathbf{r}_A)\mathbf{d}_{A^{ej}_{\nu\epsilon}}\left\langle \hat{\sigma}_{A^{kj}_{\kappa\epsilon}}(t)\right\rangle\\
&-\mathbf{d}_{A^{ek}_{\nu\kappa}}\cdot \boldsymbol{\mathcal{H}}^{*}_{A,jg}(\mathbf{r}_A,\mathbf{r}_A)\mathbf{d}_{A^{jg}_{\epsilon\mu}}\left\langle \hat{\sigma}_{A^{jk}_{\epsilon\kappa}}(t)\right\rangle + \mathbf{d}_{A^{kg}_{\kappa\mu}}\cdot \boldsymbol{\mathcal{H}}^{*}_{A,jk}(\mathbf{r}_A,\mathbf{r}_A)\mathbf{d}_{A^{jk}_{\epsilon\kappa}}\left\langle \hat{\sigma}_{B^{je}_{\epsilon\nu}}(t)\right\rangle\Bigg\}. \qquad \text{(B.30)}
\end{aligned}$$

We conduct the rotating wave approximation by inserting the incident field, $\mathbf{E}_{\mathrm{inc}}(\mathbf{r},t) = \mathbf{E}_{\mathrm{inc}}(\mathbf{r})e^{-i\omega_L t}$, multiplying with $e^{i\omega_L t}$, and discarding all the fast rotating terms that are not proportional to $e^{it(\omega_L-\omega_{A,eg})}$. This still allows expressions like $\left\langle \hat{\sigma}_{A^{gk}_{\mu\kappa}}(t)\right\rangle \left\langle \hat{\sigma}_{B^{ke}_{\delta\epsilon}}(t)\right\rangle$. However, since we assumed the transitions $g \to k$ and $k \to e$ to be far detuned from the laser field, we can self-consistently neglect these contributions. Terms containing $\mathbf{d}_{A,ek}\mathbf{d}_{A,kg}$ or $\mathbf{d}_{A^{kk}_{\nu\mu}}$ vanish due to the dipole selection rule $\Delta l = \pm 1$. We can abbreviate our result by introducing the slowly varying amplitudes $\left\langle \hat{\hat{\sigma}}_{A^{ge}_{\mu\nu}}\right\rangle = e^{i\omega_L t}\left\langle \hat{\sigma}_{A^{ge}_{\mu\nu}}\right\rangle$, such that the left-hand side of our equation becomes $\frac{d}{dt}\left\langle \hat{\sigma}_{A^{ge}_{\mu\nu}}(t)\right\rangle = \frac{d}{dt}\left\langle \hat{\hat{\sigma}}_{A^{ge}_{\mu\nu}}(t)\right\rangle - i\omega_L \hat{\hat{\sigma}}_{A^{ge}_{\mu\nu}}(t)$. The equation of motion takes the form

$$\begin{aligned}
\frac{d}{dt}\left\langle \hat{\hat{\sigma}}_{A^{ge}_{\mu\nu}}(t)\right\rangle &= i(\omega_{A,ge}+\omega_L)\hat{\hat{\sigma}}_{A^{ge}_{\mu\nu}}(t) + \frac{i}{\hbar}\sum_{\kappa}\left(\left\langle \hat{\hat{\sigma}}_{A^{gg}_{\mu\kappa}}(t)\right\rangle \mathbf{d}_{A^{eg}_{\nu\kappa}} - \left\langle \hat{\hat{\sigma}}_{A^{ee}_{\kappa\nu}}(t)\right\rangle \mathbf{d}_{A^{eg}_{\kappa\mu}}\right)\cdot \mathbf{E}_{\mathrm{inc}}(\mathbf{r}_A)\\
&+\sum_{B\neq A}\sum_{\delta\epsilon\kappa}\Bigg\{\mathbf{d}_{A^{eg}_{\nu\kappa}}\cdot\left[\boldsymbol{\mathcal{H}}_{B,eg}(\mathbf{r}_A,\mathbf{r}_B) - \boldsymbol{\mathcal{H}}^{*}_{B,ge}(\mathbf{r}_A,\mathbf{r}_B)\right]\mathbf{d}_{B^{ge}_{\delta\epsilon}}\left\langle \hat{\hat{\sigma}}_{A^{gg}_{\mu\kappa}}(t)\right\rangle \left\langle \hat{\hat{\sigma}}_{B^{ge}_{\delta\epsilon}}(t)\right\rangle\\
&+\mathbf{d}_{A^{eg}_{\kappa\mu}}\cdot\left[\boldsymbol{\mathcal{H}}^{*}_{B,ge}(\mathbf{r}_A,\mathbf{r}_B) - \boldsymbol{\mathcal{H}}_{B,eg}(\mathbf{r}_A,\mathbf{r}_B)\right]\mathbf{d}_{B^{ge}_{\delta\epsilon}}\left\langle \hat{\hat{\sigma}}_{A^{ee}_{\kappa\nu}}(t)\right\rangle \left\langle \hat{\hat{\sigma}}_{B^{ge}_{\delta\epsilon}}(t)\right\rangle\Bigg\}\\
&+\sum_{\substack{k\\ \epsilon\kappa}}\Bigg\{\mathbf{d}_{A^{ek}_{\nu\kappa}}\cdot \boldsymbol{\mathcal{H}}_{A,ek}(\mathbf{r}_A,\mathbf{r}_A)\mathbf{d}_{B^{ke}_{\kappa\epsilon}}\left\langle \hat{\hat{\sigma}}_{A^{ge}_{\mu\epsilon}}(t)\right\rangle + \mathbf{d}_{A^{kg}_{\kappa\mu}}\cdot \boldsymbol{\mathcal{H}}^{*}_{A,gk}(\mathbf{r}_A,\mathbf{r}_A)\mathbf{d}_{B^{gk}_{\epsilon\kappa}}\left\langle \hat{\hat{\sigma}}_{B^{ge}_{\epsilon\nu}}(t)\right\rangle\Bigg\}. \qquad \text{(B.31)}
\end{aligned}$$

Computing

$$
\begin{aligned}
&\boldsymbol{\mathcal{H}}_{B,eg}(\mathbf{r}_A,\mathbf{r}_B)-\boldsymbol{\mathcal{H}}^*_{B,ge}(\mathbf{r}_A,\mathbf{r}_B)\\
&=-\frac{1}{2}\boldsymbol{\mathcal{E}}_{B,eg}(\mathbf{r}_A,\mathbf{r}_B)-i\boldsymbol{\mathcal{F}}_{B,eg}(\mathbf{r}_A,\mathbf{r}_B)+\frac{1}{2}\boldsymbol{\mathcal{E}}_{B,ge}(\mathbf{r}_A,\mathbf{r}_B)-i\boldsymbol{\mathcal{F}}_{B,ge}(\mathbf{r}_A,\mathbf{r}_B) &\text{(B.32)}\\
&=-\frac{1}{2}\boldsymbol{\mathcal{A}}_{B,eg}(\mathbf{r}_A,\mathbf{r}_B)+\frac{1}{2}\boldsymbol{\mathcal{A}}_{B,ge}(\mathbf{r}_A,\mathbf{r}_B)-i\boldsymbol{\mathcal{B}}_{A,eg}(\mathbf{r}_A,\mathbf{r}_B)-i\boldsymbol{\mathcal{B}}_{A,ge}(\mathbf{r}_A,\mathbf{r}_B) &\text{(B.33)}\\
&=i\frac{\mu_0}{\hbar}\omega^2_{B,eg}\,\boldsymbol{G}(\mathbf{r}_A,\mathbf{r}_B,\omega_{B,eg}) &\text{(B.34)}
\end{aligned}
$$

and introducing the line shifts and broadenings according to

$$
\delta\omega_{A^n_{\nu\delta}}=\sum_{\substack{k\\ \kappa}}\mathbf{d}_{A^{nk}_{\nu\kappa}}\cdot\boldsymbol{\mathcal{F}}_{A,nk}(\mathbf{r}_A,\mathbf{r}_A)\mathbf{d}_{A^{kn}_{\kappa\delta}},\quad \Gamma_{A^n_{\nu\delta}}=\sum_{\substack{k\\ \kappa}}\mathbf{d}_{A^{nk}_{\nu\kappa}}\cdot\boldsymbol{\mathcal{E}}_{A,nk}(\mathbf{r}_A,\mathbf{r}_A)\mathbf{d}_{A^{kn}_{\kappa\delta}}. \tag{B.35}
$$

we arrive at Eq. (2.95).

B.8. The two-atom coupled dipole model at zero temperature

We solve the coupled dipole model (2.106) for two atoms at zero temperature analytically. In matrix notation, the problem takes the form

$$
\begin{bmatrix}\boldsymbol{\alpha}_{A,ge}\,\mathbf{E}_{\mathrm{inc}}(\mathbf{r}_A)\\ \boldsymbol{\alpha}_{B,ge}\,\mathbf{E}_{\mathrm{inc}}(\mathbf{r}_B)\end{bmatrix}=\begin{bmatrix}\boldsymbol{I} & -\boldsymbol{\alpha}_{A,ge}\,\boldsymbol{\mathcal{G}}(\mathbf{r}_A,\mathbf{r}_B,\omega_{B,eg})\\ -\boldsymbol{\alpha}_{B,ge}\,\boldsymbol{\mathcal{G}}(\mathbf{r}_B,\mathbf{r}_A,\omega_{A,eg}) & \boldsymbol{I}\end{bmatrix}\begin{bmatrix}\mathbf{p}_{A,ge}\\ \mathbf{p}_{B,ge}\end{bmatrix}. \tag{B.36}
$$

Using the Schur complement, the inverse of a block matrix can be written as [228]

$$
\begin{bmatrix}\boldsymbol{A} & \boldsymbol{B}\\ \boldsymbol{C} & \boldsymbol{D}\end{bmatrix}^{-1}=\begin{bmatrix}(\boldsymbol{A}-\boldsymbol{B}\boldsymbol{D}^{-1}\boldsymbol{C})^{-1} & (\boldsymbol{C}-\boldsymbol{D}\boldsymbol{B}^{-1}\boldsymbol{A})^{-1}\\ (\boldsymbol{B}-\boldsymbol{A}\boldsymbol{C}^{-1}\boldsymbol{D})^{-1} & (\boldsymbol{D}-\boldsymbol{C}\boldsymbol{A}^{-1}\boldsymbol{B})^{-1}\end{bmatrix}. \tag{B.37}
$$

For our problem, we can infer

$$
\begin{bmatrix}\boldsymbol{I} & \boldsymbol{B}\\ \boldsymbol{C} & \boldsymbol{I}\end{bmatrix}^{-1}=\begin{bmatrix}(\boldsymbol{I}-\boldsymbol{B}\boldsymbol{C})^{-1} & -(\boldsymbol{I}-\boldsymbol{B}\boldsymbol{C})^{-1}\boldsymbol{B}\\ -(\boldsymbol{I}-\boldsymbol{C}\boldsymbol{B})^{-1}\boldsymbol{C} & (\boldsymbol{I}-\boldsymbol{C}\boldsymbol{B})^{-1}\end{bmatrix}, \tag{B.38}
$$

using $[\boldsymbol{C}-\boldsymbol{B}^{-1}]^{-1}\boldsymbol{B}^{-1}\boldsymbol{B}=[\boldsymbol{B}\boldsymbol{C}-\boldsymbol{I}]^{-1}\boldsymbol{B}$. The solution of Eq. (B.36) is

$$
\begin{aligned}
\mathbf{p}_{A,ge}&=[\boldsymbol{I}-\boldsymbol{\alpha}_{A,ge}\,\boldsymbol{\mathcal{G}}(\mathbf{r}_A,\mathbf{r}_B,\omega_{B,eg})\boldsymbol{\alpha}_{B,ge}\,\boldsymbol{\mathcal{G}}(\mathbf{r}_B,\mathbf{r}_A,\omega_{B,eg})]^{-1}\\
&\quad\times\{\mathbf{E}_{\mathrm{inc}}(\mathbf{r}_A)+\boldsymbol{\alpha}_{A,ge}\,\boldsymbol{\mathcal{G}}(\mathbf{r}_A,\mathbf{r}_B,\omega_{A,eg})\mathbf{E}_{\mathrm{inc}}(\mathbf{r}_B)\}\,, &\text{(B.39)}\\
\mathbf{p}_{B,ge}&=[\boldsymbol{I}-\boldsymbol{\alpha}_{B,ge}\,\boldsymbol{\mathcal{G}}(\mathbf{r}_B,\mathbf{r}_A,\omega_{A,eg})\boldsymbol{\alpha}_{A,ge}\,\boldsymbol{\mathcal{G}}(\mathbf{r}_A,\mathbf{r}_B,\omega_{A,eg})]^{-1}\\
&\quad\times\{\mathbf{E}_{\mathrm{inc}}(\mathbf{r}_B)+\boldsymbol{\alpha}_{B,ge}\,\boldsymbol{\mathcal{G}}(\mathbf{r}_B,\mathbf{r}_A,\omega_{B,eg})\mathbf{E}_{\mathrm{inc}}(\mathbf{r}_A)\}\,. &\text{(B.40)}
\end{aligned}
$$

C. Transition dipole moments

The transition dipole moment of the valence electron between states $|n\rangle$ and $|m\rangle$ is $\langle m|\hat{\mathbf{d}}|n\rangle = \langle m|e\hat{\mathbf{r}}|n\rangle$. We compute it in a spherical basis given by [106]

$$\hat{d}_{-1} = \frac{1}{\sqrt{2}}(\hat{d}_x - i\hat{d}_y), \qquad \hat{d}_0 = \hat{d}_z, \qquad \hat{d}_{+1} = -\frac{1}{\sqrt{2}}(\hat{d}_x + i\hat{d}_y), \tag{C.1}$$

when the quantization axis lies along the z-direction. The components $\{-1, 0, 1\}$ correspond to the usual $\{\sigma^{-1}, \pi, \sigma^{+1}\}$ transitions and are directly related to the spherical harmonics by $\hat{d}_q = er\sqrt{4\pi/3}\,Y_1^q(\theta, \varphi)$ [229]. The Wigner–Eckart theorem states that transition dipole moments can always be decomposed into an integral over radial wave functions and an angular coupling part [106]. Between two fine structure states with $j = l + s$, the decomposition takes the form [106, 229, 230]

$$\langle n_1 l_1 j_1 m_{j_1}|\hat{d}_q|n_2 l_2 j_2 m_{j_2}\rangle = (-1)^{j_1 - m_{j_1}} \begin{pmatrix} j_1 & 1 & j_2 \\ -m_{j_1} & q & m_{j_2} \end{pmatrix} \langle j_1||\hat{d}_q||j_2\rangle\,, \tag{C.2}$$

$$\langle j_1||\hat{d}_q||j_2\rangle = (-1)^{l_1 + s_1 + j_2 + 1}\delta_{s_1, s_2}\sqrt{(2j_1+1)(2j_2+1)} \begin{Bmatrix} j_1 & 1 & j_2 \\ l_2 & s & l_1 \end{Bmatrix} \langle l_1||\hat{d}_q||l_2\rangle\,, \tag{C.3}$$

$$\langle l_1||\hat{d}_q||l_2\rangle = (-1)^{l_1}\sqrt{(2l_1+1)(2l_2+1)} \begin{pmatrix} l_1 & 1 & l_2 \\ 0 & 0 & 0 \end{pmatrix} \langle n_1 l_1 j_1|e\hat{r}|n_2 l_2 j_2\rangle\,, \tag{C.4}$$

where the round and curly brackets denote Wigner-3j and Wigner-6j symbols [106, 230], respectively. Combining the above expressions, we have

$$\begin{aligned} \langle n_1 l_1 j_1 m_{j_1}|\hat{d}_q|n_2 l_2 j_2 m_{j_2}\rangle = &\begin{Bmatrix} j_1 & 1 & j_2 \\ l_2 & s & l_1 \end{Bmatrix} \begin{pmatrix} l_1 & 1 & l_2 \\ 0 & 0 & 0 \end{pmatrix} \begin{pmatrix} j_1 & 1 & j_2 \\ -m_{j_1} & q & m_{j_2} \end{pmatrix} \\ &\times \langle n_1 l_1 j_1|er|n_2 l_2 j_2\rangle\,(-1)^{j_1 - m_{j_1} + s + j_2 + 1}\sqrt{(2j_1+1)(2j_2+1)(2l_1+1)(2l_2+1)}. \end{aligned} \tag{C.5}$$

Our alkali atoms have spin $s = 1/2$. The radial part, also called reduced dipole moment, $\langle n_1 l_1 j_1|er|n_2 l_2 j_2\rangle$ can be easily computed for Rydberg states with large principal quantum numbers. In that case, the inner electrons are accounted for by a quantum defect and we are left with a hydrogen-like Schrödinger equation that can be solved using Numerov's method [126]. For states with low principal quantum numbers, the many-electron Schrödinger equation has to be solved. We use the tabulated values for rubidium transitions from Refs. [128, 231] that have been obtained by a coupled cluster approach [232]. If no tabulated value is available, we resort to our Numerov code that utilizes tabulated effective quantum defects to include the exact energies of the levels with low principal quantum numbers. The splitting between reduced dipole moment and angular coupling contribution is not unique. Factors like $\sqrt{(2j_1+1)}$ may be included in one or the other. Therefore, it is advisable to pay close attention to the definition used in each reference and to cross check the extracted transition dipole moments by computing known values like spontaneous emission rates and/or (static) polarizabilities. We have also implemented a cross-link to the ARC code [233, 234] that provides dipole moments for all alkali species utilizing techniques analogous to those described above.

We can treat the hyperfine structure analogously to the fine structure. Taking into account the additional coupling $f = j + I$, we obtain

$$\begin{aligned}&\langle n_1 l_1 j_1 f_1 m_{f_1} | \hat{d}_q | n_2 l_2 j_2 f_2 m_{f_2} \rangle = \langle n_1 l_1 j_1 f_1 | er | n_2 l_2 j_2 f_2 \rangle \, (-1)^{f_1+f_2+j_1+j_2+s+I-m_{f_1}} \\ &\times \begin{Bmatrix} f_1 & 1 & f_2 \\ j_2 & I & j_1 \end{Bmatrix} \begin{Bmatrix} j_1 & 1 & j_2 \\ l_2 & s & l_1 \end{Bmatrix} \begin{pmatrix} l_1 & 1 & l_2 \\ 0 & 0 & 0 \end{pmatrix} \begin{pmatrix} f_1 & 1 & f_2 \\ -m_{f_1} & q & m_{f_2} \end{pmatrix} \\ &\times \sqrt{(2f_1+1)(2f_2+1)(2j_1+1)(2j_2+1)(2l_1+1)(2l_2+1)}. \end{aligned} \tag{C.6}$$

Due to the very small hyperfine splitting, we can usually neglect the F dependence of the reduced dipole moment, $\langle n_1 l_1 j_1 f_1 | er | n_2 l_2 j_2 f_2 \rangle \approx \langle n_1 l_1 j_1 | er | n_2 l_2 j_2 \rangle$. The Wigner 3j and 6j symbols vanish unless certain bounds are fulfilled. From these inequalities and the above expressions, we obtain the well-known dipole selection rules[1]:

$$\Delta l = \pm 1; \quad \Delta j = 0, \pm 1; \quad \Delta m_j = 0, \pm 1; \quad \Delta f = 0, \pm 1; \quad \Delta m_f = 0, \pm 1. \tag{C.7}$$

After we have computed the dipole moments in a spherical basis, we return to the Cartesian basis used to evaluate the Green's tensor. With the quantization axis in z- or x-direction, we have [106]

$$\mathbf{d}_z = \left(\frac{d_{-1,z} - d_{+1,z}}{\sqrt{2}}, i\frac{[d_{-1,z} + d_{+1,z}]}{\sqrt{2}}, d_{0,z} \right)^T, \tag{C.8}$$

$$\mathbf{d}_x = \left(d_{0,x}, i\frac{[d_{-1,x} + d_{+1,x}]}{\sqrt{2}}, \frac{d_{-1,x} - d_{+1,x}}{\sqrt{2}} \right)^T, \tag{C.9}$$

respectively. The atomic energy levels can be found in the NIST Atomic Spectra Database [235].

---

[1] Additionally $0 \leftrightarrow 0$ transitions of j and f are forbidden and if $\Delta j = 0$ or $\Delta f = 0$ the corresponding $m_{j_1} = 0$ to $m_{j_2} = 0$ is also forbidden.

D. Permittivity models

The computation of dispersion interactions such as the Casimir–Polder shift requires knowledge of the permittivity across the electromagnetic spectrum. Permittivity models have to be Kramers–Kronig consistent, Eqs. (2.10) and (2.11), to provide reliable results at imaginary frequencies. We present techniques that meet these high demands and hint at their limitations.

The simplest causal description of a medium is a combined Drude and Drude–Lorentz model. The Drude–Lorentz terms account for bound charges through a set of harmonic oscillators. Free charges are described by an additional Drude term with a resonance or plasma frequency ω_p. The permittivity takes the form [236]

$$\epsilon(\omega) = 1 - \frac{f_0 \omega_P}{\omega(\omega + i\Gamma_0)} + \sum_j \frac{f_j \omega_P^2}{(\omega_j^2 - \omega^2 - i\omega\Gamma_j)}, \tag{D.1}$$

with damping constant Γ_j, resonance frequency ω_j, and oscillator strength f_j of the jth oscillator, respectively. Ref. [236] provides the parameters for various metallic films. Furthermore, the optical constants of many materials may be found in the five-volume book set by Palik [201].

Besides the intraband transitions accounted for by the Drude and Drude–Lorentz terms, there are also interband transitions where electrons have to bridge an energy gap E_g. At small frequencies ($\omega \ll E_g/\hbar$), the contribution of these terms can be written as a real constant $\epsilon(\infty)$. Since our frequency integrals reach beyond the regime where a constant is a valid description, it is sensible to look for a better model. A harmonic oscillator is no viable choice because it does not describe the sudden onset of absorption when the photon energy reaches the gap band energy. Instead, one can combine a model for the joint density of states (following Tauc) with a quantum mechanical calculation (sometimes named after Lorentz) and obtains an expression for the imaginary part of the permittivity that is referred to as Tauc–Lorentz model [237, 238]. Through Kramers–Kronig transformation, one obtains a lengthy but closed-form expression for the real part. The susceptibility of a single Tauc–Lorentz transition reads [237, 238]

$$\begin{aligned}
\chi_{\mathrm{TL}}(\omega) = {} & \frac{AC}{2\pi\zeta^4\alpha E_0}\left[(E_g^2 - E_0^2)\hbar^2\omega^2 + E_g^2C^2 - E_0^2(E_0^2 + 3E_g^2)\right]\ln\left(\frac{E_0^2 + E_g^2 + \alpha E_g}{E_0^2 + E_g^2 - \alpha E_g}\right)\\
& - \frac{A}{\pi\zeta^4 E_0}\left[(\hbar^2\omega^2 - E_0^2)(E_0^2 + E_g^2) + E_g^2C^2\right]\left(\pi - \arctan\left(\frac{2E_g + \alpha}{C}\right) + \arctan\left(\frac{\alpha - 2E_g}{C}\right)\right)\\
& + 2AE_0E_g\frac{\hbar^2\omega^2 - \gamma^2}{\pi\zeta^4\alpha}\left(\pi + 2\arctan\left(\frac{2(\gamma^2 - E_g^2)}{\alpha C}\right)\right) - AE_0C\frac{\hbar^2\omega^2 + E_g^2}{\pi\zeta^4\hbar\omega}\ln\left(\frac{|\hbar\omega - E_g|}{\hbar\omega + E_g}\right)\\
& + \frac{2AE_0CE_g}{\pi\zeta^4}\ln\left(\frac{|\hbar\omega - E_g|(\hbar\omega + E_g)}{\sqrt{(E_0^2 - E_g^2)^2 + E_g^2C^2}}\right) + i\frac{\Theta(\hbar\omega - E_g)AE_0C(\hbar\omega - E_g)^2}{\hbar\omega[(\hbar^2\omega^2 - E_0^2)^2 + C^2\hbar^2\omega^2]},
\end{aligned} \tag{D.2}$$

using the abbreviations

$$\alpha = \sqrt{4E_0^2 - C^2}, \quad \gamma = \sqrt{E_0^2 - C^2/2}, \quad \zeta^4 = (\hbar^2\omega^2 - \gamma^2)^2 + (\alpha^2 C^2)/4. \tag{D.3}$$

Here E_0 is the peak transition energy, C is a broadening parameter and A is the proportionality factor of the absorption strength. Bear in mind that the correct form of the model is stated in the erratum [238] not in Ref. [237]. The model can be further improved, e.g., by taking into account that the band edge is not sharp but possesses an exponential tail [239]. In practice, one fits tabulated high-frequency data, e.g., from Ref. [201] to one or more Tauc–Lorentz transitions. The total permittivity is the sum of Drude–Lorentz and Tauc–Lorentz terms.

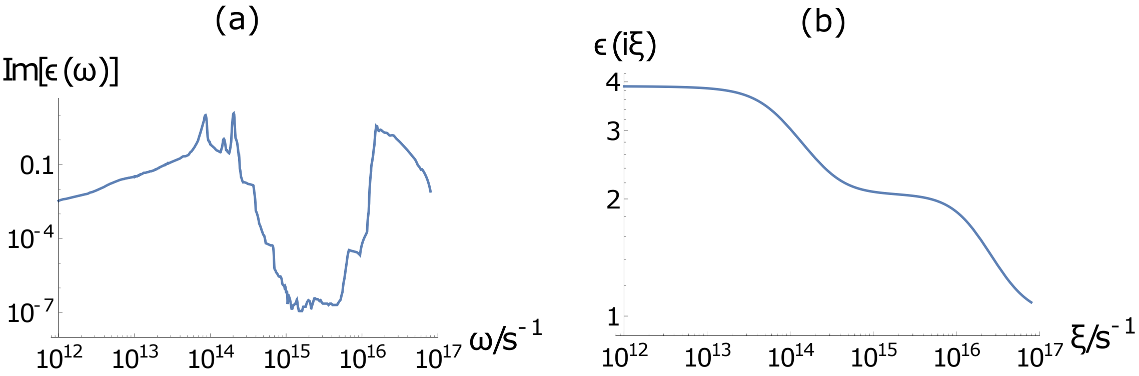

Figure D.1: Permittivity of fused silica [126]. The real frequencies data (a) was taken from Ref. [240]; the data at imaginary frequencies (b) was obtained through Kramers–Kronig transformation. The extremely low losses in the optical window between $\omega = 2.7 \times 10^{15}$ Hz and $\omega = 4.7 \times 10^{15}$ Hz are a distinctive feature of glass.

In rare cases, the literature offers complete permittivity data over all relevant frequencies, e.g., for fused silica [240]. Then, the permittivity at imaginary frequencies can also be obtained through a numerical Kramers–Kronig transformation, Eq. (2.10),

$$\epsilon(i\xi) = 1 + \frac{2}{\pi}\int_0^\infty d\omega \frac{\omega \mathrm{Im}\,\epsilon(\omega)}{\omega^2 + \xi^2}. \tag{D.4}$$

The results are shown in Fig. D.1. Notice that due to the reflection principle (2.9), the permittivity of purely imaginary frequencies is always a real function. We can check the consistency of our data by comparing the static value of the permittivity with the result of the Kramers–Kronig transformation. We find that $\lim_{\omega\to 0} \epsilon(\omega) = 3.7$ and $\lim_{\xi\to 0} \epsilon(i\xi) = 3.9$ deviate by about 6% [126]. This is acceptable given the fact that we are integrating uncertainties over many orders of magnitude and across the many different experimental works that have been compiled in Ref. [240]. The Kramers–Kronig can also be used at real frequencies

$$\begin{aligned}\operatorname{Re}\epsilon(\omega)-1=&\frac{1}{\pi}\mathcal{P}\int_0^\infty d\omega'\frac{\operatorname{Im}\epsilon(\omega')}{\omega'-\omega}+\frac{1}{\pi}\mathcal{P}\int_0^\infty d\omega'\frac{\operatorname{Im}\epsilon(\omega')}{\omega'+\omega} &\text{(D.5)}\\ \approx&\frac{1}{\pi}\mathcal{P}\int_a^b d\omega'\frac{\operatorname{Im}\epsilon(\omega')}{\omega'-\omega}+\frac{1}{\pi}\mathcal{P}\int_a^b d\omega'\frac{\operatorname{Im}\epsilon(\omega')}{\omega'+\omega}, &\text{(D.6)}\end{aligned}$$

where a and b border the interval where $\operatorname{Im}\epsilon(\omega)$ is appreciable larger than 0. The divergence at $\omega=\omega'$ requires special treatment. A standard approach is to add a term $0=I-I$ with

$$I=\frac{1}{\pi}\int_a^b d\omega'\frac{\operatorname{Im}\epsilon(\omega)}{\omega'-\omega}=\frac{\operatorname{Im}\epsilon(\omega)}{\pi}\ln\left(\frac{b-\omega}{\omega-a}\right), \tag{D.7}$$

where $a<\omega<b$. Then,

$$\operatorname{Re}\epsilon(\omega)\approx 1+\frac{1}{\pi}\mathcal{P}\int_a^b d\omega'\left(\frac{\operatorname{Im}\epsilon(\omega')-\operatorname{Im}\epsilon(\omega)}{\omega'-\omega}+\frac{\operatorname{Im}\epsilon(\omega')}{\omega'+\omega}\right)+\frac{\operatorname{Im}\epsilon(\omega)}{\pi}\ln\left(\frac{b-\omega}{\omega-a}\right), \tag{D.8}$$

which can be handled by standard numerical integration techniques. Due to the added zero, the integrand approaches the well-defined derivative $\operatorname{Im}\epsilon'(\omega)$ at $\omega'=\omega$ instead of running into a logarithmic divergence.

In the context of dispersion interactions, even extensive permittivity data and models must always be taken with a grain of salt. The permittivity depends on many factors that will vary across different experiments, such as variations in the material preparation or composition, layer sizes, dopants, impurities, temperature, and so on. When a dominant atomic transition is very close to a material resonance, the Casimir–Polder shift strongly depends on the exact modeling of the material resonances as observed in [159, 160].

E. Additions regarding spectra and their computation

E.1. Oscillation correction

Suppose we have a function $g(x)$ that is obtained through an expensive numerical computation[1]. It shall feature a rapid oscillation on top of a slow or constant trend $c(x)$ that we seek to extract from it. We assume $g(x)$ to be of the form

$$g(x) = \cos\left(2\pi\frac{x}{L} + \varphi_0\right) f(x) + c(x), \tag{E.1}$$

where the oscillation period L is known, but φ_0, $f(x)$, and $c(x)$ are unknown. Furthermore, we assume that over the course of one oscillation period, we can approximate $c(x) \approx c(x_0)$ as constant and $f(x) \approx f(x_0) + (x - x_0)f'(x_0)$ by the linear part of its Taylor series. Then, starting from an arbitrary x_0, we evaluate $g(x)$ at

$$g(x_0) = \cos\left(2\pi\frac{x_0}{L} + \varphi_0\right) f(x_0) + c(x_0), \tag{E.2}$$

$$g(x_0 + L/2) = -\cos\left(2\pi\frac{x_0}{L} + \varphi_0\right) \left[f(x_0) + \frac{L}{2}f'(x_0)\right] + c(x_0), \tag{E.3}$$

$$g(x_0 + L) = \cos\left(2\pi\frac{x_0}{L} + \varphi_0\right) \left[f(x_0) + Lf'(x_0)\right] + c(x_0). \tag{E.4}$$

Solving this linear equation system, one finds that

$$c(x_0) = \frac{g(x_0) + 2g(x_0 + L/2) + g(x_0 + L)}{4}, \tag{E.5}$$

which may be much cheaper to compute than $g(x \to \infty)$ at a given precision. If $g(x)$ contains multiple oscillation frequencies, the oscillation correction is subsequently applied for each one of them.

E.2. Input-output relation for multilayered media

To obtain the reflectivity and transmissivity of a dielectric stack for normal incidence, we have used the input-output formalism of Ref. [138] that is reproduced in the following. The input-output matrix $\boldsymbol{S}$, illustrated in Fig. E.1 b, is directly connected to standard transmission and reflection coefficients. The $\boldsymbol{M}$ matrix, on the other hand, swaps particular input and output variables as shown in Fig. E.1 a. It is less intuitive but has the advantage that a stack of layers can be described by consecutively applying the $\boldsymbol{M}$ matrices of the individual layers,

---

[1] Here this is usually a selective reflection integral whose upper bound has been truncated to the finite value x.

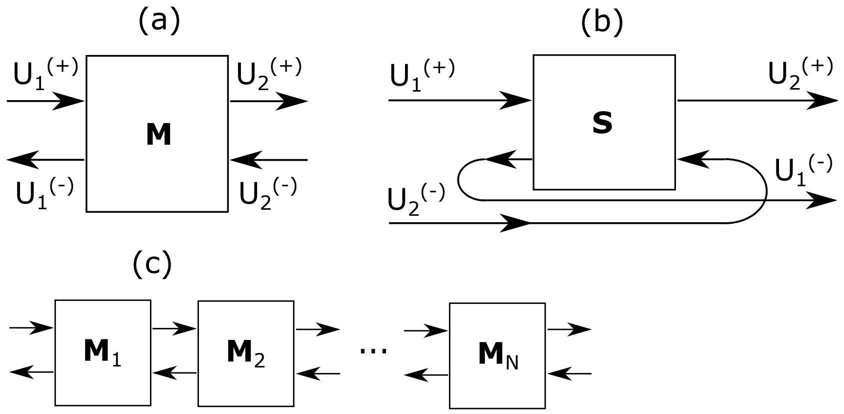

Figure E.1: Illustration of matrix input-output relations, compare [138].

$\boldsymbol{M} = \boldsymbol{M}_N \cdots \boldsymbol{M}_2 \boldsymbol{M}_1$ as in Fig. E.1 c. The $\boldsymbol{S}$ and $\boldsymbol{M}$ matrices are given as

$$\begin{pmatrix} U_2^{(+)} \\ U_1^{(-)} \end{pmatrix} = \underbrace{\begin{pmatrix} t_{12} & r_{21} \\ r_{12} & t_{21} \end{pmatrix}}_{=\boldsymbol{S}} \begin{pmatrix} U_1^{(+)} \\ U_2^{(-)} \end{pmatrix}, \quad \begin{pmatrix} U_2^{(+)} \\ U_2^{(-)} \end{pmatrix} = \underbrace{\begin{pmatrix} A & B \\ C & D \end{pmatrix}}_{=\boldsymbol{M}} \begin{pmatrix} U_1^{(+)} \\ U_1^{(-)} \end{pmatrix}. \tag{E.6}$$

To describe each layer of a dielectric stack, we need two types of $\boldsymbol{M}$ matrices: One for the propagation over a distance w in a medium of refractive index n and one for the transition from a medium of index n_1 to a medium of index n_2 [138]

$$\boldsymbol{M}_w = \begin{pmatrix} e^{inkw} & 0 \\ 0 & e^{-inkw} \end{pmatrix}, \quad \boldsymbol{M}_{12} = \frac{1}{2n_2} \begin{pmatrix} n_2 + n_1 & n_2 - n_1 \\ n_2 - n_1 & n_2 + n_1 \end{pmatrix}. \tag{E.7}$$

The total $\boldsymbol{M}$ matrix can be computed and is then converted into the $\boldsymbol{S}$ matrix form. Following the definitions (E.6) we can obtain it from the $\boldsymbol{M}$ matrix elements as

$$\boldsymbol{S} = \frac{1}{D} \begin{pmatrix} AD - BC & B \\ -C & 1 \end{pmatrix}. \tag{E.8}$$

The elements of $\boldsymbol{S}$ can be identified as transmission or reflection coefficients of the total stack according to Eq. (E.6).

E.3. Casimir–Polder effect with an atom-surface resonance

In this section, we investigate the strong Casimir–Polder shift and Purcell broadening of a rubidium $5P_{3/2} \rightarrow 6D_{3/2}$ transition in front of a sapphire surface. First, let us take a closer look at the $6D_{3/2}$ state and the transitions in Fig. E.2 that determine its Casimir–Polder shift against a perfect reflector and its linewidth in free space. We can infer a general characteristic

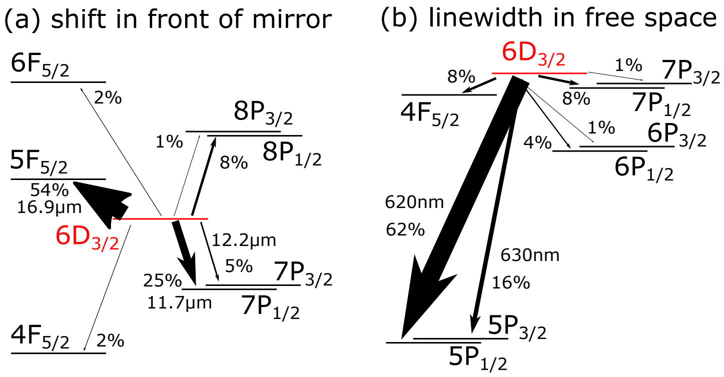

Figure E.2: Selected transitions from the energy level diagram of rubidium around the $6D_{3/2}$ state that are (a) important for its Casimir–Polder shift in front of a perfect reflector or (b) important its free-space linewidth at zero temperature. The percent values alongside the arrows indicate the relative contribution of the transition to the total C_3 coefficient (a) or the linewidth (b). The lengths refer to the transition wavelength in vacuum.

of higher excited states: The line shift is governed by transitions to adjacent states because it predominantly depends on the atomic transition dipoles moment. The linewidth, on the other hand, favors transitions to the lowest energy states with the largest $\omega_{A,nm}$ as it depends on $\omega^3_{A,nm}|d_{A,nm}|^2$, recall Eq. (2.26). Since the wave functions of the excited states are much larger than those of the lowest energy states, there is little spatial overlap between them. The transition dipole moments are small. The larger $\omega_{A,nm}$ values cannot compensate this so that usually the higher the atom is excited, the smaller the linewidth becomes [8]. Despite its small principal quantum number, the state $6D_{3/2}$ behaves almost like a Rydberg state. Its free space linewidth (3.9 MHz rad) is ten times smaller compared to the $5P_{3/2}$ state, while its Casimir–Polder shift at a perfect reflector is roughly 40 times larger due to its high polarizability.

However, the most important property of the rubidium $6D_{3/2}$ state for this section is that its atom-wall interaction is impacted by the $6D_{3/2} \to 7P_{1/2}$ transition, whose wavelength of 11.7 µm (see Fig. E.2) coincides with a strong resonance of the sapphire surface[2] at 12 µm [159, 160]. Such a match between a material resonance and an atomic transition frequency leads to a strong, resonant Casimir–Polder interaction [159, 160]. In order to probe it, the $6D_{3/2}$ state can be reached with a dipole-allowed transition starting from the $5P_{3/2}$ state[3] that we already investigated in Sec. 3.1.2. The results for our state pair at zero temperature are shown in Fig. E.3. The effective C_3 coefficient features a positive[4] sign. This can be understood, as so often, with the help of a harmonic oscillator. When driven close to its resonance, a harmonic oscillator features a phase shift between driving force and response. Here, such a resonance-induced phase shift reverses the orientation of the mirror dipole in Fig. 3.1, which leads to a repulsive force between atom and surface and an inverted sign in the interaction

---

[2] More precisely, it is the resonance of image charge factor $[\epsilon_2(\omega) - 1]/[\epsilon_2(\omega) + 1]$ of the sapphire-vacuum interface that determines the surface Green's function, recall App. A.2.

[3] One could also use a $5P_{1/2} \to 6D_{3/2}$ transition, which has an even more preferable dipole moment, see Fig. E.2.

[4] Other works define their potential as $-\tilde{C}_3/z^3$ and hence find a negative $\tilde{C}_3$.

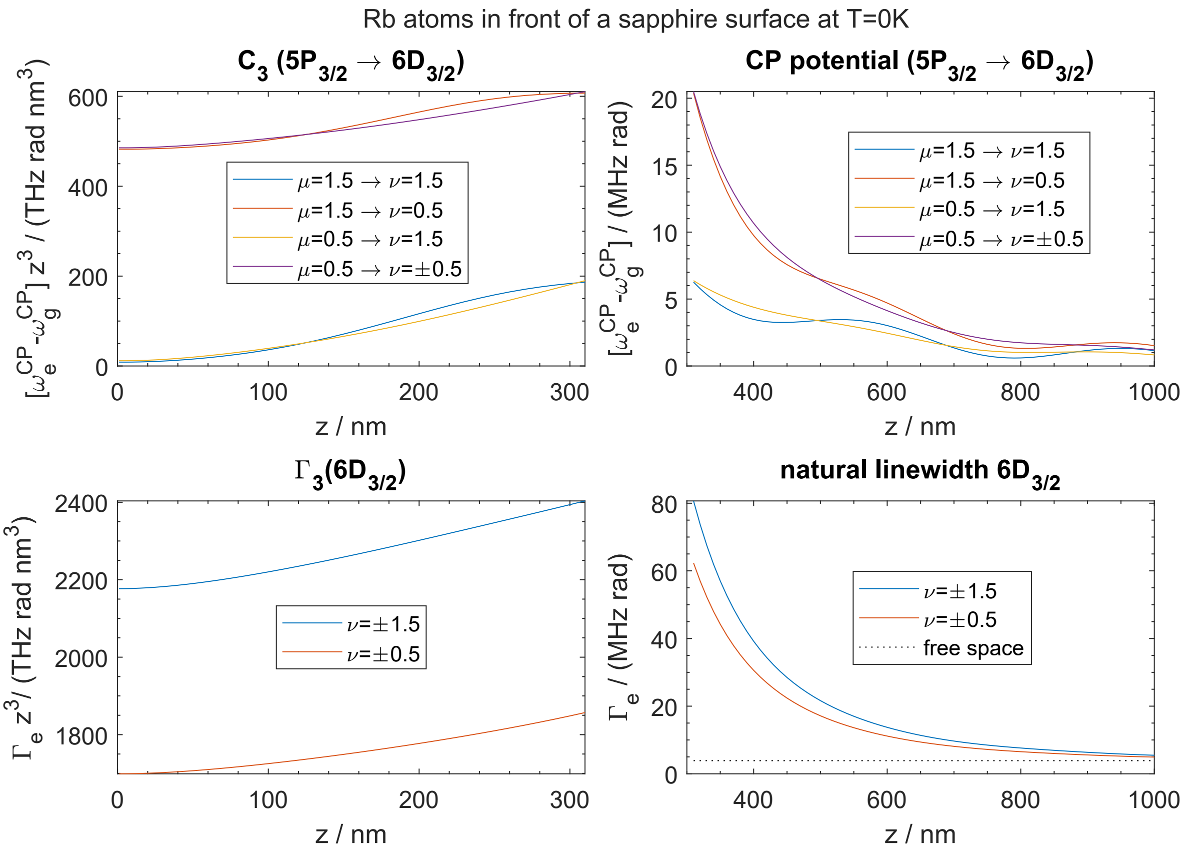

Figure E.3: Casimir–Polder line shift of the rubidium $5P_{3/2} \to 6D_{3/2}$ transition (upper part) and Purcell line broadening of a $6D_{3/2}$ state (lower part) over the distance z between rubidium atom and a sapphire surface at zero temperature. They are given with respect to the m_j sublevel of the lower (μ) and upper state (ν) state. The results are the same when the signs of μ and ν are reversed, e.g., from $\mu = 0.5 \to \nu = 1.5$ to $\mu = -0.5 \to \nu = -1.5$. At short distances, potential and linewidth are multiplied by z^3 to obtain an effective C_3 or Γ_3 coefficient. The properties of the $5P_{3/2} \to 6D_{3/2}$ transition also depend on the broadening of the $5P_{3/2}$ state shown in Fig. 3.4.

potential. It is important to note that the CP shift depends not only on the resonant transition but also on many others (recall Fig. E.2) that contribute to an attractive interaction. The overall result is a balance of both effects. Due to the large transition wavelength $> 10\,\mu\mathrm{m}$, finite temperature plays an important role for the interaction. Since it affects transitions with different wavelengths unequally, it can tilt the balance of attractive and repulsive terms or the relative strength of the upper and lower level shift, such that the sign of the Casimir–Polder shift can change as shown in Fig. E.4.

Another signature of atom-surface resonance is the fact that the linewidth is approximately proportional to $1/z^3$ over the same distance regime as the shift. Due to the large surface absorption, the nonretarded approximation in Eq. (3.3) applies to both real and imaginary part of the Green's tensor. We encounter large shifts and broadenings on the order of 0.5 THz rad and 2 THz rad, respectively, already at a 10 nm distance from the surface. The angular frequency of the $6D_{3/2} \to 7P_{1/2}$ transition is only $\omega_{eg} \approx 160\,\mathrm{THz\,rad}$. Therefore our assumption that the

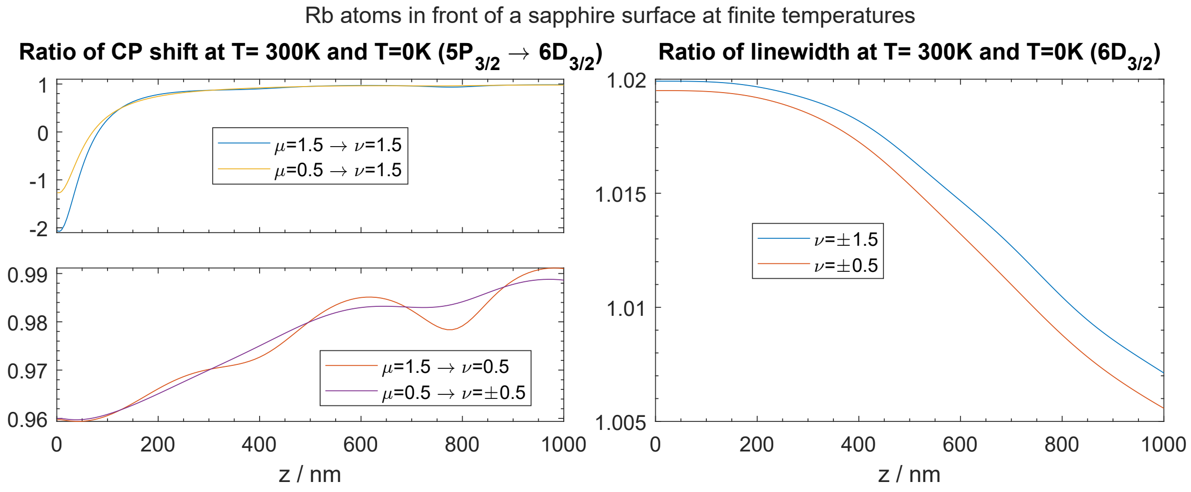

Figure E.4: Casimir–Polder shift of the rubidium $5P_{3/2} \rightarrow 6D_{3/2}$ transition and Purcell line broadening of the $6D_{3/2}$ state at $T = 300\,\mathrm{K}$ and divided by the respective $T = 0\,\mathrm{K}$ value over the distance z between rubidium atom and a sapphire surface. The ratios are given with respect to the m_j sublevel of the lower (μ) and upper state (ν) state.

effect of the atom-wall interaction is perturbatively small compared to the original transition frequency will likely not hold for atoms much closer than 10 nm to the surface. However, due to the large linewidth, such atoms only have a very small polarizability, decay almost instantaneously and should have no significant impact on the vapor cell spectra.

In presence of an atom-surface resonance, the predication of the atom-wall interaction is notoriously difficult as it depends sensitively on the exact atomic dipole moments and surface properties. For sapphire, for example, the orientation of the optical axis is relevant [218]. But many other factors like roughness, impurities, preparation methods, temperature[5] take effect too. Usually, not all of these influences are known or well characterized, which leads to uncertainties that must be carefully considered when comparing theory and experiment.

E.3.1. Frequency-modulated selective reflection spectrum

Analogously to Sec. 3.4.1, we have computed the FMSR spectrum of the rubidium $5P_{3/2} \rightarrow 6D_{3/2}$ transition at a sapphire surface at $T = 300\,\mathrm{K}$ using Eqs. (3.52) and (3.64). Again, we assume that the m_j sublevels of the lower state, here the $5P_{3/2}$ state, are equally populated. In an experiment, this requires a careful state preparation protocol, see Ref. [160]. We have again used the oscillation correction scheme[6] from App. E.1 to truncate the computational domain to a maximum atom-surface distance of 5.6 µm. The resulting spectrum is shown in Fig. E.5.

---

[5] Temperature may modify not only fluctuations but also the material's permittivity such that $\epsilon = \epsilon(\omega, T)$.

[6] We start at $w = 3.0\,\mu\mathrm{m}$ and average out three different oscillation periods. First the usual two, the probe field with 630 nm and half of it 315 nm = 630/2 nm and then a third that is a mixture of the CP oscillation period of the $5P_{3/2}$ state with 390 nm = 780/2 nm and half the probe field period that becomes roughly 1640 nm, where $-1/390 + 1/315 \approx 1/1638$.

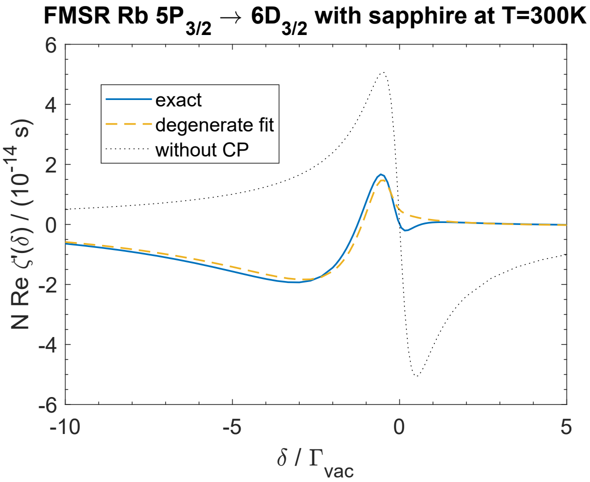

Figure E.5: FMSR spectra of the rubidium $5\mathrm{P}_{3/2} \to 6\mathrm{D}_{3/2}$ at a sapphire surface at $T = 300\,\mathrm{K}$ and a density of $N = 0.01k^3$. The dashed line indicates the result one would obtain if no atom-wall interaction was present. Additionally, a four-parameter fit is shown that includes a prefactor, a constant linewidth, a constant C_3, and a Γ_3 coefficient that are equal for all substates.

Besides the usual line shape, we see another dip in the blue that cannot be described by our simplified fit model (see Sec. 3.4.1), although the model has been extended by a fourth parameter Γ_3. The dip also appears when the zero temperature shifts and broadening of Fig. E.3 are used. To the best of my knowledge, it has no precedence in experimental studies. It appears to be caused by the long-range behavior of the exact linewidth and shift that at some point no longer obey the $1/z^3$ law. It is quite possible that the dip is an artifact with no physical significance as it could originate from the assumption of a flat velocity distribution in Eq. (3.52). This treatment was based on the assertion that the relevant Casimir–Polder shift, the Purcell line broadening, and detuning are small compared to the Doppler shift kv_{th}. For the D-line FMSR spectra in Sec. 3.4.1, the assertion seems to hold. In a sample computation at $\delta = 0$, we found that the integrand of Eq. (3.64) agrees with an exact numerical velocity integration on the order of 1%[7]. However, the transition considered here features much larger shifts and broadenings, and the same comparison shows deviations on the order 10%. In the z and z' plane, the integrand looks like a series of mountains and valleys. The integral involves the cancellation of positive and negative contributions, which makes it possible for even small deviations to have a considerable effect on the total. Therefore, the spectra must be recalculated using the full velocity distribution $W(v_z)$ before any inferences can be made. This requires a considerable numerical effort and/or a sophisticated implementation of the highly oscillatory v integral and must be left to future work.

---

[7] On a grid of sample points z_i, z_i' that covers the area important for the z and z' double integral, we computed the difference between an integrand $f(z_i, z_i')$ obtained from the flat distribution and an integrand $g(z_i, z_i')$ obtained from the Maxwell-Boltzmann distribution. We normalised the result with the largest value of $g(z_i, z_i')$. The largest deviation found like this was 1%.

E.4. Additional dense vapor spectra

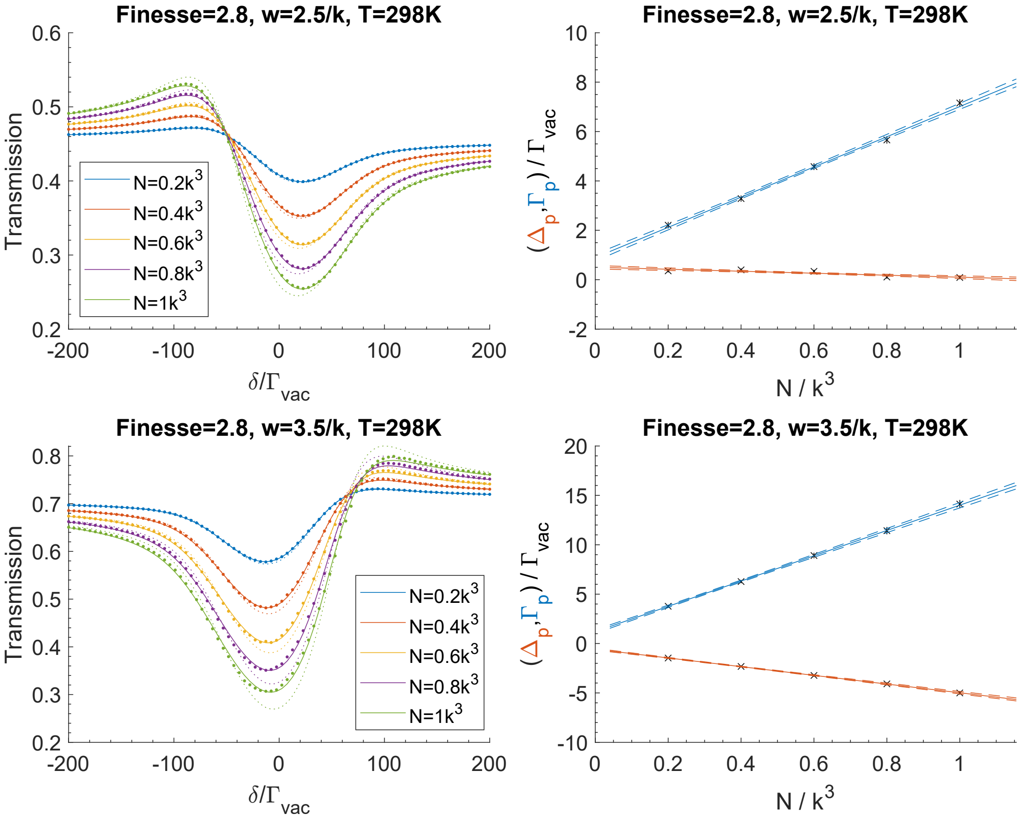

Figure E.6: Left: Transmission spectra through a nanocavity filled with rubidium vapor for two different cavity widths w. Right: Fitted collective broadening and shift Δ_p, Γ_p plotted against the vapor density. The graphs are analogous to Fig. 4.3 but for a coated cavity with Finesse 2.8, see Fig. 4.6.

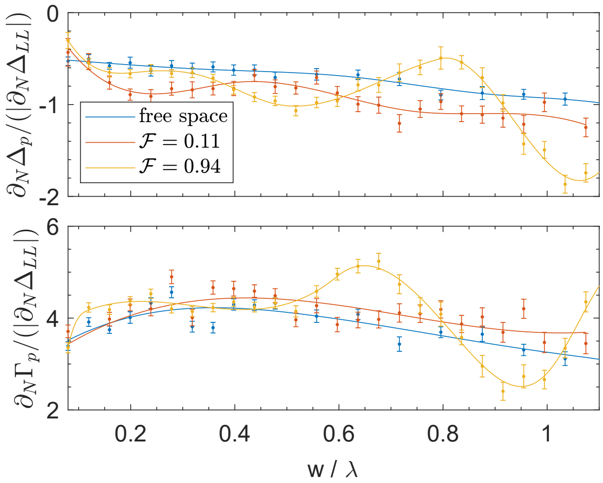

Figure E.7: Slope of collective shift (top) and broadening (bottom) over width d of an atomic layer in free space, a sapphire cavity, or a cavity with anti-reflection coating depicted in Fig. 4.6. Error bars correspond to 1σ. The solid lines are spline interpolations. Compare Ref. [194].

Bibliography

[1] J. P. Dowling and G. J. Milburn, *Quantum technology: the second quantum revolution*, Philos. Trans. R. Soc. London, Ser. A **361**, 1655–1674 (2003).

[2] A. Acín, I. Bloch, H. Buhrman, T. Calarco, C. Eichler, J. Eisert, D. Esteve, N. Gisin, S. J. Glaser, F. Jelezko, S. Kuhr, M. Lewenstein, M. F. Riedel, P. O. Schmidt, R. Thew, A. Wallraff, I. Walmsley, and F. K. Wilhelm, *The quantum technologies roadmap: a European community view*, New J. Phys. **20**, 080201 (2018).

[3] *International Roadmap for Devices and Systems (IRDS™): Cryogenic Electronics and Quantum Information Processing*, Available: `https://irds.ieee.org` (2020).

[4] R. Löw and T. Pfau, *Hot atoms rotate light rapidly*, Nat. Photon. **3**, 197–199 (2009).

[5] D. E. Chang, J. S. Douglas, A. González-Tudela, C.-L. Hung, and H. J. Kimble, *Colloquium: Quantum matter built from nanoscopic lattices of atoms and photons*, Rev. Mod. Phys. **90**, 031002 (2018).

[6] D. A. Steck, *Alkali D Line Data*, Available: `http://steck.us/alkalidata/` (2015).

[7] T. G. Tiecke, *Properties of Potassium (rev. 1.03)*, Available: `https://tobiastiecke.nl/archive/PotassiumProperties.pdf` (2019).

[8] T. F. Gallagher, *Rydberg atoms*, 1st ed. (Cambridge University Press, 1994).

[9] E. Urban, T. A. Johnson, T. Henage, L. Isenhower, D. D. Yavuz, T. G. Walker, and M. Saffman, *Observation of Rydberg blockade between two atoms*, Nat. Phys. **5**, 110–114 (2009).

[10] A. Gaëtan, Y. Miroshnychenko, T. Wilk, A. Chotia, M. Viteau, D. Comparat, P. Pillet, A. Browaeys, and P. Grangier, *Observation of collective excitation of two individual atoms in the Rydberg blockade regime*, Nat. Phys. **5**, 115–118 (2009).

[11] F. Ripka, H. Kübler, R. Löw, and T. Pfau, *A room-temperature single-photon source based on strongly interacting Rydberg atoms*, Science **362**, 446–449 (2018).

[12] K. Hammerer, A. S. Sørensen, and E. S. Polzik, *Quantum interface between light and atomic ensembles*, Rev. Mod. Phys. **82**, 1041 (2010).

[13] O. Katz and O. Firstenberg, *Light storage for one second in room-temperature alkali vapor*, Nat. Commun. **9**, 1–6 (2018).

[14] N. Sangouard, C. Simon, H. De Riedmatten, and N. Gisin, *Quantum repeaters based on atomic ensembles and linear optics*, Rev. Mod. Phys. **83**, 33 (2011).

[15] R. Ritter, *Interfacing thermal atoms with integrated photonic waveguides*, Ph.D. thesis, Universität Stuttgart (2018).

[16] R. Ritter, N. Gruhler, H. Dobbertin, H. Kübler, S. Scheel, W. Pernice, T. Pfau, and R. Löw, *Coupling Thermal Atomic Vapor to Slot Waveguides*, Phys. Rev. X **8**, 021032 (2018).

[17] J. Keaveney, *Collective Atom-Light Interactions in Dense Atomic Vapours* (Springer, 2014).

[18] J. Keaveney, A. Sargsyan, U. Krohn, I. G. Hughes, D. Sarkisyan, and C. S. Adams, *Cooperative Lamb Shift in an Atomic Vapor Layer of Nanometer Thickness*, Phys. Rev. Lett. **108**, 173601 (2012).

[19] M. A. Zentile, D. J. Whiting, J. Keaveney, C. S. Adams, and I. G. Hughes, *Atomic Faraday filter with equivalent noise bandwidth less than 1 GHz*, Opt. Lett. **40**, 2000–2003 (2015).

[20] S. L. Portalupi, M. Widmann, C. Nawrath, M. Jetter, P. Michler, J. Wrachtrup, and I. Gerhardt, *Simultaneous Faraday filtering of the Mollow triplet sidebands with the Cs-*D_1 *clock transition*, Nat. Commun. **7**, 1–6 (2016).

[21] L. Weller, K. S. Kleinbach, M. A. Zentile, S. Knappe, I. G. Hughes, and C. S. Adams, *Optical isolator using an atomic vapor in the hyperfine Paschen–Back regime*, Opt. Lett. **37**, 3405–3407 (2012).

[22] J. Schmidt, M. Fiedler, R. Albrecht, D. Djekic, P. Schalberger, H. Baur, R. Löw, N. Fruehauf, T. Pfau, J. Anders, E. R. Grant, and H. Kübler, *Proof of concept for an optogalvanic gas sensor for NO based on Rydberg excitations*, Appl. Phys. Lett. **113**, 011113 (2018).

[23] Z. Chen, H. M. Lim, C. Huang, R. Dumke, and S.-Y. Lan, *Quantum-Enhanced Velocimetry with Doppler-Broadened Atomic Vapor*, Phys. Rev. Lett. **124**, 093202 (2020).

[24] A. K. Mohapatra, M. G. Bason, B. Butscher, K. J. Weatherill, and C. S. Adams, *A giant electro-optic effect using polarizable dark states*, Nat. Phys. **4**, 890–894 (2008).

[25] J. A. Sedlacek, A. Schwettmann, H. Kübler, R. Löw, T. Pfau, and J. P. Shaffer, *Microwave electrometry with Rydberg atoms in a vapour cell using bright atomic resonances*, Nat. Phys. **8**, 819–824 (2012).

[26] J. A. Sedlacek, A. Schwettmann, H. Kübler, and J. P. Shaffer, *Atom-Based Vector Microwave Electrometry Using Rubidium Rydberg Atoms in a Vapor Cell*, Phys. Rev. Lett. **111**, 063001 (2013).

[27] A. Horsley, G.-X. Du, M. Pellaton, C. Affolderbach, G. Mileti, and P. Treutlein, *Imaging of relaxation times and microwave field strength in a microfabricated vapor cell*, Phys. Rev. A **88**, 063407 (2013).

[28] A. Horsley, G.-X. Du, and P. Treutlein, *Widefield microwave imaging in alkali vapor cells with sub-100 μm resolution*, New J. Phys. **17**, 112002 (2015).

[29] S. Knappe, V. Shah, P. D. D. Schwindt, L. Hollberg, J. Kitching, L.-A. Liew, and J. Moreland, *A microfabricated atomic clock*, Appl. Phys. Lett. **85**, 1460–1462 (2004).

[30] V. Maurice, J. Rutkowski, E. Kroemer, S. Bargiel, N. Passilly, R. Boudot, C. Gorecki, L. Mauri, and M. Moraja, *Microfabricated vapor cells filled with a cesium dispensing paste for miniature atomic clocks*, Appl. Phys. Lett. **110**, 164103 (2017).

[31] J. Kitching, S. Knappe, and E. A. Donley, *Atomic Sensors — a Review*, IEEE Sens. J. **11**, 1749–1758 (2011).

[32] J. Kitching, *Chip-scale atomic devices*, Appl. Phys. Rev. **5**, 031302 (2018).

[33] I. K. Kominis, T. W. Kornack, J. C. Allred, and M. V. Romalis, *A subfemtotesla multichannel atomic magnetometer*, Nature **422**, 596–599 (2003).

[34] M. V. Balabas, D. Budker, J. Kitching, P. D. D. Schwindt, and J. E. Stalnaker, *Magnetometry with millimeter-scale antirelaxation-coated alkali-metal vapor cells*, JOSA B **23**, 1001–1006 (2006).

[35] D. Budker and M. Romalis, *Optical magnetometry*, Nat. Phys. **3**, 227–234 (2007).

[36] D. Budker and D. F. J. Kimball, *Optical Magnetometry*, 1st ed. (Cambridge University Press, 2013).

[37] E. Klinger, H. Azizbekyan, A. Sargsyan, C. Leroy, D. Sarkisyan, and A. Papoyan, *Proof of the feasibility of a nanocell-based wide-range optical magnetometer*, Appl. Opt. **59**, 2231–2237 (2020).

[38] K. Jensen, R. Budvytyte, R. A. Thomas, T. Wang, A. M. Fuchs, M. V. Balabas, G. Vasilakis, L. D. Mosgaard, H. C. Stærkind, J. H. Müller, T. Heimburg, S.-P. Olesen, and E. S. Polzik, *Non-invasive detection of animal nerve impulses with an atomic magnetometer operating near quantum limited sensitivity*, Sci. Rep. **6**, 1–7 (2016).

[39] G. Bison, R. Wynands, and A. Weis, *A laser-pumped magnetometer for the mapping of human cardiomagnetic fields*, Appl. Phys. B **76**, 325–328 (2003).

[40] O. Alem, T. H. Sander, R. Mhaskar, J. LeBlanc, H. Eswaran, U. Steinhoff, Y. Okada, J. Kitching, L. Trahms, and S. Knappe, *Fetal magnetocardiography measurements with an array of microfabricated optically pumped magnetometers*, Phys. Med. Biol. **60**, 4797 (2015).

[41] H. Xia, A. Ben-Amar Baranga, D. Hoffman, and M. V. Romalis, *Magnetoencephalography with an atomic magnetometer*, Appl. Phys. Lett. **89**, 211104 (2006).

[42] T. H. Sander, J. Preusser, R. Mhaskar, J. Kitching, L. Trahms, and S. Knappe, *Magnetoencephalography with a chip-scale atomic magnetometer*, Biomed. Opt. Express **3**, 981–990 (2012).

[43] E. Boto, S. S. Meyer, V. Shah, O. Alem, S. Knappe, P. Kruger, T. M. Fromhold, M. Lim, P. M. Glover, P. G. Morris, R. Bowtell, G. R. Barnes, and M. J. Brookes, *A new generation of magnetoencephalography: Room temperature measurements using optically-pumped magnetometers*, NeuroImage **149**, 404–414 (2017).

[44] T. Peyrot, Y. R. P. Sortais, A. Browaeys, A. Sargsyan, D. Sarkisyan, J. Keaveney, I. G. Hughes, and C. S. Adams, *Collective Lamb Shift of a Nanoscale Atomic Vapor Layer within a Sapphire Cavity*, Phys. Rev. Lett. **120**, 243401 (2018).

[45] L. Stern, B. Desiatov, I. Goykhman, and U. Levy, *Nanoscale light-matter interactions in atomic cladding waveguides*, Nat. Commun. **4**, 1548 (2013).

[46] L. Knöll, S. Scheel, and D.-G. Welsch, in *Coherence and Statistics of Photons and Atoms* edited by J. Peřina (2001), available: `https://arxiv.org/abs/quant-ph/0006121`.

[47] S. Scheel and S. Y. Buhmann, *Macroscopic quantum electrodynamics — concepts and applications*, Acta Phys. Slov. **58**, 675–809 (2008), available: `http://www.physics.sk/aps/pub.php?y=2008&pub=aps-08-05`.

[48] W. Vogel and D.-G. Welsch, *Quantum optics*, 3rd ed. (Wiley, 2006).

[49] T. Gruner and D.-G. Welsch, *Green-function approach to the radiation-field quantization for homogeneous and inhomogeneous Kramers-Kronig dielectrics*, Phys. Rev. A **53**, 1818 (1996).

[50] S. Scheel, L. Knöll, and D.-G. Welsch, *QED commutation relations for inhomogeneous Kramers-Kronig dielectrics*, Phys. Rev. A **58**, 700 (1998).

[51] S. Y. Buhmann, *Dispersion forces I: Macroscopic quantum electrodynamics and ground-state Casimir, Casimir–Polder and van der Waals Forces*, 1st ed. (Springer, 2012).

[52] S. Y. Buhmann, *Dispersion Forces II: Many-Body Effects, Excited Atoms, Finite Temperature and Quantum Friction*, 1st ed. (Springer, 2012).

[53] H. B. G. Casimir and D. Polder, *The influence of retardation on the London-van der Waals forces*, Phys. Rev. **73**, 360 (1948).

[54] D. Sarkisyan, D. Bloch, A. Papoyan, and M. Ducloy, *Sub-Doppler spectroscopy by sub-micron thin Cs vapour layer*, Opt. Commun. **200**, 201–208 (2001).

[55] T. Peyrot, C. Beurthe, S. Coumar, M. Roulliay, K. Perronet, P. Bonnay, C. S. Adams, A. Browaeys, and Y. R. P. Sortais, *Fabrication and characterization of super-polished wedged borosilicate nano-cells*, Opt. Lett. **44**, 1940–1943 (2019).

[56] N. Sekiguchi, T. Sato, K. Ishikawa, and A. Hatakeyama, *Spectroscopic study of a diffusion-bonded sapphire cell for hot metal vapors*, Appl. Opt. **57**, 52–56 (2018).

[57] D. Bloch and M. Ducloy, Atom-wall interaction, in *Adv. At., Mol., Opt. Phys.*, Vol. 50 (Elsevier, 2005) pp. 91–154.

[58] R. W. Wood, *XX. The selective reflexion of monochromatic light by mercury vapour*, Sci. London, Edinburgh Dublin Philos. Mag. **18**, 187–193 (1909).

[59] J. D. Thompson, T. G. Tiecke, N. P. de Leon, J. Feist, A. V. Akimov, M. Gullans, A. S. Zibrov, V. Vuletić, and M. D. Lukin, *Coupling a single trapped atom to a nanoscale optical cavity*, Science **340**, 1202–1205 (2013).

[60] M. Ducloy and M. Fichet, *General theory of frequency modulated selective reflection. Influence of atom surface interactions*, J. Phys. II France **1**, 1429–1446 (1991).

[61] M. Gross and S. Haroche, *Superradiance: An essay on the theory of collective spontaneous emission*, Phys. Rep. **93**, 301–396 (1982).

[62] W. Guerin, M. O. Araújo, and R. Kaiser, *Subradiance in a Large Cloud of Cold Atoms*, Phys. Rev. Lett. **116**, 083601 (2016).

[63] R. H. Dicke, *Coherence in Spontaneous Radiation Processes*, Phys. Rev. **93**, 99 (1954).

[64] D. E. Chang, J. Ye, and M. D. Lukin, *Controlling dipole-dipole frequency shifts in a lattice-based optical atomic clock*, Phys. Rev. A **69**, 023810 (2004).

[65] S. L. Bromley, B. Zhu, M. Bishof, X. Zhang, T. Bothwell, J. Schachenmayer, T. L. Nicholson, R. Kaiser, S. F. Yelin, M. D. Lukin, A. M. Rey, and J. Ye, *Collective atomic scattering and motional effects in a dense coherent medium*, Nat. Commun. **7**, 11039 (2016).

[66] S. L. Campbell, R. B. Hutson, G. E. Marti, A. Goban, N. D. Oppong, R. L. McNally, L. Sonderhouse, J. M. Robinson, W. Zhang, B. J. Bloom, and J. Ye, *A Fermi-degenerate three-dimensional optical lattice clock*, Science **358**, 90–94 (2017).

[67] R. J. Bettles, S. A. Gardiner, and C. S. Adams, *Enhanced Optical Cross Section via Collective Coupling of Atomic Dipoles in a 2D Array*, Phys. Rev. Lett. **116**, 103602 (2016).

[68] E. Shahmoon, D. S. Wild, M. D. Lukin, and S. F. Yelin, *Cooperative Resonances in Light Scattering from Two-Dimensional Atomic Arrays*, Phys. Rev. Lett. **118**, 113601 (2017).

[69] H. A. Lorentz, *Über die Beziehung zwischen der Fortpflanzungsgeschwindigkeit des Lichtes und der Körperdichte*, Ann. Phys. **245**, 641–665 (1880).

[70] L. Lorenz, *Über die Refractionsconstante*, Ann. Phys. **247**, 70–103 (1880).

[71] J. Javanainen, J. Ruostekoski, Y. Li, and S.-M. Yoo, *Shifts of a Resonance Line in a Dense Atomic Sample*, Phys. Rev. Lett. **112**, 113603 (2014).

[72] J. Javanainen, J. Ruostekoski, Y. Li, and S.-M. Yoo, *Exact electrodynamics versus standard optics for a slab of cold dense gas*, Phys. Rev. A **96**, 033835 (2017).

[73] J. Pellegrino, R. Bourgain, S. Jennewein, Y. R. P. Sortais, A. Browaeys, S. D. Jenkins, and J. Ruostekoski, *Observation of Suppression of Light Scattering Induced by Dipole-Dipole Interactions in a Cold-Atom Ensemble*, Phys. Rev. Lett. **113**, 133602 (2014).

[74] S. D. Jenkins, J. Ruostekoski, J. Javanainen, S. Jennewein, R. Bourgain, J. Pellegrino, Y. R. P. Sortais, and A. Browaeys, *Collective resonance fluorescence in small and dense atom clouds: Comparison between theory and experiment*, Phys. Rev. A **94**, 023842 (2016).

[75] L. Corman, J.-L. Ville, R. Saint-Jalm, M. Aidelsburger, T. Bienaimé, S. Nascimbène, J. Dalibard, and J. Beugnon, *Transmission of near-resonant light through a dense slab of cold atoms*, Phys. Rev. A **96**, 053629 (2017).

[76] H.-P. Breuer and F. Petruccione, *The theory of open quantum systems*, 1st ed. (Oxford University Press, 2002).

[77] O. Stenzel, *The physics of thin film optical spectra*, 2nd ed. (Springer, 2016).

[78] L. Novotny and B. Hecht, *Principles of nano-optics*, 2nd ed. (Cambridge University Press, 2012).

[79] Y. Chen, T. R. Nielsen, N. Gregersen, P. Lodahl, and J. Mørk, *Finite-element modeling of spontaneous emission of a quantum emitter at nanoscale proximity to plasmonic waveguides*, Phys. Rev. B **81**, 125431 (2010).

[80] T. Søndergaard and B. Tromborg, *General theory for spontaneous emission in active dielectric microstructures: Example of a fiber amplifier*, Phys. Rev. A **64**, 033812 (2001).

[81] R. Carminati, A. Cazé, D. Cao, F. Peragut, V. Krachmalnicoff, R. Pierrat, and Y. De Wilde, *Electromagnetic density of states in complex plasmonic systems*, Surf. Sci. Rep. **70**, 1–41 (2015).

[82] V. Weisskopf and E. P. Wigner, *Berechnung der natürlichen Linienbreite auf Grund der Diracschen Lichttheorie*, Z. Physik **63**, 54–73 (1930).

[83] L.-W. Li, P.-S. Kooi, M.-S. Leong, and T.-S. Yeo, *On the eigenfunction expansion of dyadic Green's function in planarly stratified media*, J. Electromagn. Waves Appl. **8**, 663–678 (1994).

[84] L.-W. Li, M.-S. Leong, T.-S. Yeo, and P.-S. Kooi, *Electromagnetic dyadic Green's functions in spectral domain for multilayered cylinders*, J. Electromagn. Waves Appl. **14**, 961–985 (2000).

[85] L.-W. Li, P.-S. Kooi, M.-S. Leong, and T.-S. Yee, *Electromagnetic dyadic Green's function in spherically multilayered media*, IEEE Trans. Microw. Theory Tech. **42**, 2302–2310 (1994).

[86] W. C. Chew, *Waves and fields in inhomogeneous media*, 1st ed. (IEEE press, 1995).

[87] M. A. Yurkin and A. G. Hoekstra, *The discrete dipole approximation: an overview and recent developments*, J. Quant. Spectrosc. Radiat. Transf. **106**, 558–589 (2007).

[88] E. M. Purcell and C. R. Pennypacker, *Scattering and absorption of light by nonspherical dielectric grains*, Astrophys. J. **186**, 705–714 (1973).

[89] K. Sander, C. Peltz, C. Varin, S. Scheel, T. Brabec, and T. Fennel, *Influence of wavelength and pulse duration on single-shot x-ray diffraction patterns from nonspherical nanoparticles*, J. Phys. B **48**, 204004 (2015).

[90] P. J. Flatau, G. L. Stephens, and B. T. Draine, *Light scattering by rectangular solids in the discrete-dipole approximation: a new algorithm exploiting the Block-Toeplitz structure*, J. Opt. Soc. Am. A **7**, 593–600 (1990).

[91] B. E. Barrowes, F. L. Teixeira, and J. A. Kong, *Fast algorithm for matrix-vector multiply of asymmetric multilevel block-Toeplitz matrices in 3-D scattering*, Microw. Opt. Technol. Lett. **31**, 28–32 (2001).

[92] A. Rodriguez, M. Ibanescu, D. Iannuzzi, J. D. Joannopoulos, and S. G. Johnson, *Virtual photons in imaginary time: Computing exact Casimir forces via standard numerical electromagnetism techniques*, Phys. Rev. A **76**, 032106 (2007).

[93] A. W. Rodriguez, A. P. McCauley, J. D. Joannopoulos, and S. G. Johnson, *Casimir forces in the time domain: Theory*, Phys. Rev. A **80**, 012115 (2009).

[94] W. C. Chew, E. Michielssen, J. M. Song, and J.-M. Jin, *Fast and efficient algorithms in computational electromagnetics*, 1st ed. (Artech House, Inc., 2001).

[95] M. T. H. Reid and S. G. Johnson, *Efficient computation of power, force, and torque in BEM scattering calculations*, IEEE Trans. Antennas Propag. **63**, 3588–3598 (2015).

[96] M. H. Reid, *Scuff-em: free, open-source boundary-element software*, Available: `http://homerreid.github.io/scuff-em-documentation/` (2018).

[97] P. Y. Chen, D. J. Bergman, and Y. Sivan, *Generalizing normal mode expansion of electromagnetic Green's tensor to open systems*, Phys. Rev. Appl. **11**, 044018 (2019).

[98] H. Gan, Q. Dai, T. Xia, W. C. Chew, and C.-F. Wang, *Broadband spectral numerical Green's function for electromagnetic analysis of inhomogeneous objects*, IEEE Antennas Wirel. Propag. Lett. **19**, 1063–1067 (2020).

[99] C. Cohen-Tannoudji, J. Dupont-Roc, and G. Grynberg, *Photons and Atoms: Introduction to Quantum Electrodynamics*, 1st ed. (Wiley, 1997).

[100] R. E. Raab and O. L. De Lange, *Multipole theory in electromagnetism: classical, quantum, and symmetry aspects, with applications*, 1st ed. (Oxford University Press, 2005).

[101] J. D. Jackson, *Classical electrodynamics*, 3rd ed. (Wiley, 1999).

[102] S. Y. Buhmann, L. Knöll, D.-G. Welsch, and H. T. Dung, *Casimir-Polder forces: A nonperturbative approach*, Phys. Rev. A **70**, 052117 (2004).

[103] E. Clementi and D. L. Raimondi, *Atomic screening constants from SCF functions*, J. Chem. Phys. **38**, 2686–2689 (1963).

[104] E. Clementi, D. L. Raimondi, and W. P. Reinhardt, *Atomic screening constants from SCF functions. II. Atoms with 37 to 86 electrons*, J. Chem. Phys. **47**, 1300–1307 (1967).

[105] W. C. Röntgen, *Über die durch Bewegung eines im homogenen electrischen Felde befindlichen Dielectricums hervorgerufene electrodynamische Kraft*, Ann. Phys. **271**, 264–270 (1888).

[106] M. Weissbluth, *Atoms and Molecules*, 1st ed. (Academic Press, 1978).

[107] P. W. Milonni, *The quantum vacuum: an introduction to quantum electrodynamics*, 1st ed. (Academic press, 1994).

[108] P. W. Milonni, *An introduction to quantum optics and quantum fluctuations*, 1st ed. (Oxford University Press, 2019).

[109] H.-P. Breuer, B. Kappler, and F. Petruccione, *Stochastic wave-function method for non-Markovian quantum master equations*, Phys. Rev. A **59**, 1633 (1999).

[110] G. P. Hildred, S. S. Hassan, R. R. Puri, and R. K. Bullough, *Thermal reservoir effects in resonance fluorescence*, J. Phys. B **16**, 1703 (1983).

[111] S. S. Hassan and R. K. Bullough, *Atoms in coherent and incoherent fields: I. Microscopic theory of Einstein's rate equation*, Physica A **151**, 397–424 (1988).

[112] S. S. Hassan and R. K. Bullough, *Atoms in coherent and incoherent fields: II. Resonance fluorescence in mixed coherent-chaotic fields*, Physica A **151**, 425–446 (1988).

[113] S. Y. Buhmann, M. R. Tarbutt, S. Scheel, and E. A. Hinds, *Surface-induced heating of cold polar molecules*, Phys. Rev. A **78**, 052901 (2008).

[114] W. Greiner and J. Reinhardt, *Field quantization*, 1st ed. (Springer, 1996).

[115] S. Weinberg, *The Quantum Theory of Fields: Volume 1, Foundations*, 1st ed. (Cambridge University Press, 1995).

[116] M. D. Lee, S. D. Jenkins, and J. Ruostekoski, *Stochastic methods for light propagation and recurrent scattering in saturated and nonsaturated atomic ensembles*, Phys. Rev. A **93**, 063803 (2016).

[117] E. M. Purcell, H. C. Torrey, and R. V. Pound, *Resonance absorption by nuclear magnetic moments in a solid*, Phys. Rev. **69**, 37 (1946).

[118] E. M. Purcell, Spontaneous emission probabilities at radio frequencies, in *Confined Electrons and Photons* (Springer, 1995) pp. 839–839.

[119] M. Donaire, M.-P. Gorza, A. Maury, R. Guérout, and A. Lambrecht, *Casimir–Polder-induced Rabi oscillations*, EPL **109**, 24003 (2015).

[120] H. T. Dung, L. Knöll, and D.-G. Welsch, *Resonant dipole-dipole interaction in the presence of dispersing and absorbing surroundings*, Phys. Rev. A **66**, 063810 (2002).

[121] S. Ribeiro, S. Y. Buhmann, T. Stielow, and S. Scheel, *Casimir-Polder interaction from exact diagonalization and surface-induced state mixing*, EPL **110**, 51003 (2015).

[122] M. Fleischhauer and S. F. Yelin, *Radiative atom-atom interactions in optically dense media: Quantum corrections to the Lorentz-Lorenz formula*, Phys. Rev. A **59**, 2427 (1999).

[123] S. Scheel, L. Knöll, and D.-G. Welsch, *Spontaneous decay of an excited atom in an absorbing dielectric*, Phys. Rev. A **60**, 4094 (1999).

[124] H. T. Dung, S. Y. Buhmann, and D.-G. Welsch, *Local-field correction to the spontaneous decay rate of atoms embedded in bodies of finite size*, Phys. Rev. A **74**, 023803 (2006).

[125] H. Alaeian, R. Ritter, M. Basic, R. Löw, and T. Pfau, *Cavity QED based on room temperature atoms interacting with a photonic crystal cavity: a feasibility study*, Appl. Phys. B **126**, 1–10 (2020).

[126] H. Dobbertin, *Van der Waals interaction in structured hollow-core fibres*, Master's thesis, Universität Rostock (2016).

[127] A. Derevianko, W. R. Johnson, M. S. Safronova, and J. F. Babb, *High-precision Calculations of Dispersion Coefficients, Static Dipole Polarizabilities, and Atom-Wall Interaction Constants for Alkali-Metal Atoms*, Phys. Rev. Lett. **82**, 3589 (1999).

[128] M. S. Safronova, C. J. Williams, and C. W. Clark, *Relativistic many-body calculations of electric-dipole matrix elements, lifetimes, and polarizabilities in rubidium*, Phys. Rev. A **69**, 022509 (2004).

[129] A. Derevianko, S. G. Porsev, and J. F. Babb, *Electric dipole polarizabilities at imaginary frequencies for hydrogen, the alkali-metal, alkaline-earth, and noble gas atoms*, At. Data Nucl. Data Tables **96**, 323–331 (2010).

[130] V. P. A. Lonij, C. E. Klauss, W. F. Holmgren, and A. D. Cronin, *Atom Diffraction Reveals the Impact of Atomic Core Electrons on Atom-Surface Potentials*, Phys. Rev. Lett. **105**, 233202 (2010).

[131] P. R. Berman, R. W. Boyd, and P. W. Milonni, *Polarizability and the optical theorem for a two-level atom with radiative broadening*, Phys. Rev. A **74**, 053816 (2006).

[132] R. Loudon and S. M. Barnett, *Theory of the linear polarizability of a two-level atom*, J. Phys. B **39**, S555 (2006).

[133] P. W. Milonni, R. Loudon, P. R. Berman, and S. M. Barnett, *Linear polarizabilities of two-and three-level atoms*, Phys. Rev. A **77**, 043835 (2008).

[134] D.-w. Wang, A.-j. Li, L.-g. Wang, S.-y. Zhu, and M. S. Zubairy, *Effect of the counterrotating terms on polarizability in atom-field interactions*, Phys. Rev. A **80**, 063826 (2009).

[135] A. Thorne, *Spectrophysics*, 2nd ed. (Springer, 1988).

[136] A. Corney, *Atomic and Laser Spectroscopy*, 1st ed. (Oxford University Press, 1977).

[137] L. Chomaz, L. Corman, T. Yefsah, R. Desbuquois, and J. Dalibard, *Absorption imaging of a quasi-two-dimensional gas: a multiple scattering analysis*, New J. Phys. **14**, 055001 (2012).

[138] B. E. A. Saleh and M. C. Teich, *Fundamentals of photonics*, 3rd ed., Vol. 1–2 (Wiley, 2019).

[139] D. M. Harber, J. M. Obrecht, J. M. McGuirk, and E. A. Cornell, *Measurement of the Casimir–Polder force through center-of-mass oscillations of a Bose-Einstein condensate*, Phys. Rev. A **72**, 033610 (2005).

[140] I. Carusotto, L. Pitaevskii, S. Stringari, G. Modugno, and M. Inguscio, *Sensitive measurement of forces at the micron scale using Bloch oscillations of ultracold atoms*, Phys. Rev. Lett. **95**, 093202 (2005).

[141] J. M. Obrecht, R. J. Wild, M. Antezza, L. P. Pitaevskii, S. Stringari, and E. A. Cornell, *Measurement of the temperature dependence of the Casimir–Polder force*, Phys. Rev. Lett. **98**, 063201 (2007).

[142] C. Brand, J. Fiedler, T. Juffmann, M. Sclafani, C. Knobloch, S. Scheel, Y. Lilach, O. Cheshnovsky, and M. Arndt, *A Green's function approach to modeling molecular diffraction in the limit of ultra-thin gratings*, Ann. Phys. **527**, 580–591 (2015).

[143] R. E. Grisenti, W. Schöllkopf, J. P. Toennies, G. C. Hegerfeldt, and T. Köhler, *Determination of atom-surface van der Waals potentials from transmission-grating diffraction intensities*, Phys. Rev. Lett. **83**, 1755 (1999).

[144] R. Brühl, P. Fouquet, R. E. Grisenti, J. P. Toennies, G. C. Hegerfeldt, T. Köhler, M. Stoll, and C. Walter, *The van der Waals potential between metastable atoms and solid surfaces: Novel diffraction experiments vs. theory*, EPL **59**, 357 (2002).

[145] J. D. Perreault, A. D. Cronin, and T. A. Savas, *Using atomic diffraction of Na from material gratings to measure atom-surface interactions*, Phys. Rev. A **71**, 053612 (2005).

[146] J. D. Perreault and A. D. Cronin, *Observation of atom wave phase shifts induced by van der Waals atom-surface interactions*, Phys. Rev. Lett. **95**, 133201 (2005).

[147] A. Landragin, J.-Y. Courtois, G. Labeyrie, N. Vansteenkiste, C. I. Westbrook, and A. Aspect, *Measurement of the van der Waals force in an atomic mirror*, Phys. Rev. Lett. **77**, 1464 (1996).

[148] H. Bender, P. W. Courteille, C. Marzok, C. Zimmermann, and S. Slama, *Direct measurement of intermediate-range Casimir–Polder potentials*, Phys. Rev. Lett. **104**, 083201 (2010).

[149] F. Shimizu, *Specular reflection of very slow metastable neon atoms from a solid surface*, Phys. Rev. Lett. **86**, 987 (2001).

[150] C. I. Sukenik, M. G. Boshier, D. Cho, V. Sandoghdar, and E. A. Hinds, *Measurement of the Casimir–Polder force*, Phys. Rev. Lett. **70**, 560 (1993).

[151] V. Sandoghdar, C. I. Sukenik, E. A. Hinds, and S. Haroche, *Direct measurement of the van der Waals interaction between an atom and its images in a micron-sized cavity*, Phys. Rev. Lett. **68**, 3432 (1992).

[152] V. Sandoghdar, C. I. Sukenik, S. Haroche, and E. A. Hinds, *Spectroscopy of atoms confined to the single node of a standing wave in a parallel-plate cavity*, Phys. Rev. A **53**, 1919 (1996).

[153] J. Guo, J. Cooper, A. Gallagher, and M. Lewenstein, *Theory of selective reflection spectroscopy*, Opt. Commun. **110**, 732–743 (1994).

[154] M. Chevrollier, M. Fichet, M. Oria, G. Rahmat, D. Bloch, and M. Ducloy, *High resolution selective reflection spectroscopy as a probe of long-range surface interaction: measurement of the surface van der Waals attraction exerted on excited Cs atoms*, J. Phys. II France **2**, 631–657 (1992).

[155] P. Wang, A. Gallagher, and J. Cooper, *Selective reflection by Rb*, Phys. Rev. A **56**, 1598 (1997).

[156] M. Fichet, G. Dutier, A. Yarovitsky, P. Todorov, I. Hamdi, I. Maurin, S. Saltiel, D. Sarkisyan, M.-P. Gorza, D. Bloch, and M. Ducloy, *Exploring the van der Waals atom-surface attraction in the nanometric range*, EPL **77**, 54001 (2007).

[157] A. Sargsyan, A. Papoyan, I. G. Hughes, C. S. Adams, and D. Sarkisyan, *Selective reflection from an Rb layer with a thickness below $\lambda/12$ and applications*, Opt. Lett. **42**, 1476–1479 (2017).

[158] T. Peyrot, N. Šibalić, Y. Sortais, A. Browaeys, A. Sargsyan, D. Sarkisyan, I. Hughes, and C. Adams, *Measurement of the atom-surface van der Waals interaction by transmission spectroscopy in a wedged nanocell*, Phys. Rev. A **100**, 022503 (2019).

[159] H. Failache, S. Saltiel, M. Fichet, D. Bloch, and M. Ducloy, *Resonant van der Waals Repulsion between Excited Cs Atoms and Sapphire Surface*, Phys. Rev. Lett. **83**, 5467 (1999).

[160] H. Failache, S. Saltiel, M. Fichet, D. Bloch, and M. Ducloy, *Resonant coupling in the van der Waals interaction between an excited alkali atom and a dielectric surface: an experimental study via stepwise selective reflection spectroscopy*, Eur. Phys. J. D **23**, 237–255 (2003).

[161] A. Laliotis, T. P. De Silans, I. Maurin, M. Ducloy, and D. Bloch, *Casimir–Polder interactions in the presence of thermally excited surface modes*, Nat. Commun. **5**, 1–8 (2014).

[162] J. N. Israelachvili, *Intermolecular and Surface Forces*, 3rd ed. (Academic Press, 2011).

[163] M. Fichet, F. Schuller, D. Bloch, and M. Ducloy, *van der Waals interactions between excited-state atoms and dispersive dielectric surfaces*, Phys. Rev. A **51**, 1553 (1995).

[164] S. Lubkin, *A method of summing infinite series*, J. Res. Nat. Bur. Standards **48**, 228–254 (1952).

[165] A. D. Yaghjian, *Electric dyadic Green's functions in the source region*, Proceedings of the IEEE **68**, 248–263 (1980).

[166] N. Papageorgiou, *Spectroscopie de réflexion à très haute résolution sur la vapeur de Césium: Déplacement collisionnel, structure Zeeman et effets de saturation sur la raie D_2*, Ph.D. thesis, Université Paris 13 Nord (1994).

[167] T. Peyrot, Y. R. P. Sortais, J.-J. Greffet, A. Browaeys, A. Sargsyan, J. Keaveney, I. G. Hughes, and C. S. Adams, *Optical Transmission of an Atomic Vapor in the Mesoscopic Regime*, Phys. Rev. Lett. **122**, 113401 (2019).

[168] M. Born and E. Wolf, *Principles of Optics*, 7th ed. (Cambridge University Press, 1999).

[169] R. Loudon, *The Quantum Theory of Light*, 3rd ed. (Oxford University Press, 2000).

[170] R. Friedberg, S. R. Hartmann, and J. T. Manassah, *Frequency shifts in emission and absorption by resonant systems of two-level atoms*, Phys. Rep. **7**, 101–179 (1973).

[171] E. L. Lewis, *Collisional relaxation of atomic excited states, line broadening and interatomic interactions*, Phys. Rep. **58**, 1–71 (1980).

[172] N. Allard and J. Kielkopf, *The effect of neutral nonresonant collisions on atomic spectral lines*, Rev. Mod. Phys. **54**, 1103 (1982).

[173] L. Weller, R. J. Bettles, P. Siddons, C. S. Adams, and I. G. Hughes, *Absolute absorption on the rubidium D_1 line including resonant dipole-dipole interactions*, J. Phys. B **44**, 195006 (2011).

[174] J. J. Maki, M. S. Malcuit, J. E. Sipe, and R. W. Boyd, *Linear and nonlinear optical measurements of the Lorentz local field*, Phys. Rev. Lett. **67**, 972 (1991).

[175] G. Comsa and R. David, *Dynamical parameters of desorbing molecules*, Surf. Sci. Rep. **5**, 145–198 (1985).

[176] M. Knudsen, *Das Cosinusgesetz in der kinetischen Gastheorie*, Ann. Phys. **353**, 1113–1121 (1916).

[177] P. Todorov and D. Bloch, *Testing the limits of the Maxwell distribution of velocities for atoms flying nearly parallel to the walls of a thin cell*, J. Chem. Phys. **147**, 194202 (2017).

[178] D. Grischkowsky, Angular and velocity distribution of desorbed sodium atoms, Appl. Phys. Lett. **36**, 711–713 (1980).

[179] M. F. H. Schuurmans, *Spectral narrowing of selective reflection*, J. Phys. France **37**, 469–485 (1976).

[180] G. C. Bjorklund, *Frequency-modulation spectroscopy: a new method for measuring weak absorptions and dispersions*, Opt. Lett. **5**, 15–17 (1980).

[181] J. L. Hall, L. Hollberg, T. Baer, and H. G. Robinson, *Optical heterodyne saturation spectroscopy*, Appl. Phys. Lett. **39**, 680–682 (1981).

[182] G. C. Bjorklund, M. D. Levenson, W. Lenth, and C. Ortiz, *Frequency modulation (FM) spectroscopy*, Appl. Phys. B. **32**, 145–152 (1983).

[183] F. W. J. Olver, D. W. Lozier, R. F. Boisvert, and C. W. Clark, *NIST handbook of mathematical functions hardback and CD-ROM*, 1st ed. (Cambridge University Press, 2010).

[184] G. Dutier, A. Yarovitski, S. Saltiel, A. Papoyan, D. Sarkisyan, D. Bloch, and M. Ducloy, *Collapse and revival of a Dicke-type coherent narrowing in a sub-micron thick vapor cell transmission spectroscopy*, EPL **63**, 35 (2003).

[185] D. Sarkisyan, T. Varzhapetyan, A. Sarkisyan, Y. Malakyan, A. Papoyan, A. Lezama, D. Bloch, and M. Ducloy, *Spectroscopy in an extremely thin vapor cell: Comparing the cell-length dependence in fluorescence and in absorption techniques*, Phys. Rev. A **69**, 065802 (2004).

[186] A. Sargsyan, Y. Pashayan-Leroy, C. Leroy, and D. Sarkisyan, *Collapse and revival of a Dicke-type coherent narrowing in potassium vapor confined in a nanometric thin cell*, J. Phys. B **49**, 075001 (2016).

[187] R. H. Dicke, *The effect of collisions upon the Doppler width of spectral lines*, Phys. Rev. **89**, 472 (1953).

[188] T. Peyrot, *Dipole dipole interactions in dense alkali vapors confined in nanoscale cells*, Ph.D. thesis, Université Paris-Saclay (2019), available: `https://pastel.archives-ouvertes.fr/tel-02321334`.

[189] J. C. de Aquino Carvalho, P. Pedri, M. Ducloy, and A. Laliotis, *Retardation effects in spectroscopic measurements of the Casimir–Polder interaction*, Phys. Rev. A **97**, 023806 (2018).

[190] D. Levin, *Procedures for computing one-and two-dimensional integrals of functions with rapid irregular oscillations*, Math. Comput. **38**, 531–538 (1982).

[191] D. Levin, *Fast integration of rapidly oscillatory functions*, J. Comput. Appl. Math. **67**, 95–101 (1996).

[192] J. Guo, J. Cooper, and A. Gallagher, *Selective reflection from a dense atomic vapor*, Phys. Rev. A **53**, 1130 (1996).

[193] A. V. Ermolaev and T. A. Vartanyan, *Rigorous theory of thin-vapor-layer linear optical properties: The case of specular reflection of atoms colliding with the walls*, Phys. Rev. A **101**, 053850 (2020).

[194] H. Dobbertin, R. Löw, and S. Scheel, *Collective dipole-dipole interactions in planar nanocavities*, Phys. Rev. A **102**, 031701 (2020).

[195] F. Andreoli, M. J. Gullans, A. A. High, A. Browaeys, and D. E. Chang, *Maximum refractive index of an atomic medium*, Phys. Rev. X **11**, 011026 (2021).

[196] S. J. Roof, K. J. Kemp, M. D. Havey, and I. M. Sokolov, *Observation of Single-Photon Superradiance and the Cooperative Lamb Shift in an Extended Sample of Cold Atoms*, Phys. Rev. Lett. **117**, 073003 (2016).

[197] R. Röhlsberger, K. Schlage, B. Sahoo, S. Couet, and R. Rüffer, *Collective Lamb Shift in Single-Photon Superradiance*, Science **328**, 1248–1251 (2010).

[198] J. Haber, J. Gollwitzer, S. Francoual, M. Tolkiehn, J. Strempfer, and R. Röhlsberger, *Spectral control of an x-ray l-edge transition via a thin-film cavity*, Phys. Rev. Lett. **122**, 123608 (2019).

[199] S. G. Johnson, *Faddeeva Package*, Available: `http://ab-initio.mit.edu/wiki/index.php/Faddeeva_Package` (2017).

[200] D. York, N. M. Evensen, M. L. Martınez, and J. De Basabe Delgado, *Unified equations for the slope, intercept, and standard errors of the best straight line*, Am. J. Phys. **72**, 367–375 (2004).

[201] E. D. Palik, *Handbook of optical constants of solids, Five-Volume Set*, 1st ed., Vol. 1-5 (Academic press, 1997).

[202] A. Rohatgi, *Webplotdigitizer: Version 4.5*, Available: `https://automeris.io/WebPlotDigitizer` (2021).

[203] J. Ruostekoski and J. Javanainen, *Emergence of correlated optics in one-dimensional waveguides for classical and quantum atomic gases*, Phys. Rev. Lett. **117**, 143602 (2016).

[204] A. Goban, C.-L. Hung, J. D. Hood, S.-P. Yu, J. A. Muniz, O. Painter, and H. J. Kimble, *Superradiance for Atoms Trapped along a Photonic Crystal Waveguide*, Phys. Rev. Lett. **115**, 063601 (2015).

[205] A. González-Tudela, C.-L. Hung, D. E. Chang, J. I. Cirac, and H. J. Kimble, *Subwavelength vacuum lattices and atom-atom interactions in two-dimensional photonic crystals*, Nat. Photonics **9**, 320 (2015).

[206] A. Asenjo-Garcia, J. D. Hood, D. E. Chang, and H. J. Kimble, *Atom-light interactions in quasi-one-dimensional nanostructures: A Green's-function perspective*, Phys. Rev. A **95**, 033818 (2017).

[207] D. W. Vernooy, A. Furusawa, N. P. Georgiades, V. S. Ilchenko, and H. J. Kimble, *Cavity QED with high-Q whispering gallery modes*, Phys. Rev. A **57**, R2293 (1998).

[208] E. Vetsch, D. Reitz, G. Sagué, R. Schmidt, S. T. Dawkins, and A. Rauschenbeutel, *Optical Interface Created by Laser-Cooled Atoms Trapped in the Evanescent Field Surrounding an Optical Nanofiber*, Phys. Rev. Lett. **104**, 203603 (2010).

[209] S. Ghosh, A. R. Bhagwat, C. K. Renshaw, S. Goh, A. L. Gaeta, and B. J. Kirby, *Low-Light-Level Optical Interactions with Rubidium Vapor in a Photonic Band-Gap Fiber*, Phys. Rev. Lett. **97**, 023603 (2006).

[210] H. Hattermann, D. Bothner, L. Y. Ley, B. Ferdinand, D. Wiedmaier, L. Sárkány, R. Kleiner, D. Koelle, and J. Fortágh, *Coupling ultracold atoms to a superconducting coplanar waveguide resonator*, Nat. Commun. **8**, 2254 (2017).

[211] R. H. Lehmberg, *Radiation from an N-atom system. I. General formalism*, Phys. Rev. A **2**, 883 (1970).

[212] R. H. Lehmberg, *Radiation from an N-atom system. II. Spontaneous emission from a pair of atoms*, Phys. Rev. A **2**, 889 (1970).

[213] R. Bennett and S. Y. Buhmann, *Inverse design of light–matter interactions in macroscopic QED*, New J. Phys. **22**, 093014 (2020).

[214] R. Bennett, *Inverse design of environment-induced coherence*, Phys. Rev. A **103**, 013706 (2021).

[215] P. Gay-Balmaz and O. J. F. Martin, *Validity domain and limitation of non-retarded Green's tensor for electromagnetic scattering at surfaces*, Opt. Commun. **184**, 37–47 (2000).

[216] L.-W. Li, P.-S. Kooi, M.-S. Leong, and T.-S. Yeo, *On the eigenfunction expansion of dyadic Green's function in planarly stratified media*, J. Electromagn. Waves Appl. **8**, 663–678 (1994).

[217] M. Paulus, P. Gay-Balmaz, and O. J. F. Martin, *Accurate and efficient computation of the Green's tensor for stratified media*, Phys. Rev. E **62**, 5797 (2000).

[218] M.-P. Gorza, S. Saltiel, H. Failache, and M. Ducloy, *Quantum theory of van der Waals interactions between excited atoms and birefringent dielectric surfaces*, Eur. Phys. J. D **15**, 113–126 (2001).

[219] J. J. Saarinen and J. E. Sipe, *A Green function approach to surface optics in anisotropic media*, J. Mod. Opt. **55**, 13–32 (2008).

[220] H. Fearn, D. F. V. James, and P. W. Milonni, *Microscopic approach to reflection, transmission, and the Ewald–Oseen extinction theorem*, Am. J. Phys. **64**, 986–995 (1996).

[221] P. C. Chaumet, A. Sentenac, and A. Rahmani, *Coupled dipole method for scatterers with large permittivity*, Phys. Rev. E **70**, 036606 (2004).

[222] D. E. Livesay and K.-M. Chen, *Electromagnetic fields induced inside arbitrarily shaped biological bodies*, IEEE Trans. Microw. Theory Tech. **22**, 1273–1280 (1974).

[223] A. Lakhtakia and G. W. Mulholland, *On two numerical techniques for light scattering by dielectric agglomerated structures*, J. Res. Natl. Inst. Stand. Technol. **98**, 699 (1993).

[224] R. Barrett, M. Berry, T. F. Chan, J. Demmel, J. Donato, J. Dongarra, V. Eijkhout, R. Pozo, C. Romine, and H. Van der Vorst, *Templates for the solution of linear systems: building blocks for iterative methods* (SIAM, 1994).

[225] R. Schmehl, B. M. Nebeker, and E. D. Hirleman, *Discrete-dipole approximation for scattering by features on surfaces by means of a two-dimensional fast Fourier transform technique*, J. Opt. Soc. Am. A **14**, 3026–3036 (1997).

[226] M. A. Yurkin and M. Huntemann, *Rigorous and fast discrete dipole approximation for particles near a plane interface*, J. Phys. Chem. C **119**, 29088–29094 (2015).

[227] B. Renaud, R. M. Whitley, and C. R. Stroud Jr, *Correlation functions and the AC Stark effect*, J. Phys. B **9**, L19 (1976).

[228] F. Zhang, *The Schur Complement and Its Applications*, 1st ed. (Springer, 2005).

[229] J. D. Pritchard, *Cooperative Optical Non-linearity in a blockaded Rydberg ensemble* (Springer, 2012).

[230] I. I. Sobelman, *Atomic spectra and radiative transitions*, 2nd ed. (Springer, 1992).

[231] M. S. Safronova and U. I. Safronova, *Critically evaluated theoretical energies, lifetimes, hyperfine constants, and multipole polarizabilities in Rb 87*, Phys. Rev. A **83**, 052508 (2011).

[232] I. Shavitt and R. J. Bartlett, *Many-body methods in chemistry and physics: MBPT and coupled-cluster theory*, 1st ed. (Cambridge University Press, 2009).

[233] N. Šibalić, J. D. Pritchard, C. S. Adams, and K. J. Weatherill, *ARC: An open-source library for calculating properties of alkali Rydberg atoms*, Comput. Phys. Commun. **220**, 319–331 (2017).

[234] E. J. Robertson, N. Šibalić, R. M. Potvliege, and M. P. A. Jones, *ARC 3.0: An expanded Python toolbox for atomic physics calculations*, Comput. Phys. Commun. **261**, 107814 (2021).

[235] A. Kramida, Yu. Ralchenko, J. Reader, and NIST ASD Team, *NIST Atomic Spectra Database (ver. 5.8)*, Available: `https://physics.nist.gov/asd` (2016).

[236] A. D. Rakić, A. B. Djurišić, J. M. Elazar, and M. L. Majewski, *Optical properties of metallic films for vertical-cavity optoelectronic devices*, Appl. Opt. **37**, 5271–5283 (1998).

[237] G. E. Jellison Jr and F. A. Modine, *Parameterization of the optical functions of amorphous materials in the interband region*, Appl. Phys. Lett. **69**, 371–373 (1996).

[238] G. E. Jellison Jr and F. A. Modine, *Erratum:"Parameterization of the optical functions of amorphous materials in the interband region"[Appl. Phys. Lett. 69, 371 (1996)]*, Appl. Phys. Lett. **69**, 2137–2137 (1996).

[239] L. V. Rodríguez-de Marcos and J. I. Larruquert, *Analytic optical-constant model derived from Tauc-Lorentz and Urbach tail*, Opt. Express **24**, 28561–28572 (2016).

[240] R. Kitamura, L. Pilon, and M. Jonasz, *Optical constants of silica glass from extreme ultraviolet to far infrared at near room temperature*, Appl. Opt. **46**, 8118–8133 (2007).

Danksagungen

Ich möchte mich bei allen bedanken, die mich während meiner Promotions- und Studienzeit unterstützt haben. Mein besonderer Dank gilt Stefan Scheel für die hervorragende Betreuung dieser Arbeit, das Vermitteln von Austausch und Zusammenarbeit mit anderen Wissenschaftlern, die große Offenheit gegenüber meinen Forschungsideen und -Ansätzen, die Verlässlichkeit und die Hilfe bei allen meinen Anliegen. Ich bitte, die Verwendung von amerikanischem Englisch in dieser Arbeit zu verzeihen. Darüber hinaus bedanke ich mich bei Maxim Yurkin für die Literatur, Tipps und Diskussionen zur DDA, bei Ralf Ritter und Robert Löw für die gute Zusammenarbeit sowie bei letzterem für die Einladungen zu Konferenzen, die mich sehr gefreut und geehrt haben. Darüber hinaus danke ich Tom Peyrot für das Teilen seiner Daten und Einsichten und bei Johannes Block für die technische Unterstützung als Admin und den wissenschaftlichen Austausch. Die Forschungsarbeit wäre nicht möglich gewesen ohne die stete Aufmunterung, die Geduld und Unterstützung meiner großartigen Familie und meiner wunderbaren Freundin Gerry. Schließlich bleibt mir, meinen besonderen Dank meinen fantastischen Freunden auszusprechen, von denen mich viele mein ganzes Studium lang begleitet haben. Niemand rechnet mit der spanischen Inquisition oder dem Glück diesen Weg mit euch zu gehen.

Selbständigkeitserklärung

Ich versichere hiermit an Eides statt, dass ich die vorliegende Arbeit selbstständig angefertigt und ohne fremde Hilfe verfasst habe, keine außer den von mir angegebenen Hilfsmitteln und Quellen dazu verwendet habe und die den benutzten Werken inhaltlich und wörtlich entnommenen Stellen als solche kenntlich gemacht habe.

Rostock, den 10.11.2021